J. Bangladesh Acad. Sci. Volume 50, Issue 1, March 2026

ISSN 2224-7270 (Online), 0378-8121 (Print)

Journal of Bangladesh Academy of Sciences is published four times a year (March, June, September and December comprising one volume) in English. Original research articles, review articles, and short communications of all branches of Science and Technology are considered for publication in this journal. Review articles are generally by invitation.

Disclaimer

Submission

All correspondence regarding contributions for publication in the journal should be addressed to the *Editor, Journal of Bangladesh Academy of Sciences* <jbas.editor@yahoo.com>. Authors should consult the contributor’s guideline at the back of the journal before submitting their manuscripts.

Published by

Bangladesh Academy of Sciences, National Science and Technology Complex, Agargaon, Dhaka-1207.

Design and Printed by

Sucharu Desktop Publishing, 1/E/1, Paribagh, Dhaka-1000, Bangladesh

Annual Subscription: Tk. 500.00 (Bangladesh); US $ 60.00; £ 21.50 plus postage.
Single Copy: Tk. 250.00 (Bangladesh); US $ 30.00; £ 11.25 plus postage.

Obituary

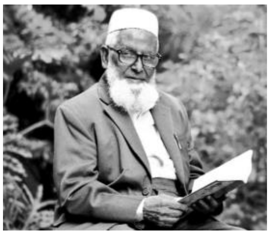

National Professor Dr. A. K. M. Aminul Haque
(1929-2022)

National Professor Dr. A. K. M. Aminul Haque was born on 02 July, 1929 in Char Jamail village of Husainpur upazila under Kishoreganj district and died on 29 August 2022 at the age of 93 in Gulshan, Dhaka, Bangladesh. He left behind two sons, one daughter, a wife and many relatives.

Professor Haque was the eminent Fisheries Scientist who had remarkable contribution to Fisheries Biology, especially Cetacean (dolphin, porpoise and whale). He is the Founder of Fisheries education in Bangladesh since he introduced the first ever fisheries education as a distinct academic and development discipline in this subcontinent by establishing the Faculty of Fisheries at Bangladesh Agricultural University, Mymensingh, in 1967.

Professor Haque was exceedingly meritorious with the record that he received a merit-based scholarship at the most public examinations from primary education to Ph.D. degree study. He passed the Matriculation examination under Calcutta University in 1946, securing first division with the 10th position among all students and first position among all Muslim students in the whole university. He passed I. Sc. examination under Dhaka University in 1948, obtaining first division, B. Sc. from Dhaka University in 1950, acquiring first division with distinction, and M. Sc. from Panjab University in 1952, getting a first class. He obtained a Ph.D. from Nottingham University in 1957 and did SEATO Post-doctoral study at Tokyo University from 1970-1971.

Professor Haque has a brilliant and outstanding professional career. He started his career as a Lecturer of Zoology at Dhaka University during 1952-1954; Senior Lecturer of Zoology at Dhaka University during 1957-1962; Reader of Zoology at East Pakistan (now Bangladesh) Agricultural University (BAU) during 1962-1967; Professor of Fisheries at BAU during 1967-1989; Dean of the Faculty of Fisheries for 12 years from 1968 to 1980; Visiting Professor of Tokyo University, Japan in 1970-1971; Guest Teacher, Chulalongkorn University, Thailand in 1971. He was the Vice Chancellor of Bangladesh Agricultural University for eight years, during 1980-1988.

Professor Haque received many prestigious awards, honors and distinctions, notably UNESCO prizes for a school textbook (1961-1962) and a book “Chil-Myna-Doel-Koel” (1963-1964), Fish Fortnight Gold Medal 1996 & 2003, National Teachers Day Gold Medal Award in the University Category 2003, Dr. S. D. Chaudhuri Gold Medal 2004, National Professorship 2006, Life Time Achievement Award 2008, and CSRL, GROW and OXFAM Award 2011. He was a BAS Fellow from1988 until his death.

Professor Haque was interests in other aspects such as wildlife and environment conservation, bird-watching, dolphin and whale watching, star-gazing, and community welfare. He is recognized as an extraordinarily talented and successful teacher, researcher and science writer. Professor Haque will remain ever reminisced in the minds of thousands of his favorite students, colleagues, friends, and well-wishers at home and abroad.

- M. Jahiruddin

J. Bangladesh Acad. Sci. 47(1); 1-20: June 2023 DOI: https://doi.org/10.3329/jbas.v47i1.66442

Journal of Bangladesh Academy of Sciences

Journal homepage: http://www.bas.org.bd/publications/jbas.html

Review Article

The chemistry of rhenium and manganese carbonyl complexes bearing heterocyclic thiolate ligands: Mono–, di–, tri–, and tetranuclear complexes

Md. Tuhinur Rahman Joy, Jagodish Chandra Sarker[1] and Shariff Enamul Kabir[1,*]

Department of Chemistry, Jashore University of Science and Technology, Jashore, Bangladesh

ARTICLE INFO

Article History

Received: 21 May 2023
Revised: 01 June 2023
Accepted: 11 June 2023

Keywords: Rhenium, Manganese, Carbonyls, Heterocyclic thiols, Polynuclear, Self-assembly, Mixed-metal clusters

ABSTRACT

This article provides an overview of the rich chemistry of rhenium and manganese decacarbonyls, $M_2(CO)_{10}$ (M = Re, Mn) and their acetonitrile derivatives $[M_2(CO)_8(NCMe)_2]$ as precursors for synthesis of new di–, tri– and tetranuclear complexes derived from a wide range of heterocyclic thiols such as pyridine-2-thiol, pyrimidine-2-thiol, tetrahydropyrimidine-2-thiol, 2-mercapto-1-methylimidazole, benzimidazole-2-thiol etc. A comparative study of the reactivities of these complexes with various mono– and bidentate ligands is also the subject of this review. In some instances, the structural aspects of the complexes are also discussed. The applications of these complexes as precursors for the synthesis of a wide variety of mixed-metal cluster complexes are highlighted.

Introduction

The chemistry of transition metal complexes bearing heterocyclic-thiolate ligands is of considerable interest because of their unique structural diversity (Deeming et al., 1988a; Umakoshi et al., 1990; Rose et al., 1994), important biological traits (Rosenfield et al., 1987; Castro et al., 1990; Kienitz et al., 1996; Liaw et al., 1998), and use as precursors for metallosulfide materials (Berardini et al., 1995; Rose et al., 1995; Cheng et al., 1996; Lee et al., 1997). Heterocyclic thiols such as pyridine-2-thiol and pyrimidine-2-thiol exist predominantly in the thiol and tautomeric thionate form (Chart 1).

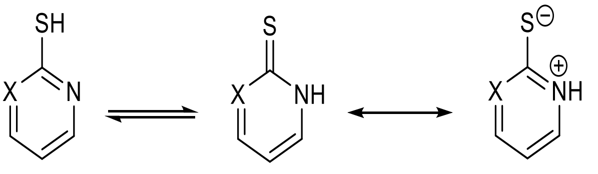

Chart 1. Major tautomers of pyridine-2-thiol (X = C) and pyrimidine -2-thiol (X = N).

Heterocyclic thiols are attractive ligands to synthetic inorganic and organometallic chemists as they are capable of coordinating to the metal centers in a wide variety of ways (Chart 2) due to the presence of both nitrogen and sulfur as potential electron-donating atoms which in turn is expected to influence the nature of the products formed (Deeming et al., 1988b).

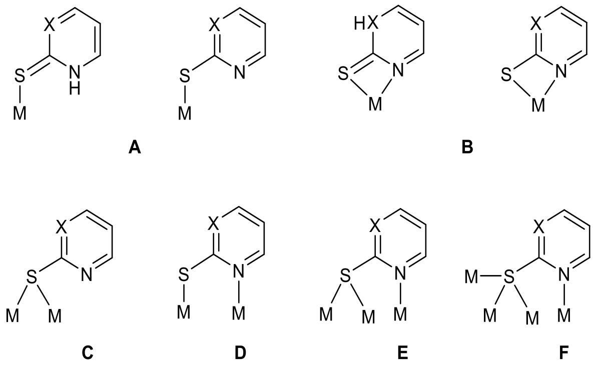

Chart 2. Coordination modes of pyridine-2-thiol (X = C) and pyrimidine -2-thiol (X = N).

The reactivity of heterocyclic thiols such as pyridine-2-thiol (Deeming et al. 1988b; Kabir et al., 2000), pyrimidine-2-thiol (Kabir et al., 2000), tetrahydropyrimidine-2-thiol (Ghosh et al., 2011),

---

*Corresponding author: <skabir_ju@yahoo.com>

[1] *Department of Chemistry, Jagannath University, Dhaka, Bangladesh*

2-mercapto-1-methylimidazole (Ghosh et al., 2009b), 2-mercapto-1-benzothiazole (Ghosh et al., 2010b), thiazole (Kabir et al., 2007; Azam et al., 1998a; Azam et al., 1998b), 4-methylthiazole (Azam et al., 1996), thiazolidine (Hanif et al., 1999), thiomorpholine (Hanif et al., 1999), benzothiazole and benzimidazole-2-thiol (Dilshad et al., 1999) with group 7 metal carbonyls have been investigated over the last three decades. It has been observed from these studies that the reactivity pattern of the heterocyclic thiols is not only determined by the structures of the thiols but also by the intrinsic reactivity of the metal carbonyls used.

Manganese and rhenium carbonyls showed varied reactivity toward pyridine-2-thiol and pyrimidine-2-thiol; pyridine-2-thiol produces dimeric complexes, while pyrimidine-2-thiol forms tetrameric complexes (Deeming et al., 1988b; Kabir et al., 1996). Moreover, carbonyls of these two transition metals experienced different reactivity towards 2-mercapto-1-methylimidazole (five-membered heterocyclic thiol ligand), yielding di–, tri– and tetranuclear complexes (Ghosh et al., 2009b). In addition to exhibiting distinctive structural characteristics, the products isolated from these reactions also showed promise as potential precursors for synthesizing a wide range of mixed-metal complexes (Cockerton et al., 1991; Ghosh et al., 2009b).

The chemistry of mixed-metal clusters of low-valent transition metals has been of enduring interest due to their unique structural properties and various applications resulting from having disparate metals with different chemical properties in close proximity and also because of potential catalytic applications (Muetterties et al., 1977; Broussard et al., 1993; Braunstein et al., 1995; Adams et al., 1998a; Adams et al., 1998b; Quebatte et al., 2004; Gauther et al., 2004). In fact, they have also been used in homogeneous catalysis. Incorporating several metal types in clusters could provide synergistic benefits for catalytic conversion (Muetterties et al., 1977; Fusi et al., 1982; Broussard et al., 1993; Braunstein et al., 1995). The combining catalytic properties of several different metal centers are also provided by mixed-metal clusters, which contain non-equivalent binding sites and hence can be employed in homogeneous catalysis (Beuken et al., 1998; Kalck 1988; Braunstein et al., 1999).

In this review, we aim to summarize some exciting developments in low-valent transition metal carbonyl complexes bearing heterocyclic thiolate ligands, emphasizing their systematic synthesis, structural characterization, and reactivity with mono– and bidentate ligands. To make this article diverse and inclusive, we have also logically incorporated the synthesis and structural properties of mixed-metal cluster complexes of low-valent transition metals.

Reactivity of [$M_2(CO)_{10}$] (M = Re, Mn) towards pyridine-2-thiol (pySH) and pyrimidine-2-thiol (pymSH): Synthesis of di– and tetranuclear square-type complexes

In 1988, Deeming et al. first reported the dinuclear hexhacarbonyl compound [$Re_2(\mu\text{-pyS})_2(CO)_6$] (**1**) in almost quantitative yield (Deeming et al., 1988b) from the reaction of [$Re_2(CO)_{10}$] with pyridine-2-thiol (pySH) in refluxing xylene. The corresponding 6-methylpyridine-2-thiolate analog [$Re_2(\mu\text{-MepyS})_2$-$(CO)_6$] (**2**) was prepared following similar procedures but in lower yield. These dimers contain three fused four-membered rings. Importantly, they observed slow scrambling of [$Re_2(CO)_6(\mu\text{-pyS})_2$] with the 6-methylsubstituted analog [$Re_2(CO)_6$ $(\mu\text{-MepyS})_2$], for which the X-ray structure is reported (Fig. 1), at ambient temperature giving an equilibrium involving [$Re_2(CO)_6(\mu\text{-pyS})(\mu\text{-MepyS})$] (**3**) and suggested that the scrambling process occurred via the 16-electron mononuclear species [$Re(CO)_3(pyS)$] or a related solvent-stabilized 18-electron species. After 8 years, in 1996, we reported the manganese analogs [$Mn_2(\mu\text{-pyS})_2(CO)_6$] **(4)** and [$Mn_2(\mu\text{-MepyS})_2(CO)_6$] (**5**) from the Me_3NO initiated reactions of $Mn_2(CO)_{10}$ with pyridine-2-thiol and 6-methylpyridine-2-thiol, respectively (Kabir et al., 1996).

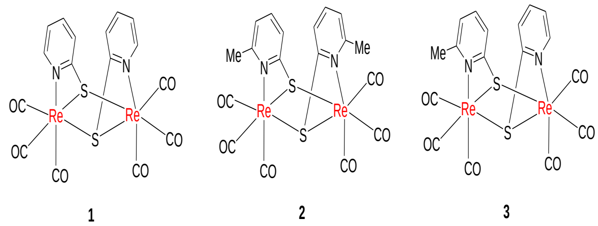

Chart 3. Complexes derived from [$Re_2(CO)_{10}$] reactions with pyS/MepyS.

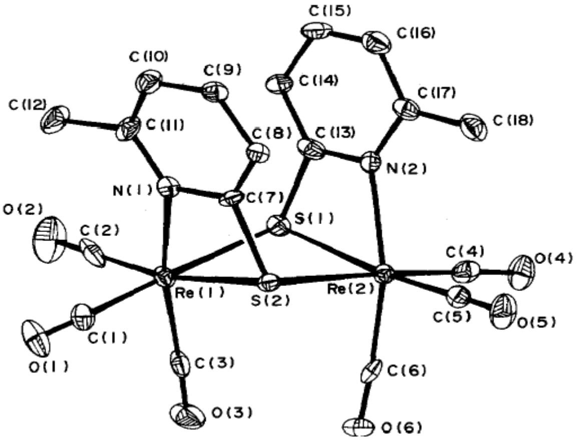

Fig. 1. The solid-state structure of [$Re_2(\mu\text{-}MepyS)_2CO)_6$] (2). Adapted from Kabir et al. 1996.

In these complexes, pyS and MepyS function as five electron donors and span the binuclear center by coordinating sulfur and nitrogen. From the X-ray determined structure of **4** (Fig. 2), it was apparent that it has a chiral structure with C_2 symmetry. The overall structure is very similar to that of its rhenium analog [$Re_2(\mu\text{-}MepyS)_2(CO)_6$] (**2**) (Deeming et al., 1988b). A four-membered chelate ring is formed when each pyS ligand connects two manganese centers through the sulfur atom and one manganese center through the nitrogen atom. Compound **5** is a dinuclear manganese complex that consists of three fused four-membered rings and auxiliary ligands (Fig. 2).

In the last thirty years, quite a large number of tetranuclear square-type complexes have been reported mostly by Stang, Fujita, and their co-workers by applying the self-assembly phenomena (Stanget al., 1994a; Stang et al., 1995; Stang et al., 1996a; Stang et al., 1996b; Stang et al., 1994b; Fujita et al., 1990; Fujita et al., 1996). Most of these complexes are based on a square-planar metal coordination geometry. Kabir and our group has pioneered the synthesis of novel tetranuclear square-type complexes [$M_4(CO)_{12}$ (μ-pymS)$_4$] (**6**, M = Re; **7**, M = Mn) from trimethylamine-N-oxide initiated reactions of $M_2(CO)_{10}$ (M = Re, Mn) with pyrimidine-2-thiol (pymSH) (Kabir et al., 2009). The single crystal X-ray structures of **1** and **6** (Fig. 3) confirm that these molecules are tetranuclear; the four separate *fac*-$M(CO)_3$ units are held together by tridentate pyrimidine-2-thiolate ligands.

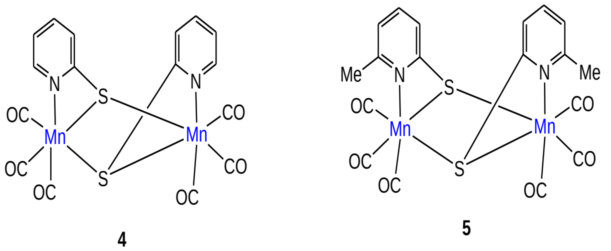

Chart 4. Complexes derived from the reaction of [$Mn_2(CO)_{10}$] and pyS/MepyS.

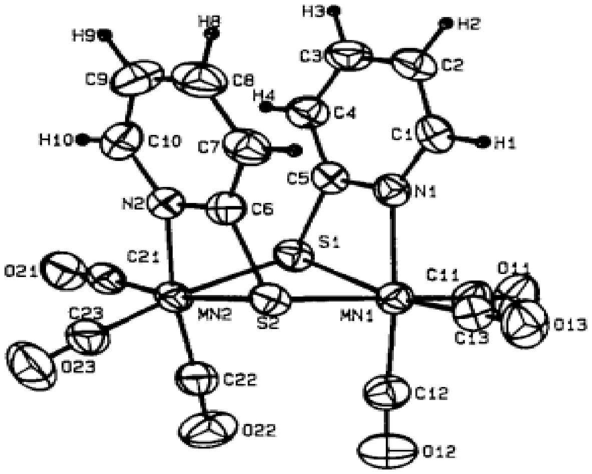

Fig. 2. The molecular structure of [$Mn_2(\mu\text{-}pyS)_2(CO)_6$] (4). Adapted from Kabir et al. 1996.

Two of the pyrimidine-2-thiolate ligands lie above and two below the M_4 plane. The coordination geometry of each metal atom is a distorted octahedron with a *cis*-arrangement of the pyrimidine-2-thiolate ligands. Each metal atom achieves an 18-electron configuration without any appreciable metal-metal interaction considering that each pyrimidine-2- thiolate ligand donates five electrons. Complexes **6** and **7** provide unusual examples of tetranuclear square-type structures bearing heterocyclic thiolate ligands and *fac*-$M(CO)_3$ fragments.

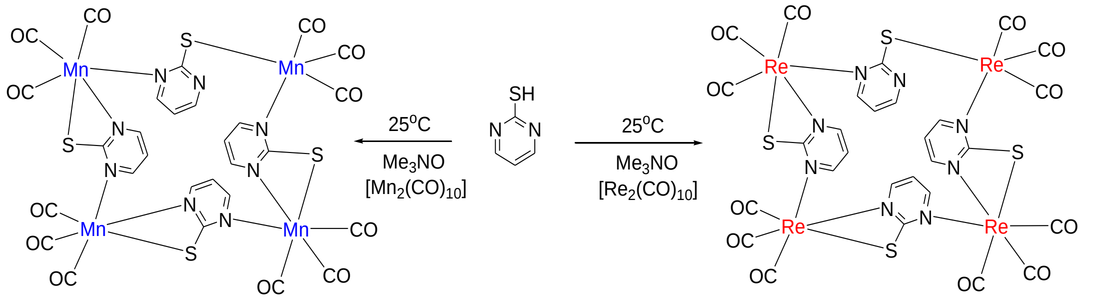

7

6

Scheme 1. Synthesis of square-type complexes $[Re_4(CO)_{12}(\mu\text{-pymS})_4]$(6) and $[Mn_4(CO)_{12}(\mu\text{-pymS})_4]$ (7).

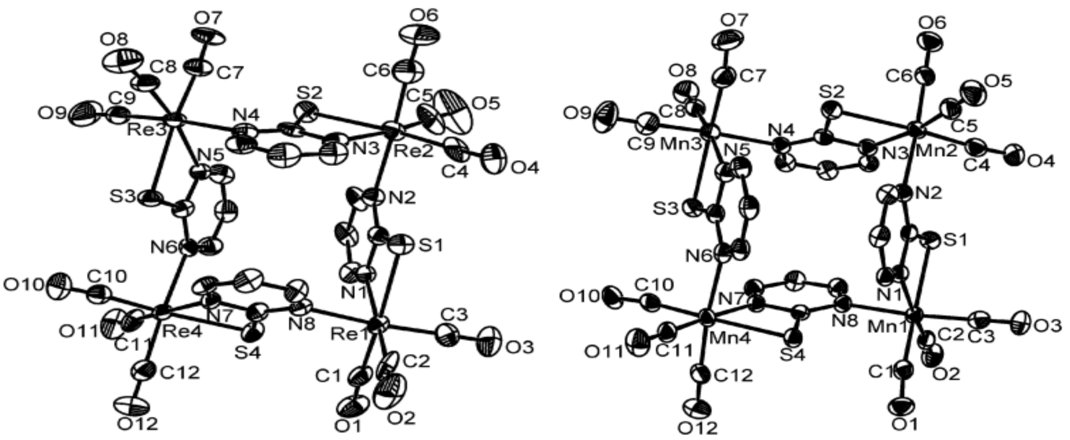

(A) **(B)**

Fig. 3. Molecular structures of (A) $[Re_4(CO)_{12}(\mu\text{-pymS})_4]$ (6) and (B) $[Re_4(CO)_{12}(\mu\text{-pymS})_4]$ (7). Adapted from Kabir et al., 2009.

Reactivity of $[M_2(CO)_6(\mu\text{-pyS})_2]$ (1, M = Re; 4, M = Mn) towards mono–and bidentate ligands.

To explore whether the dinuclear complexes $[M_2(CO)_6(\mu\text{-pyS})_2]$ (**1**, M = Re; **4**, M = Mn) can form mixed-metal clusters when reacted with $(Ph_3P)_2Ni(CO)_2$, the reactions of **1** and **4** with the latter have been investigated. Treatment **4** with $(Ph_3P)_2Ni(CO)_2$ at room temperature furnished the dinuclear complex $[Mn_2(CO)_5(PPh_3)(\mu\text{-pyS})_2]$ (**9**) and the mononuclear *fac*-$[Mn(CO)_3(PPh_3)(\kappa^2\text{-pyS})]$ (**10**), the former being the first example of a carbonyl-substituted product of **4** (Rahman et al., 2012). In contrast, **1** reacts with $(Ph_3P)_2Ni(CO)_2$ at ambient temperature to give mononuclear complex *fac*-$[Re(CO)_3(PPh_3)(\kappa^2\text{-pyS})]$ (**8**). Both **8** and **10** produce $[M(CO)_2(PPh_3)_2(\kappa^2\text{-pyS})]$ (**11**, M = Re; **12**, M = Mn) by CO substitution reaction when they are reacted further with $(Ph_3P)_2Ni(CO)_2$ at

latter have been investigated. Treatment **4** with

room temperature. Additionally, complex **9** reacts further with $(Ph_3P)_2Ni(CO_2)$ to produce **10** and **12**.

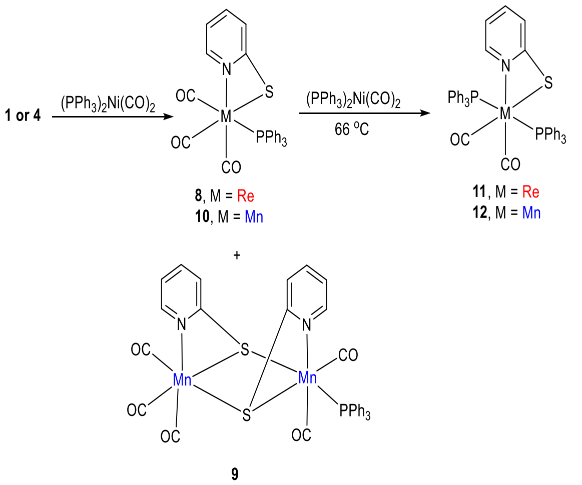

Scheme 2. Reactivity of $[M_2(CO)_6(\mu\text{-pyS})_2]$ (1, M = Re; 4, M = Mn) towards monodentate ligands.

Compound **5** reacts with PPh_3 and dppm [dppm = $Ph_2PCH_2PPh_2$ = bis(diphenylphosphino)methane] in refluxing cyclohexane to give $[Mn(MepyS)(PPh_3)(CO)_3]$ (**13**) and $[Mn(MepyS)(\eta^1\text{-dppm})_2(CO)_2]$ (**14**), respectively (Kabir et al., 1996), the latter containing a dangling dppm ligand. The NMR spectrum identified the η^1 mode of coordination of dppm in compound 14. The two $^2J_{PH}$ values (8 and 1.5 Hz) designate that the two phosphorus atoms in dppm are not equivalent; one is bonded to metal while the other is free from coordination.

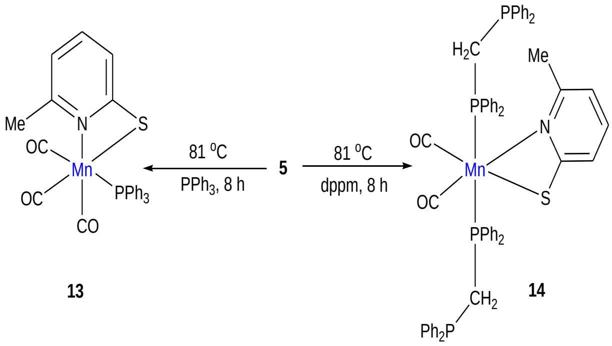

Scheme 3. Reactivity of $[Mn_2(\mu\text{-MepyS})_2(CO)_6]$ (5) towards mono– and bidentate ligands.

Formation of mixed-metal clusters: Reactivity of complexes 1 and 4 towards $[M_3(CO)_{10}(L)_2]$ (M = Fe, Os, Ru; L = CO, NCMe)

The reactions of **1** and **4** with group 8 metal carbonyl clusters have yet to be explored systematically, but the reaction of **1** towards $Ru_3(CO)_{12}$ has received some attention (Cockerton et al., 1991). Heating **1** with $Ru_3(CO)_{12}$ in toluene at 138 °C affords a series of Re–Ru mixed-metal clusters with varying nuclearity like $ReRu_3$, Re_3Ru, and Re_2Ru_2 groups which are formally built up by the combination of the 16-electron mononuclear species $Re(pyS)(CO)_n$ and $Ru(CO)_n$ (n = 2, 3 or 4) units. In contrast, reactions of $[M_2(CO)_6(\mu\text{-pyS})_2]$ (**1**, M = Re; **4**, M = Mn) with $[Os_3(CO)_{10}(NCMe)_2]$ in refluxing benzene at 80 °C furnish the mixed-metal clusters $[MOs_3(CO)_{13}(\mu_3\text{-pyS})]$ (**15**, M = Re; **16**, M = Mn) (Ghosh et al., 2010a). Similar reaction between **1** and $Ru_3(CO)_{12}$ at 80 °C produces $[ReRu_3(CO)_{13}(\mu_3\text{-pyS})]$ (**17**), whereas at 110 °C the tetraruthenium cluster $[Ru_4(CO)_{12}(\mu\text{-py})_2(\mu_4\text{-S})]$ (**18**) has been obtained as the only product (Scheme 4). Thus, the products obtained from reaction **1** with $Ru_3(CO)_{12}$ are temperature dependent. Compound 18 comprises two $Ru_2(CO)_6(\mu\text{-py})$units linked by a quadruply bridging sulfur ligand. The solid-state structure shows that the 2-pyridyl ligands, formed by cleavage of the C–S bond of the coordinated pyS ligand, span across two different Ru–Ru edges. Compound $[Mn_2(CO)_6(\mu\text{-pyS})_2]$ (**4**) reacts with $Ru_3(CO)_{12}$ to afford $[MnRu_3(CO)_{13}(\mu_3\text{-pyS})]$ (**19**) as the sole product. Introduction of PPh_3 to 15 in the presence of Me_3NO yields both the rnono– and bis(phosphine) substituted products $[ReOs_3(CO)_{12}\text{-}(PPh_3)(\mu_3\text{-pyS})]$ (**20**) and $[ReOs_3(CO)_{11}(PPh_3)_2(\mu_3\text{-pyS})]$ (**21**), respectively (Scheme 4).

They then examined the reactions of **1** and **4** with $Fe_3(CO)_{12}$ at 110 °C, from which two completely different products have been isolated; the Fe_2Re_2 mixed-metal sulfido cluster $[Fe_2Re_2(CO)_{13}(\mu\text{-py})(\mu\text{-pyS})(\mu_4\text{-S})]$ (**22**) and the tetrairon cluster $[Fe_4(CO)_{12}(\mu\text{-py})_2(\mu_4\text{-S})]$ (**23**) (Scheme 5), respectively. All the mixed-metal clusters have been structurally characterized.

To see whether the manganese dimer $[Mn_2(CO)_6(pyS)_2]$ (**4**) can act as a precursor for the synthesis of Mo–Mn mixed metal complexes, Begum et al. investigated the reaction of $[Mn_2(CO)_6(pyS)_2]$**(4)** with $[CpMo(CO)_3]_2$. Thus boiling a toluene solution of the dimer **4** at 110 °C yields the Mo–Mn mixed metal complex $[CpMoMn(CO)_3(\mu\text{-CO})(\mu\text{-}\eta^2\text{-pyS})(\mu\text{-}\eta^1\text{-pyS})]$, the

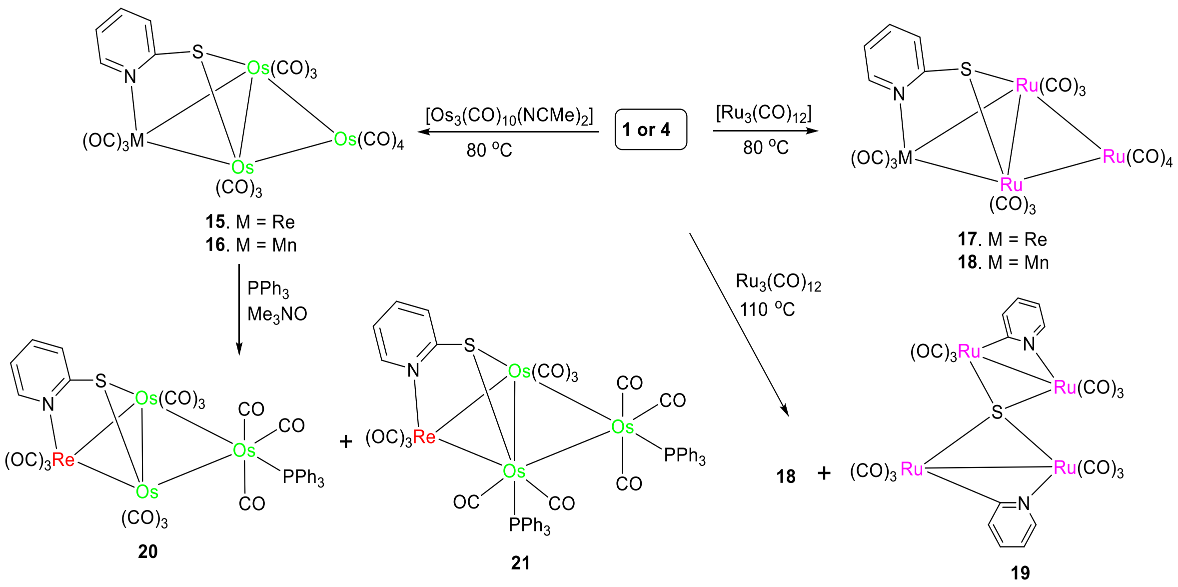

Scheme 4. Formation of mixed-metal clusters from the reactions of $[M_2(CO)_6(\mu\text{-pyS})_2]$ (M = Re, Mn) with $[M_3(CO)_{10}(L)_2]$ (M = Os, Ru; L = CO, NCMe).

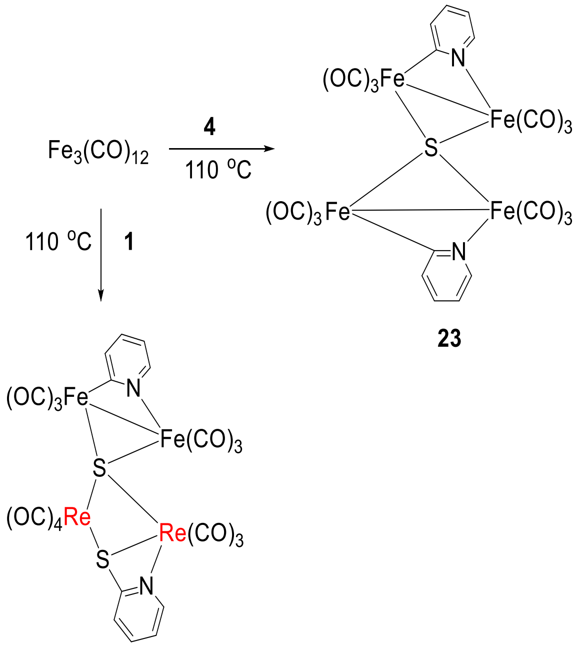

Scheme 5. Reactivity of $[M_2(CO)_6(\mu\text{-pyS})_2]$ (M = Re, Mn) towards $Fe_3(CO)_{12}$.

unsaturated trimolybdenum cluster $[Cp_3Mo_3(\mu\text{-}CO)_2(\mu\text{-}S)(\mu_3\text{-}S)(\mu\text{-}\eta^2\text{-}NC_5H_4)]$ (**26**) and the mononuclear molybdenum complex $[CpMo(\mu\text{-}CO)_2)(\eta^2\text{-pyS})]$ (Begum et al., 2005). Diffraction studies have determined the structures of all three compounds. Complex **24** represents an unusual example of a Mo–Mn heterodinuclear complex containing a μ-η^2-pyridine-2-thiolato, a μ-η^1-pyridine-2- thiolato, and a cyclopentadienyl ligand. The 46-electron cluster **26** is a rare example of a 46-electron trimolybdenum cluster bearing three cyclopentadienyl ligands, an orthometalated pyridyl ligands, a capping sulfide, a bridging sulfido, and two semi bridging ligands. The facile cleavage of the sulfur–carbon bond illustrated by the formation of **26** is reminiscent of numerous literature examples (Neumann et al., 1988).

Reactivity of tetranuclear complexes $[M_4(CO)_{12}(\mu\text{-pymS})_4]$ (6, M = Re; 7, M = Mn) towards mono– and bidentate ligands

Kabir and co-workers reported that the reactions of $[M_4(CO)_{12}(\mu\text{-pymS})_4]$ (**6**, M = Re; **7**, M = Mn) with donor ligands result in breaking the square-type skeleton to produce mononuclear species containing either mono– or bidentate pyrimidine-2-thiolate ligands (Kabir et al., 2009; Rahman et al., 2012). In those articles, they showed that a 2-electron donor ligand, PPh_3 reacts with **7** to

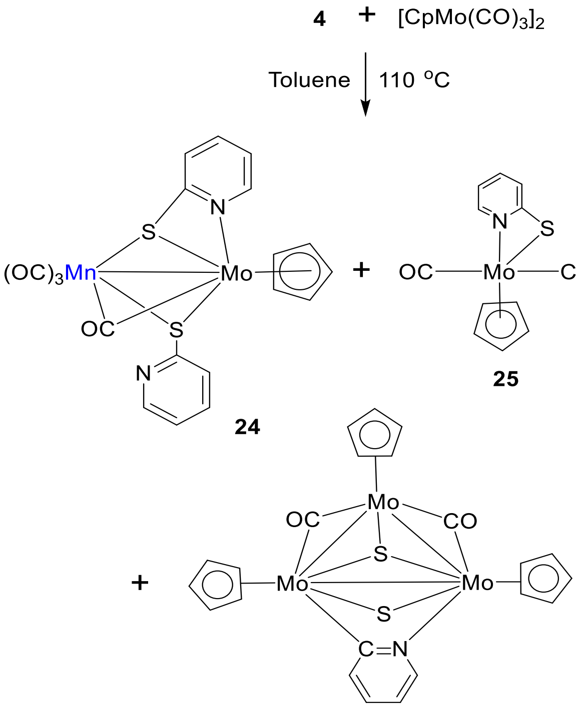

Scheme 6. Reactivity of $[Mn_2(CO)_6(\mu\text{-pyS})_2]$ towards $(CpMo(CO)_3)_2$.

produce $[Mn(CO)_3(PPh_3)(\kappa^2\text{-pymS})]$ (**27**) in which the pyrimidindne-2-thiolate ligand binds in a bidentate fashion while the bidentate N-donor diamines react with **6** and **7** to furnish $[M(CO)_3(\kappa^2\text{-L})(\kappa^1\text{-pymS})]$ (**28–31**) (M = Re, Mn; L = 2,2′-bipyridine, 1,10-phenanthroline) in which the pyrimidine-2-thiolate coordinates in a monodentate fashion via sulfur. Depending on the nature of the metals and diphosphines, complexes with various stoichiometries and pyrimidine-2-thiolate binding modes can be produced using diphosphines. With dppm and dppe, **6** affords $[Re(CO)_2(\kappa^1\text{-pymS})(\kappa^2\text{-dppm})]$ (**32**) and $[Re(CO)_2(\kappa^2\text{-pymS})(\kappa^1\text{-dppe})_2]$ (**33**), respectively, whereas **7** gives $[Mn(CO)_2(\kappa^2\text{-pymS})(\kappa^1\text{-dppm})_2]$ (**34**) and $[Mn(CO)_2(\kappa^2\text{-pyS})(\kappa^2\text{-dppe})]$ (**35**) under similar experimental conditions (Chart 5).

They also reported that the reaction of $[Mn_4(CO)_{12}(\mu\text{-pymS})_4]$ (**7**) and $(PPh_3)_2Ni(CO)_2$ follows a similar route to that of **4** yielding the dinuclear complex $[Mn_2(CO)_5(\mu\text{-pymS})_2(PPh_3)]$ **(36)** and the mononuclear *fac*-$[Mn(CO)_3(\kappa^2\text{-pymS})(PPh_3)]$ (**27**) and $[Mn(CO)_2(\kappa^2\text{-pymS})(PPh_3)_2]$ (**37**) (Scheme 7).

Instead of producing any dinuclear compounds, the reaction of $[Re_4(CO)_{12}(\mu\text{-pymS})_4]$ **(6)** with $(PPh_3)_2Ni(CO)_2$ at room temperature gives the monophosphine substituted compound *fac*-$[Re(CO)_3(\kappa^2\text{-pymS})(PPh_3)]$ (**38**) as the sole product.When compound **27** is treated with PPh_3 at a high temperature (100 °C), compound **37** is also produced. An analogous reaction of **6** with triphenylphosphine at 110 °C affords $[Re(CO)_2(\kappa^2\text{-pymS})(PPh_3)_2]$ (**39**).

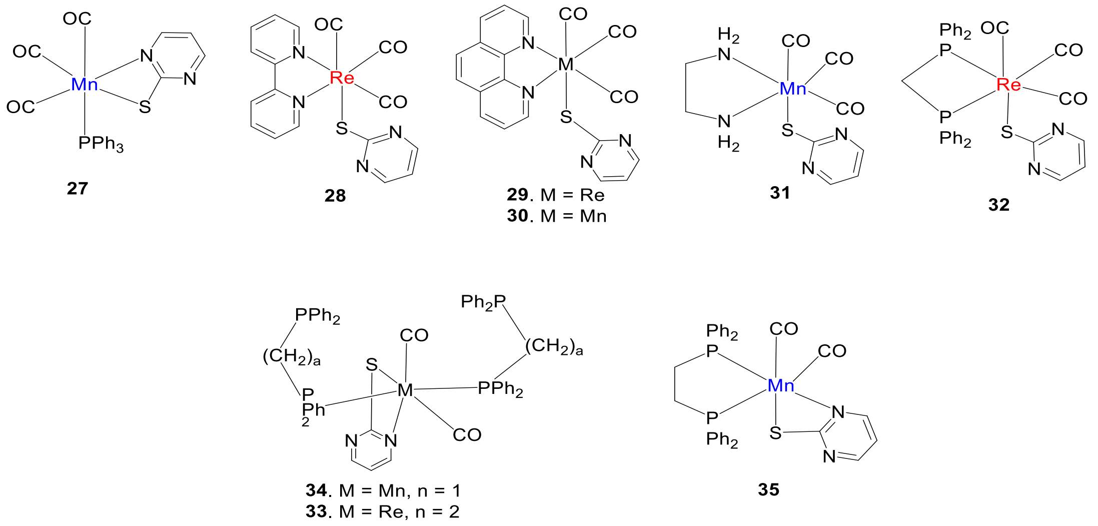

Chart 5. Products of the reactions of 6 or 7 with mono– and bidentate ligands

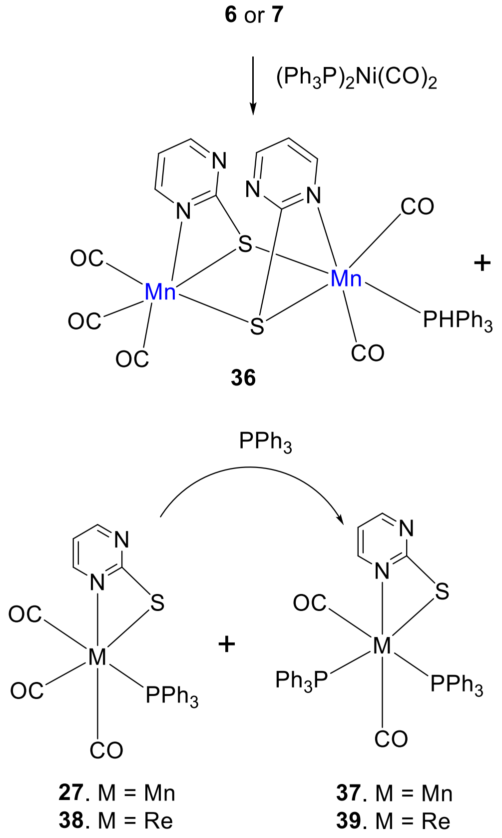

Scheme 7. Reactivity of square-type complexes $[M_4(CO)_{12}(\mu\text{-pymS})_4]$ (6, M = Re; 7, M = Mn) towards $(PPh_3)_2Ni(CO)_2$.

Reactivity of tetranuclear square-type complexes 6 or 7 towards $[M_3(CO)_{10}(L)_2]$ (M = Fe, Os, Ru; L = CO, NCMe)

Kabir and co-workers have detailed the reactivity **6** and **7** towards $[M_3(CO)_{10}(L)_2]$ (M = Fe, Os, Ru; L = CO, NCMe). Heating the tetrameric complexes **6** and **7** with $[Os_3(CO)_{10}(NCMe)_2]$ furnish butterfly mixed-metal clusters $[MOs_3(CO)_{13}(\mu_3\text{-}\kappa^2\text{-pymS})]$ (**40**, M = Re; **41**, M = Mn) in which the pyrimidine-2-thiolate ligand covers a triangular Os2M face, while the group **7** metal is located at the wing-tip. $Ru_3(CO)_{12}$ undergoes carbon-sulfur bond cleavage, resulting in the formation of tetranuclear clusters $[MRu_3(CO)_{14}(\mu_4\text{-}S)(\mu\text{-}\kappa^1\text{:}\eta^1\text{-pym})]$ (**42**, M = Re; **43**, M = Mn) (Chart 6). The heterocyclic ring and the extruded sulfur are present in **42** and **43** (Kabir et al., 2009).

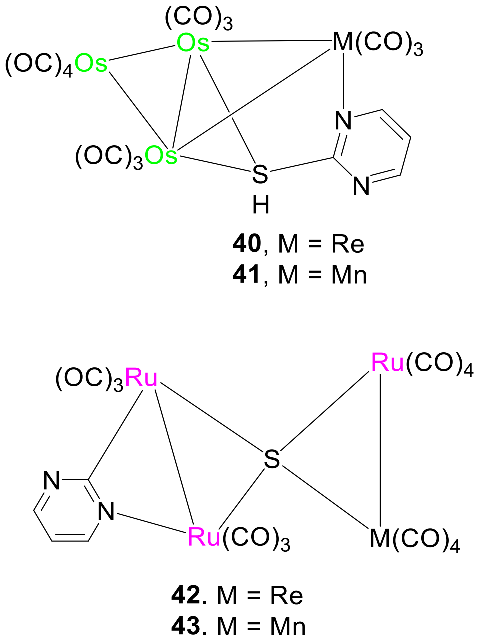

Chart 6. Products of the reactions of $[M_4(CO)_{12}(\mu\text{-pymS})_4]$ (6, M = Re; 7, M = Mn) with $[Os_3(CO)_{10}(NCMe)_2]$.

Reactions of $[M_2(CO)_{10}]$ (M = Re, Mn) with tetrahydropyrimidine-2-thiol (thpymSH)

The reactivity of $[Re_2(CO)_{10}]$ towards tetrahydropyrimidine-2-thiol (thpymSH) follows a different and unique path. Two dirhenium complexes $[Re_2(CO)_6(\mu\text{-thpymS})_2]$ (**44**) and eq-$Re_2(CO)_9\{\kappa^1\text{-}(S)\text{-}SN_2C_4H_8\}$ (**45**) (Scheme 8) have been obtained from the reactions of thpymSH with $[Re_2(CO)_8(NCMe)_2]$or $[Re_2(CO)_{10}]$ (Ahmad et al., 2013). Compound **44** proves to be an excellent precursor to a range of mono– and polymetallic complexes acting as a source of “$Re(CO)_3$(thpymS)”. On the other hand, reaction of $[Mn_2(CO)_9(NCMe)]$ with thpymSH at 25 °C affords the mono– and dinu clear complexes $[Mn(CO)_4(\kappa^1\text{:}\eta^1\text{-}SCNH\text{-}C_3H_6\,NCO)]$ (**46**) and $[Mn_2(CO)_6(\mu\text{-thpymS})_2]$ (**47**), respectively (Ghosh et al., 2011). Carbon–nitrogen coupling is observed in compound 46, resulting in the formation of $\kappa^1\text{:}\eta^1\text{-}SCNHC_3H_6NCO$ ligand, while compound 47 adopts a centrosymmetric structure (Scheme 8).

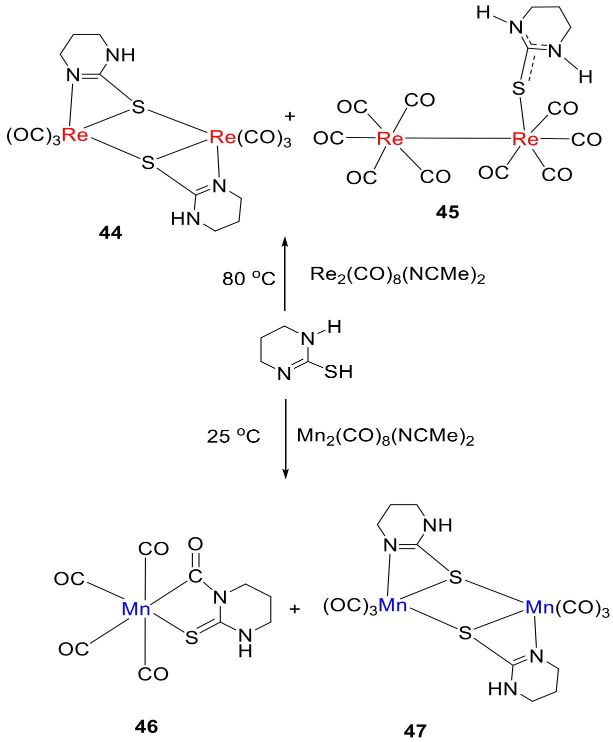

Scheme 8. Reactivity of $[M_2(CO)_8(NCMe)_2]$ (M = Re, Mn) towards thpymSH.

Reactivity of $[Re_2(CO)_6(\mu\text{-thpymS})_2]$ towards mono– and bidentate ligands.

The dimer $[Re_2(CO)_6(\mu\text{-thpymS})_2]$ (**44**) shows moderate reactivity towards mono– and diphosphines. The reactions of **44** with PPh_3 and dppm yield the mononuclear complexes *fac*-$Re(CO)_3(PPh_3)(\kappa^2\text{-thpymS})$ (**48**) and *fac*-$Re(CO)_3$-$(\kappa^1\text{-dppm})(\kappa^2\text{-thpymS})$ (**49**), respectively (Ahmad et al., 2013). The solid-state structure determination shows that in **48**, the pyrimidine-2-thiolate ligand binds in a chelating fashion. Rigid dppm reacts with **44** to give $[Re(CO)_3(\kappa^1\text{-dppm})(\kappa^2\text{-thpymS})]$ (**50**) resulting from phosphine-promoted scission of the dithiolate bridges (Moni et al., 2018). When **50** is heated in toluene at 110 °C, CO is lost, and dinuclear $[Re_2(CO)_4(\mu\text{-dppm})(\mu,\kappa^2\text{-thpymS})_2]$ (**51**) is formed (Scheme 9), which has two thiolates and one dppm ligand bridging Re–Re bond. On the other hand, the reaction of **44** with more flexible dppe at room temperature affords $[Re(CO)_3(\kappa^2\text{-thpymS})_2(\mu,\kappa^1,\kappa^1\text{-dppe})$ (**52**) where each phosphine center is

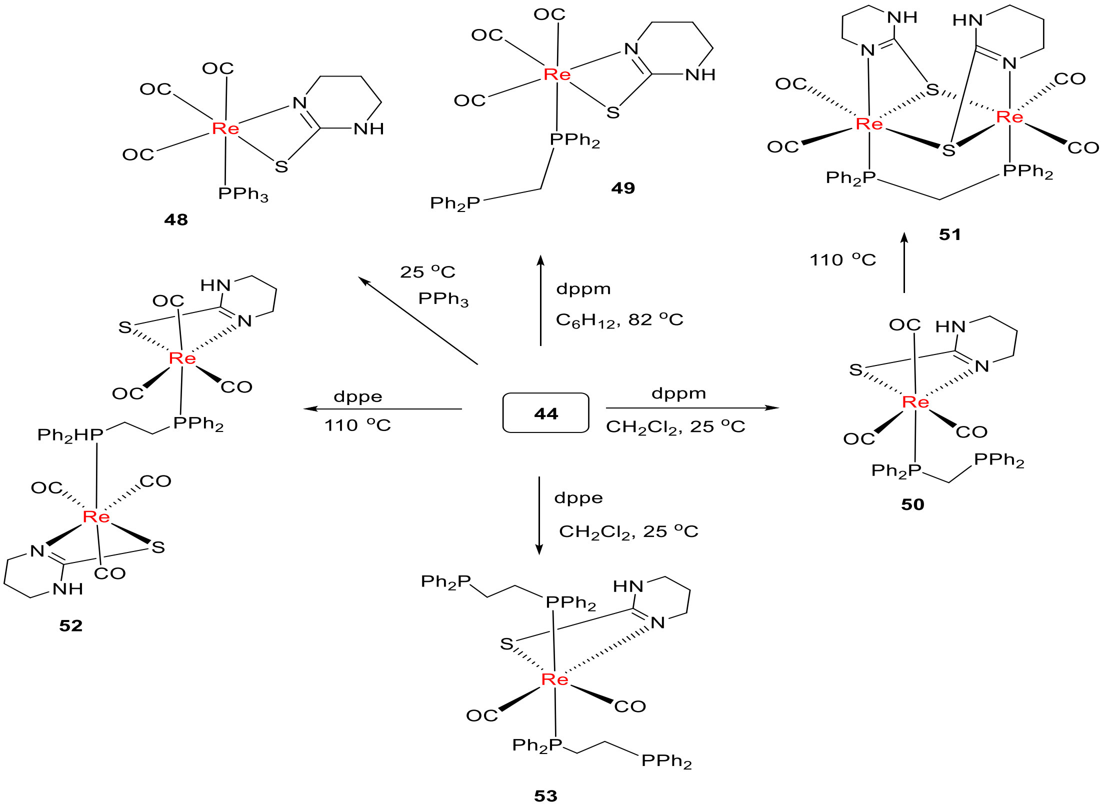

Scheme 9. Products of the reaction of $[Re_2(CO)_6(\mu\text{-thpymS})_2]$ towards mono– and bidentate ligands.

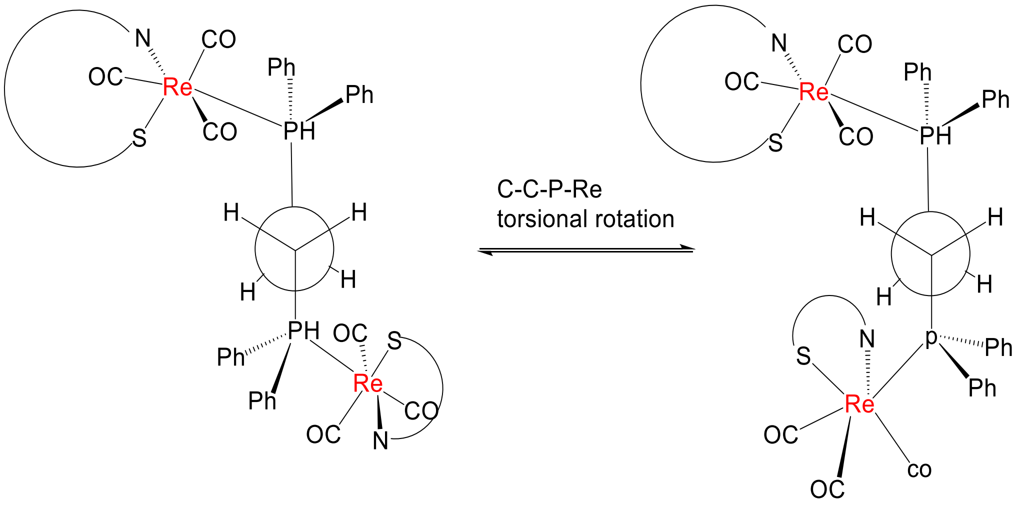

52a **52b**

Scheme 10. Two configurational isomers (52a and 52b) of complex 52.

bonded to a d^6-ML_5 rhenium moiety. Two different configurational isomers (**52a** and **52b**) of complex **52** have been isolated (Scheme 10), and their solid-state structures have been crystallographically determined. The orientation of the two $[Re(CO)_3(\kappa^2\text{-thpymS})]$ moieties at the anti-staggered Newman projection involving the P–C–C–P backbone of the dppe ligand accounts for the majority of the differences between the stereoisomeric products. Both stereoisomers remain distinct in solution at room temperature, but after being heated at 363 K for one hour, they combine to form a 1:1 combination. In toluene at 383 K, complex **44** reacts with dppe to furnish $[Re(CO)_2(\kappa^1\text{-dppe})_2(\kappa^2\text{-thpymS})]$ (**53**) containing two dangling dppe ligands (Scheme 10).

Reactivity of $[M_2(CO)_6(\mu\text{-thpymS})_2]$ (M = Re, Mn) towards $[M_3(CO)_{10}(L)_2]$ (M = Fe, Os, Ru; L = CO, NCMe)

The reaction of **44** with $Ru_3(CO)_{12}$ in refluxing THF results tetranuclear butterfly complexes $ReRu_3(CO)_{13}(\mu_3\text{-thpymS})$ (**54**, **55**) where the capping pyrimidine-2-thiolate ligand is positioned differently on the cluster surface (Ahmad et al., 2013) (Scheme 11). The Ru_3 face is covered by the tetrahydro pyrimidine-2-thiolate in the thermodynamic isomer **55**, whereas the $ReRu_2$ face is covered in the kinetic isomer **54**. In refluxing benzene, a similar reaction with $[Os_3(CO)_{10}(NCMe)_2]$ yields mostly the $ReOs_3$ cluster $[ReOs_3(CO)_{13}(\mu_3\text{-thpymS})]$ (**56**), together with trace quantities of $[(\mu\text{-H})Os_3(CO)_9(\mu_3\text{-thpymS})]$ (**57**) due to rhenium loss. Cluster **56** is stable in boiling toluene, although it progressively transforms into isomeric **58** in xylene at 140 °C, albeit with low yields. Only minor differences in the cluster core shape may be seen in the isomeric **54** and **55** crystal structures.

Reaction of **47** with $[Os_3(CO)_{10}(NCMe)_2]$ in refluxing benzene furnishes the MnOs mixed-metal cluster $[MnOs_3(CO)_{13}(\mu_3\text{-thpymS})]$ (**59**) which has a butterfly-shaped skeleton made up of four metal atoms whereas $Ru_3(CO)_{12}$ at 110 °C produces the mixed Mn–Ru cluster $[MnRu_3(CO)_{14}(\mu_4\text{-S})(\kappa^1\text{:}\eta^1\text{-thpym})]$ (**60**) (Ghosh et al., 2011). In contrast, reaction of **47** with $Fe_3(CO)_{12}$ at 80 °C affords two triiron clusters $[Fe_3(CO)_9(\mu_3\text{-S})(\mu_3\text{-}\kappa^1\text{:}\eta^1\text{-}C_4H_6N_2)]$ (**61**) and $[Fe_3(CO)_8(\mu_3\text{-S})_2(\eta^1\text{-}C_4H_8N_2)]$ (**62**). The former is also formed from the direct reaction of thpymSH with $Fe_3(CO)_{12}$, and it reacts with H_2S to produce **62** (Scheme 12).

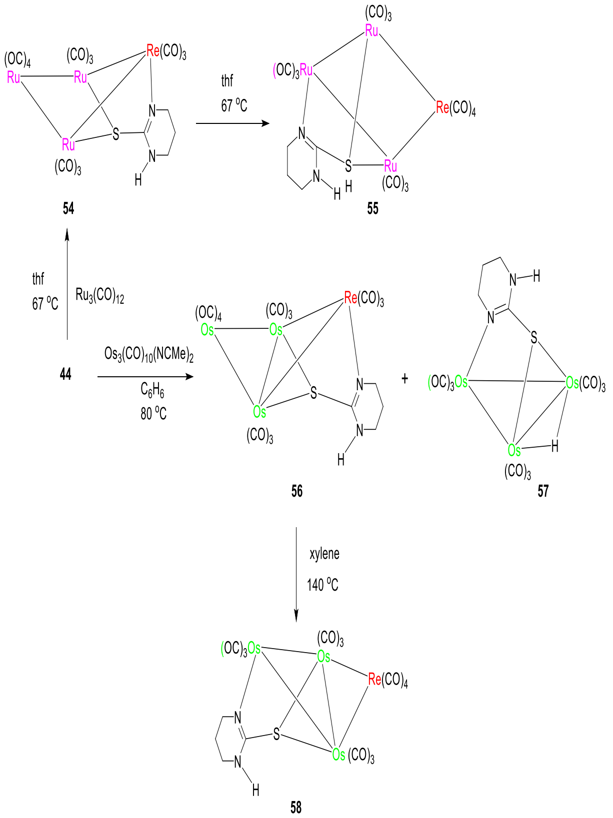

Scheme 11. Schematic representation of the reactions of $[Re_2(CO)_6(\mu\text{-thpymS})_2]$ (44) with $[Os_3(CO)_{10}(NCMe)_2]$ and $Ru_3(CO)_{12}$.

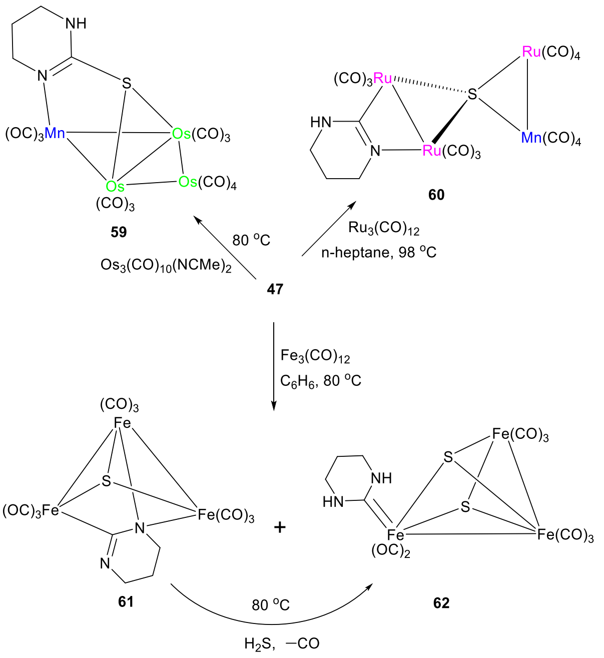

Scheme 12. Reaction of $[Mn_2(CO)_6(\mu\text{-thpymS})_2]$ (47) with group 8 trimetallic clusters

Reactivity of $[M_2(CO)_{10}]$ (M = Re, Mn) towards 2-mercapto-1-methylimidazole: Formation of di–, tri–, and tetranuclear compounds

The neutral heterocyclic thiolate ligand 2-mercapto-1-methylimidazole can also coordinate to transition metals both in the thiol and tautomeric thione form (-NH-C=S ↔ -N=C-SH). This thiol has attracted considerable attention due to its biomedical significance and use as medicinal substances (Katiyar et al., 2003). An unprecedented reaction took place when $[Re_2(CO)_8(NCMe)_2]$ was reacted with 2-mercapto-1-methylimidazole at 80 °C affording a mixture of di-, tri-, and tetrarhenium complexes $[Re_3(CO)_8(\mu\text{-}CO)(\mu_3\text{-}SN_2C_4H_5)_2(\mu\text{-}H)]$ (**63**), $[Re_4(CO)_{12}(\mu\text{-}SN_2C_4H_5)_4]$ (**64**), and $[Re_2(CO)_6(\mu\text{-}SN_2C_4H_5)_2]$ (**65**) (Ghosh et al., 2009b) (Scheme 13).

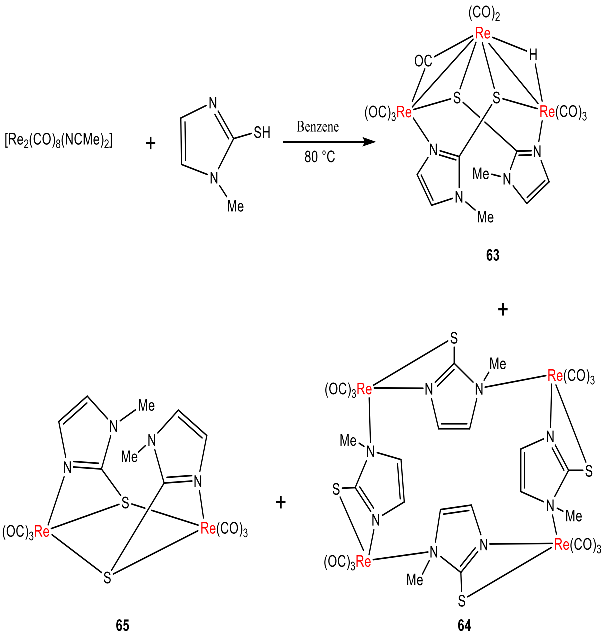

Scheme 13. Reaction of $[Re_2(CO)_8(NCMe)_2]$ with 2-mercapto-1-methylimidazole.

The tetranuclear **64** is isostructural with **6**, and the dinuclear **65** is a structural analog of **2**. Compound **63** provides a unique example of a bent open trirhenium cluster bearing two triply bridging 2-mercapto-1-methylimidazolate ligands, a semi-bridging CO, and a bridging hydride ligand.

In sharp contrast, two new dimeric products $[Mn_2(CO)_6(\mu\text{-}SN_2C_4H_5)_2]$ (**66**) and $[Mn_2(CO)_7(\mu\text{-}SN_2C_4H_5)_2]$ (**67**) have been obtained from the reaction of $[Mn_2(CO)_{10}]$ with 2-mercapto-1-methylimidazole in the presence of Me_3NO at 25 °C (Ghosh et al., 2009b). Both compounds are structurally characterized. Compound **66** consists of two $\mu\text{-}SN_2C_4H_5$ ligands, each of which is linked to two Mn atoms via the sulfur atom and one Mn atom via the nitrogen atom, producing a four-membered chelate ring. A comparable bonding mode to compound **66** exists in compound **67**. Still, one of the $\mu\text{-}SN_2C_4H_5$ ligands coordinates through one sulfur atom to an Mn atom and a nitrogen atom to another Mn atom. Complex **66** has also been synthesized as the sole product from the reaction of the bis-acetonitrile compound $[Mn_2(CO)_8(NCMe)_2]$ with 2-mercapto-1-methylimidazole at 80 °C.

Reactivity of $[M_2(CO)_6(\mu\text{-}SN_2C_4H_5)_2]$ (M = Re, Mn) towards $[M_3(CO)_{10}(L)_2]$ (M = Fe, Os, Ru; L = CO, NCMe)

Over the last three decades, considerable attention has been focused on the chemistry of bimetallic complexes because of their unique structural properties and various potential catalytic applications (Braunstein et al., 1995; Gade, 2000; Herberhold and Jin, 1994; Dennett et al., 2004). The group 7 metal dinuclear complexes $[M_2(CO)_6(\mu\text{-}SN_2C_4H_5)_2]$ (**65**, M = Re; **66**, M = Mn) show a moderate reactivity toward group 8 metal trinuclear carbonyl clusters (Ghosh et al., 2009c). Thus treatment of **65** and **66** with $[Os_3(CO)_{10}\text{-}(NCMe)_2]$ at 80 °C furnish the tetranuclear mixed-metal clusters $[Os_3Re(CO)_{13}(\mu_3\text{-}SN_2C_4H_5)]$ (**68**) and $[Os_3Mn(CO)_{13}(\mu_3\text{-}SN_2C_4H_5)]$ (**69**), respectively. Similar treatment of **65** and **66** with $Ru_3(CO)_{12}$ affords the ruthenium analogs $[Ru_3Re(CO)_{13}(\mu_3\text{-}SN_2C_4H_5)]$ (7**0**), and $[Ru_3Mn(CO)_{13}(\mu_3\text{-}SN_2C_4H_5)]$ (**71**), but in case of **66**, another product $[Mn_3(CO)_{10}(\mu\text{-}Cl)\text{-}(\mu_3\text{-}SN_2C_4H_5)_2]$ (**72**) has also been formed (Scheme 14). Compounds **68–71** possess a noncrystallographic mirror plane of symmetry and a butterfly-shaped core of four metal atoms, with the M (Mn or Re) located at the wingtip. This finding offers a viable strategy for synthesizing several novel group **7/8** mixed metal complexes with bifunctional heterocyclic ligands. A 54-electron trimanganese complex with bridging 2-mercapto-1-methylimidazolate and chloride ligands is only found in compound **72**, a rare instance of this type of complex. Surprisingly, treatment of 65 with $Fe_3(CO)_{12}$ at 70–75 °C afford the trirehenium and dirhenium complexes $[Re_3(CO)_{10}(\mu\text{-}H)(\mu_3\text{-}SN_2C_4H_5)_2]$ (**73**) and $[Re_2(CO)_6(N_2C_4H_5)(\mu\text{-}SN_2C_4H_5)_2]$ (7**4**), respectively instead of the formation of the expected mixed-metal clusters. The former is an interesting example of a 52-electron trirhenium-hydride complex with a bridging 2-mercapto-1-methylimidazolate ligand, and the latter may be thought of as a 1-methylimidazole adduct of **65**. It is interesting to note that the reaction has not produced any Fe–Re mixed-metal complexes.

Reactions of **66** with group 6 metal carbonyls such as $[Cr(CO)_3(NCMe)_3]$ and $[Mo(CO)_3(NCMe)_3]$ in boiling THF produced the mixed-metal clusters $[CrMn_2(CO)_8(\mu\text{-}CO)_2(\mu_3\text{-}SN_2C_4H_5)_2]$ (**75**) and $[MoMn_2(CO)_8(\mu\text{-}CO)_2(\mu_3\text{-}SN_2C_4H_5)_2]$(76), respectively, in which two Mn–M (M = Mo, Cr) bonds were created (Ghosh et al., 2009b). In contrast, an analogous reaction of $[W(CO)_3(NCMe)_3]$ with **66** affords two W–Mn clusters $[Mn_2W(CO)_8(\mu\text{-}CO)_2(\mu_3\text{-}SN_2C_4H_5)_2]$ (**77**) and $[Mn_2W(CO)_7(\mu\text{-}CO)_2(SN_2C_4H_5)(\mu_3\text{-}SN_2\text{-}C_4H_5)_2]$ (**78**). The reaction of **66** with $[Fe_3(CO)_{12}]$ at 70–75 °C yields the mixed-metal cluster $[FeMn_2(CO)_8(\mu\text{-}CO)(\mu_3\text{-}SN_2C_4H_5)_2]$ (**79**) and the by-product $[Fe_2(CO)_6(\mu\text{-}S_2N_2C_4H_5)_2]$ (**80**) (Scheme 15). All compounds, except **78** and **79**, have a noncrystallographic two-fold axis of symmetry. Compounds **75–79** have a bent open structure composed of three metal atoms connected by two

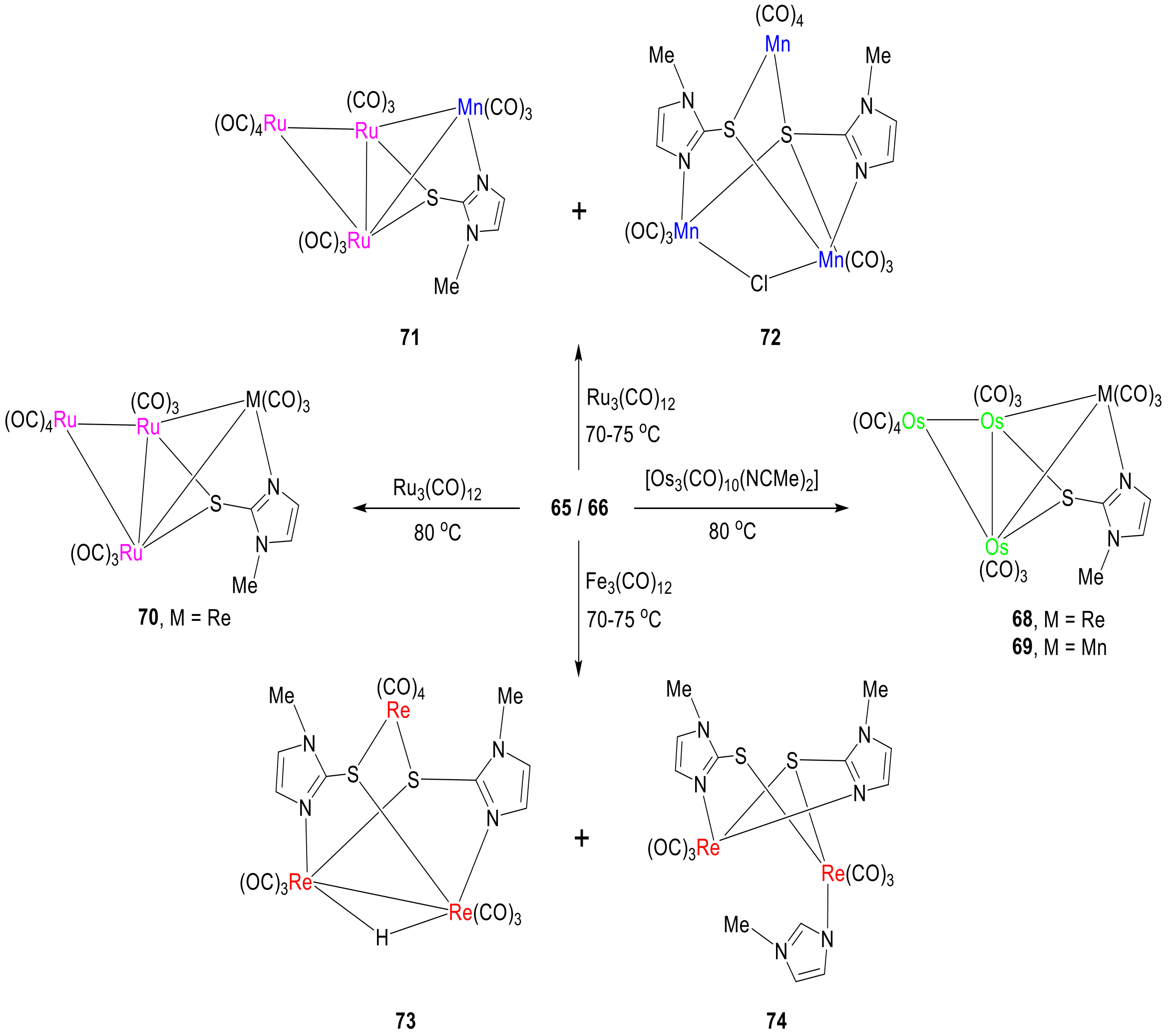

Scheme 14. Reactions of $[M_2(CO)_6(\mu\text{-}SN_2C_4H_5)_2]$ (65, M = Re; 66, M = Mn) with group 8 trimetallic carbonyls.

metal-metal bonds. Structure-wise, compound 78 is identical to compound 77, except it has an Mn–Mn bond rather than an Mn–W bond and an $SN_2C_4H_6$ ligand mono coordinated through the exocyclic sulfur atom to the W atom.Two bridging $S_2N_2C_4H_5$ ligands, produced by combining 2-mercapto-1-methylimidazole with sulfur, make up compound 80. Compound 79 provides an unusual example of a Mn_2Fe trimetallic cluster with two Fe–Mn bonds.

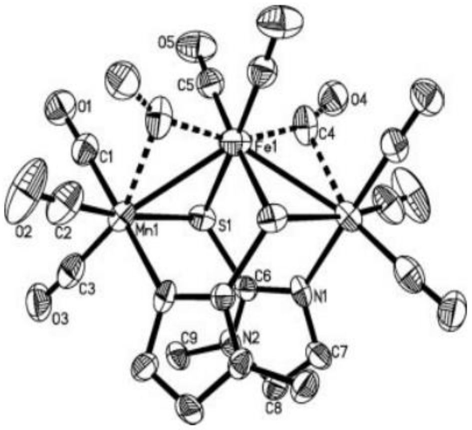

Fig. 4. The solid-state structure of $[FeMn_2(CO)_8(\mu\text{-}CO)(\mu_3\text{-}SN_2C_4H_5)_2]$ (79).

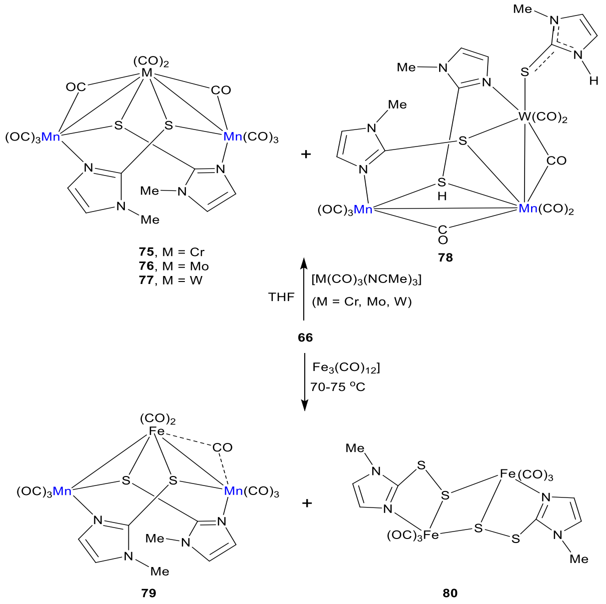

Scheme 15. Reactions of $[Mn_2(CO)_6(\mu\text{-}SN_2C_4H_5)_2]$ (66) with $Fe_3(CO)_{12}$ and $[M_3(CO)_3(NCMe)]$ (M = Cr, Mo, W).

Reactions of $[M_2(CO)_{10}]$ (M = Re, Mn) with 2-mercaptobenzothazole-2-thiol (MBTH) and 2-mercaptobenzooxazol.

Following a method analogous to that reported by Kabir and co-workers for the synthesis of $[Mn_2(CO)_6(\mu\text{-pyS})_2]$ (Kabir et al., 1996), compound $[Re_2(CO)_6(\mu\text{-MBT})_2]$ (**81**) has been synthesized from the Me_3NO-mediated reaction of $Re_2(CO)_{10}$ with 2-mercaptobenzothiazole at room temperature (Ghosh et al., 2010b). The complex has a chiral structure with C_2 symmetry being similar to that of previously reported for compound $[Re_2(CO)_6(\mu\text{-pyS})_2]$ (Deeming et al., 1988b). Each 2-mercaptobenzothiazolate ligand forms a four-membered chelate ring by coordinating with one metal atom, while the sulfur serves as a bridge between the ligand and the dirhenium core. On the other hand, a reaction between $Mn_2(CO)_{10}$ and 2-mercaptobenzothiazole in the presence of Me_3NO at 25 °C gives the dimanganese complex $[Mn_2(CO)_6(\mu\text{-MBT})_2]$ (**82**) (Scheme 16) (Ghosh et al., 2012). In **82**, two manganese atoms are arranged in a dinuclear framework that is held together by two MBT ligands, six carbonyls, and two other atoms. Three carbonyls that are organized in a face pattern are linked to each manganese atom. Both MBT ligands bind with a single manganese atom through the nitrogen atom and create a bridge between the manganese atoms, forming four-membered chelate rings.

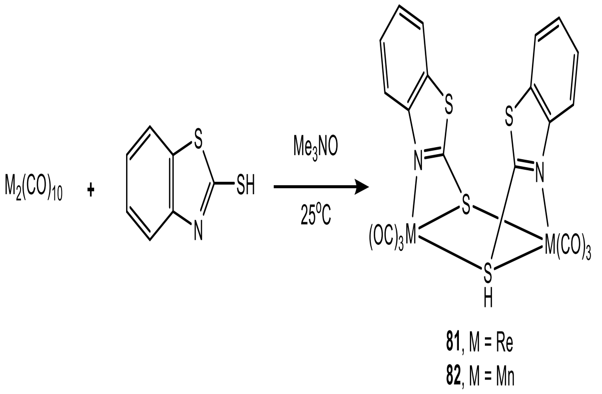

Scheme 16. Reactivity of $[M_2(CO)_{10}]$ (M = Re, Mn) towards MBTH.

Hoque and co-workers carried out analogous reactions of 2-mercaptobenzoxazol with $[Mn(CO)_8(NCMe)_2]$ and observed the unexpected formation of trimanganese cluster $[Mn_3(CO)_{10}(\mu\text{-}SCNOC_6H_4)_3]$ (**83**), which has been structurally characterized. The most striking feature of 83 is three different binding modes (A–C) of 2-mercaptobenzoxazolate (Chart 6) in one molecule. Bonding modes A–B has been found in other complexes (Brodie et al., 1983; Brodie et al., 1986; Wang et al., 2012), while C is found in **83**. Ligand A formally acts as a 3-electron donor, while B and C are 5-electron donors. Thus cluster 83 has a VEC of 54 electrons, consistent with the absence of any direct metal-metal interaction.

A similar reaction of 2-mercaptobenzoxazol with $Re_2(CO)_8(NCMe)_2$ also resulted in the isolation of a trinuclear product, namely $[Re_3(CO)_{12}(\mu\text{-}SCNOC_6H_4)_3]$ (**84**). The solid-state structure determination **84** confirms that each 2-mercaptobenzoxazolate ligand is of type A (Chart 7), spanning $Re(CO)_4$ centers through nitrogen and sulfur atoms. Since each 2-mercaptobenzoxazolate ligand is a 3-electron donor, cluster **84** also has a VEC of 54 electrons.

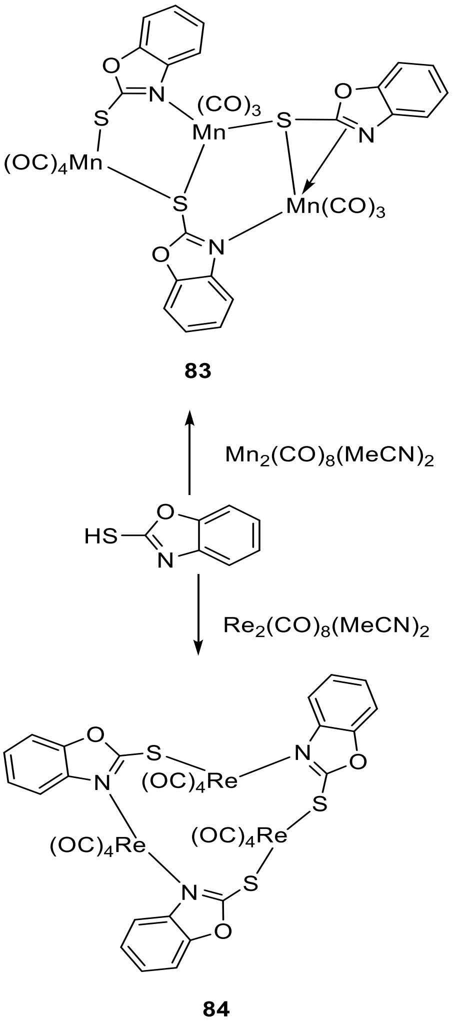

Scheme 17. **Reactivity of $[M_2(CO)_8(NCMe)_2]$ (M = Re, Mn) towards 2-mercaptobenzooxazol.**

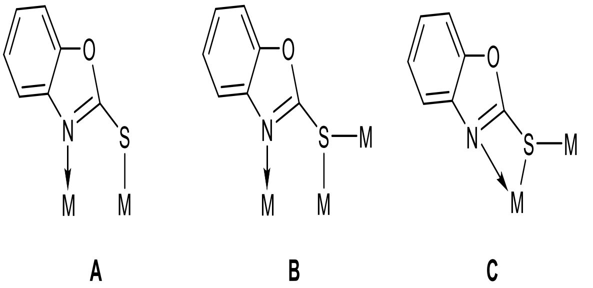

Chart 7. Three different coordination modes of 2-mercaptobenzoxazol.

Reactivity of $[Mn_2(CO)_6(\mu\text{-MBT})_2]$ (82) towards mono– and bidentate ligands

Compound **82**, in turn, acts as a useful precursor to mononuclear complexes upon the addition of diphosphines and diamines. Thus reactions of **82** with 1,2-bis(diphenylphosphino)ethane (dppe) and 1,3-bis(diphenylphosphino)propane (dppp) in cyclohexane at boiling temperature furnish cis-$[Mn(CO)_2(\kappa^2\text{-MBT})(\kappa^2\text{-dppe})]$ (**85**) and cis-$[Mn(CO)_2(\kappa^2\text{-MBT})(\kappa^2\text{-dppp})]$ (**86**), respectively which have been crystallographically characterized (Ghosh et al., 2012). As predicted for an octahedral compound with two carbonyl ligands in the cis orientation, 85 and 86 show two absorption bands in the carbonyl stretching region in the infrared spectra. Molecule 85 comprises a single manganese atom coordinated by two terminal carbonyls, a dppe, and MBT ligands. The carbonyls are in the cis position in relation to one another, and the MBT and diphosphine form chelates with manganese. Under the assumption that the MBT ligand acts as a 3-electron donor, complexes 85 and 86 are 18-electron species. Again, the reactions of 82 with diamines, e.g., 2,2′-bipyridine (bipy), 1,10-phenanthroline (phen), and ethylenediamine (en) at room temperature afford fac-$[Mn(CO)_3(\kappa^1\text{-MBT})(\kappa^2\text{-bipy})]$ (**87**), fac-$[Mn(CO)_3(\kappa^1\text{-MBT})(\kappa^2\text{-phen})]$ (**88**) and fac-$[Mn(CO)_3(\kappa^1\text{-MBT})(\kappa^2\text{-en})]$ (**89**), respectively (Scheme 18) (Ghosh et al., 2012).

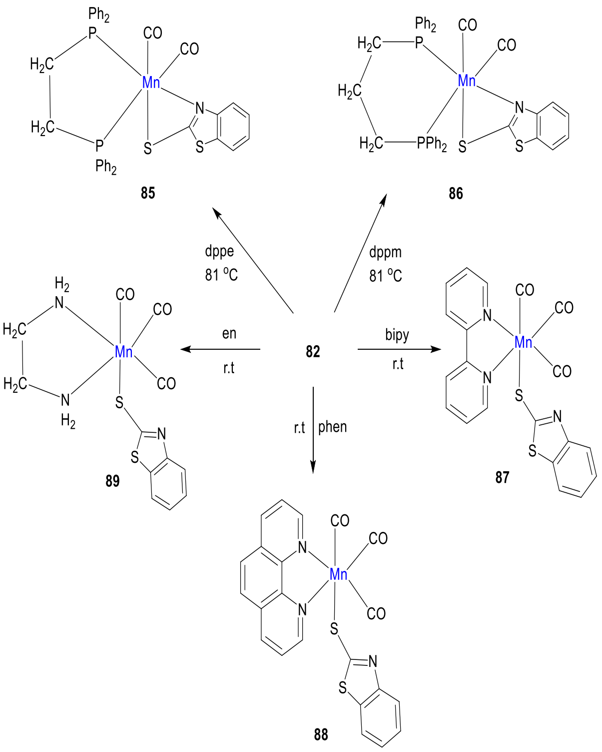

Scheme 18. Reactivity of $[Mn_2(CO)_6(\mu\text{-MBT})_2]$ (82) towards bidentate ligands.

Reactivity of $[M_2(CO)_6(\mu\text{-}MBT)_2]$ (81, M = Re; 82, M = Mn)) towards the trinuclear clusters $[M_3(CO)_{10}(L)_2]$ (M = Fe, Os, Ru; L = CO, NCMe)

The group 8 trimetallic carbonyl clusters show reactivity towards dirhenium compound $[Re_2(CO)_6(\mu\text{-}S_2NC_7H_4)_2]$ (**81**) to afford new tri- and tetranuclear mixed-metal clusters (Ghosh et al., 2010b). $[Os_3(CO)_{10}(NCMe)_2]$ reacts with 81 in refluxing benzene to yield the tetranuclear mixed-metal cluster $[Os_3Re(CO)_{13}(\mu_3\text{-}C_7H_4NS_2)]$ (**90**) (Scheme 18) as the sole product. Interestingly, for $Ru_3(CO)_{12,}$ the reaction products are temperature dependent. At 80 °C, $[Ru_3Re(CO)_{13}(\mu_3\text{-}MBT)]$ (**91**) and $Ru_3(CO)_9(\mu\text{-}H)(\mu_3\text{-}MBT)]$ (**92**) are formed, while at 110 °C a completely different tetranuclear mixed-metal cluster (93), is formed resulting from C-S bond cleavage. On the other hand, the reaction of **81** with $Fe_3(CO_{12}$ at 80 °C affords 94. The reactivity of **94** (Scheme 19) with PPh_3 in the presence of Me_3NO at 25 °C results in ligand substitution to furnish mono- and disubstituted derivatives $[Os_3Re(CO)_{12}(PPh_3)(\mu_3\text{-}MBT)]$ (**95**) and $[Os_3Re(CO)_{11}(PPh_3)_2(\mu_3\text{-}MBT)]$ (**96**). In **95**, the PPh_3 ligand is located at an axial position on the wingtip osmium. In contrast, in **91**, one PPh_3 ligand is equatorially coordinated to the wingtip osmium, and the other is bound to the hinge osmium.

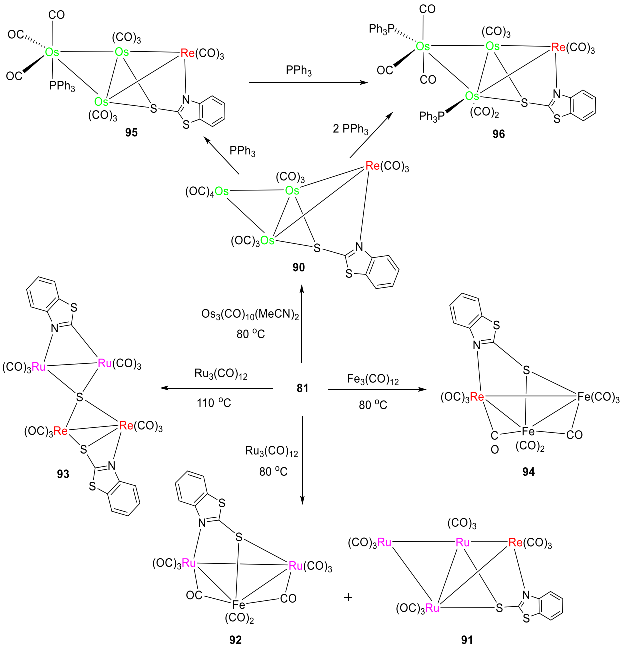

Scheme 19. Reactions of $[Re_2(CO)_6(\mu\text{-}S_2NC_7H_4)_2]$ (81) with M3(CO)12 different metal carbonyls.

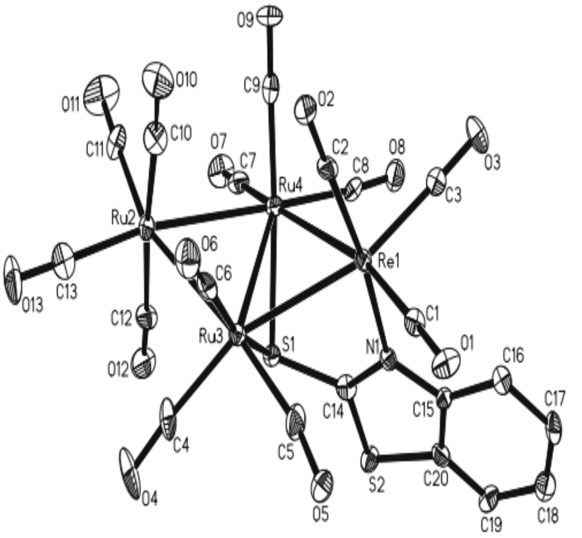

Fig. 5. The ORTEP structure of $[Ru_3Re(CO)_{13}(\mu_3\text{-}MBT)]$ (91).

Concluding remarks

It is clear from this review that many rhenium and manganese carbonyl complexes bearing heterocyclic thiolate ligands are reported. These compounds range from mononuclear to tetranuclear. Moderate to high yielding synthetic routes to binuclear $[M_2(CO)_6(\mu\text{-}L)_2]$ and the tetranuclear square-type complexes $[M_4(CO)_{12}(\mu\text{-}L)_4]$ (L = pyridine-2-thiolato, pyrimidine-2-thiolato, tetrahydropyrimidine-2-thiolato, 2-mercapto-1-methyl- imidazolato, 2-mercapto-benzothiolate, etc. as appropriate) are described. These compounds contain labile M-S bonds which make them excellent sources of the 16-electron mononuclear species $[M(CO)_3(\kappa^2\text{-}L)]$ in solution. The further reactivity of the resultant $[M(CO)_3(\kappa^2\text{-}L)]$ species with various mono and bidentate ligands reveals that they are versatile precursors for mononuclear products of differing coordination of the $M(CO)_3(L)$ fragments. The lability of the M-S bonds makes these di and tetranuclear complexes excellent precursors for the synthesis of two isostructural series of mixed-metal cluster complexes, namely $[MM'_3(CO)_{13}(\mu_3\text{-}L)]$ (M = Re, Mn; M´ = Ru, Os) and $[MM''_2(CO)_{10}(\mu_3\text{-}L)]$ (M = Re, Mn; M´´= Mo, Cr, W). The trinuclear mixed-metal clusters consist of an open structure of two rhenium or manganese atoms and a third metal atom, M (M = W, Mo, Cr), connected by two M−Re/Mn bonds, two triply bonded thiolato ligands, and two asymmetrically bound μ-CO ligands.

In contrast, the tetranuclear mixed-metal clusters consist of a butterfly skeleton of four metal atoms, with the unique metal atom occupying wingtip positions. A notable feature is that the reactivity Fe3(CO)12 reactivitytowards the synthesis of mixed-metal clusters is quite different from those of its heavier congeners. In the case of their group 7 metal carbonyl chemistry, although most of the heterocyclic thiols share a common reactivity trait, in some cases, their outcome is completely different.

Acknowledgments

One of us (SEK) gratefully acknowledges the University Grants Commission Bangladesh for the award of a UGC Professorship and Jagannath University for support.

Conflicts of interests

The authors declare that they have no known competing financial interests or personal relationships that could have appeared to influence the work reported in this review.

References

Adams RD and Barnard TS. Does a metal to metal "ligand" effect influence the catalytic activity of bimetallic cluster complexes? Synthesis and catalytic activity of $Pt_3Ru_6(CO)_{19}(SMe_2)(\mu_3\text{-}PhC_2Ph)(\mu_3\text{-}H)(\mu\text{-}H)$. *Organometallics* 1998b; 17: 2885-2890.

Adams RD and Cotton FA (eds.). *Catalysis by Di– and Polynuclear Metal Cluster Complexes* Wiley-VCH, Newyork 1998a.

Ahmad MF, Sarker JC, Azam KA, Kabir SE, Ghosh S, Hogarth G, Siddiquee TA, and Richmond MG. $Re_2(CO)_6(\mu\text{-}thpymS)_2$ (thpymSH = tetrahydropyrimidine-2-thiol) as a versatile precursor to mono– and polynuclear complexes: X-Ray crystal structures of *fac*-$Re(CO)_3(PPh_3)(\kappa^2\text{-}thpymS)$ and two isomers of $ReRu_3(CO)_{13}(\mu_3\text{-}thpymS)$. *J. Organomet. Chem.* 2013; 728: 30-37.

Azam K, Hursthouse M, Hussain S, Kabir S, Malik K, Rahman M, and Rosenberg E. Triosmium clusters containing thiazolide ligand: Crystal structures of $[(\mu\text{-}H)Os_3(CO)_{10}(\mu\text{-}3,4\text{-}\eta^2\text{-}HC{=}NC{=}CHS)]$ and $[(\mu\text{-}H)Os_3(CO)_9(\mu\text{-}3,4\text{-}\eta^2\text{-}HC{=}NC{=}CHS)(PPh_3)]$. *J. Organomet. Chem.* 1998a; 559: 81-89.

Azam KA, Dilshad R, Kabir SE, Khatoon K, Nessa L, Rahman MM, Rosenberg E, Hursthouse MB, Malik KMA, and Deeming AJ. Triosmium and triruthenium clusters containing the 4-methylthiazolide ligand: Crystal structures of $[Os_3(\mu\text{-}H)(CO)_{10}(\mu\text{-}2,3\text{-}\eta^2\text{-}CNC\text{-}MeCHS)]$, $[Os_3(\mu\text{-}H)(CO)_9(\mu\text{-}2,3\text{-}\eta^2\text{-}CNCMeCHS)(PPh_3)]$ and $[Os_3(\mu\text{-}H)(CO)_8(\mu\text{-}2,3\text{-}\eta^2\text{-}CNCMe\text{-}HS)(PPh_3)_2]$. *J. Chem. Soc., Dalton Trans.*1996: 1731-1739.

Azam KA, Hursthouse MB, Kabir SE, Malik KA, Tesmer M, and Vahrenkamp H. A novel pentaruthenium cluster containing three thiazole derived ligands; X-xay structure of $[Ru_3(CO)_9(\mu\text{-}H)(\mu_5\text{-}\eta^5\text{-}HC\text{-}NC\text{-}CHS)Ru_2(CO)_4(\mu\text{-}H)(\eta^1\text{-}HC{=}NCH{=}CHS)(\mu\text{-}2,3\text{-}\eta^3\text{-}C{=}NCH{=}CHS)]$. *Inorg. Chem. Commun.* 1998b; **1**: 402-404.

Begum N, Kabir SE, Hossain GMG, Rahman AM, and Rosenberg E. Investigations of pyridine-2-thiol as a ligand: Synthesis and X-ray structures of the mixed Mo–Mn dinuclear complex $CpMoMn(CO)_3(\mu\text{-}CO)(\mu\text{-}\eta^2\text{-}pyS)(\mu\text{-}\eta^1\text{-}pyS)$, the electron-deficient trimolybdenum cluster $Cp_3Mo_3(\mu\text{-}CO)_2(\mu\text{-}S)(\mu_3\text{-}S)(\mu\text{-}\eta^2\text{-}NC_5H_4)$, and the mononuclear $CpMo(CO)_2(\mu\text{-}\eta^2\text{-}pyS)$. *Organometallics* 2005; 24: 266-271.

Berardini M and Brennan J. Europium pyridinethiolates: Synthesis, structure, and thermolysis. *Inorg. Chem.* 1995; 34: 6179-6185.

Beuken van den EK, Feringa BI. Bimetallic catalysis by late transition metal complexes. Tetrahedron 1998; 54: 12985.

Braunstein P and Rosé J. 7– Catalysis and related reactions with compounds containing hetero-nuclear metal–metal bonds. *Comprehensive Organometallic Chemistry* (1995) pp. 351-385.

Braunstein P and Rosé J., in Metal Clusters in Catalysis, ed. P. Braunstein, L. A. Oro and P. R. Raithby, Wiley-VCH, Weinheim, Germany, 1999, vol. 2, pp. 616.

Brodie AM, Holden HD, Lewis J and Taylor MJ. The interaction of heterocyclic thioamides with triosmium clusters: the X-ray crystal structure of $(\mu\text{-}H)Os_3(CO)_{10}(\mu\text{-}SC{=}NCH_2CH_2S)$. *J. Organomet. Chem.* 1983; 253**:** C1-C4.

Brodie AM, Holden HD, Lewis J and Taylor MJ. The reaction of $[Os_3(CO)_{10}(MeCN)_2]$ with heterocyclic thioamides. The crystal and molecular structure of $[Os_3(\mu\text{-}H)(CO)_{10}(\mu\text{-}SC{=}NCH_2CH_2S)$. *J. Chem. Soc., Dalton Trans.* 1986; 633-639.

Broussard ME, Juma B, Train SG, Peng W-J, Laneman SA, and Stanley GG. A bimetallic hydroformylation catalyst: High regioselectivity and reactivity through homobimetallic cooperativity. *Science* 1993; 260: 1784-1788.

Castro R, Durán ML, García-Vázquez JA, Romero J, Sousa A, Castiñeiras A, Hiller W, and Strähle J. Direct electrochemical synthesis of pyridine-2-thionato complexes of nickel (II): The crystal structure of (2,2′-bipyridine)bis(pyridine-2-thionato)nickel(II)-2,2′-bipyridine. *J. Chem. Soc. Dalton Trans.*1990: 531–534.

Cheng Y, Emge T, and Brennan J. Pyridineselenolate complexes of tin and lead: $Sn(2\text{-}SeNC_5H_4)_2$, $Sn(2\text{-}SeNC_5H_4)_4$, $Pb(2\text{-}SeNC_5H_4)_2$, and $Pb(3\text{-}Me_3Si\text{-}2\text{-}SeNC_5H_3)_2$. Volatile CVD precursors to group IV−group VI semiconductors. *Inorg. Chem*. 1996; 35: 342-346.

Cockerton B, Deeming AJ, Karim M, and Hardcastle KI. Mixed tetranuclear rhenium–ruthenium compounds formed by carbon–sulphur bond cleavage in reactions of $[Re_2(pyS)_2(CO)_6]$ (pyS = pyridine-2-thionate) with $[Ru_3(CO)_{12}]$. Crystal structures of $[ReRu_3(\mu_4\text{-}S)(\mu\text{-}C_5\text{-}H_4N)(CO)_{14}]$ and $[Re_2Ru_2(\mu\text{-}S)(\mu\text{-}C_5H_4N)(\mu\text{-}pyS)(CO)_{13}]$. *J. Chem. Soc., Dalton Trans.* 1991; 431-437.

Deeming AJ, Karim M, Bates PA, and Hursthouse MB. A new type of pyridine-2-thionato bridge: X-ray crystal structure of the complex $[Re_2(Mepys)_2(CO)_6]$ where MepyS is the 6-methylpyridine-2-thionato ligand. *Polyhedron* 1988b; 7: 1401-1403.

Deeming AJ, Karim M, Bates PA, and Hursthouse MB.Di- and tri-nuclear complexes of palladium(II) containing doubly- and triply-bridging pyridine-2-thionato (pyS) ligands: Crystal structure of $[Pd_3(C_6H_4CH_2NMe_2)_3(pyS)_2][BF_4]$. *J. Chem. Soc., Dalton Trans* 1988a; 2193-2199.

Deeming AJ, Hardcastle KI and Karim M. Suppression of cluster unsaturation by formation of extensive but long-range metal-metal bonding: crystal structures of $[Ru_3H\text{-}(pyS)(CO)_9]$ and $[\{Ru_3H(pyS)\ (CO)_7\}_3]$, where pyS Is the pyridine-2-thiolato ligand. *Inorg. Chem*. 1992; 31: 4792-4796.

Dennett JN, Jacke J, Nilsson G, Rosborough A, Ferguson MJ, Wang M, McDonald R, and Takats J. Alkene carbon−hydrogen bond activation at a heterobimetallic center: $[RuCo(CO)_3(\mu\text{-}CO)(\eta\text{-}C_5Me_5)\{\mu\text{-}\eta^2{:}\eta^2\text{-}C(CF_3)\text{-}C(CF_3)\}]$. *Organometallics* 2004; 23: 4478-4485.

Dilshad R, Hanif KM, Hursthouse MB, Kabir SE, Malik KA, and Rosenberg E. Triruthenium clusters derived from the reactions of $[Ru_3(CO)_{12}]$ with benzothiazole, pyrimidine-2-thione and benzimidazole-2-thione; X-Ray structures of $[Ru_3(\mu\text{-}H)(\mu\text{-}2,3\text{-}\eta^2\text{-}NSC_7H_4)\text{-}(CO)_{10}]$ and $[Ru_3(\mu\text{-}H)(\mu_3\text{-}\eta^2\text{-}SN_2C_4H_3)(CO)_9]$. *J. Organomet. Chem.*1999; 585: 100-105.

Fujita M, Ibukuro F, Seki H, Kamo O, Imanari M, and Ogura K. Catenane formation from two molecular rings through very rapid slippage. A möbius strip mechanism. *J. Am. Chem. Soc.* 1996; 118: 899-900.

Fujita M, Yazaki J, and Ogura K. Preparation of a macrocyclic polynuclear complex, $[(en)Pd(4,\ 4'\text{-}bpy)]_4(NO_3)_8$ (en = ethylenediamine, bpy = bipyridine), which recognizes an organic molecule in aqueous media. *J. Am. Chem. Soc.* 1990; 112: 5645-5647.

Fusi A, Ugo R, Psaro R, Braunstein P, and Dehand J. Homogeneous catalysis with transition metal complexes. Part VII: Heteronuclear platinum clusters as hydrogenation catalysts of carbon–carbon multiple bonds. *J. Mol. Catal.* 1982; 16: 217-230.

Gade LH. Highly polar metal–metal bonds in "early-late" heterodimetallic complexes. *Angew. Chem., Int. Ed. Engl.* 2000; 39: 2658-2678.

Gauther S, Scopelliti R, and Severin K. A Heterobimetallic Rhodium (I)- Ruthenium (II) Catalyst for the Oppenauer-Type Oxidation of Primary and Secondary Alcohols under Mild Conditions. *Organometallics* 2004; 23: 3769-3771.

Ghosh S, Ahmed F, Al-Mamun R, Haworth DT, Lindeman SV, Siddiquee TA, Bennett DW, and Kabir SE. Investigations of 2-thiazoline-2-thiol as a ligand: Synthesis and X-ray structures of $[Mn_2(CO)_7(\mu\text{-}NS_2C_3H_4)_2]$ and $[Mn(CO)_3(PPh_3)\text{-}$

$(\kappa^2\text{-NS}_2\text{C}_3\text{H}_4)]$. *J. Chem. Crystallogr.* 2009a; 39: 595-602.

Ghosh S, Camellia FK, Fatema K, Hossain MI, Al-Mamun MR, Hossain GMG, Hogarth G and Kabir SE. Centrosymmetric $[\text{Mn}_2(\text{CO})_6(\mu\text{-thpymS})_2]$ (thpymS = tetrahydropyrimidine-2-thionato) as a synthon to mixed–metal clusters. *J. Organomet. Chem.* 2011; 696: 2935-2942.

Ghosh S, Kabir SE, Pervin S, Hossain GMG, Haworth DT, Lindeman SV, Siddiquee TA, Bennett DW, and Roesky HW. New mixed-metal carbonyl complexes containing bridging 2-mcapto-1-methylimidazole ligand. *Z. Anorg. Allg. Chem.* 2009b; 635: 76-87.

Ghosh S, Kabir SE, Pervin S, Raha AK, Hossain GMG, Haworth DT, Lindeman SV, Bennett DW, Siddiquee TA, and Salassa L. Tetranuclear group 7/8 mixed-metal and open trinuclear group 7 metal carbonyl clusters bearing bridging 2-mercapto-1-methylimidazole ligands. *Dalton Trans.*2009c: 3510-3518.

Ghosh S, Khanam KN, Hossain GMG, Haworth DT, Lindeman SV, Hogarth G and Kabir SE. The rational synthesis of tetranuclear heterometallic butterfly clusters: Reactions of $[\text{M}_2(\text{CO})_6(\text{-pyS})_2]$ (M = Re, Mn) with Group VIII metal carbonyls. *New J. Chem*. 2010a; 34: 1875-1884.

Ghosh S, Khanam KN, Hossain MK, Hossain GMG, Haworth DT, Lindeman SV, Hogarth G, and Kabir SE. Mixed-metal cluster synthesis: $[\text{Re}(\text{CO})_3(\mu\text{-S}_2\text{NC}_7\text{H}_4)]_2$ as a precursor for tri- and tetranuclear 2-mercaptobenzothiolato capped clusters. *J. Organomet. Chem.* 2010b; 695: 1146-1154.

Ghosh S, MA Mia, E Begum, GG Hossain, and SE Kabir. Synthesis, structure and reactivity of $[\text{Mn}_2(\text{CO})_6(\mu\text{-MBT})_2]$ (MBT = 2-mercaptobenzothiazolato): A Versatile precursor for mono- and polynuclear compounds. *Inorg. Chim. Acta* 2012; 384: 76-82.

Hanif KM, Hursthouse MB, Kabir SE, and Malik KMA, Rosenberg E. Ring-opening reactions of thiomorpholine and thiazolidine by $[\text{Ru}_3(\text{CO})_{12}]$: Crystal structures of $[\text{Ru}_3(\mu\text{-H})(\mu\text{-}\eta^2\text{-SCH}_2\text{CH}_2\text{NH}_2)(\text{CO})_9]$ and $[\text{Ru}_2(\mu\text{-}\eta^3\text{-SCH}_2\text{CH}_2\text{NHCH}_2)(\text{CO})_6]$. *J. Organomet. Chem.* 1999; 580: 60-65.

Herberhold M and Jin GX. Heterodimetallic complexes with an unbridged, polar metal–metal bond. *Angew. Chem., Int. Ed. Engl.*1994; 33: 964-966.

Hoque A, Islam S, Karim M, Ghosh S and Hogarth G. Variations in binding modes of 2-mercaptobenzoxazolates in the novel cyclic trinuclear complexes $[\text{Mn}_3(\text{CO})_{10}(\mu\text{-SCNOC}_6\text{H}_4)_3]$ and $[\text{Re}_3(\text{CO})_{12}(\mu\text{-SCNOC}_6\text{H}_4)_3$. *Inorg. Chem. commun.* 2015; 54: 69-72.

Kabir S, Alam J, Ghosh S, Kundu K, Hogarth G, Tocher DA, Hossain GMG, and Roesky HW. *Dalton Trans.* 2009; 4458-4467.

Kabir SE, Ahmed F, Das A, Hassan MR, Haworth DT, Lindeman SV, Hossain GMG, Siddiquee TA, and Bennett DW. Reactivity of $[\text{Re}_2(\text{CO})_8(\text{NCMe})_2]$ with thiazoles: Hydrido bridged dirhenium compounds bearing thiazoles in different coordination modes. *J. Organomet. Chem.* 2007; 692: 4337-4345.

Kabir SE, Karim MM, Kundu K, Ullah SB, and Hardcastle KI. Some pyridine-2-thiolato and 6-methylpyridine-2-thiolato complexes of manganese: Crystal structure of $[\text{Mn}_2(\mu\text{-pyS})_2(\text{CO})_6]$ (pyS = pyridine-2-thiolato ligand). *J. Organomet. Chem.*1996; 517: 155-159.

Kabir SE, Malik KA, Molla E, and Mottalib MA. Reactivity of $[(\mu\text{-H})\text{Os}_3(\text{CO})_8\{\text{Ph}_2\text{PCH}_2\text{P(Ph)C}_6\text{H}_4\}]$ with organic heterothiols: X-ray structures of $[\text{H}((\mu\text{-H})\text{Os}_3(\text{CO})_8(\eta^2\text{-pyS})\{\text{Ph}_2\text{PCH}_2\text{P(Ph)C}_6\text{H}_4\}]$ and $[\text{Os}_3(\text{CO})_8(\mu\text{-}\eta^2\text{-pyS})\{\text{Ph}_2\text{PCH}_2\text{P(Ph)C}_6\text{H}_4\}]$. *J. Organomet. Chem.* 2000; 616: 157-164.

Kalck P. Cooperative effect between two metal centres in hydroformylation: Routes towards heterobimetallic catalysis. *Polyhedron* 1988; 7: 2441-2450.

Katiyar D, Tiwari VK, Tripathi RP, Srivastava A, Chaturvedi V, R. Srivastava, Srivastava BS. Synthesis and antimycobacterial activity of 3,5-disubstituted thiadiazine thiones. *Bioorg. Med. Chem.* 2003; 11:4369-4375.

Kienitz CO, Thöne C, and Jones PG. Coordination chemistry of 2, 2 ‘-dipyridyl diselenide: X-ray crystal structures of pysesepy, $[\text{Zn}(\text{pySeSepy})\text{Cl}_2]$,$[(\text{pySeSepy})\text{Hg}(\text{C}_6\text{F}_5)_2]$, $[\text{Mo}(\text{Sepy})_2(\text{CO})_3]$, $[\text{W}(\text{Sepy})_2(\text{CO})_3]$, and $[\text{Fe}(\text{Sepy})_2(\text{CO})_2]$(pySeSepy = $\text{C}_5\text{H}_4\text{NSeSeC}_5\ \text{H}_4\text{N}$; Sepy = $[\text{C}_5\text{H}_4\text{N}(2\text{-Se})\text{N,Se}]$). *Inorg. Chem.* 1996; 35: 3990-3997.

Lee J, Emge T, and Brennan J. Heterometallic lanthanide-group 14 metal chalcogenolates. *Inorg. Chem.* 1997; 36: 5064-5068.

Liaw W-Fe, Chen C-H, Lee G-H, and Peng S-M. Iron pyridine-2-thiolate complexes: Interconversion of $[Fe^0(CO)_4(SC_5H_4N)]^-$, *cis*-$[Fe^{II}(CO)_2(SC_5H_4N)_2]$, and $[Fe^{II}(SC_5H_4N)_2]^-$ Organometallics, 1998; 17: 2370.

Moni MR, Ghosh S, Mobin SM, Tocher DA, Hogarth G, Richmond MG, and Kabir SE. Diphosphine-induced thiolate-bridge scission of $[Re(CO)_3(\mu\text{-}k^2\text{-}S,N\text{-}thpymS)]_2$ (thpymS = 1,4,5,6-tetrahydropyrimidine-2-thiolate): Structural and computational studies of configurational isomers of $[Re(CO)_3(k^2\text{-}S,N\text{-}thpymS)]_2(\mu\text{-}k^1, k^1\text{-}dppe)]$, *J. Organomet. Chem.* 2018; 871: 167-177.

Muetterties E, Rhodin T, Band E, Brucker C, and Pretzer W. Clusters and Surfaces. *Chem. Rev.*1979; 79: 91-137.

Muetterties E. Molecular metal clusters: Cluster chemistry may provide valuable Insights to Chemisorption and Catalysis on Surfaces. *Science* 1977; 196: 839-848.

Neumann HP and Ziegler ML. μ_3-Arsenic trimolybdenum clusters with oxygen and sulphur bridging the transition metals. *J. Chem. Soc., Chem. Commun*. 1988: 498-500.

Quebatte L, Scoppelliti R, and Severin K. Combinatorial catalysis with bimetallic complexes: robust and efficient catalysts for atom-transfer radical additions.*Angew. Chem., Int. Ed.* 2004; 43: 1520-1524.

Rahman MdS, Sarker JC, Ghosh S, and Kabir SE. The first carbonyl substituted derivative of $[Mn_2(CO)_6 (\mu\text{-}pyS)_2 (CO)_6]$. *Aust. J. Chem.* 2012; 65: 796-801.

Rose DJ, Chang Y-D, Chen Q, and Zubieta JReactions of uranyl thiolate complexes with molecular oxygen: Syntheses and crystal and molecular structures of the uranyl thiolate peroxo species $(HNEt_3)_2[(UO_2)_2(O_2)(SC_4N_2H_3)_4]$ and $(HNEt_3)[H(UO_2)_2(O_2)(SC_4N_2H_2Me)_4]\cdot Me_2CO\cdot 0.5Et_3N$ and of the uranyl thiolate oxo cluster $(HNEt_3)_2[(UO_2)_4(O)_2(SC_5NH_4)_6]\cdot Me_2CO$. *Inorg. Chem.* 1994; 33: 5167-5168.

Rose DJ, Chang YD, Chen Q, Kettler PB, and Zubieta J. Synthesis and characterization of Gallium and Indium thiolate Complexes. Crystal and Molecular Structures of $[M(SC_5H_4N)_3]$(M = Ga, In), $[In(SC_5H_3N\text{-}3\text{-}SiMe_3)_3]$, and $[M_2(OC_2H_4)_2(SC_5H_4N)_4]$ (M = Ga, In). *Inorg. Chem.* 1995; 34: 3973-3979.

Rosenfield SG, Berends HP, Gelmini L, Stephan DW, and Mascharak PK. New octahedral thiolato complexes of divalent nickel: Syntheses, structures, and properties of $(Et_4N)[Ni(SC_5H_4N)_3]$ and $(Ph_4P)[Ni(SC_4H_3N_2)_3].CH_3CN$. *Inorg. Chem.* 1987; 26: 2792-2797.

Stang PJ and Cao DH. Transition metal based cationic molecular boxes. Self-assembly of macrocyclic platinum (II) and palladium (II) tetranuclear complexes. *J. Am. Chem. Soc.* 1994a; 116: 498-4982.

Stang PJ and Olenyuk B. Directed self-assembly of chiral, optically active macrocyclic tetranuclear molecular squares. *Angew. Chem., Int. Ed. Engl.* 1996a; 35: 732-736.

Stang PJ and Whiteford JA. Mixed, neutral-charged, platinum-platinum and platinum-palladium macrocyclic tetranuclear complexes. *Organometallics* 1994b; 13: 3776-3777.

Stang PJ, Cao DH, Saito S, and Arif AM. Self-assembly of cationic, tetranuclear, Pt (II) and Pd (II) macrocyclic squares. X-ray crystal structure of $[Pt^{2+}(dppp)(4,4'\text{-}bipyridyl)^{2-}OSO_2CF_3]_4$. *J. Am. Chem. Soc.* 1995; 117: 6273-6283.

Stang PJ, Olenyuk B, Fan J, and Arif AM. Combining ferrocenes and molecular squares: Self- assembly of heterobimetallic macrocyclic squares incorporating mixed transition metal systems and a main group element. Single-crystal X-ray structure of $[Pt(dppf)(H_2O)_2][OTf]_2$. *Organometallics* 1996b; 15: 904-908.

Umakoshi K, Ichimura A, Kinoshita I, and Ooi S. The dinuclear palladium(II) complex of pyridine-2-thiol: Synthesis, structure, and electrochemistry. *Inorg. Chem.* 1990; 29: 4005-4010.

Wang Z, Jiang L, Liu Z, Gan CRR, Liu Z,Zhang X, Zhao J and Hor TSA. Facile formation and redox of benzoxazole-2-thiolate-bridged dinuclear Pt(II/III) complexes. *Dalton Trans.* 2012; 12568-12576.

J. Bangladesh Acad. Sci. 47(1); 21-25: June 2023 DOI: https://doi.org/10.3329/jbas.v47i1.61704

Journal of Bangladesh Academy of Sciences

Journal homepage: http://www.bas.org.bd/publications/jbas.html

Research Article

Study on wave power regarding Bangladesh

Mohammad Asadul Haque*, Tasibana Chowdhury and Mamunur Rashid

Department of Physics, University of Chittagong, Chittagong, Bangladesh

ARTICLE INFO

Article History

Received: 11 September 2022
Revised: 6 November 2022
Accepted: 2 April 2023

Keywords: Wave power, Periodic up and down, Bay of Bengal, Surface attenuator, Seashore, Intensity.

ABSTRACT

Wave Energy is a type of renewable energy that uses the power of waves to generate electricity, and it is the largest estimated global resource form of ocean energy. This study deals with various techniques of wave power and focuses on the present scenario in the world and its potentiality in Bangladesh. The analysis of parameters of wave height, wavelength, and wave period; indicates the bright prospects of wave power in Bangladesh.

Introduction

The economic development of a state depends on the power sector. Bangladesh can be enriched in the power sector by using wave energy to alleviate poverty and fight environmental degradation, such as desertification, bio-diversity depletion and climate change. The state is trying to overcome the problem of costly rental power plants and looking for long-term nuclear power that is unsuitable for the state (Salimullah et al., 2014). It has been estimated that if less than one percent of the total capacity of tidal electricity is generated, it will cover five times the total global requirements (WEC, 2022). Wave power converts the periodic up-and-down movement of the ocean waves into electricity by setting up equipment on the surface of the oceans that captures the energy produced by the wave movement. The world energy council has estimated that approximately 2 terawatts of power could be produced from the ocean via wave power (Siddique, 2013). Bangladesh has a huge ocean area with various power resources such as wave energy, Ocean Thermal Energy (OTE) and tidal energy. In the Bay of Bengal, the wave height varies from 0.5 m to 3.5 m, and the wave period from 3 to 12 sec indicates the potentiality of wave power generation in Bangladesh (Haque et al., 2010). The state can easily meet its huge power demand by proper utilization of the above mentioned energies, where wave power can play a vital role in integrating as a new source of renewable energy to the off-grid power connection in isolated coastal areas, namely Sandwip, Saint Martin, Koakata, Kutubdia, dublar char, Cox's bazar tourist zone, etc. and improve the social, environmental and economic perspective of Bangladesh (Anam and Bustam, 2011; Rahman and Khan, 2014). This study aims to concentrate on the progress of wave power world wide and its prospects in Bangladesh.

Wave energy in details

When the wave travels through a medium, it will experience some local oscillations, but the particles do not travel with the wave. Water waves are surface waves with circular particle movement directions involving longitudinal and transverse wave movements. Waves are generated by the wind blowing over large ocean areas and once generated, travel immense distances with only small energy losses. Waves travel vast distances across oceans at great speed. The longer and stronger the wind blows over the sea surface, the

---

*Corresponding author: <asad.physics@cu.ac.bd>

higher, longer, faster, and more powerful the sea is. The energy within a wave is proportional to the square of the wave height, so a two-meter-high wave has four times the power of a one-meter high wave. The amount of energy transferred depends mainly on the wind speed, period, and distance over the surface on which it blows. In 2008, the first experimental wave farm was opened in Portugal at the Agucadoura Wave Park (World's first commercial wave power station, 2018). The standard formula for wave power calculation (Salimullah et al., 2014):

Where, P is the power of a wave in deep water,

$$P = \frac{\rho g^2 T H^2 L}{32\pi} \text{..........} (1)$$

measured in watts; ρ is the density of seawater (1,025 kg/m^3); g is the acceleration due to gravity (9.81 m/s^2); T is the wave period in seconds; H is the wave height in meters; L is the length of the wave front (perpendicular to the direction of travel, across), in meters; π is the mathematical constant 3.1416 (Calisal, 1983; Tucker and Pitt, 2001).

Fig. 1. Images of wave power technologies

Image of power buoy point absorber

Image of surface attenuator

Image of oyster wave surge converter device

Image of AWS pressure differential device

Image of wave dragon overtopping device

Image of oscillating water column

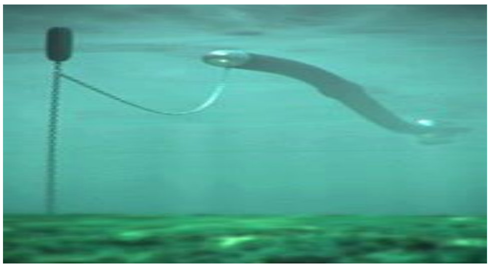

Image of the anaconda bulge wave power device

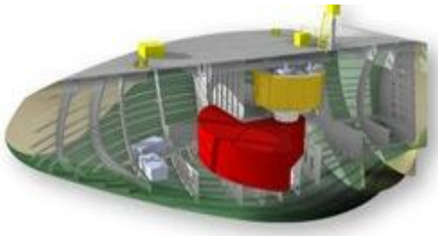

Image of the rotating mass device

Wave power devices are generally categorized by the method used to capture the energy of the waves by location, and by the power take-off system. Generic wave energy concepts are shown through several images of Fig.1 (McCormick and Ertekin, 2009; Kurniawan et al., 2014; Shareslide. net, 2022).

Present scenario of wave power in the world

The current status of wave power stations in the world as of 2022 is listed below: (Rahman and Khan, 2011; Vicinanza et al., 2011; Joao and Babcock, 2015; You et al., 2012; WEC, 2022).

Country	Details
United Kingdom	Islay Limpet, Scotland (the world's first commercial Wave Power plant) 250 kW; 2000 [Decommissioned in 2018]
	Pelamis P2 generator (wave farm off the Portuguese coast) Orkney wave power station; Estimated 120 GW.
Portugal	Aguçadoura Wave Park 2.25 MW (22.5 MW Planned); 2008
Germany	North sea coast; 250 kW; 2000
France	France's Brittany (largest tidal 240 MW); 10 MW; 2021
Sweden	Sotenas Wave Power Project; 10 MW; 2015
Greece	SINN power (Island of Halki in Greece); 1 MW; 2015
Finland	Penguin; 1 MW; 2020
Canada	25 GWh wave power plants are investigated at five locations on Canada's Pacific coast; 2017
Italy	1 MW; 2018
U S A	2.64 trillion kilowatt hours has been estimated theoretically; 2021
India	Total potential comes to around 40,000 MW; 2010
China	Ten regions of China, the energy. Estimated near shore wave energy of 249.7 TWh/year; Practicing wave energy since 1980
Myanmar	Has 1,930 Km of coastline on the Indian Ocean; Wave energy theoretical potentials (Twh/year): 211 Wave energy applicable potentials (Twh/year): 11; 2016
Ireland	Wave energy conversion project located 4-6 km offshore Co. Clare, Starting with 5MW capacity. [Estimated 1875 TW]; 2021
South Korea	The average 30 kW power could be increased in the Korean Peninsula, which is surrounded by the Yellow Sea, East China Sea, and East Sea.
Bangladesh	The vast energy potential of the wave energy from the Bay of Bengal has yet to be harnessed significantly.

Methodology, Results, and Discussion

For experimental data, wave parameters such as wave height, wavelength, and wave period are measured using a direct measurement system. A new shape iron frame that is scaled in centimeters has been constructed to measure the wave height vertically and wavelength horizontally. A stopwatch has been used to record the time and a floating boat from where the data have been taken.

Bangladesh's large and long coastal area can be used for electricity generation to minimize the energy crisis. The scope of wave power in Bangladesh has been assessed by calculating wave power production in the ocean area. Most of the recent research indicates that the wave height produces in the coastal regions of the Bay of Bengal lies between (0.5-3.5) m, which is very much suitable for wave power (Haque et al., 2010). In the Bay of Bengal, the wave height remains the same in all general day conditions. For these reasons, it has been considered four spots in the Bay of Bengal at Chittagong and Cox's Bazar districts as Station-one: Potenga Sea shore area at Chittagong; Station-two: Anowara Sea shore area at Chittagong; Station three: Cox's Bazar Sea shore area and Station four: Saint Martin Island at Cox's Bazar as shown in Fig. 2 (Southern part map of Bangladesh) from where the primary data have been collected.

Fig. 2. The study area is shown in the map of Bangladesh (Southern part)

In this research, the average wave height is from 0. 45 m to 3.42 m, and the wave period is about (3 to 11) sec in the above survey area. The recorded data have been analyzed for power production and presented through several graphs. The wave height, wave period, and the possibilities of power production with time in other months have been presented below:

The wave height has been recorded from 9 am to 6 pm from 2 to 14th April-2018, after every 30 minutes at station-1; from 9 am to 6 pm from 4 to 13th May-2018 after every 30 minutes at station-2; from 9 am to 6 pm from 4 to 11th June-2018 after every 30 minutes at station-3 and from 9 am to 6 pm during 12 to 19th June-2018 after every 30 minutes.

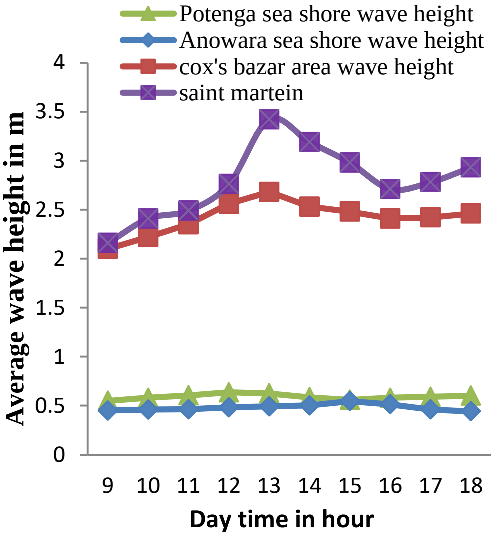

Fig. 3. Average wave height versus day time of the survey area.

The average wave height has been found to be from 0. 55 m to 0.63 m and the wave period is about (3 to 4) sec at station-1; from 0. 45 m to 0.55 m and the wave period is about (3 to 4) sec at station-2; from 2.1 m to 2.68 m and the wave period is about (8 to 10) sec at station-3 and from 2.2 m to 3.42 m and the wave period is about (9 to 11) sec at station-4.

The average wave height versus daytime of the survey areas at a glance is shown in Fig. 3:

Fig. 3 indicates that the wave height continuously has an increasing and decreasing tendency with the variation of the tides. It follows six hours rotation, after six hours, it goes maximum and then tells to a minimum. The wave height and time are also related to wind speed, and vast space (free front side and back side) is required for more wind speed.

Due to the high wave height Fig. 4 indicates the wave takes more time at Saint Martin than at the other three places.

Fig. 5 shows more wave height produces more power which is clear that the wave height is maximum at Saint Martin and minimum at the Anwara Seashore area. The reason is that at Potenga and Anwara seashores, the front side has huge free

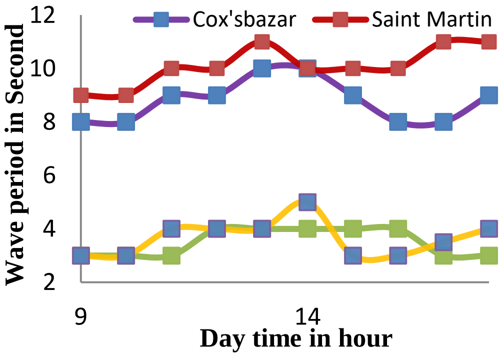

Fig. 4. Average wave period versus daytime of the survey areas

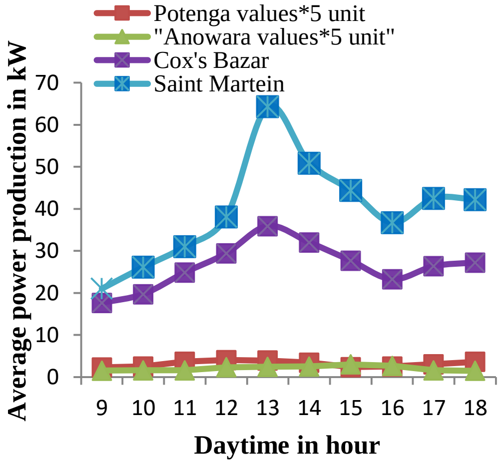

Fig. 5. Possible power production with daytime in survey areas

space for incoming wind, but the back side is blocked by human habitation, so the incoming wind can't pass properly. Since urbanization and human habitation are not so much developed in Cox's Bazar long Seashore area, the place is much better than Chittagong. The island of Saint Martin is the best place for wave power production because of the maximum wind speed. Fig. 5 shows that getting an average of 27 kW power from a single wave device could be possible. Available space in the Bay of Bengal indicates a chance to set up several wave machines quickly. Finally, wave power could be a new renewable energy source that can play an essential role in solving the present energy crisis in Bangladesh.

Conclusion

The summary of this study shows that there is a considerable opportunity for Bangladesh to meet its future power demand and thus, economic growth through wave power. It can help the state produce more power to reduce the Load-shedding problem. The time has come to look forward and work with wave energy to produce electricity rather than depending wholly on conventional methods. Therefore, the Government and the private sector should work hand in hand to emphasize wave energy more to produce electricity to solve our power crisis.

References

Anam K and Bustam HA. Power crisis & its solution through renewable energy in Bangladesh. *Multidiscip. J. Sci. Technol.,* 2011, 13-18.

Calisal SM. A note on the derivation of potential energy for two dimensional water waves. *Ocean Eng.* 1983; 10(2): 133-138.

Haque A, Rahman J and Mahmood H. Power crisis and solution in Bangladesh. *Bangladesh J. Sci. Ind. Res.* 2010; 45(2): 155-165.

Joao L and Babcock JL. EDP and efacec to collaborate on wave energy projects. *The Way back Machine Bloomberg,* September 24, 2015.

Kurniawan A, Greaves D and Chaplin J. Wave energy devices with compressible volumes. *Proc. R. Soc. A*: *Math., Phys. Eng. Sci.* 2014; 470(2172): 20140559.

McCormick ME and Ertekin RC. Renewable sea power: Waves, tides, and thermals– new research funding seeks to put them to work for us. *Mech. Eng.* 2009; 131(5): 36-39.

Rahman AA and Khan KA. Feasibility studies on WEC (Wave Energy Converter) for use in coastal belt at Cox's Bazar of Bangladesh under the climate condition of the Bay of Bengal. *Int. J. Eng. Innov. Technol.,* 2014; 4(2): 12-19.

Rahman AA and Khan KA. The present situation of the wave energy in some different countries of the world. *Int. J. Comput. Info. Technol.* 2011; 2(1): 110754.

Salimullah SM, Rafi MME and Sheikh MRI. Prospects of wave power in Bangladesh. *Am. J. Eng. Res.,* 2014; 3(5): 29-35.

Shareslide. net: Types of wave convertor device. *Retrived on March* 2022.

Siddiqui MS. Tidal power an alternative source of electricity. *The Financial Express.* February 10, 2013.

Tucker MJ and Pitt EG. Waves in Ocean Engineering *(1st ed.).* Elsevier Ocean Engineering book series, volume 5, eds. Bhattacharyya R and Mccormick ME. *Oxford: Elsevier,* 2001(2): 35-36.

Vicinanza D, Cappietti L, Ferrante V and Contestabile P. Estimation of the wave energy in the Italian offshore. *J. Coast. Res.;* 2011 (special issue 64): 613-617.

"World's first commercial wave power station activated in Scotland". *Archived from the original on* August 5, 2018.

World Energy Council (WEC). World Energy Resources, Marine Energy, 2022. [www.wec.com]

You Y, Sheng S, Wu B and He Y. Wave energy technology in China. *Phil. Trans. R. Soc.* 2012; 370**:** 472-480.

J. Bangladesh Acad. Sci. 47(1); 27-31: June 2023 DOI: https://doi.org/10.3329/jbas.v47i1.64909

Journal of Bangladesh Academy of Sciences

Journal homepage: http://www.bas.org.bd/publications/jbas.html

Research Article

First record on the occurrence of long fingered gurnard *Lepidotrigla longimana* (Scorpaeniformes: Triglidae) from Bangladesh

Md. Sagir Ahmed, Mysha Mahjabin, Durjoy Raha Antu[1] and Sujan Kumar Datta

Department of Zoology, University of Dhaka, Dhaka, Bangladesh

ARTICLE INFO

Article History

Received: 05 March 2023
Revised: 14 May 2023
Accepted: 11 June 2023

Keywords: *Lepidotrigla longimana,* COI, DNA barcoding, Phylogeny

ABSTRACT

This study confirmed the presence of triglid fish *Lepidotrigla longimana* Li (1981) for the first time in Bangladesh waters. Four individuals of this species were collected from Cox's Bazar (21.77 N 91.62 E) on 5 October 2018 as bycatch. The species was taxonomically identified through the traditional morphometric method, which was further validated by a molecular approach based on partial cytochrome c oxidase subunit I (COI) sequences (DNA barcodes). The total length was three times the head length and 4.1 times the body height. The head length was 2.5 times larger than the snout length and 3.2 times the eye diameter. The number of scales on the lateral line was 60. A smaller blue spot is present on the inner side of the pectoral fin. The average K2P distances of the COI sequence within species were 0.53. The sequences clustered together under a single clade in the Maximum likelihood (ML) tree. Morphometric, meristic, and molecular data thus confirmed the species as *L. longimana*.

Introduction

Lepidotrigla Günther (1860), the most diverse genus of the family Triglidae, are small fishes less than 200 mm in standard length and are commonly known as gurnards or sea robins. They are found in the Bay of Bengal, the Andaman Sea off Myanmar (Gomon and Kawai, 2018), and temperate and tropical waters of the eastern Atlantic, Indian, and Western Pacific oceans (Richards, 1992). Richards and Saksena (1977) revised the genus *Lepidotrigla* from the Western Indian Ocean and noted the difficulty of diagnosing it. The presence of two species *L. bispinosa and L. piloptera,* has been documented so far from Bangladesh waters (Fanning et al., 2019; Singha et al., 2019). Due to its small size, muddy flavor, and highly bony muscles, the species is non-targeted and has low market demand. But a recent study attempted the production of bioactive peptides from this species for their abundant protein content (Hu et al., 2022).

Ahmed et al. (2021) have mentioned the presence of this species on the Bangladesh coast, and here in this paper, we describe this gurnard fish, *Lepidotrigla longimana* Li (1981) based on morphometric and molecular approach.

Material and Methods

Sampling and morphological analysis

Four specimens of *L. longimana* were collected on 5 October 2018 from Cox's Bazar (21.77 N 91.62 E) off the coast of the Bay of Bengal. The fishermen caught it during fishing as bycatch along with the fishes of the genus *Nemipterus*

---

*Corresponding author: sagir@du.ac.bd

[1] *Department of Zoology, Jagannath University, Dhaka, Bangladesh*

(Threadfin bream). The specimens were carried to the lab with ice in a coolbox for further analysis. Following Li's (1981) and Richards's (1992) guideline, the specimens were examined. The length was measured in cm scale. A small portion of muscle was taken for DNA extraction and tagged the specimen with a voucher ID (DUZM_MF_159C, DUZM_MF_159C.2, DUZM_MF_159C.3, DUZM_MF_159C.4).

DNA extraction and amplification by PCR

The extraction of genomic DNA was performed by Monarch® Genomic DNA Purification Kit, USA, following the manufacturer's protocol. PCR amplification of the target MT-COI gene and purification of amplified PCR products were performed following Ahmed et al. (2021) and Datta et al. (2020). Approximately 658 bp was amplified from the 5′ regions of the MT-COI gene using the primers FishF2 5′TCGACTAATCATAAAGATATCGGCAC3′ and FishR2 5′ACTTCAGGGTGACCGAAGAATCAGAA3′ (Ward et al., 2005). The quality amplicons were viewed by the Nanodrop spectrophotometer (NanoDrop™ One Microvolume UV-Vis Spectrophotometer).

Sequencing and Phylogenetic Analysis

The sequencing was performed in First BASE Laboratories SdnBhd, Malaysia. CHROMAS software was used to view the raw sequences and edited manually using MUSCLE. BLAST verified the sequence, and only the best matches with more than 96% similarity were submitted to the NCBI GenBank. Analyses were performed by MEGA X software (Kumar et al., 2018). The Maximum-Likelihood (ML) phylogenetic tree was constructed using the K2P model (Kimura, 1980).

Diagnosis

L. longimana closely resembles to *L. venusta* Fowler (1938). Both throat and breast are covered with scales. Pectoral fin rays are long and finger-like and reach the origin of the anal fin. A dark spot is present on the anterior dorsal fin where in posterior is absent. The species can be separated from *L. venusta* by the number of scales on the lateral line. The number of scales on the lateral line is 60 in the former species and 52-54 in the latter. A smaller blue spot is present on the inner side of the pectoral fin in *L. longimana*.

Results & Discussion

Description

The color of the body and head is red, and the ventral side is lighter. The center of the inner surface of the chest is long and blue (Fig. 1). The throat and breast are covered with scales, dorsal fin with 9 spines and 14 rays. A dark black spot is

Fig. 1. ***Lepidotrigla longimana*** **(10 cm), family Triglidae, voucher ID DUZM_MF_159C.2, collection date: 5-October-2018, place: Cox's Bazar (21.77 N 91.62 E)**

present on the anterior and posterior dorsal fin without a spot (Fig. 1). The pectoral fin is long and finger-like and reaches the origin of the anal fin with 11 and 3 free rays. A smaller central blue spot is present on the inner side of the pectoral fin. The total length is 3 times of the head length and 4.1 times the body height (Table 1). The head length is 2.5 times larger than the snout length and 3.2 times the eye diameter. A total of 60 scales are present on the lateral line.

Table 1. Morphometric data of the specimens of *Lepidotrigla longimana* (DUZM_MF_159C to 159C.4)

Measurements (cm)	Present study (N=4)	Li (1981)
Total length (TL)	9.5	
Body height	2.3	
Standard length (SL)	7.5	
Head length (HL)	3.2	
Eye diameter (ED)	1.0	
Inter orbital length (IOL)	0.7	
Snout length (SnL)	1.3	
Pectoral length (PL)	3.0	
Free pectoral length (FPL)	1.7	
Caudal Fin length (CFL)	2.0	
Caudal peduncle length (CPL)	1.2	
Caudal peduncle depth (CPD)	0.4	
HL/SnL	2.5	2.1-2.6
HL/ED	3.2	3-3.5
TL/HL	3.0	2.9-3.3
TL/BH	4.1	4-4.8
Counts		
Dorsal fin	IX+14	IX+1-14
Anal fin	15	15
Pectoral fin	11+ 3 free	11+ 3 free
Ventral fin	I+5	I+5
Caudal fin		
Scales in lateral line	60	60

Molecular analysis

The generated three partial sequences of the COI gene with an average of 634 bp of the three specimens were submitted to the NCBI database with assigned accession numbers MN083140, MN083141, and MN083142. The species was confirmed through BLAST search having 99% query coverage and 95.59% identity with the pre-existing JQ681320 and 95.53% with KP266831, which validated the morpho-taxonomic identification of the species. The mean nucleotide base frequencies were T: 27.17%, C: 33.00%, A:22.18%, and G: 17.66%. GC content analysis showed that the average GC was 50.66% and AT 49.34%. The GC contents were found at the first, second, and third codon positions at 57.17%, 42.43%, and 52.36%, respectively. The K2P distance within species was 0.53. The nearest species were found, *L. hime,* which was 5.33% distant from *L. longimana*, and *L. abyssalis* was the distant species (Table 2). Phylogenetic analyses showed that highly similar species formed a distinctive clade.

Table 2. Genetic divergence (% K2P distance) of *L. longimana* with other species

Species		Interspecies Distance %
L. longimana	*L. hime*	5.33
	L. kishinouyi	5.63
	L dieuzeidei	5.66
	L. bispinosa	6.30
	L. alata	6.61
	L. argus	7.66
	L. multispinosa	7.70
	L. cavillone	7.84
	L. mulhalli	9.39
	L. abyssalis	12.04

A total of 22 sequences of 12 species were used, where three were from the present study, and the rest were retrieved from NCBI Genbank. *Pterygotrigla hemisticta* was used as an outer genus of triglidae family. *L. longimana* formed a distinctive clade with a bootstrap value of 98 in the phylogenetic tree, and other species formed clades as of their similarities (Fig. 2). Classical taxonomy based on morphometric and meristic characters along with DNA barcoding confirms the species as *L. longimana*.

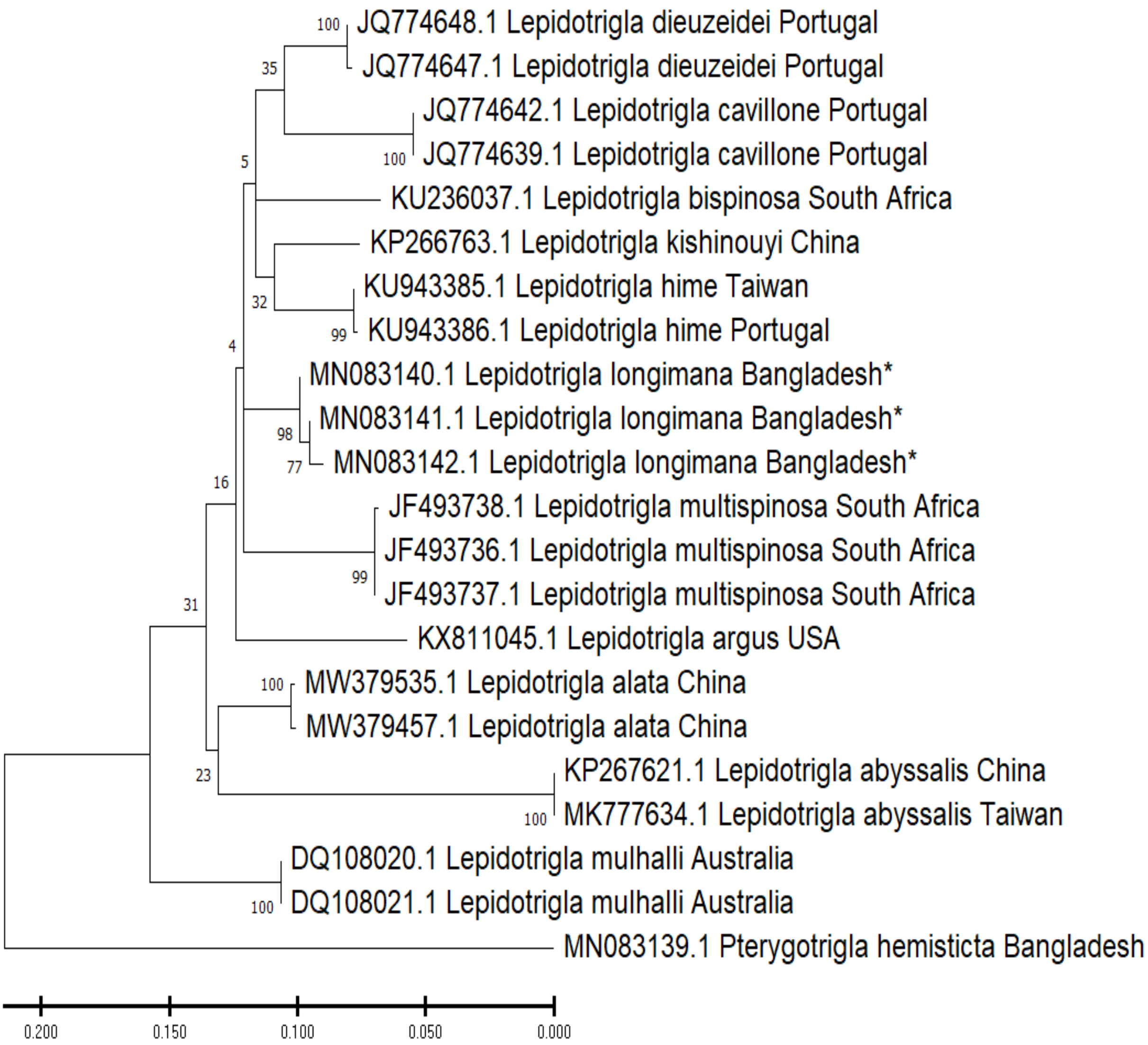

Fig. 2. Maximum Likelihood tree of the COI sequences showing the relationships among *Lepidotrigla longimana* with the pre-existing sequences of *Lepidotrigla* species of the NCBI GenBank. *Pterygotrigla hemisticta* was taken as an outgroup. (The sequences generated in this study are marked as Bangladesh*).

References

Ahmed MS, Datta SK, Saha T and Hossain Z. Molecular characterization of marine and coastal fishes of Bangladesh through DNA barcodes. *Ecol. Evol.* 2021; 11(9): 3696-3709.

Datta SK, Saha T, Sanzida NJ, Ahmed S, Akhand MA and Ahmed MS. New distributional record of Hasselt's bamboo shark Chiloscyllium hasseltii (Orectolobiformes: Hemiscylliidae) from Bangladesh waters. *Int. J. Mar. Sci.* 2020; 36: 291-295.

Fanning LP, Chowdhury SR, Uddin MS and Al-Mamun MA. Marine fisheries survey reports and stock assessment 2019. *Department of Fisheries, Government of Bangladesh*. 2019.

Fowler HW. Descriptions of new fishes obtained by the United States Bureau of Fisheries steamer Albatross, chiefly in Philippine seas and adjacent waters. *Proceedings of the United States National Museum*. 1938; 85(3032): 31-135.

Gomon MF and Kawai T. A review of Indonesia's Indian Ocean species of Lepidotrigla gurnards (Teleostei: Scorpaeniformes: Triglidae) with descriptions of three new species from southern coastal waters. *Raffles Bull. Zool.* 2018; 66: 624-651

Günther ACLG. Catalogue of the Fishes in the British Museum: Acanthopterygian fishes: *Squamipinnes, Cirrhitidœ, Triglidœ, Trachinidœ, Sciœnidœ, Polynemidœ, Sphyrœnidœ, Trichiuridœ, Scombridœ, Carangidœ, Xiphiidœ*. 1860. *Arkose Press*, 2015. pp. 1-580.

Hu X, Dai Z and Jin R. Purification and identification of a novel angiotensin converting enzyme inhibitory peptide from the enzymatic hydrolysate of Lepidotrigla microptera. *Foods.* 2022; 11(13): 1889.

Kimura M. A simple method for estimating evolutionary rates of base substitutions through comparative studies of nucleotide sequences. *J. Mol. Evol.* 1980; 16: 111-120.

Kumar S, Stecher G, Li M, Knyaz C and Tamura K. MEGA X: molecular evolutionary genetics analysis across computing platforms. *Mol. Biol. Evol.* 2018; 35(6): 1547-1549.

Li SZ. On two new species of triglid fishes of the genus lepidotriga from the South China Sea. *Zool. Res.* 1981; 2(4): 295-300.

Richards WJ. Comments on the genus Lepidotrigla (Pisces: Triglidae) with descriptions of two new species from the Indian and Pacific oceans. *Bull. Mar. Sci.* 1992; 51(1): 45-65.

Richards WJ and Saksena VP. Systematics of the gurnards, genus Lepidotrigla (Pisces, Triglidae), from the Indian Ocean. *Bull. Mar. Sci.* 1977; 27(2): 208-222.

Singha Nk, Parvej MR, Uddin MS and Chowdhury SR. (Eds. Uddin MS and Chowdhury SR). Bangladesh Samudrik O Upokolio Matsya Projatir Album (Species Album of Marine and Coastal Fisheries Researches of Bangladesh). *Department of Fisheries, Ministry of Fisheries and Livestock*; 2019. p. 264.

Ward RD, Zemlak TS, Innes BH, Last PR and Hebert PD. DNA barcoding Australia's fish species. *Philos. Trans. R. Soc. Lond., B, Biol. Sci.* 2005; 360(1462): 1847-1857.

J. Bangladesh Acad. Sci. 47(1); 33-42: June 2023 DOI: https://doi.org/10.3329/jbas.v47i1.62976

Journal of Bangladesh Academy of Sciences

Journal homepage: http://www.bas.org.bd/publications/jbas.html

Research Article

Prevalence of different bacterial species in the uterine fluid of repeat breeder cows

Md. Farhad Hossain Chowdhury, Mir Md. Iqbal Hasan[1], Moinul Hasan, Md. Siddiqur Rahman[2], Marzia Rahman[3] and Nasrin Sultana Juyena[*]

Department of Surgery and Obstetrics, Faculty of Veterinary Science, Bangladesh Agricultural University, Mymensingh, Bangladesh

ARTICLE INFO

Article History

Received: 01 December 2022
Revised: 07 May 2023
Accepted: 11 June 2023

Keywords: Bacteria, Repeat breeding cows, Prevalence of bacteria, Uterine fluid.

ABSTRACT

Among the diverse factors, bacterial infections in the reproductive tract potentially cause of repeat breeding in dairy cows. The present research was conducted to appraise the uterine organism in healthy fertile cows (HFC) and repeat breeder cows (RBC) and to establish a relationship with previous disease or disease conditions. A total of 43 uterine samples were collected from 10 healthy fertile and 33 RB cows for bacteriological study. Among RBC, 39.4% harbored bacterial isolates of *E. coli* (30.3%), *Staphylococcus aureus* (27.3%), *Staphylococcus epidermidis* (15.2%), and *Bacillus spp.* (18.2%). Total Viable Count (TVC) of RBC with isolates was higher (1.81 x 10^{10}CFU/mL) than in normal fertile cows (1.3x10^{10} CFU/mL). No bacterial isolates were recovered from 60.6% RBCs and 80.0% healthy fertile cows. A single, mixed infection of two, three and four bacterial species was observed in the uterine discharge of 12.1%, 9.1%, 12.1% and 6.1% RBC, respectively. From animal demographic data of RBC, the sub-clinical mastitis, acute mastitis, endometritis, dystocia, retention of placenta, and abortion were 42.4%, 39.4%, 39.4%, 12.1%, 9.1%, and 6.1%, respectively. In contrast, the presence of dystocia, endometritis, subclinical mastitis, retention of placenta and abortion was recorded in 50%, 30%, 30.8%, 23.1%, and 15.4% of healthy cows, respectively. This result could help the veterinarian to design the proper antibacterial therapy based on bacteria isolates in RBCs.

Introduction

Lactating cows with good reproductive performance is necessary for a profitable dairy farm (Ahuja et al., 2017). A good economic return depends on a one-year calving interval and maximum milk production by a cow per year (Gani et al., 2008). Among various reproductive diseases, repeat breeding syndrome reduces the conception rate and causes huge financial losses for Bangladeshi dairy farmers (Talukder et al., 2005; (Khair et al., 2013). Repeat breeders are defined as cows that have calved at least once, are less than 10 years of age, accounted to be healthy cyclic and continued as infertile even after three times of breeding and had no sign of any infection of reproductive diseases and no anomalous releases by reproductive tract (Yousuf et al., 2010; Regmi and Dhakal, 2020). Causes of the repeat breeding syndrome (RBS) are generally uncertain but possibly comprise dairy farm environment, management, estrus detection, breeding methods, and animal factors (Katagiri and Takahashi, 2004). The RBS is often associated with subclinical endometritis, late ovulation and ovarian dysfunction, and others which are the root cause of fertilization failure or early embryonic mortality (Parkinson, 2009). However, it is noticed that infections with diverse pathogens in the reproductive tract cause conception failure in cows (Bardos et al., 2020). Breeding heifers or cows with contaminated semen increases the uterus tract's

---

[*] Corresponding author: <nsjuyena@bau.edu.bd>

[1] *Department of Physiology, Faculty of Veterinary, Animal and Biomedical Sciences, Sylhet Agricultural University, Sylhet, Bangladesh*

[2] *Department of Medicine, Faculty of Veterinary Science, Bangladesh Agricultural University, Mymensingh, Bangladesh*

[3] *Department of Microbiology and Hygiene, Faculty of Veterinary Science, Bangladesh Agricultural University, Mymensingh, Bangladesh*

microbial load (Cojkic et al., 2021). Moreover, bacterial infections play a significant role in infertility (Yoo, 2010). Therefore, the huge occurrence (20.48%) of RBS in cows in Bangladesh, the present research was conducted to assess the bacterial colonization in the uterine discharge of normal fertile and repeat breeder cows and study previous disease history associated with repeat breeder cows in dairy farms.

Materials and Methods

The study was conducted in the Department of Surgery and Obstetrics, Bangladesh Agricultural University, Bangladesh.

Study design

The research was divided into two parts. The first part included an investigation to categorize the repeat breeder cows with clinical abnormality. In the second part, an effort was made to estimate the prevalence of bacteria in the uterine discharge of repeat breeder cows and the HFC.

Collection of animal demographic data

A well-defined pre-structured questionnaire was prepared to record the animal data like age, breed, parity, date of last calving and their types, number of previous services, nutritional status (Body condition score), and nature of the genital discharge. Most of the data in this research was obtained through face-to-face interviews with the farm owners of the animal.

Selection of animal

Out of 172 Frisian, Jersey, and Sahiwal crossbreed cows, 33 repeat breeding cows and 10 randomly selected healthy fertile cows were selected from Khaja Dairy Farm, Chorlokkha, Karnaphuli, Chattogram in the present study during the estrous cycle. These animals were reared under an intensive farming system and fed by farmer's practice. Recorded cows were 30 to 110 months old with 1 to 6 parties. As regard breed quality, the animals belonged to cross-bred (n=43). We excluded the pregnant cow and the cows with anestrus or cystic ovaries detected by rectal palpation. Insemination before seven to eight days of sampling time and vaginal examination were avoided at the time of sampling.

Bacteriological media and broth

Bacteriological agar media used for the bacteriological study were Blood Agar (5% sheep blood, BA, Difco), Nutrient Agar (NA; Oxoid), Manitol Salt Agar (MSA), MacConkey Agar (MA; Merk), Peptone Agar (PA; HiMedia, USA), and Plate Count Agar (PCA). The liquid media (Broth), such as Nutrient Broth (NB; BBL™ Nutrient Broth, USA) was used for the bacteriological analysis.

Collection of specimens and culture of the bacteriological sample

The uterine discharge was collected at the time of estrus directly from the uterus of cows by a clean and disinfected intrauterine catheter (a 10 ml syringe and an AI gun) to perform bacteriological examination following the method described by (Singh et al., 1996). Aerobic (nutrient broth) transport media was used for the survival of bacteria during transportation. The strict aseptic precaution was maintained during the collection of uterine fluid. Initially, the NB was used for the collection and transportation of samples.

Examination of bacterial cultures

The cultural examination of the uterus fluid for bacteriological analysis was completed using standard bacteriological methods described by Hasan (2021) to find out the different species of bacteria.

The NB-containing samples were cultured again the NB overnight to enrich of bacteria. Then samples were divided and inoculated individually in Nutrient agar (NA), Blood agar (BA), Mannitol Salt Agar (MSA), and MacConkey Agar (MA) to promote bacterial growth. The pure culture with homogenous colonies was obtained in this study, as described by Cheesbrough (1985). The isolation and identification of bacteria were made from the examined bacterial cultures. Characterization into respective genera and species was performed on account of colony morphologic characters and reactions in the biochemical tests, including sugar fermentation test for acid and/or gas formation, catalase test and coagulase test, described by Hasan (2021).

Sugar fermentation test

The sugar (carbohydrate) fermentation test in purple broth was performed by inoculating a loop-full of overnight NB culture of the organisms into 5 tubes containing 5 basic sugars (dextrose, sucrose, lactose, maltose, mannitol) separately. Then the mixtures containing tubes were incubated aerobically at 37˚C for 24 hours. Acid production by *E. coli* was indicated by the color change from reddish to yellow in the medium, and the gas production was noted by the appearance of gas bubbles in the inverted Durham’s tube.

Catalase test

The catalase test was performed to differentiate the bacteria that produce the enzyme catalase (*Staphylococci spp.*) from the non-catalase-producing bacteria (*Streptococci spp*.). The slide catalase test was done by pouring 2-3 drops of 3% H_2O_2 solution on an over-bacterial culture. A positive reaction was indicated by a rapid effervescence.

Coagulase test

A simple slide coagulase test was performed as a presumptive test. In this case, 1-2 drop of diluted rabbit plasma was mixed with an equal volume of a particular organism’s emulsified colony (in a drop of water) on a microscopic slide. A positive result was indicated by macroscopical clumping of the bacterial cells within 5 seconds due to coagulase production that converts fibrinogen to fibrin-like fibrin thread. Pathogenic *Staphylococci aureus* showed a positive reaction but non-pathogenic *Staphylococci epidermidis* showed a negative reaction.

Determination of total viable count (TVC)

Determination of TVC of bacteria was performed in this study from the collected fresh uterine fluid samples using PCA as described by ISO (1995) and Hasan (2021). The result of TVC was expressed as the number of CFU per ml of samples.

Statistical analysis

Both descriptive and statistical analyses were performed. Chi-square Test was done to determine a significant variation in the prevalence of bacterial isolates among the experimental groups. All the statistical analysis in the experiment was done by the use of computerized SPSS software version 20.

Results

Animal demographic findings

The result of the general investigation of the cows is presented in Table 1. Out of 172 crossbred cows, 33 repeat breeder cows and 10 randomly selected normal fertile cows were included in this study. Among 43 cross-bred animals (33 RBC and 10 HFC) about 46.5% were Holstein-Friesian crossbred, 23.3% were Jersey crossbred and 30.2% were Sahiwal crossbred cows. The maximum proportion of cows aged between 55 to 72 months (Table 1). About 32% of the animals had at least 3 parties; however, only 3 had as many as 7 parties. The breeding history of these cows is disclosed in Table 2.

Prevalence of different bacterial species in RBC uterine fluid

A total of 3 specific aerobic bacteria were isolated from 33 RBC and 10 HFC, which belong to 3 different genera such as *Staphylococcus* spp., *Escherichia coli*, and *Bacillus* spp. Among the isolated bacteria *E. coli* (Figure 1, Figure 2, Figure 3) was predominant in 30.3% of RBC, followed by *S. aureus* (Figure 4 and Figure 5) in 27.3%, *Bacillus* spp. (Figure 6 and Figure 7) in 18.2% and *S. epidermidis* (Figure 8 and Figure 9) in 15.2 % RBC. Figure 10 and Figure 11 present the identifying characteristic of *Staphylococcus* spp.

Table 1. Demographic data obtained in this study

Crossbred cows	Total population	Study group		Age group	Frequency (%)	Parity group	Frequency (%)
		RBC	HFC				
Holstein-Friesian	75	15	5	30-42 months	10	1	11
Jersey	48	8	2	43-54 months	8	2	9
				55-72 months	15	3	14
Sahiwal	49	10	3	73-90 months	5	4	6
				9-120 months	5	≥5	3

RBC= Repeat breeding cows; HFC= Healthy fertile cows

Table 2. Number of times the animals returned to estrus without completing the pregnancy

Parameter	Experimental animals							Total
	HFC	RBC						
Number of times repeated	0	3	4	5	6	7	8≥	43
sNumber of animals	10	7	10	6	5	3	2	

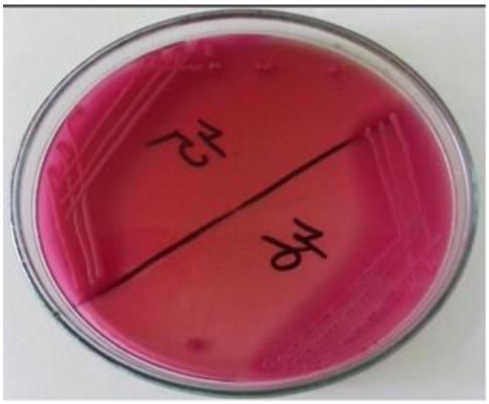

Fig. 1. Colonies of *Escherichia coli* in MacConkey agar (Aerobic culture; 48 hours)

The bacteriological study showed the presence of isolated bacteria in 39.4% of RBC. No isolates were present in 60.6% RBC and 80.0% HFC. Moreover, 12.1%, 9.1%, 12.1%, and 6.1% of RBC included a single species of bacteria and mixtures of two, three, and four species in uterine discharge, respectively. In comparison, 10% of HFC contained two isolates in uterine discharge.

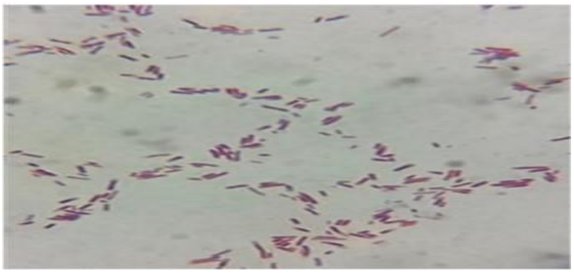

Fig. 2. Gram-negative bacilli of *Escherichia coli* (x1000; Gram's stain)

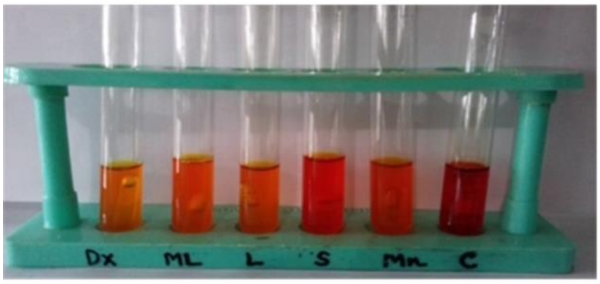

Fig. 3. Sugar fermentation test of *Escherichia coli*, producing acid and gas by fermenting 5 basic sugars (Positive, tube no. 1-5; Negative control, tube no. 6, from Left to the right)

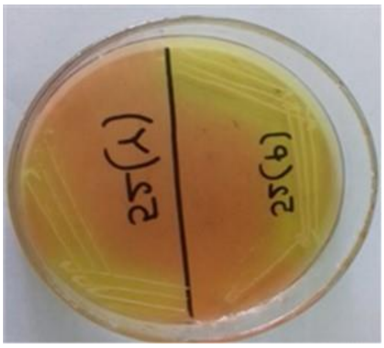

Fig. 4. Isolated colony agar plate-golden-yellow colonies of *Staphylococcus aureus* in Mannitol

Salt agar.

Fig. 5. Coagulase test showing positive reaction as an indication of *Staphylococcus aureus*

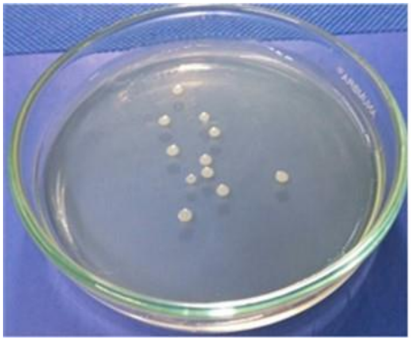

Fig. 6. Colonies of *Bacillus* spp., large, rough, flat, irregular with whip-like outgrowths on Nutrient agar (Aerobic cultures; 48 hours)

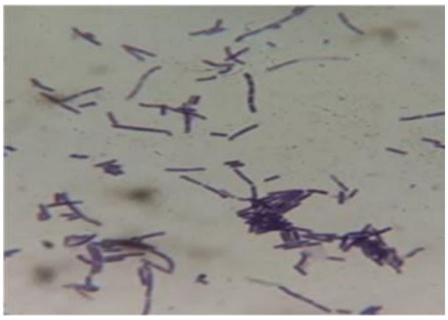

Fig. 7. *Bacillus* spp., gram-positive rods, sometimes in chains (×1000; Gram's stain).

Fig. 8. Round, smooth, shiny, opaque, pink colonies of *Staphylococcus epidermidis* in

Manitol salt agar.

Fig. 9. Coagulase test showing negative reaction as an indication of *Staphylococcus epidermidis*

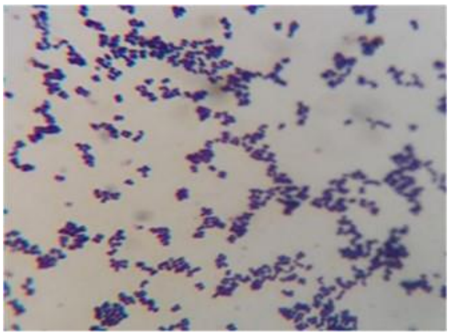

Fig. 10. *Staphylococcus* spp., Gram-positive, spherical shape, cellular arrangements in grape-like clusters (×1000; gram's stain)

Fig. 11. Catalase test showing gas bubbles as an indication of positive reaction for *Staphylococcus spp.*

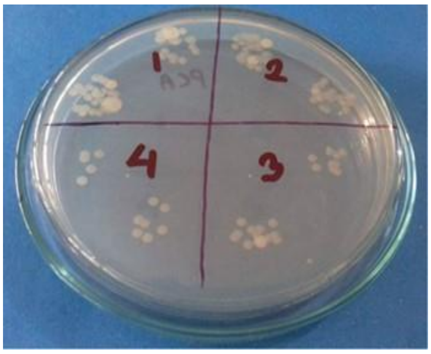

Fig. 12. Total Viable Count (TVC) on PCA.

Previous disease history of the selected cows

Table 3 shows different diseases recorded in selected cows. Most of the RBC was affected with more than one disease simultaneously, and multiple number of the bacterial isolate was found. Data were shown in Table 3, Table 4 and Table 5.

Table 3. Previous disease history in the selected cows

Name of the diseases	RBC (%) n=33	HFC (%) n=10
Sub-clinical mastitis	42.4*	20
Acute mastitis	39.4*	10
Endometritis	39.4	30
Dystocia	12.1	50
Retention of placenta	9.1	10
Abortion	6.1	10

*5% level of significance

Total viable count (TVC) of uterine samples

Figure 12 presents the TVC of samples. Results revealed that the average TVC was higher in RBC ($1.81x10^{10}$ CFU/mL) than in the HFC ($1.3x10^{10}$ CFU/mL). Among affected RBCs, the highest TVC was $2.05x10^{10}$ CFU/mL and the lowest TVC was $1.60x10^{10}$ CFU/mL (Table 4).

Table 4. Isolated bacteria and Total viable count (TVC) in the study population

Bacterial isolates		Cows with isolated bacteria			
Group	Isolates	RBC (n=33)		HFC (n=10)	
		Number	Percentage	Number	Percentage
Gram +ve cocci	*Staphylococcus aureus*	9	27.3	2	20
	Staphylococcus epidermidis	5	15.2	0	0.0
Gram +ve rods	*Bacillus* spp.	6	18.2	0	0.0
Gram –ve rods	*Escherichia coli*	10	30.3	1	10
TVC (CFU/mL)		1.81×10^{10} ($1.60x10^{10}$ - $2.05x10^{10}$)		1.3×10^{10} (1.2×10^{10} - 1.4×10^{10}	

Table 5. Presence of bacteria isolates in repeat breeder cows having diseases history

Previous diseases	RBC with no isolates (%); n=20	RBC with isolates; n=13				
		Single (%)	Two (%)	Three (%)	Four (%)	Total (%)
Endometritis	10	23.1	23.1	30.8	7.7	84.6
Acute mastitis	40	15.4	15.4	7.7	-	38.5
Sub-clinical mastitis	50	-	15.4	15.4	-	30.8
Dystocia	15	-	7.7	-	-	7.7
Retention of placenta	5	7.7	7.7	7.7	-	23.1
Abortion	0	-	-	-	15.4	15.4

Discussion

In most cases, the microbial study of the dam's uterus is ignored to identify the cause of RBCs. In the present study, 39.4%of repeat breeding cows were positive for bacterial infection. This finding coincides with several previous findings of bacterial isolation from the uterine fluid of infertile cows. Some previous studies opined that bacteria were found in the uterine fluid of 9-14% to 75-100% (Singh et al., 2000; Bhat et al., 2013; Bhat et al., 2014; Aghamiri et al., 2020) repeat breeder cows. However, different studies reported a higher percentage (73.91%) of bacterial infections in RBCs and in repeat breeding buffaloes (Khair et al., 2018; Kumar et al., 2004).

Results reveal that the major bacteria isolated from RBC and HFC were *E. coli, Staphylococcus* spp. and *Bacillus* spp., which resembles the report of Gani et al. (2008) and Patel et al. (2019). However, several previous studies also reported recovery of *Staphylococcus* spp., *Proteus* spp., *Streptococcus* spp., *Diplococcus* spp., *Peptococcus* spp., *Escherichia* spp., *Klebsiella* spp., *Pseudomonas* spp., *Bacteroides* spp., *Fusobacterium* spp., *Bacillus* spp., and *Corynebacterium* sp. from the cases of the cows of RBS (Singh *et al.*, 1998; Oliveria et al., 2011; Cakici and Akoz, 2019). These organisms were discriminated against as potential pathogens which render the female genital tract more harmful to the viability of the fertilized ovum to the uterine floor (Rosales and Ametaj, 2021). The qualitative study of the organisms from both groups of cows provides a means for comparison between the two sets of samples. Though most of the organisms isolated are categorized as non-specific agents of reproductive disorders, they can play a vital role as secondary invaders of the genital tract, changing the uterine and vaginal pH, interfering with the activity of spermatozoa and thereby resulting in infectious infertility (Dahiya et al., 2018).

The healthy uterine defense mechanisms (UDM) are important in inhibiting the immigration of invading bacteria (Rosales and Ametaj, 2021), which results from the damage of gamete and embryos leading to infertility (Sheldon et al., 2009). The presence of opportunistic bacteria in ($1.81x10^{10}$ CFU/ml) samples may reduce the resistance of endometrium and favor the access and immigration of pathogenic secondary bacteria, which in turn can make conditions unfavorable for successful fertility in cows.

The metabolic product of bacteria and endometritis exudates modify the uterus environment and hamper gestation (Osawa, 2021).

Moreover, we cannot ignore the relationship of age and body condition score to reproduction, production, and bacterial infections in the uterus.

It was found that most of the RBCs had a history of mastitis (both clinical and sub-clinical). Scientific studies on the negative effect of mastitis on fertility or reproduction are limited. The prevalence of subclinical mastitis and acute mastitis was significantly ($P<0.05$) higher in RBC compared to HFC, which resembles the findings of Chowdhury (2017) and Sikder (2018). Dairy cows that are milked tend to have weakened immune systems, making them more susceptible to illness, particularly infections that cause mastitis (Sordillo and Aitken, 2009). There is a theory that endotoxins, which cause the secretion of prostaglandins, mediate the adverse effect of mastitis on reproductive rates (Kumar et al., 2017). Besides these, the prevalence of endometritis was significantly ($P<0.05$) higher in RBC compared to HFC. Chowdhury (2017) reported a higher frequency of endometritis in RBC, parallel to the present findings. Endometritis causes early embryonic mortality (EEM) because of an inadequate uterine environment (Sheldon et al., 2009; Walsh et al., 2011). All the factors could affect the dairy cows' recurring estrus, which causes RBC. Hossain et al. (2016) found that 8-27% of cow reproductive failure occurred due to endometritis in Bangladesh. The endocrine, metabolic, and physiological condition of lactating cows during pregnancy is noticeably altered by prenatal stress and negative energy balance (Walsh et al., 2011). The interaction of the above mentioned stresses and oxidative stress may compromise to the dairy cow's immun and inflammatory response (Sordillo and Aitken, 2009). Due to their impaired immune systems, high-yielding dairy cows are more susceptible to metabolic diseases, which act as a risk factor for utero-vaginal prolapse, dystocia, and retained placenta (Roche et al., 2009)

Conclusion

A bacteriological study of uterine samples of cows needs to be performed to identify the causes of repeat breeding cows. The higher pathogenic and opportunistic bacterial load may cause repeated conception failure in RBC. Infection of cows with endometritis may act as a predisposing factor for repeat breeders. A bacteriological study of uterine samples and previous disease history of cows could help identify the cause of RBS and proper treatment regimen, which in turn could help set proper strategies for preventing RBS in dairy cows.

Acknowledgments

The authors thank the farmers for responding to the survey and sample collections. This research work was funded by Krishi Gobeshona Foundation (KGF) through the grants project (Project ID: TF 24–EM/15).

Conflict of interests

There is no conflict in interest to publishing the article.

Authors' contribution

MFHC and NSJ were designed for the study. MFHC was involved in sample collection and experimentation. MFHC, MMIH, MH, MR, and NSJ were involved in interpretating data and preparing the manuscript. MSR, MR, and NSJ were involved in the critical review of the manuscript.

References

Aghamiri SM, Ahmadi MR, Haghkhah M and Derakhshandeh A. Identification of pathogenic microorganisms of repeat breeder dairy cows and a hyper immune treatment approach. *Asian Pac. J. Reprod.* 2020; 9(1): 44-48.

Ahuja AK, Cheema RS, Narang D and Dhindsa SS. Bacterial pathogens and antibiotic susceptibility patterns of cervico-vaginal discharges in cross bred repeat breeding Heifer Cows. *Int. J. Curr. Microbiol. Appl. Sci.* 2017; 6(6): 1769-1775.

Bardos J, Fiorentino D, Longman RE and Paidas M. Immunological role of the maternal uterine microbiome in pregnancy: Pregnancies pathologies and alternated microbiota. *Front. Immunol.* 2020; 10: 2823.

Bhat FA, Bhattacharya HK, Hussain A, Nadeem M and Wani AR. Microbial profile, antibiogram and conception rate following treatment in repeat breeder cows. *Intas Polivet.* 2013; 14(1): 42-49.

Bhat FA, Bhattacharyya HK and Hussain SA. White side test: A simple and rapid test forevaluation of nonspecific bacterial genitalinfections of repeat breeding cattle. *Vet. Res. Forum.* 2014;5(3):177-180.

Çakici Y and Aköz M. Histopathological and microbiological evaluation of uterus in repeat breeder cows shipped to slaughterhouse. *Eurasian J. Vet. Sci.* 2019; 35(2): 71-78.

Cheesbrough M. Culturing of anaerobes. In: Medical Laboratory manual for tropical countries, Butterworth Co. Kent, UK, 1985; 248-264.

Chowdhury MFH. Microbiological study of uterine fluid in repeat breeder cows. MS Thesis, Department of Surgery and Obstetrics, Faculty of Veterinary Science, Bangladesh Agricultural University, Mymensingh, 2017.

Cojkic A, Niazi A, Guo Y, Hallap T, Padrik P and Morrell JM. Identification of bull semen microbiome by 16S sequencing and possible relationships with fertility. *Microorganisms* 2021; 9(12): 2431.

Dahiya S, Kumari S, Rani P, Onteru SK and Singh D. Postpartum uterine infection & ovarian dysfunction. *Indian J. Med. Res.* 2018; 148(Suppl): 64-70.

Gani MO, Amin MM, Alam MGS, Kayesh MEH, Karim MR, Samad MA and Islam MR. Bacterial flora associated with repeat breeding anduterine infections in dairy cows. *Bangladesh J. Vet. Med.* 2008; 6(1): 79-86.

Hasan MMI. Repeat breeding syndrome in dairy cows of Bangladesh. PhD Thesis, Department of Surgery and Obstetrics, Faculty of Veterinary Science, Bangladesh Agricultural University, Mymensingh, 2021.

Hossain MK, Uddin AHMM, Yasmin N, Hossain MM, Lucky NS, Haque MM, Aktaruzzaman M and Alam S. Risk factors of postpartum uterine infection and its subsequent effect on fertility of crossbred dairy-cows in Bangladesh. *Int. J. Nat. Sci.* 2016; 5(2): 107-111.

International Organization for Standardization (ISO). Recommendation of the meeting of thesubcommittee, on meat and meat products. ISO/TC-36/Sc-6. The Netherlands. 1995; p.10-18.

Katagiri S and Takahashi Y. Changes in EGF concentrations during estrous cyclein bovine endometrium and their alterations in repeat 2004; 62(12): 103-112.

Khair A, Alam MM, Rahman AKMA, Islam MT, Azim A and Chowdhury EH. Incidence of reproductive and production diseases of cross-bred dairy cattle in Bangladesh. *Bangl. J. Vet. Med.* 2013; 11(1): 31-36.

Khair A, Asaduzzaman M, Sultana Z, Talukder AK, Das ZC, Alam M and Shamsuddin M. Economic benefit in repeat breeder cows usingintrauterine infusion of penicillinandestrus synchronzation followed by timed artificial insemination. *J. Adv. Vet. Anim. Res.* 2018; 5(4): 454-458.

Kumar N, Manimaran A, Kumaresan A, Jeyakumar S, Sreela L, Mooventhan P and Sivaram M. Mastitis effects on reproductive performance in dairy cattle: a review. *Trop. Anim. Health Prod.* 2017; 49: 663-673.

Kumar P, Srivastava SK, Rawat M, Yadav MC and Kumar H. Effect of certain immunomodulators on uterine infections and fertility in postpartum Buffaloes. *Asian-Australas. J. Anim. Sci.* 2004; 17(7): 930-935.

Oliveira CS, Oliveira Z, Gonalves WM, Magalhães H, brandao FZ and Nogueira L. Endometritis diagnosis in repeat breeder cows from embryotransfer programs. *Ars Vet.* 2011; 27(2): 116-119.

Osawa T. Predisposing factors, diagnostic and therapeutic aspects of persistent endometritis inpostpartum cows. *J. Reprod. Dev*. 2021;67(5): 91-299.

Parkinson, TJ. The repeat breeder syndrome. In: Veterinary reproduction and obstetrics. 9th ed. Saunders Elsevier, Edinburgh. 2009; p.463-466.

Patel CI, Panchal MT, Dhami AJ, Bhanderi BB and Mathakiya RA. Isolation of bacteria from the vaginal aspirates of cyclic, acyclic, endometriotic and pregnant crossbred cows. *Int. J. Curr. Microbiol. Appl. Sci.* 2019; 8(3): 536-542.

Regmi G and Dhakal IP. Systemic levels of iron, phosphorus, and total protein innormocyclic versus repeat breeder Holstein Friesian crossbred cows of Kesharbag, Chitwan, Nepal. *Vet. World.* 2020; 13(11): 2353-2357.

Roche JR, Friggens NC, Kay JK, Fisher MW, Stafford KJ, Berry DP. Body condition score and its association with dairy cow productivity, health, and welfare. *J. Dairy Sci.* 2009; 92: 5769–5801.

Rosales EB and Ametaj BN. Reproductive tract infections in dairy cows: Can probiotics curb down the incidence rate? *Dairy*. 2021; 2(1): 40-64.

Sheldon IM, Cronin J, Goetze L, Donorfio G and Schuberth HJ. Defining postpartum uterine disease and the mechanisms of infection and immunity in the female reproductive tract in cattle. *Biol. Reprod.* 2009; 81(6): 1025-1032.

Sikder MS. Correlative study of mastitis and repeat breeding syndrome in dairy cows. MS Thesis, Department of Surgery and Obstetrics, Faculty of Veterinary Science, Bangladesh Agricultural University, Mymensingh, 2018.

Singh J, Sidhu SS, Dhaliwal GS, Pangaonkar GR, Nanda AS and Grewal AS. Effectiveness of lipopolysaccharide as an intrauterine immunomodulator in curing bacterial endometritis in repeat breeding cross-bred cows. *Anim. Reprod. Sci.* 2000; 59(3-4): 159-166.

Singh M, Sharma M and Pant HC. Microbiological study on cervical mucus of repeat breeder cows in Himachal Pradesh. *Indian Vet. J.* 1998; 75(8): 710-712.

Singh NP, Chaturvedi VK and Singh DP. Bacteriological studies on repeat breeder bovines. *Indian Vet. J.* 1996; 73: 462-463.

Sordillo LM and Aitken SL. Impact of oxidative stress on the health and immune function of dairy cattle. *Vet. Immunol. Immunopathol.* 2009;128:104-109.

Talukder MAS, Khandoker MAMY, Rahman MGM, Islam MR and Khan MAA. Reproductive problems of cows at Bangladesh Agricultural University dairy farm and possible remedies. *Pak. J. Biol. Sci.* 2005; 8(11): 1561-1567.

Walsh SW, Williams EJ and Evans ACO. A review of the causes of poor fertility in high milk producingdairy cows. *Anim. Reprod. Sci.* 2011; 123(3-4): 127-138.

Yoo HS. Infectious causes of reproductive disorders in cattle. *J. Reprod. Dev*. 2010; 56(Supple): S53-60.

Yusuf M, Nakao T, Ranasinghe RB, Gautam G, Long ST, Yoshida C, Koike K and Hayashi A. Reproductive performance of repeat breeders in dairy herds. *Theriogenology* 2010; 73(9): 1220-1229.

J. Bangladesh Acad. Sci. 47(1); 43-52: June 2023 DOI: https://doi.org/10.3329/jbas.v47i1.66683

Journal of Bangladesh Academy of Sciences

Journal homepage: http://www.bas.org.bd/publications/jbas.html

Research Article

Commercial Nile tilapia *Oreochromis niloticus* production in net cages at the River Dakatia, Chandpur, Bangladesh

Md. Robiul Awal Hossain[1], Md. Eilious Hosain, Anika Tabassum and Md. Niamul Naser[*]

Department of Zoology, Faculty of Biological Sciences, University of Dhaka, Dhaka, Bangladesh

ARTICLE INFO

Article History

Received: 20 November 2022
Revised: 21 May 2023
Accepted: 11 June 2023

Keywords: GIFT, Growth, river ecosystem, Net-cage farming, Mono-sex tilapia, *Oreochromis niloticus*, River Dakatia, Bangladesh

ABSTRACT

This study examined the intensification of mono-sex Nile tilapia *Oreochromis niloticus* aquaculture in riverine net cages installed at the River Dakatia, Roghunathpur, Chandpur. This study performed 120-day cage grow-out trials with densities of 50, 75, and 100 tilapia m^{-3} under three replications with an average initial weight of 28.92±8.37 g per juvenile fish. The monthly water quality parameters (temperature, pH, dissolved oxygen, total alkalinity and hardness, ammonia-N and Nitrite-N) in the cage installation water area of the River Dakatia were found to be suitable for tilapia cage culture. The monthly average weight gain was significantly ($p < 0.05$) higher in 50 tilapia m^{-3} stocking density than in the other two stocking densities tested. The mean final weight and specific growth rate were significantly ($p < 0.05$) higher in 50 tilapia m^{-3} stocking density than the other two stocking densities. Significantly ($p < 0.05$) higher survival (97.92%) was found in the 50 tilapia m^{-3} stocking density group and followed by 86.74% and 84.39% in the 75 and 100 tilapia m^{-3} stocking densities, respectively. Consequently, the monthly relative and specific growth rate and feed conversion ratio were significantly ($p < 0.05$) higher in 50 tilapia m^{-3} stocking density fishes for the first, third, and fourth months. Gross production was comparable between 50 and 75 tilapia m^{-3} stocking densities but was significantly ($p < 0.05$) better than 100 m^{-3} stocking density. Net production was significantly ($p < 0.05$) higher at 50 tilapia m^{-3} stocking density group than those of 75 and 100 tilapia m^{-3} stocking densities. The best feed conversion ratio (1.60) was in the 50 tilapia m^{-3} stocking density group ($p < 0.05$) than those of 1.87 and 2.44 for the stocking of 75 and 100 tilapia m^{-3}, respectively. Benefit-cost ratio and net profit were significantly ($p < 0.05$) better at 50 and 75 tilapia m^{-3} than at 100 tilapia m^{-3} stocking density. Therefore, considering maximum outputs, benefits, and performances, we recommend stocking density at 50 mono-sex tilapia m^{-3} for the best growth, cost-effective production, and highest-economic return from 120 days of grow-out net cages in the riverine culture system.

Introduction

In 2020-2021, Bangladesh was placed third and fifth in inland fish and aquaculture production country (FAO, 2018). In 2020-21, in total 4.621 million tones of fish produced, of which aquaculture contributed 57.10% of the total fish production (DoF, 2022). This magnificent fish-producing progress has substantially increased national annual fish production from 18.07 kg per person in 2009-10 to 22.85 kg per person in 2020-21 within a decade (DoF, 2011 and 2022). The success of daily national fish consumption of 62.58

---

[*] Corresponding author: <mnnaser@du.ac.bd>

[1] *Part of PhD research at DU. Bangladesh Fisheries Research Institute, Riverine Station, Chandpur, Bangladesh*

g/day/person against the set target of 60 g/day/person as animal protein is a challenge to maintain the protein sources in diets for the growing population in the future. Furthermore, the aquaculture sector plays a vast role in income generation and nutritional security through the support of fish entrepreneurs such as fish hatcheries, nursery owners, fish seed/fry and fingerlings suppliers, fish feed and other materials sellers, smallholders and improvised fish grow-out farmers, fish wholesalers and retailers in improving household income, employment opportunities, livelihoods and resilience to climate change adaptation.

Genetically Improved Farmed Tilapia (GIFT) is a selection-based improved strain of Nile tilapia, *Oreochromis niloticus,* one of the most imperative fish farming candidates worldwide. In Bangladesh, it was revealed that the GIFT strain had the better growth rate, yield, feed conversion ratio (FCR), and benefit-cost ratio (BCR) in monoculture (growth rate: 3.3% day^{-1}; yield: 8.1 hac/cycle; FCR: 1.5; BCR: 1.7) and polyculture (growth rate: 3.1% day^{-1}; yield: 12.7 hac/cycle; FCR: 2; BCR: 2) systems than the non-GIFT tilapia cultured in monoculture (growth rate: 2.6% day^{-1}; yield: 6.2 hac/cycle; FCR: 1.8; BCR: 1.1) and polyculture (growth rate: 2.4% day^{-1}; yield: 10.2 hac/cycle; FCR: 3.1; BCR: 1.5) systems (Tran et al., 2021). Bangladesh has achieved 3rd and 4th positions among Asian and global tilapia production, respectively (DoF, 2020). It is a suitable aquaculture species in earthen pond settings for monoculture and polyculture, integrated culture in rice fields, and cages culture systems across the country (Kunda et al., 2021). One of the potential production strategies of this species involves with cage culture system that has been practiced in many countries like Bangladesh, Thailand, Vietnam, Philippines, Laos, Pakistan, India, Nepal, Cambodia, Malaysia, Indonesia, Fiji, Papua New Guinea, Ghana, Ivory Coast, Nigeria, Uganda, Zambia, Zimbabwe, Ethiopia and Brazil (Bhujel, 2019; Fialho et al., 2021; Gibtan et al., 2008).

Cage tilapia farming in ponds, reservoirs, lakes, and riverine ecosystems should be received much attention in Bangladesh because it provides good production and is considered a profitable aquaculture business from vast wetlands of the country. It is likely to ensure sustainable utilization of huge open water resources across the country (Barman et al., 2003; Naser and Khatun, 2006, 2007; Ali et al., 2011, 2019; Hossain et al., 2014; Kunda et al., 2021; Moniruzzaman et al., 2015; Shamsuddin et al., 2022). Also, this technology can be implemented in a brackish water environment (Ninh et al., 2014). In the 1980s, this technology was first initiated in cages at the Kaptai Lake, Rangamati; and later on, it was demonstrated in ponds, lakes, and riverine systems in Bangladesh (Ahmed et al., 2014; Hossain et al., 2017). The management strategies include stocking density, animal stock size, pelleted feed crude protein level, daily feeding levels, etc., influencing its viability, profitability, and sustainability. Thus, the optimal level of resource use could lead to the success and prerequisites for the community-level implementation of this technology.

An ideal stocking density is paramount in tilapia cage culture that provides higher growth andsurvival, subsequently increasing tilapia productivity and ensuring maximum economic benefits. Some studies have been tested to identify the best stocking density for Nile tilapia *O. niloticus* culturing in cages in riverine systems. In addition, Naser and Khatun (2007) recommended 200 medium-sized tilapia fingerlings per cubic meter for pond cage culture. Ali et al. (2019) found an optimal stocking density of 150 small fingerlings m^{-3} cage in the Padma River system, while Kunda et al. (2021) observed that the stocking of 40 and 60 tilapia m^{-3} of larger sized tilapia stocked higher growth, productivity, and economic return compared to the density of 80 individuals m^{-3}. These authors did not take the higher density of 100 fish m^{-3} that should be examined for open-water fish cage culture. Moniruzzaman et al. (2015) identified that a density of 50 fish m^{-3} was optimal for tilapia growth rate, feed conversion ratio, and net returns than the medium to high densities of 75, 100, and 125 fish m^{-3} in cages. But they produced relatively smaller marketable sizes of tilapia because they had stocked small sizes of fish, on average 15.20 g in cages. Similarly, Gibtan et al. (2008) showed that a stocking density of 50 individuals m^{-3} in cages had given higher growth and better feed conversion ratio than the higher density of 100, 150, and 200 tilapia m^{-3} in cages. Despite stocking of bigger size of tilapia at 45.76 g, these authors failed to achieve a suitable marketable size of tilapia after 150 days of culture; this was likely due to the minimum level of feed application at 2% of body weight as well as a powder form of feed. This study compared three densities such as low (50tilapia m^{-3}), medium (75 tilapia m^{-3}), and higher density (100 tilapia m^{-3}) of fishes in riverine cages. It assessed the density effects on the growth rate and production survival of *O. niloticus* at the River Dakatia, Chandpur. This study also addressed the benefit-cost ratio and water quality parameters to properly understand the tilapia-cage culture economics and the suitability of riverine tilapia cage culture systems in Bangladesh. This study's insights will help the farmers and policymakers extend cage tilapia culture in the riverine system.

Materials and Methods

Source of experimental fish and acclimation

Approximately 14,000 mono-sex Nile Tilapia *O. niloticus* fingerlings were acquired from the nursery ponds of Bangladesh Fisheries Research Institute (BFRI), Riverine Station, Chandpur. These tilapia fingerlings were healthy and naturally active. Before this experiment, fingerlings were acclimatized in the floating cages for a week. The fingerlings were fed tilapia pellet feed twice daily (09:00 and 16:00 h) to apparent satiation during acclimatization, containing 30% crude protein and 5% fat. Then these tilapia fingerlings were distributed among the experimental cages according to the experimental design.

Cage setting, experimental protocol, and feeding schedule

The experimental cages were installed in the River Dakatia, Roghunathpur, and Chandpur. Floating net cages were installed as the outer and inner layer, being an area of 3 m × 3 m × 2 m made of the plastic net (mesh size 2.5 cm) and knot-less polyethylene net (mesh size 1.1 cm), which were installed as outer and inner layer, respectively. The frames of net cages were made with GI pipe. The 250-liters capacity of empty iron drams was attached for floating the cages. The experimental duration was 120 days. The experiment consisted of three treatments with three replicas for each density. The treatments were low stocking density (50 fishes m^{-3}, i.e., in total 900 tilapia fingerlings per net cage), medium stocking density (75 fishes m^{-3}, i.e., in total 1,350 tilapia fingerlings per net cage), and high stocking density (100 fishes m^{-3}, i.e., in total 1,800 tilapia fingerlings per net-cage). The experimental tilapia fingerlings had an average initial weight of 28.92±8.37 g. The fish were fed twice daily with tilapia commercial floating pellets (30% crude protein, 5% fat). The daily feeding was done with a half ration of the feed in the morning (09:30 to10:00 h) and the rest of the half in the afternoon (16:00 to 16:30 h). The feeding rate was at 5% of the total body weight for the first and second months, then at 4% for the third month, and finally, in the fourth month, at 3% of the total body weight of the cage fish. On each sampling day, fish were visually checked for their overall physical condition to observe any dead or diseased fish in each cage. The sampling was performed each month to adjust the feeding ratio and determine the growth performance, which will be discussed in the next section below. Each cage net was cleaned once a month.

Tilapia harvesting, estimation of growth performance

A monthly sample of 50 tilapia was randomly collected from each cage, and their live body weights were measured. After the 4-month grow-out phase, the final harvest was performed, while all tilapia were counted to estimate the tilapia survival. One hundred fifty tilapias (50 tilapia from each experimental cage) were randomly selected, and the live body weight was measured to determine the growth performance. Tilapia survival, final weight, weight gain, relative growth rate, specific growth rate, production, and feed conversion ratio were calculated using the following formulas.

Survival rate (%) = (Final live tilapia count / Initial live tilapia count) × 100.

Gross production = Mean final tilapia weight (kg) × final live tilapia harvested.

Net production = Mean final tilapia weight (kg) – initial tilapia weight (kg) × final live tilapia harvested.

Weight gain (g) = mean final weight tilapia – mean initial weight.

Relative growth rate (RGR) (%) = $(W_2-W_1) / W_1 \times 100$. Where, W_1 = Live body weight of tilapia (g) at time T_1 (day).W_2 = Live body weight of tilapia (g) at time T_2 (day)

Specific growth rate (SGR) (% day^{-1}) = $[(\ln W_1 - \ln W_0)]/ t \times 100$, where, W_1 = final weight of tilapia, W_0 = initial weight of tilapia, and t = culture days

Feed conversion ratio (FCR) = total feed weight offered / (final fish biomass - initial fish biomass).

Economic analysis

An economic analysis was performed to estimate the mono-sex Nile tilapia *O. niloticus* grow-out production economics of the riverine cage culture system. The profitability of tilapia grow-out production in cages was calculated using the following formula:

$R = PbiBi - (PxjXj + TFC)$

where,

R = net return, *Pbi* = unit price of *i*th products (BDT kg^{-1}), *Bi* = quantity of *i*th products sold (Kg BDT^{-1}), *Pxj* = unit price of *j*th inputs, *Xj* = quantity of *j*th inputs, *i* = 1, 2, 3, … n, *TFC* = fixed costs (Hosain et al., 2021a,b).

BCR = Total income / total expenditure.

Profit (BDT) = Total income in
BDT = Total expenditure in BDT.

Water quality parameters

Cage water quality parameters such as temperature, pH, water transparency, water depth, current river water velocity, dissolved oxygen, free carbon dioxide, total alkalinity, total hardness, ammonia-N, and nitrite-N were determined every 14 days interval. These were done for all cages between 08:30 to 11:00 hours. The determination procedure of these water quality variables was described by Hossain et al. (2022). In brief, water temperature (°C) was estimated with a centigrade thermometer. Water transparency was measured with the aid of a Secchi disk. A HANNA pH meter (Model HI 8424, Italy) was used to estimate the cage water pH. The dissolved oxygen (DO) values were determined with the Lutron DO meter (Model DO 5509, Singapore). The HACH water quality testing kit (Model FF-2, USA) was used to determine the cage water ammonia-N, nitrite-N, total alkalinity, hardness, and Free carbon dioxide.

Statistical analysis

One-way analysis of variance (ANOVA) was carried out to check the differences among three stocking density treatmentsusing a software package R version 3.0.0 for Windows.Pearson correlation coefficients were used for the inter-relationship of water quality parameters using SPSS (version 25.0 for Windows). The mean values of tilapia growth performance parameters, production, and culture economics, including BCR, were compared between the treatments using the least significant difference (LSD) and coefficient of variation.

Results and Discussion

Water quality parameters

The maximum water temperature was 32.1°C in October, and the minimum was 31.1°C in July (Table 1). Cage adjacent water depth of the River Dakatia varied from 5.0 m in June to 5.5 m in October. The current velocity of cage water ranged from 25 cm sec^{-1}in June to 37 cm sec^{-1} in October (Table 1). The highest value of water transparency was 71 cm in October, and the lowest was 38 cm in June (Table 1).

The current velocity of cage water had a significant positive correlation with water transparency (p<0.05; r = 0.951) (Table 2). Dissolved oxygen ranged from 5.68 mg L^{-1} in July to 7.2 mg L^{-1} in June (Table 1). The free CO_2 values of the River Dakatia cage water varied from 4.2 mg L^{-1} in October to 4.6 mg L^{-1} in August. The cage water pH values fluctuated between 7.0 in July to 8.4 in October. The cage water pH values showed a strong positive correlation with water temperature (p<0.05; r =0.927) and water current velocity (p<0.05; r =0.916) (Table 2). The lowest total hardness of cage water was 46.32 mg L^{-1} in September, and the highest was 54.28 mg L^{-1} in June (Table 1). The total alkalinity of cage water varied from 52.62 mg L^{-1} in September to 68.62 mg L^{-1} in June (Table 1). The total alkalinity of cage water in the River Dakatia had a significant positive correlation with dissolved oxygen (p<0.01; r=0. 967) and total hardness (p<0.05; r=0.944) (Table2). The ammonia-N concentration of cage water varied from 0.002 mg L^{-1} in September to 0.006 mg L^{-1} in June (Table 1). Nitrite-N_2 was not recorded during the study period (Table 1). In this study, the water quality variables of cages in the River Dakatia were within reasonable limits for *O. niloticus* (Ross, 2000). Additionally, the quality parameters, i.e., water temperature, pH, dissolved oxygen, free CO_2, total alkalinity, total hardness, ammonia-N, and NO_2-N, were more or less similar to the following previous studiesin the River Dakatia, Meghna, Gumti, Titas and Hoara, Bangladesh (Hossain et al., 2022; Ahmed et al., 2014).

Table 1. Monthly mean values of water quality parameters of cage water during mono-sex Nile Tilapia *Oreochromis niloticus* cultured in the River Dakatia, Roghunathpur, Chandpur

Parameters	Months						
	June	July	August	September	October	Range	Mean ±SD
Depth of water (m)	5	5.1	5.3	5.4	5.5	5-5.5	5.26±0.21
Current velocity (cm sec^{-1})	25	28	29	31	37	25-37	30±4.47
SD transparency (cm)	38	49	56	63	71	38-71	55.40±12.70
Water temperature (°c)	31.5	31.1	31.3	31.8	32.1	31.1-32.1	31.56±0.39
DO (mg L^{-1})	7.2	5.68	5.82	5.74	6.04	5.68-7.2	6.10±0.63
Free CO_2 (mg L^{-1})	4.58	4.42	4.6	4.52	4.2	4.2-4.6	4.46±0.16
pH	7.25	7	7.5	7.75	8.4	7-8.4	7.58±0.54
Total hardness (mg L^{-1})	54.28	48.12	47.2	46.32	52.68	46.32-54.28	49.72±3.53
Total alkalinity (mg L^{-1})	68.62	53.72	54.37	52.62	60.14	52.62-68.62	57.89±6.67
Ammonia-N (mg L^{-1})	0.006	0.004	0.004	0.002	0.002	0.002-0.006	0.004±0.001
Nitrite-N (mg L^{-1})	0	0	0	0	0	0	0

Table 2. Correlation matrix of water quality parameters in cage water when culturing mono-sex *Oreochromis niloticus* in the River Dakatia, Roghunathpur, Chandpur

	WCV	SDT	WT	DO	CO_2	pH	TH
SDT	0.951*						
WT	0.773	0.697					
DO	-0.456	-0.632	0.081				
CO_2	-0.828	-0.644	-0.582	0.251			
pH	0.916*	0.861	0.927*	-0.153	-0.657		
TH	0.004	-0.280	0.338	0.832	-0.310	0.194	
TA	-0.263	-0.493	0.202	0.967**	0.014	0.008	0.944*

WCV: water current velocity; SDT: secchi disk transparency; WT: water temperature; TDS: total dissolved solids; DO: dissolved oxygen; CO_2: carbon dioxide; pH: negative hydrogen ion concentration; TH: total hardness; TA: total alkalinity. *Correlation is significant at the 0.05 level (2-tailed). **Correlation is significant at the 0.01 level (2-tailed).

Growth, survival, production, and economics

Tilapia final weight (376.72 g) was Significantly ($p<0.05$) higher in the low stocking density (50 fish m^{-3}) group than those of 276.64 g and 201.15g in the medium stocking density (75 fish m^{-3}) and high stocking density (100 fish m^{-3}), respectively (Table 3 and 5). In this study, the market-desirable size of tilapia (376.72 g) has been achieved in low stocking density treatment after 120 days of culture period by the stock of 28.92 g weight of fish. This result is better than those reported by Gibtan et al. (2008) and Moniruzzaman et al. (2015). They obtained 219.71 g and 255.53 g body weight tilapia in 50 ind. m^{-3} stocking density after 150 and 120 days of culture period by stocked of 45.76 g and 15.20 g tilapia, respectively (Gibtan et al., 2008; Moniruzzaman et al., 2015). The final SGR and RGR were substantially ($p<0.05$) betterin the low stocking density (50 fish m^{-3}) treatment then, followed by the medium (75 fish m^{-3}) and high (100 fish m^{-3}) density groups, respectively (Table 3 and 5). Kunda et al. (2021) stated that the higher final weight and SGR of mono-sex Nile tilapia had had in the 40 and 60 fish m^{-3} stocking densities than 80 fish m^{-3} stocking density when the suitable density of tilapia was optimized in the cages culture condition at the River Gurukchi, Gowainghat, Sylhet, Banbladesh.

The monthly and final weight gains were significantly better at the low stocking density (50 fish m^{-3}) treatment than in the medium (75 fish m^{-3}) and high (100 fish m^{-3}) densities ($p<0.05$) (Table 3, 4 & 5). Similarly, better RGR and SGR were found in the low-density group than in the medium and high-density groups in the first month ($p<0.05$). At the same time, the RGR and SGR were comparable ($p>0.05$) between the medium and high stocking density groups (Table 4). In the second month, the RGR and SGR were higher ($p<0.05$) at the medium stocking density group than at the low and high stocking densities (Table 4). In the third month, the RGR and SGR were better ($p<0.05$) in the 50 individuals m^{-3} stocking density treatment than these, followed by the densities of 75 and 100 individuals m^{-3}, respectively (Table 4). For the fourth month, the RGR and SGR were similar ($p>0.05$) between the densities of 50 and 75 individuals in m^{-3} treatments. However, these lower and medium stocking density treatments achieved significantly better tilapia growth than in the high stocking density group ($p<0.05$) (Table 4).

Table 3. Growth performance of mono-sex Nile tilapia *Oreochromis niloticus* cultured under the different stocking densities in the River Dakatia, Roghunathpur, Chandpur during 120 days

Parameters	**Stocking density**			Range	Mean ± SD
	50 Tilapia m^{-3}	**75 Tilapia m^{-3}**	**100 Tilapia m^{-3}**		
Initial weight (g)	28.92	28.92	28.92	28.92 - 28.92	28.92±0
Final weight (g)	376.72	276.64	201.15	201.15 - 376.72	284.84±88.07
Weight gain (g)	347.80	247.72	172.23	172.23 - 347.80	255.92±88.07
Relative growth rate (%)	94.63	80.14	66.62	66.62 - 94.63	80.46±14.00
Specific growth rate (% day^{-1})	2.13	1.87	1.61	1.61- 2.13	1.87±0.26
Food conversion ratio	1.59	1.87	2.43	1.59 - 2.43	1.96±0.43
No. of fish harvested	881	1171	1519	881 - 1519	1190.33±319.44
Survival (%)	97.92	86.73	84.38	84.38 - 97.92	89.68±7.23
Gross production (kg cage^{-1})	331.96	323.92	305.54	305.54 - 331.96	320.47±13.54
Net production (kg cage^{-1})	306.48	290.05	261.60	261.60 - 306.48	286.04±22.71
Net profit (BDT cage^{-1})	17215	9740	2211	2211 - 17215	9722±7502.01
Benefit-cost ratio	1.81	1.37	1.07	1.07 - 1.81	1.42±0.37

Feeding: 5-3% body weight feed daily in each treatment.

Table 4. Monthly growth performance parameters of mono-sex Nile Tilapia *Oreochromis niloticus* cultured under various stocking densities in cages of River Dakatia, Roghunathpur, Chandpur during 120 days

Stocking density (Tilapia m^{-3})	**Monthly growth parameters**															
	Mean weight gain (g)				**Mean relative growth rate (%)**				**Mean specific growth rate (% day^{-1})**				**Mean feed conversion ratio**			
	Months				**Months**				**Months**				**Months**			
	1st	**2nd**	**3rd**	**4th**	**1st**	**2nd**	**3rd**	**4th**	**1st**	**2nd**	**3rd**	**4th**	**1st**	**2nd**	**3rd**	**4th**
50	40.5^{a}	85.1^{a}	125.5^{a}	96.5^{a}	140.2^{a}	122.5^{b}	81.2^{a}	34.5^{a}	2.92^{a}	2.66^{b}	1.98^{a}	0.98^{a}	1.06^{b}	1.22^{a}	1.47^{c}	2.64^{b}
75	24.9^{b}	75.7^{b}	76.83^{b}	70.1^{b}	86.16^{b}	141.0^{a}	9.45^{b}	33.9^{a}	2.06^{b}	2.93^{a}	1.55^{b}	0.97^{a}	1.76^{a}	1.06^{b}	2.02^{b}	2.65^{b}
100	22.4^{b}	63.6^{c}	46.66^{c}	39.5^{c}	77.46^{b}	123.9^{b}	40.6^{c}	24.4^{b}	1.91^{b}	2.68^{b}	1.13^{c}	0.73^{b}	1.93^{a}	1.20^{a}	2.95^{a}	3.67^{a}
LSD	4.45*	4.36**	7.84***	15.1*	15.39**	13.49*	6.81**	6.31*	0.27*	0.19*	0.14*	0.16*	0.30*	0.07*	0.12*	0.52*
CV (%)	7.61	2.92	4.72	11.00	7.60	5.22	5.64	10.20	5.90	3.42	4.46	8.81	9.41	2.81	2.76	8.74

Means bearing the same letter(s) in a column do not differ significantly. $^{***}p<0.001$; $^{**}p<0.01$; $^{*}p<0.05$.

In this study, the best final feed conversion ratio (FCR) at 1.6 was obtained in the low-density (50 fish m^{-3}) treatment, and it was followed by 1.87 and 2.44 in the medium-density (75 fish m^{-3}) and high-density (100 fish m^{-3}) groups, respectively (Table 3 and 5). In the first month, a better FCRwas recorded in the low-density treatment than in medium and high-density treatments (p<0.05), while FCRs were not significantly different between medium and high-density groups (p<0.05) (Table 4). Whereas, for the second month, the FCR was (p<0.05) better in the medium stocking density treatment than in low and high stocking treatments. In the third month, the best FCR was found in the low-density group than it, followed by medium and high-density groups, respectively (Table 4). In the fourth month, the FCR was similar (p>0.05) between low and medium stocking density treatments; these were significantly (p<0.05) better than the high stocking density group (Table 4). This study shows that the low and medium stocking density groups have better FCR than the high-density tilapia cage culture throughout the trial. This finding concurred with Gibtan et al. (2008), who recorded more than two-fold higher FCR when the Nile tilapia density increased from 50 individuals m^{-3} (FCR: 2.48) to 100 individuals m^{3} (FCR: 5.64).

The mean survival rate at 97.92% was significantly (p<0.05) higher in the low (50 fish m^{-3}) stocking density treatment then it followed by 86.73% and 84.38% for the medium density (75 fish m^{-3}) and the higher (100 fish m^{-3}) stocking densities, respectively (Table 3 and 5). In this study, tilapia survival has remained within the feasible range (84.38-97.92%). These results have in agreement with Gibtan et al. (2008) and Kunda et al. (2021), who have obtained the range of *O. niloticus* survival from 94.0% to 98.17% when optimizing suitable stocking density for cage-tilapia grow-out production. Their trials tested various stocking densities of 40, 60, and 80 individuals m^{-3}(Kunda et al., 2021) and 50, 100, 150, and 200 individuals m^{-3} (Gibtan et al., 2008). However, their studies have indicated that the low to higher tilapia densities (40-200 ind. m^{-3}) provide excellent tilapia survival in net cage-tilapia culture in the lake (Gibtan et al., 2008) or in a riverine cage culture system (Kunda et al., 2021).

Mean gross production was similar (p>0.05) between the low and medium stocking density groups, and these were significantly (p<0.05) better than that of the high stocking density group (Tables 3 and 5). Significantly (p<0.05), a higher mean net production (306.48 kg cage^{-1}) was in the low-density group then it followed by 290.05 and 261.60 kg cage^{-1} in the medium and high-density treatments, respectively (Tables 3 and 5). Benefit-cost ratio and net profit were better (p<0.05) in the low stocking treatment than those in the medium and high tilapia densities (Tables 3 and 5). This study obtained higher net production and economic returns in the low-density tilapia stocking group than in the medium-density and high-density riverine cage culture systems. These were due to the better mono-sex Nile tilapia final weight/growth, survival, and FCR in the low stocking density culture. Moreover, aquaculture candidates` growth, survival, and FCR in feeding costs are the key drivers in higher production, economic returns, and sustainability (Garcia et al., 2017; Hosain et al., 2021b). Therefore, this study suggests a stocking density of 50 fish m^{-3} in the cages for better growth, survival, production, and economic return of mono-sex *O. niloticus* intensive production in the riverine systems in Bangladesh.

Table 5. Mean values of growth performance parameters of mono-sex Nile Tilapia *Oreochromis niloticus* awell as cage economics when cultured using various stocking densities in cages in the River Dakatia, Roghunathpur, Chandpur during 120 days

Stocking density (Tilapia m^{-3})	Parameters									
	Mean FW (g)	Mean WG (g)	Mean RGR (%)	Mean SGR (% day^{-1})	Mean FCR	Mean survival (%)	Mean GR (kg)	Mean NP (kg)	Mean BCR	Mean net profit (Tk)
50	376.72^{a}	347.80^{a}	94.63^{a}	2.13^{a}	1.60^{c}	97.92^{a}	331.96^{a}	306.48^{a}	1.81^{a}	17215^{a}
75	276.65^{b}	247.73^{b}	80.17^{b}	1.87^{b}	1.87^{b}	86.74^{b}	323.92^{a}	290.06^{b}	1.37^{b}	9740^{b}
100	201.15^{c}	172.23^{c}	66.63^{c}	1.61^{c}	2.44^{a}	84.39^{c}	305.54^{b}	261.61^{c}	1.07^{c}	2211^{c}
LSD	12.95***	12.95***	2.17***	0.03***	0.14***	1.25***	10.43**	10.72***	0.05***	1282.55***
CV (%)	2.28	2.53	1.35	0.85	3.53	0.70	1.63	1.88	1.81	6.60

FW: final weight; WG: weight gain; SGR: specific growth rate; FCR: feed conversion ratio; GR: gross production; NP: net production; BCR: benefit-cost ratio. The Means bearing the same letter(s) in a column do not differ significantly. ***indicates $p < 0.001$; **indicates $p < 0.01$.

Conclusion

This study indicates that, in river net-cages, mono-sex Nile tilapia *O. niloticus* growth, survival, FCR, and production were best in the density of 50 tilapia m^{-3}, compared to 75 and 100 tilapia m^{-3} stocking densities. These better growth, productivity, and lower feed costs have documented the increasing economic return in the density of 50 tilapia m^{-3} treatments. This study suggests a density of 50 fish m^{-3} for higher growth, yield, and economic return of mono-sex Nile tilapia for intensive grow-out net-fish cages in the riverine ecosystem. Future research should be conducted on the super-intensification of GIFT in lake or riverine cages to examine the partial harvest and their relation to production economics and household nutrition whenadopted at the community levels. Moreover, these studies should address cage culture's environmental issues while using the lake or riverine systems.

Acknowledgments

The first author (MRAH) acknowledged the funding for Ph.D. research through BARC-NATP scholarships. The support from Bangladesh Fisheries Research Institute and Zoology, DU-Bergen University laboratory facilities from Zoology, University of Dhaka are acknowledged.

References

Ahmed T, Hasan JS, Hossain MRA, Haidar I, Rubel ASA and Pramanik MH. Assessment on the impact of dietary probiotic supplementation on growth indices of mono-sex tilapia (*Oreochromis niloticus*) cage culture at Dakatia River, Chandpur, Bangladesh. *World J. Fish Mar. Sci.* 2014; 6(5): 441-446.

Ali MS, Hossain MA and Naser MN. Optimization of stocking density for cage farming of Nile Tilapia (*Oreochromis niloticus* L.) in the river in ecosystem of northern Bangladesh. *EBAUB J.* 2019; 1: 57-64.

Ali MS, Hossain MA and Naser MN. Species suitability for small scale cage aquaculture in river ecosystem of northern Bangladesh. *Bangladesh J. Prog. Sci. Tech.*2011; IX (2): 197-200.

Barman BK, Little DC and Janssen J. Tilapia culture systems in Bangladesh. *Glob. Aquac. Advocate.* 2003; 6(4): 31–33.

Bhujel RC. Cage culture of monosex tilapia for food and financial security. Klinbunga S, Karoonuthaisiri N. and Piyapattanakorn S.(eds.) In: *Proceedings of the Sixth International Symposium on Cage Aquaculture in Asia.* 2019; pp. 19-28.

DoF. Yearbook of Fisheries Statistics of Bangladesh 2009-2010. Fisheries Resources Survey System, Department of Fisheries, Bangladesh Ministry of Fisheries and Livestock, Government of the

People's Republic of Bangladesh, 2011; 27: p 43.

DoF. Yearbook of Fisheries Statistics of Bangladesh 2020-21. Fisheries Resources Survey System, Department of Fisheries, Bangladesh Ministry of Fisheries and Livestock, Government of the People's Republic of Bangladesh, 2022; 37: p141.

FAO. The State of World Fisheries and Aquaculture. Meeting the sustainable development goals., Food and Agriculture Organization of the United Nations, Rome. *Licence*: 2018; CC BY-NC-SA 3.0 IGO.

Fialho NS, Valenti WC, David FS, Godoy EM, Proença DC, Roubach R and Wolff Bueno G. Environmental sustainability of Nile tilapia net-cage culture in a neotropical region. *Ecol. Indic*. 2021; 129(3-4):108008.

Garcia F, Sabbag OJ, Kimpara JM, Romera DM, Sousa NS, Onaka EM and Ramos IP. Periphyton-based cage culture of Nile tilapia: An interesting model for small-scale farming. *Aquaculture*. 2017; 479: 838-844.

Gibtan A, Getahun A and Mengistou S. Effect of stocking density on the growth performance and yield of Nile tilapia *Oreochromis niloticus* (L., 1758) in a cage culture system in Lake Kuriftu, Ethiopia. *Aquac. Res.* 2008; 39(13): 1450-1460.

Hosain ME, Amin SMN, Kamarudin MS, Arshad A and Karim M. Effects of carbon sources on the culture of giant river prawn in biofloc system during nursery phase. *Aquac. Reports*. 2021a; 19: 100607.

Hosain ME, Amin SMN, Kamarudin MS, Arshad A and Karim M and Romano N. Effect of salinity on growth, survival, and proximate composition of *Macrobrachium rosenbergii* post larvae as well as zooplankton composition reared in a maize starch based biofloc system. *Aquaculture*. 2021b; 533: 736235.

Hossain MRA, Hosain ME, Tabassum A and Naser MN. Effects of stocking density on production performance of Nile Tilapia (*Oreochromis niloticus*) grow-out culture in cages. *Bangladesh J. Zool.* 2022; 50(2): 239-250.

Hossain MRA, Rahman MA, Akter S, Hosain ME and Naser MN. 2017. Intervention of tilapia cage culture in the River Dakatia: Threaten or blessed to local fish diversity. *Int. J. Fish. Aquat. Stud.* 2017; 5(1): 228-232.

Hossain, MAR, Naser, MN, Hoq, ME, and Islam, MS. The fry/fingerling production of Tilapia: Hatchery and Culture Management. A training manual (in Bengali) 2014. Bangladesh Fisheries Research Forum, Dhaka, Bangladesh, p 40.

Kunda M, Pandit D and Harun-Al-Rashid A. Optimization of stocking density for mono-sex Nile tilapia (*Oreochromis niloticus*) production in riverine cage culture in Bangladesh. *Heliyon*, 2021; 7(11): e08334.

Moniruzzaman M, Uddin KB, Basak S, Mahmud Y, Zaher M and Bai SC. Effects of stocking density on growth, body composition, yield and economic returns of monosex tilapia (*Oreochromis niloticus* L.) under cage culture system in Kaptai Lake of Bangladesh. *J. Aquac. Res. Dev.* 2015; 6(8): 1000357.

Naser MN and Khatun T. Easy methods for fish culture in small cages (In Bangla). Extension manual, published by Voluntary Organization for Social Development (VOSD), Lalmatia, Dhaka, Bangladesh, 2006. p 32.

Naser MN and Khatun T. Small scale Tilapia culture in Cages (In Bangla). Extension manual, published by Voluntary Organization for Social Development (VOSD), Lalmatia, Dhaka, Bangladesh, 2007. p 24.

Ninh NH, Thoa NP, Knib W and Nguyen NH. Selection for enhanced growth performance of Nile tilapia (*Oreochromis niloticus*) in brackish water (15-20 ppt) in Vietnam. *Aquaculture*, 2014; 428-429: 1-6.

Ross LG. Environmental physiology and energetics. In: Beveridge, M.C.M., McAndrew, B.J. (Eds.), Tilapias: Biology and Exploitation. Springer, Dordrecht.2000; 89-128.

Shamsuddin M, Hossain MB, Rahman M, Kawla MS, Tazim MF, Albeshr MF and Arai T. Effects of stocking larger-sized fish on water quality, growth performance, and the economic yield of Nile Tilapia (*Oreochromis niloticus* L.) in floating cages. *Agric.* 2022; 12(7): 1-19.

Tran N, Shikuku KM, Rossignoli CM, Barman BK, Cheong KC, Ali MS and Benzie JAH. Growth, yield and profitability of genetically improved farmed tilapia (GIFT) and non-GIFT strains in Bangladesh. *Aquac.* 2021; 536: 736486.

J. Bangladesh Acad. Sci. 47(1); 53-60: June 2023 DOI:https://doi.org/10.3329/jbas.v47i1.65576

Journal of Bangladesh Academy of Sciences

Journal homepage: http://www.bas.org.bd/publications/jbas.html

Research Article

Computational analysis of functional single nucleotide polymorphisms associated with *NPAS2* gene

Sumaiya Farah Khan*, Fahmida Sultana Rima[1] and Fuad Hasan

Department of Genetic Engineering and Biotechnology, Faculty of Life and Earth Science, Jagannath University, Dhaka, Bangladesh

ARTICLE INFO

Article History

Received: 11 April 2023
Revised: 22 May 2023
Accepted: 11 June 2023

Keywords: Single nucleotide polymorphisms (SNPs), *NPAS2* gene, Circadian rhythm, Computational analysis.

ABSTRACT

Circadian rhythm is a natural physiological process that regulates the sleep-wake cycle and occurs about every 24 hours. The fundamental molecular clock, NPAS2 (Neuronal PAS Domain Protein 2), generates and regulates mammalian circadian rhythms. Various diseases have been linked to single nucleotide polymorphisms (SNPs) in NPAS2. In this study, several computational approaches have been employed to predict the SNPs' functional and structural consequences and investigate the deleterious roles of nsSNPs. Two deleterious nsSNPs (F190L and S105I) were found with predicted functions linking to disease. Alongside, from the obtained ConSurf result, Q73, E61, K51, E167, L317, and R514 were expected as highly conserved and exposed, while T114, T328, and C299 were predicted as highly conserved and buried. However, to establish their role in disease pathogenesis, further studies need to be done on the deleterious mutations of the NPAS2 gene.

Introduction

The largest of the circadian genes and core component of the molecular clock, Neuronal PAS domain protein 2 (NPAS2) is encoded by the NPAS2 gene and resides on chromosome 2 at the band q13. It is a PAS protein 4 (MOP4) member, which acts as a human transcription factor. The amino acid sequence of NPAS2 and Circadian Locomotor Output Cycles Kaput (CLOCK), a transcription factor located in the suprachiasmatic nucleus (SCN), are highly relatable in functional domains (Reick et al., 2001). The NPAS2 gene heterodimerizes with Brain and Muscle ARNT like Protein 1 (BMAL1) and regulates other circadian genes Cryptochrome (Cry1 and Cry2) and Period (Per1, Per2, and Per3)(Albrecht, 2020). The loss of functions of NPAS2 leads to abnormal rhythms. It has several negative impacts, for example, psychiatric diseases like seasonal affective disorder (SAD), bipolar disorder, major depression, and drug addiction, changing patterns of sleep and behavior, and tumorigenesis as well (McClung, 2013; Mukherjee et al., 2010). The immunohistochemistry of the test reveals the presence of NPAS2 protein in both germ cells and Leydig cells. Since Leydig cells are found in the testicle, it functions to produce testosterone in the presence of luteinizing hormone (LH) (Zirkin and Papadopoulos, 2018). In addition, studies have revealed that single nucleotide polymorphisms (SNP) in the NPAS2 gene have been the underlying reason for mood disorders, seasonal affective disorder, and major depressive disorder. However, the mechanisms of NPAS2 in mood-related behaviors are still unclear (Albrecht, 2017 and 2020).

Individual differences are caused by single nucleotide polymorphisms (SNPs), which may be found in gene promoters, exons, and introns, as well as 5'- and 3'-untranslated regions (UTRs). The SNPs occurred in the

---

*Corresponding author: <sumaiyafarah@yahoo.com>

[1] *Department of Genetic Engineering and Biotechnology, University of Barisal, Bangladesh*

gene coding regions are mainly categorized into synonymous and non-synonymous SNPs (nsSNPs), also called missense SNPs. When mutations do not change the amino acid, it is called a synonymous SNP, whereas non-synonymous SNPs alter the amino acid in humans (Arshad et al., 2018). Substitution of amino acids in protein causes damaging effects, including protein structure destabilization, gene regulation alteration, changes of charge, stability, dynamics, inter/intra protein interactions, which affect the function and structural integrity of the protein (Akter et al., 2022). Following the previous studies, nsSNPs, associated with a large number of genes, have been responsible for about 50% of mutations that are directly implicated in cancer, inflammatory and autoimmune disorders, for instance, Ankylosing Spondylitis (AS), Autoimmune Thyroid Disease/Grave's Disease (AITD), Breast Cancer (BC), Multiple Sclerosis (MS), etc. (Khoruddin et al., 2021).

The risk of human breast and colorectal cancer are associated with a missense SNP in NPAS2 (Ala394Thr). Current research has revealed an association of NPAS2, ARNTL, and CLOCK polymorphisms with a general mood disorder and seasonal affective disorder (SAD) (Kim et al., 2015). In mood disorders, BMAL1 and NPAS2 transcriptionally activate a luciferase receptor in a circadian fashion that directly regulates Maoa transcription (Hampp et al., 2008). NPAS2 is also responsible for the development of anxiety and has a function for the regulation of GABAergic neurotransmission. Additionally, these genes may influence metabolic factors such as body weight and appetite (Albrecht, 2020). So, this study was designed using various bioinformatics tools to discover the most deleterious and damaging nsSNPs of the NPAS2 gene to develop precision medicine for treating the disorders.

Materials and Methods

Retrieval of nsSNPs

All of the nsSNPs in the human NPAS2 gene, as well as their relevant information (reference SNP ID, position, changed amino acid residues and protein accession number, etc.), were collected from NCBI (https://www.ncbi.nlm.nih.gov/). Its protein sequence was also retrieved from UniProtKB (http://www.uniprot.org/uniprot/). Only nsSNPs were chosen for further inspection.

Identification of the deleterious SNPs of NPAS2

To determine the harmful SNPs in the human NPAS2 gene, six different bioinformatics tools (PROVEAN, PolyPhen-2, SNPnexus, PMut, PON- P2, SNAP2) were used. PROVEAN (Protein Variation Effect Analyzer) [http://provean.jcvi.org/ index.php] is a software program that forecasts how an amino acid change or indel would affect a protein's biological function. PolyPhen-2 (Polymorphism Phenotyping v2) [http://genetics.bwh.harvard.edu/pph2/] program makes predictions about the probable effect of an amino acid substitution on the structure and function of a human protein using physical and comparative factors. A web-based tool for variant annotation, SNPnexus [https://www.snp-nexus.org/v4/], makes choosing and prioritizing well-known and new novel genomic variations easier. With high-quality scores, PMut [http://mmb. irbbarcelona.org/PMut] forecasts Mendelian pathogenic mutations. PON-P2 [http://structure.bmc.lu.se/PON-P2/] determines the pathogenicity-association of amino acid substitutions. Using neural networks, SNAP2 [https://github.com/Rostlab/SNAP2] annotates the results of single amino acid alterations in a protein.

Prediction of disease-related SNPs

SNPs & GO [https://snps.biofold.org/snps-and-go/snps-and-go.html] and PhD-SNP [https://snps.biofold.org/phd-snp/phd-snp.htm] were used to predict disease-related SNPs in humans with the NPAS2 gene. With an overall score accuracy of 82%, SNPs&GO (Single nucleotide polymorphism database and gene ontology) is a tool that predicts human disease-related single amino acid variation in protein combined with functional annotations. The predictions of the inputs were divided into neutral and disease in the case of SNPs&GO. With an accuracy of 78% for human proteins, PhD-SNP (Predictor of human deleterious single nucleotide polymorphisms) is used to predict the disease-associated variants. The PhD-SNP protein prediction result output format is disease and neutral. Together with the reliability index score between 0 and 9, it divides the polymorphisms into disease-associated and neutral categories.

Effect on the human NPAS2 protein stability

By either reducing or enhancing protein stability, SNPs frequently have an impact on protein strength. Several tools were utilized to increase the confidence in the discovered nsSNPs of NPAS2 protein to anticipate these effects. MUpro (http://mupro.proteomics.ics.uci.edu/) and I-Mutant (http://gpcr2.biocomp.unibo.it/I-Mutant.htm) were used to analyze protein stability. During 20-fold cross-validation, MUpro's prediction of changes in protein stability caused by single nucleotide variations in the amino acid sequence has an accuracy of more than 84%. I-Mutant [http://gpcr2.biocomp.unibo.it/I-Mutant.htm], predicts how changes in a single nucleotide will affect a protein's stability. From the protein structure, the I-Mutant predicts protein stability changes upon single-point mutation based on the neural network system.

Phylogenetic conservation of human NPAS2 gene

ConSurf (https://consurf.tau.ac.il/) was used to examine the conservation of the NPAS2 protein sequence. The high throughput characterization of functional protein domains was done using ConSurf. Each amino acid in a protein is assigned a conservation score, ranging from 1 to 9, with scores 1-3 being variable, 4-6 being average conserved, and 7-9 being highly conserved residues. The evolutionary conservation of amino acid positions was determined using protein sequence, and analysis was conducted based on evolutionary relationships between homologous sequences. The highly conserved residues close to high-risk nsSNPs locations were chosen for further study.

Prediction of molecular interaction networks

As proteins are involved in every cellular process, the interactions among them should be maintained to conserve the stability or homeostasis of the system. The online application STRING (https://string-db.org/) was used to forecast the protein-protein interactions. The interacting networks of several proteins with NPAS2 were visualized in PNG format.

Result and Discussion

Retrieval of SNPs

The dbSNP database was used to extract all of the SNPs for the NPAS2 gene. Of the 63,107 SNPs discovered in the human NPAS2 gene, only 663 missense SNPs were chosen for further examination.

Determination of deleterious nsSNPs of NPAS2 gene

Six distinct *in silico* tools were used to examine the detrimental SNPs that could change the function and structure of the NPAS2 protein. This was accomplished using *in silico* tools PROVEAN, SNPNexus, PolyPhen-2, PMut, PON-P2, and SNAP2. Using the PROVEAN software program, 663 missense SNPs were divided into harmful (155 SNPs) and neutral (360 SNPs) [Fig. 1(A)]. SNPNexus projected that 187 nsSNPs were deleterious, 17 were deleterious-low confidence, 265 were tolerated, and 17 were tolerated-low confidence [Figure 1(B)]. The outcome of PolyPhen-2 forecasts nsSNPs that are likely to be damaging, possibly damaging, and benign. This tool identified 154 SNPs as probably damaging, 102 as possibly damaging, and 259 as benign [Figure 1(C)]. The result of PMut divided 146 SNPs as disease and 369 SNPs as neutral [Fig. 1(D)]. The output of PON-P2 revealed 33 SNPs as pathogenic, 201 SNPs as neutral and 281 SNPs' effects were predicted as unknown [Figure 1(E)]. SNAP2 software predicts a score (ranges from -100 strong neutral prediction to +100 strong effect prediction). On this tool, 279 SNPs were predicted to have an impact, and 237 were predicted as neutral [Fig. 1(F)]. In Fig. 2, the percentage of damaging nsSNPs identified by six *in silico* tools are shown.

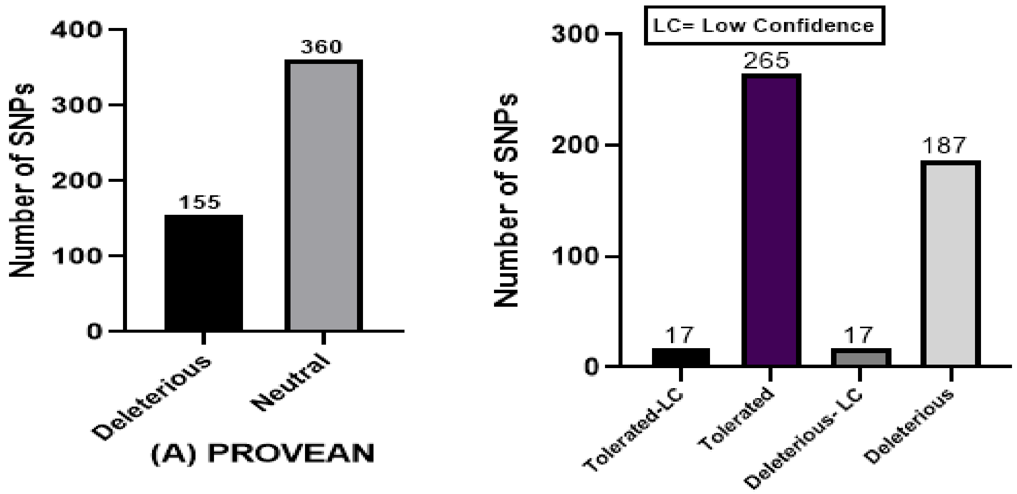

(A) PROVEAN

(B) SNPNexus

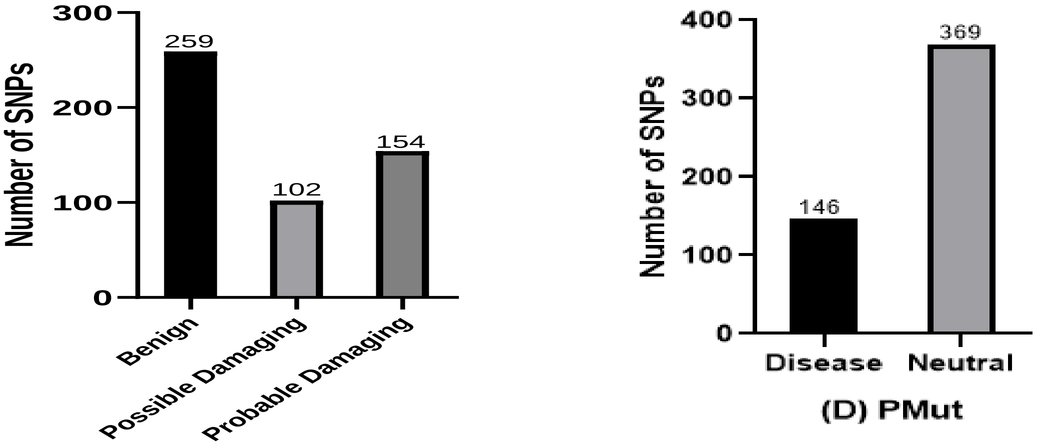

(C) PolyPhen-2

(D) PMut

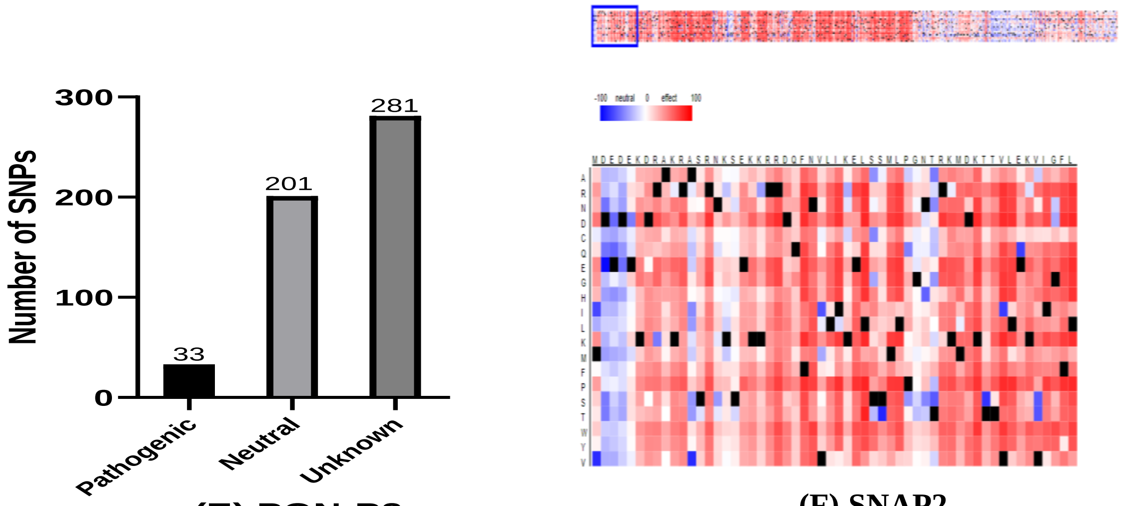

(E) PON-P2

(F) SNAP2

Fig. 1. Graphical representation of the nsSNPs that were explored by the six tools: (A) PROVEAN (B) SNPNexus (C) Polyphen-2 (D) Pmut (E) PON-P2 (F) SNAP2.

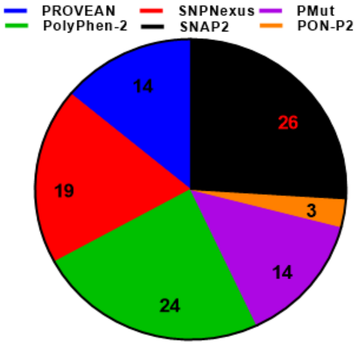

Fig. 2. Pie chart displaying the percentage of damaging nsSNPs identified by six *in silico* tools; PROVEAN, SNPNexus, PolyPhen-2, PON-P2, PMut, and SNAP2.

Analysis of the results from these six tools revealed that 17 SNPs in the NPAS2 protein had been projected to be deleterious (Table 1).

Prediction of human NPAS2 gene disease-related SNPs

Eighty-nine high-confidence nsSNPs were subjected to questions for further analysis to ensure their association with disease or not through SNPs&GO and PhD-SNP servers.

SNPs&GO predicted the impact of the disease-related mutation on the NPAS2 protein function, and it predic-

Table 1. High-risk pathogenic nsSNPs were detected by six *in silico* tools.

rsID	AA change	PROVEAN	SNPNexus (SIFT)	PolyPhen-2	PON-P2	PMut	SNAP2
rs201591122	V810I	Deleterious	Deleterious	Probably damaging	Pathogenic	Disease	effect
rs528544389	Q486H	Deleterious	Deleterious	Probably damaging	Pathogenic	Disease	effect
rs746290665	L220V	Deleterious	Deleterious	Probably damaging	Pathogenic	Disease	effect
rs768357374	M684I	Deleterious	Deleterious	Probably damaging	Pathogenic	Disease	effect
rs775639109	N193K	Deleterious	Deleterious	Probably damaging	Pathogenic	Disease	effect
rs778182952	R570K	Deleterious	Deleterious	Probably damaging	Pathogenic	Disease	effect
rs895884491	Q73K	Deleterious	Deleterious	Probably damaging	Pathogenic	Disease	effect
rs938052839	F190L	Deleterious	Deleterious	Probably damaging	Pathogenic	Disease	effect
rs1159238384	E61K	Deleterious	Deleterious	Probably damaging	Pathogenic	Disease	effect
rs1161885523	S105I	Deleterious	Deleterious	Probably damaging	Pathogenic	Disease	effect
rs1201814308	E158G	Deleterious	Deleterious	Probably damaging	Pathogenic	Disease	effect
rs1204687554	A725D	Deleterious	Deleterious	Probably damaging	Pathogenic	Disease	effect
rs1247008181	S176G	Deleterious	Deleterious	Probably damaging	Pathogenic	Disease	effect
rs1284926566	E774Q	Deleterious	Deleterious	Probably damaging	Pathogenic	Disease	effect
rs1305136363	H718Q	Deleterious	Deleterious	Probably damaging	Pathogenic	Disease	effect
rs1421402100	K51E	Deleterious	Deleterious	Probably damaging	Pathogenic	Disease	effect
rs1457843152	F666L	Deleterious	Deleterious	Probably damaging	Pathogenic	Disease	effect

ted 14 SNPs as disease and 75 SNPs as neutral [Figure 3(A)]. On the other hand, PhD-SNP predicted 86 SNPs as disease-causing and only 3 SNPs as neutral [Fig. 3(B)]. After analyzing the above result acquired from the six tools and SNPs&GO, PhD-SNP, two SNPs (F190L and S105I) were found to be harmful and disease associated.

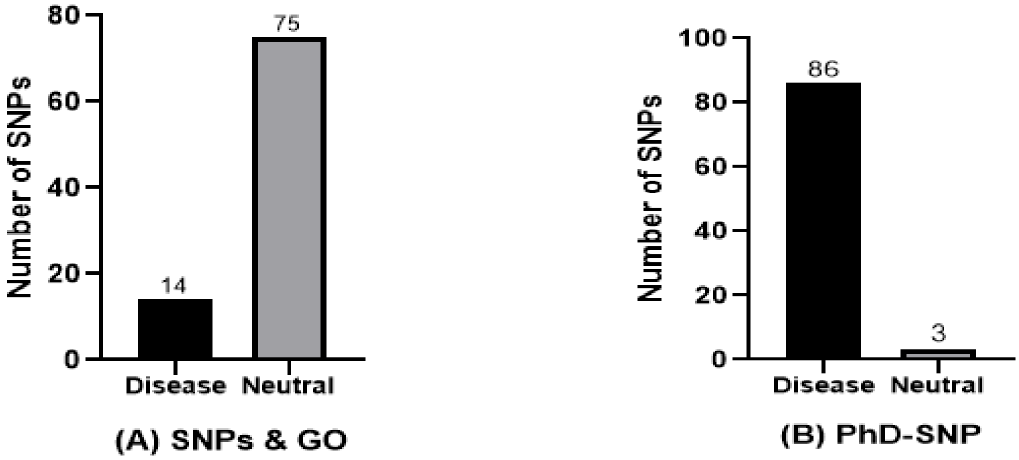

Fig. 3. Graphical representation of disease related SNPs uncovered by (A) SNPs&GO (B) PhD-SNP

Determination of protein structural ability

Due to these SNPs, protein stability may be changed, either lowering or increasing. Increased protein stability causes effective protein action, whereas decreased stability causes hindrance of protein action. A pair of tools I-Mutant and MUpro were used to project these effects, and 106 selected nsSNPs were run through these tools. Since the I-Mutant tool predicts protein structural ability based on the SNP's RI value, it predicted 81 SNPs as decreased stability and 25 as increased stability. According to MUpro, 102 SNPs were predicted to decrease stability and 4 to increase stability.

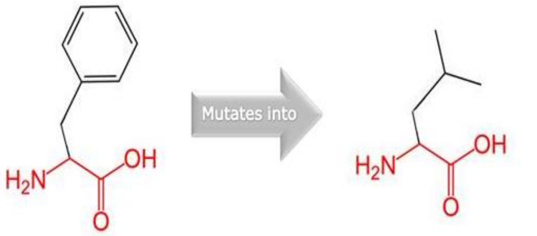

Fig. 4. The schematic structures of the amino acid Phenylalanine (left) and the mutant amino acid, Leucine (right) at 190 positions are shown in the image. Red represents the backbone, which is the same for each amino acid. The unique side chain for each amino acid is colored black.

Alongside, between F190L and S105I, the F190L SNP decreases the stability, and S105I SNP increases the stability of the protein.

Phenylalanine is changed to Leucine at amino acid position 190 due to the F190L SNP mutation (Fig. 4). The mutant residue tends to be in another secondary structure than the wild-type residue, which is anticipated to be in its preferred secondary structure, a β-strand. Therefore the local conformation will be slightly unstable. The altered residue is located in a region crucial for the protein's main activity, so changing the residue might affect the function. The sizes of the wild-type and mutant amino acids also vary, and as the mutant residue is smaller, interactions may be lost as a result.

Analysis of evolutionary conservation of NPAS2

The evolutionary conservation of the 15 most deleterious nsSNPs of NPAS2 protein was calculated by ConSurf. The cutoff value of ConSurf is scaled over nine grades. The higher the conservation score, the higher the chance to be conserved. The ConSurf result of this study predicted that most of the SNPs are highly conserved and exposed, and these highly conserved mutants may have a function in association with disease. The output of this tool predicted Q73, E61, K51, E167, L317 and R514 as functional residues making them highly conserved and exposed, while T114, T328, and C299 are likely to be structural residues making them highly conserved and buried (Supplementary Fig. 01).

Protein interacting network analysis

The protein interaction network of NPAS2 protein was constructed using the STRING web tool, which also suggested that NPAS2 protein is functionally linked with 10 other proteins, including ARNTL, NR1D1, CRY2, CRY1, BHLHE41, EP300, BHLHE40, RORA, DBP, RXRA (Fig. 5). The entire protein network connection between these 10 proteins might be impacted by changes in NPAS2 gene.

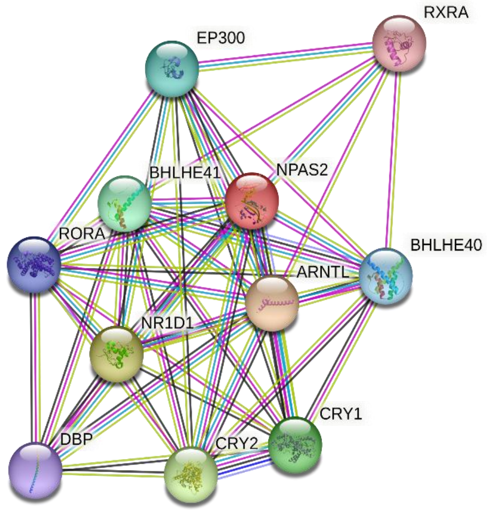

Fig. 5. Protein interaction network of NPAS2 protein

Conclusion

Three known nsSNPs (Ala394Thr, Ser471Leu, and Pro690Ala) in the largest circadian gene, Neuronal PAS domain protein 2 (*NPAS2*), were reported to be involved in breast cancer, indicating a potential array of biomarkers for breast cancer risk (Zhu et al., 2008). Few nsSNPs of the NPAS2 gene are known, while the functional and structural consequences of the nsSNPs in NPAS2 remain unknown. This study identified two potentially deleterious nsSNPs (F190L and S105I) of the NPAS2 gene; further studies are needed to validate this preliminary observation. Molecular dynamics (MD) simulations need to be used to investigate the effects of SNPs on protein structure.

Conflicts of Interest

The authors declare that they have no conflicts of interest regarding the publication of this article.

References

Akter M, Khan SF, Sajib AA and Rima FS. A comprehensive in silico analysis of the deleterious non-synonymous SNPs of human FOXP2 protein. *PLOS ONE*. 2022; 17(8): e0272625.

Albrecht U. Molecular connections between circadian clocks and mood-related behaviors. *J. Mol. Biol.* 2020; 432(12): 3714-3721.

Albrecht U. Molecular Mechanisms in Mood Regulation Involving the Circadian Clock. *Front. Neurol*. 2017; 8: 30.

Arshad M, Bhatti A, and John P. Identification and in silico analysis of functional SNPs of human TAGAP protein: A comprehensive study. *PLOS ONE*. 2018; 13(1): e0188143.

Hampp G, Ripperger JA, Houben T, Schmutz I, Blex C, Perreau-Lenz S, Brunk I, Spanagel R, Ahnert-Hilger G, Meijer JH and Albrecht U. Regulation of monoamine oxidase A by circadian-clock components implies clock influence on mood. *Curr. Biol.: CB.* 2008; 18(9): 678-683.

Khoruddin NA, Noorizhab MN, Teh LK, Mohd Yusof FZ, and Salleh MZ. Pathogenic nsSNPs that increase the risks of cancers among the Orang Asli and Malays. *Scientific Reports*. 2021; 11(1): 16158.

Kim H-I, Lee H-J, Cho C-H, Kang S-G, Yoon H-K, Park Y-M, Lee S-H, Moon J-H, Song H-M,Lee E, and Kim L. Association of CLOCK, ARNTL, and

NPAS2 gene polymorphisms and seasonal variations in mood and behavior. *Chronobiol. Int.* 2015; 32(6): 785-791.

McClung CA. How might circadian rhythms control mood? Let me count the ways. *Biol. Psychiatry*. 2013; 74(4): 242-249.

Mukherjee S, Coque L, Cao J-L, Kumar J, Chakravarty S, Asaithamby A, Graham A, Gordon E, Enwright JF, DiLeone RJ, Birnbaum SG, Cooper DC, and McClung CA. Knockdown of Clock in the ventral tegmental area through RNA interference results in a mixed state of mania and depression-like behavior. *Biol. Psychiatry*. 2010; 68(6): 503-511.

Reick M, Garcia JA, Dudley C and McKnight SL. NPAS2: An analog of clock operative in the mammalian forebrain. *Science (New York, N.Y.)*. 2001; 293(5529):506-509.

Zhu Y, Stevens RG, Leaderer D, Hoffman A, Holford T, Zhang Y, Brown HN and Zheng T. Non-synonymous polymorphisms in the circadian gene NPAS2 and breast cancer risk. *Breast Cancer Res. Treat.* 2008;107(3): 421-425.

Zirkin BR and Papadopoulos V. Leydig cells: Formation, function, and regulation. *Biol. eprod.* 2018; 99(1): 101-111.

J. Bangladesh Acad. Sci. 47(1); 61-68: June 2023 DOI: https://doi.org/10.3329/jbas.v47i1.66025

Journal of Bangladesh Academy of Sciences

Journal homepage: http://www.bas.org.bd/publications/jbas.html

Research Article

The growth and yield performances of mungbean (*Vigna radiata* L.) as influenced by the use of cow dung and chemical fertilizers

Md. Mahamudul Hasan, Saima Sultana* and Mst. Afrose Jahan

Department of Soil Science, Sher-e-Bangla Agricultural University, Dhaka, Bangladesh

ARTICLE INFO

Article History

Received: 10 May 2023
Revised: 22 May 2023
Accepted: 11 June 2023

Keywords: Inorganic fertilizer, Cowdung, Mungbean, Growth, Seed yield

ABSTRACT

To investigate the effect of cow dung and chemical fertilizers on the growth and yield performances of mungbean (BARI Mung 6), an experiment was carried out in the research field of the Sher-e-Bangla Agricultural University, Dhaka, during the kharif season of 2020. The experiment was laid out as a randomized complete block design (RCBD) with three replications comprising seven manure-fertilizer treatments. The results showed that the different levels of cow dung and fertilizers significantly influenced mungbean growth parameters and seed yield. The highest plant height (48.2 cm), number of leaves plant^{-1} (10.3), number of branches plant^{-1} (3.9), maximum number of pods plant^{-1} (19.3), seeds pod^{-1} (10.4), 1000-seed weight (43.4g), and the highest seed yield (1.42 t ha^{-1}) were obtained from the application of 80% of the recommended dose of fertilizers (RDF) plus 20% cow dung. It is concluded that applying 20% cow dung (1.2 t ha^{-1}) coupled with 80% of the recommended amount of fertilizers together produced superior results for the growth and yield of mungbean compared to applying fertilizer or cow dung alone.

Introduction

Mungbean (*Vigna radiata* L.), also known as green gram, is Bangladesh's important traditional pulse crop. It belongs to the family Leguminosae and the sub-family Papilionaceae. Mungbean ranks first in market price and third in production among the pulse crops grown in Bangladesh (BBS, 2021). Due to its high nutritional value, ease of digestion, and non-flatulent nature, it has an advantage over other pulses. It is mostly cultivated for its edible seeds, which are high in protein. Its seed contains 3.7% ash, 0.6% fat, 0.9% fiber, and 24.7% protein (Potter and Hotchkiss, 1997). Over the past 20 years, the area used to produce mungbean globally has expanded at a 2.5% annual rate. In Bangladesh, only 0.65 million tons of pulses are produced, against a demand of 2.7 million tons. Mungbean contributed 27% of the total pulse production (BBS, 2021). The low yield potential of mungbean is mostly caused by poor farming practices, unbalanced use of nutrients, insufficient plant protection measures, and the low use of high-yielding varieties (Rupa et al., 2014). By using chemical fertilizers judiciously and managing the organic manure effectively, the yield and quality of mungbean can be increased.

As a leguminous crop, one of the key characteristics of mungbean is its capability to enhance soil nitrogen and productivity by fixing atmospheric nitrogen (N_2) through a symbiotic association with *Rhizobium* bacteria (Mahmood and Athar, 2008; Mandal et al., 2009). Therefore, mungbean requires a low amount of nitrogen (N) and an optimum amount of phosphorus (P), potassium (K), sulphur (S0, zinc (Zn), and Boron (B) (FRG, 2018). Recently, emphasis has been given to the usage of organic fertilizers in order to produce crops with sustainable yields (Tejada et al., 2009). Organic materials have a great potential to significantly enhance the soil's

---

*Corresponding author: <saimasultana@sau.edu.bd>

qualities and act as a source of several nutrients (Moller, 2009; Gadi et al., 2017). Ecosystems are preserved through organic farming.

In contrast, synthetic fertilizers harm soil and the ecosystem and threaten the entire planetsince they primarily include the major nutrients NPK in high concentrations while ignoring the use of organic fertilizers. As a result, the soil's quality has declined, negatively impacting animals, plants, and people (Palai et al., 2019). In order to address this problem of low soil fertility and productivity, the management of soil organic matter is a critical concern. Nutrient availability in soil is influenced by many factors, the most important of which is fertilizer balance. The proper amount of fertilizer ensures that the plant has access to other essential nutrients while also assisting in the growth and development of crops. Hence, the balanced use of fertilizer and manure is vital to obtain the maximum yield and maintain soil health. Therefore, the present study was carried out to (i) evaluate the effect of cow dung and chemical fertilizers on the growth and yield of mungbean and (ii) determine the best combination of cow dung and fertilizer doses for improved yield and quality of mungbean.

Materials and Methods

Site and soil description

The experiment was conducted at the Sher-e-Bangla Agricultural University (SAU) research field, Dhaka during the period from March to June 2020. This region is situated between 23º46' N latitude and 90º22' E longitude. The experimental site belongs to the Tejgaon soil series under the agroecological zone Madhupur Tract (AEZ-28). The area experiences a sub-tropical monsoon climate characterized by heavy rainfall from June to September, with a little rain during the rest of the year.

Texturally the soil (0-15 cm depth) of the experimental site was silty clay loam with a pH of 6.9, 1.05% organic matter, 0.08% total N, 12.8 mg kg^{-1} available P, and 43.29 mg kg^{-1} available K. Cowdung contained 0.9% N, 0.5% P, and 1.1% K.

Treatments and design

There were seven treatments comprising different combinations of chemical fertilizers and cow dung. The 100% rates for urea, triple superphosphate, muriate of potash, gypsum, ZnO, and boric acid as per FRG. (2018) were 45 kg, 90 kg, 40 kg, 55 kg, 8.5 kg, and 10 kg per hectare, respectively. Cowdung was used at 6 tons per hectare.

The seven treatment combinations were: T_0-control, T_1-100% recommended dose of chemical fertilizer (RDF), T_2-100% cow dung, T_3-80% fertilizer and 20% cow dung, T_4-60% fertilizer and 40% cow dung, T_5-40% fertilizer and 60% cow dung, T_6-20% fertilizer and 80% cow dung.

The experiment was laid out following a randomized complete block design (RCBD) with three replications. The experiment had 21 unit plots (7 treatments × 3 replications), and each plot size was 3m × 2m. The experimental fields were tilled with a power tiller and plowed twice, followed by laddering. Then weed stubble and crop residues were removed from the field. Finally, the land was leveled, and the experimental plot was partitioned into unit plots following the experimental design.

Crop management

The entire amounts of well-decomposed cow dung, urea, triple superphosphate, muriate of potash, gypsum, ZnO, and boric acid were applied as per treatments during final land preparation.

The BARI mung-6 variety was used for the study. On 21 March 2020, mungbean seeds at the rate of 35 kg ha^{-1} were sown by hand as uniformly as possible in furrows. The line-to-line distance was maintained at 30 cm. Weeding cum thinning was done 12 days after sowing (DAS), and the second wedding was performed at 35 DAS. The plant-to-plant distance was maintained at 10 cm. The crops were harvested at a time due to the synchronous maturity of pods. Firstly, 50% of the early-maturing pods were manually picked up 55 days after sowing, and the rest 50% were harvested plot-wise a few days later in June.

Data collection

From each plot, four plants were randomly selected prior to maturity and were tagged for recording data which included plant height (cm), number of leaves per plant, branches per plant, pods per plant, seeds per pod, 1000- seed weight(g), seed yield per plot (g). The latter was converted to yield per hectare (t).

Statistical analysis

Data of the growth and yield parameters were statistically analyzed following the 'F' test using statistix-10 software. The means of the different treatments for the parameters where the 'F' value was significant were compared by Duncan's Multiple Range Test (DMRT) at a 5% probability level (Gomez and Gomez, 1984).

Results and Discussion

Effects of cow dung and chemical fertilizers on growth parameters of mungbean

Plant height

The combined application of cow dung and chemical fertilizers greatly influenced mungbean's plant height at different growth stages (Table 1). The highest plant height at 30 days after sowing (DAS), 40 DAS, and at harvest was recorded as 30.0 cm, 39.9 cm, and 48.2 cm were observed with treatment T_3 (80% RDF+20% cow dung), followed by treatment T_1 (100% RDF). The significantly lowest plant height at all the growth stages (22.9 cm, 32.3 cm, and 43.4 cm, respectively) was noted for the T_0 (control) treatment, where no fertilizer or cow dung was used. This finding is in agreement with the previous finding of Armin et al. (2016), who reported that the combined application of organic and inorganic fertilizers significantly increased the plant height of mungbean compared to the sole application at different growth stages. Comparable outcomes were observed by Rajkhowa et al. (2002) in the cases of green gram, who stated that using a combination of organic and inorganic fertilizers was preferable to using only inorganic fertilizers.

Table 1. Effects of cow dung and chemical fertilizers in different combinations on plant height and number of leaves and branches per plantof mungbean

Treatments	Plant height (cm)			Number of leaves plant^{-1}			Number of branches plant^{-1}
	30 DAS	40 DAS	At harvest	30 DAS	40 DAS	At harvest	At harvest
T_0	22.9^{f}	32.3^{g}	43.4^{e}	3.3^{e}	4.6^{e}	5.3^{c}	0.4^{f}
T_1	29.0^{b}	39.2^{b}	47.9^{ab}	7.6^{b}	8.3^{b}	8.3^{b}	3.0^{b}
T_2	24.7^{e}	34.5^{f}	44.6^{d}	4.6^{d}	5.6^{de}	$6.6b^{c}$	1.2^{e}
T_3	30.0^{a}	39.9^{a}	48.2^{a}	8.6^{a}	10.3^{a}	10.3^{a}	3.9^{a}
T_4	26.7^{c}	37.8^{c}	46.6^{b}	7.0^{b}	$7.6b^{c}$	7.3^{b}	$3.4a^{b}$
T_5	26.37^{cd}	36.6^{d}	46.5^{b}	7.0^{b}	$7.3b^{c}$	7.3^{b}	2.6^{c}
T_6	25.7^{d}	36.1^{e}	45.5^{c}	5.6^{c}	$6.6c^{d}$	$6.6b^{c}$	1.7^{d}
CV (%)	1.74	0.7	1.1	6.34	9.04	13.03	8.04

In a column means having a dissimilar letter(s) differ significantly at 0.05 probability level by DMRT. T_0-control, T_1-100% recommended dose of chemical fertilizers (RDF), T_2-100% cow dung, T_3-80% RDF+ 20% cow dung, T_4-60% RDF+40% cow dung, T_5-40% RDF+60% cow dung, T_6-20% RDF+80% cow dung.

Number of leaves plant^{-1}

T_3 treatment (80% RDF+20% cow dung) demonstrated the highest number of leaves plant^{-1} showing 8.6, 10.3, and 10.3 at 30 DAS, 40 DAS, and maturity, respectively (Table 1). Next to T_3, the T_4 treatment performed the best result. The control treatment (T_0) exhibited the lowest number of leaves per plant with a record of 3.3, 4.6, and 5.3 at different plant growth stages. Salahin et al. (2011) reported that the application of cow dung and chemical fertilizers led to a noticeably greater uptake of nutrients in mungbean, thereby producing the maximum number of leaves per plant.

Number of branches plant^{-1}

The number of branches plant^{-1} at harvest ranged from 0.4-3.9 (Table 1). The highest number of brunches plant^{-1} (3.9) was recorded from the T_3 treatment (80% RDF+ 20% cow dung), whichwas statistically similar (3.43) with the treatment T_4 (60% RDF+40% cow dung). Among the treatments, the T_0 treatment showed the lowest number of branches per plant (0.4) at harvest. Armin et al. (2016) have observed the positive effect of the integrated use of cow dung and chemical fertilizers on mungbean.

Effects of cow dung and chemical fertilizers on the yield and yield contributing characteristics of mungbean

Pod length

The highest number of pod lengths (7.9 cm) of mungbean at harvest were obtained from the T_3 treatment, i.e., 80% RDF + 20% cow dung, which is statistically different from other treatments (Table 2). In contrast, the lowest pod length (6.91 cm) was obtained from T_0 (control) treatment. Similar findings in mungbean were reported by Salahin et al. (2011) and Mahabub et al. (2016), who demonstrated that the application of cow dung combined with chemical fertilizers noticeably increased the uptake of nutrients, which in turn led to the higher number of pod length.

Table 2. Effects of cow dung and chemical fertilizers in different combinations on yield contributing characteristicsof mungbean

Treatments	Pod length (cm)	Number of pod plant^{-1}	Number of seeds pod^{-1}	1000-seed weight (gm)
T_0	6.9^{g}	9.2^{f}	6.7^{f}	38.6^{f}
T_1	7.7^{b}	15.3^{b}	9.0^{b}	43.2^{ab}
T_2	7.0^{f}	10.8^{e}	7.6^{e}	40.6^{e}
T_3	7.9^{a}	19.3^{a}	10.4^{a}	43.4^{a}
T_4	7.5^{c}	14.5^{c}	8.7^{bc}	42.8^{d}
T_5	7.3^{d}	14.0^{c}	8.4^{c}	42.6^{d}
T_6	7.2^{e}	12.8^{d}	8.0^{d}	42.2^{d}
CV (%)	0.58	3.38	2.23	0.74

In a column means having a dissimilar letter(s) differ significantly at 0.05 probability level by DMRT. T_0-control, T_1-100% recommended dose of chemical fertilizers (RDF), T_2-100% cow dung, T_3-80% RDF+20% cow dung, T_4-60% RDF+40% cow dung, T_5-40% RDF+60% cow dung, T_6-20% RDF+80% cow dung.

Number of pods plant^{-1}

The number of pods plant$^{–1}$ of mungbean at harvest varied significantly due to the different doses of cow dung and inorganic fertilizer (Table 2). The highest number of pods plant$^{–1}$ (19.3) was obtained from the combination of 80% RDF + 20% cow dung (Treatment T_3) followed by the treatment T_1 (100% RDF) and T_5 (40% RDF + 60% cow dung). The lowest number of pods plant$^{–1}$ (9.2) was recorded from the treatment T_0. This might be because using cow dung and inorganic fertilizers in combination improves the physical characteristics of the soil, which creates a healthy environment conducive to improving the efficiency of nutrient absorption. This agrees with the results of Mahabub et al. (2016), who reported that different doses of cow dung significantly increased the number of pods per plant in mungbean.

Number of seeds pod$^{–1}$

The treatment T_3 (80% RDF + 20% cow dung) produced the highest number of seeds pod$^{–1}$ (10.4), which statistically differs from all other treatments (Table 2).

Like other parameters, T_0 showed the lowest number of seeds pod$^{–1}$ (6.7). Similar results were reported by Pandey et al. (2019), who observed that combining organic and inorganic fertilizers was more effective in increasing the number of seeds per pod of mungbean than using solely chemical fertilizers.

1000-seed weight

Application of different levels of cow dung and fertilizers resulted in a significant variation in the weight of 1000 mungbean seeds at harvest(Table 2). The maximum 1000-seed weight (43.4 g)was observed in treatment T_3 (80% RDF + 20% cow dung), which is statistically identical (43.2 g) to treatment T_1 (100% RDF). The minimum 1000-seed weight (38.6 g) was noted for treatment T_0, i.e., control treatment. Comparable results were reported on mungbean by Choudhary et al. (2011) and on lentils by Singh et al. (2010).

Seed yield

Seed yield is the most critical parameter for judging the contribution of cow dung and chemical fertilizers in mungbean. The seed yield of mungbean per hectare, depending on the treatments, ranged from 0.9 to 1.42 tons (Fig. 1). Among the seven treatments, treatment T_3 receiving 80% RDF+20% cow dung has been found to be significantly better compared to the other treatments. This treatment (T_3) produced the maximum seed yield of 1.42 t ha$^{–1}$, followed by treatment T_4 (60% RDF+40% cow dung) (1.23 t ha$^{–1}$), and T_1 (100% RDF) (1.20 t ha$^{–1}$). Like other plant characters, the lowest yield (0.82 t ha$^{–1}$) was produced by treatment T_0 (control).

The findings demonstrated that the together use of cow dung and chemical fertilizers increased the seed yield of the mungbean. This could be because cow dung improved the physical and microbiological characteristics of the soil, which, combined with fertilizers, created a favorable environment for normal crop growth and yield. This result is consistent with earlier research findings (Sachan et al., 2020).

Correlation analysis between the growth and yield parameters

The results of the Pearson correlation analysis revealed that the growth and yield contributing parameters of mungbean had a significant positive correlation with the seed yield of the crop (Table 3). These results suggest that the seed yield of the crop was directly dependent on the various growth and yield parameters. The application of cow dung and inorganic fertilizer together strongly influences the mungbean's growth and yield contributing characteristics. Besides,the seed yield(t ha^{-1}) showed a significant and positive correlation with all the growth. It yielded contributing parameters, including the plant height($r=0.94$), the number of pods perplant ($r=0.97$), the number of seeds per pod ($r=0.96$), and the weight of 1000 seeds ($r=0.92$), that eventually boosted the overall yield. Comparable results were also observed by Gul et al. (2009) in mungbean and Painkra et al. (2018) in soybean.

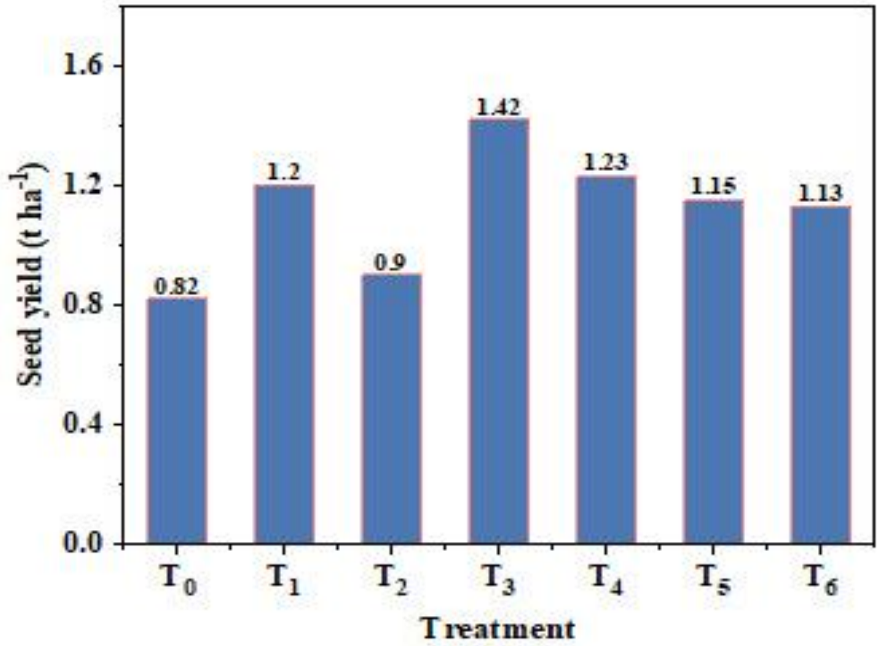

Fig. 1. Effects of cow dung and chemical fertilizers on seed yield of mungbean. T_0 control, T_1-100% recommended dose of chemical fertilizers (RDF), T_2-100 % cow dung, T_3-80% RDF+20% cow dung, T_4-60% RDF+40% cow dung, T_5-40% RDF+60% cow dung, T_6-20% RDF+80% cow dung.

Table 3. Pearson correlation matrix for the growth and yield contributing parameters of mungbean

	PH	NLP	NBP	NPP	NSP	TSW
PH	1					
NLP	0.92^{**}	1				
NBP	0.95^{**}	0.87^{*}	1			
NPP	0.95^{**}	0.97^{**}	0.94^{**}	1		
NSP	0.95^{**}	0.98^{**}	0.93^{**}	0.99^{**}	1	
TSW	0.95^{**}	0.80^{*}	0.92^{**}	0.88^{**}	0.87^{**}	1
SY	0.94^{**}	0.89^{**}	0.95^{**}	0.97^{**}	0.96^{**}	0.92^{**}
SY	0.94^{**}	0.89^{**}	0.95^{**}	0.97^{**}	0.96^{**}	0.92^{**}

PH=Plant height, NLP=Number of leaves per plant, NBP=Number of branches per plant, NPP=Number of pods per plant, NSP=Number of seeds per pod, TSW=1000-seed weight, SY=Seed yield.
** Significant at the 0.01 level (2-tailed); * Significant at the 0.05 level (2-tailed).

Conclusion

The combined use of cow dung and chemical fertilizers was more effective than the sole use of either cow dung or fertilizers for the growth and yield of mungbean. The combination of 80% RDF+ 20% of cow dung was the most suitable combination for achieving the highest seed yield of mungbean.

Author's contribution

Conceptualization: Mst. Afrose Jahan and Saima Sultana; Writing and editing: Saima Sultana and Md. Mahamudul Hasan; Research conduction: Md. Mahamudul Hasan; Data analysis: Md. Mahamudul Hasan and Saima Sultana.

Conflicts of Interest

The authors declare no conflicts of interest regarding the publication of this article.

References

Armin W, Ashraf-Uz-Zaman K, Zamil SS, Rabin MH, Bhadra AK and Khatun F. Combined effect of organic and inorganic fertilizers on the growth and yield of mung bean (Bari Mung 6). *Int. J. Sci. Res. Publ.* 2016; 6(7): 557-561.

BBS (2021). Statistical Year Book. Bangladesh bureau of statistics. Statistics Division, Ministry of planning, Govt. of the People's Republic of Bangladesh.

Choudhary HR, Sharma OP, Yadav LR and Choudhary GL. Effect of organic sources and chemical fertilizers on productivity of mungbean *J. Food Legumes,* 2011; 24(4): 324-326.

FRG. Fertilizer Recommendation Guide. Bangladesh Agricultural Research Council (BARC), 2018. Ministry of Agriculture, Govt. of the People's Republic of Bangladesh.

Gadi P, Dawson J and Shankar M. Effect of different organic manures, inorganic fertilizers and growth regulators on growth and yield of green gram (*Vigna radiata* L.*). Bull. Env. Pharmacol. Life Sci*. 2017; 6(1): 67-75.

Gomez KA and Gomez AA. Statistical Procedures for Agricultural Research. 2nd Edition, John Wiley & Sons, New York, 1984. p 680.

Gul R, Khan H, Mairaj G and Ali S. Correlation study on morphological and yield parameters of mungbean (*Vigna radiata*). *Sarhad J. Agric.* 2009; 24(1): 37-42.

Mahabub ST, Khan MS, Maed H, Sarker S and Tereque H. Effect of cow manure on growth, yield and nutrient content of mungbean. *Asian Res. J. Agric*. 2016; 2(1): 1-6.

Mahmood A and Athar M. Cross inoculation studies: Response of *Vigna mungo* to inoculation with rhizobia from tree legumes growing under arid Environment. *Int. J. Environ. Sci. Technol*. 2008; 5: 135-139.

Mandal S, Mandal M, Das A, Pati B and Ghosh A. Stimulation of indoleacetic acid production in a Rhizobium isolate of *Vigna mungo* by root nodule phenolic acids. *Arch. Microbiol.* 2009; 191: 389-393.

Moller K. Influence of different manuring systems with and without biogas digestion on soil organic matter and nitrogen inputs, flows and budgets in organic cropping systems. *Nutr. Cycl. Agroecosystems,* 2009; 84: 179-202.

Painkra P, Shrivatava R, Nag SK and Kute I. Correlation analysis for seed yield and its attributing traits in soybean (*Glycine max* L. Merrill). *Int. J. Curr. Microbiol. App. Sci*. 2018; 7(4): 2034-2040.

Palai JB, Jena J and Maitra S. Prospects of underutilized food legumes in sustaining pulse needs in India- A review. *Crop Res*. 2019; 54 (3 & 4): 82-88.

Pandey OP, Shahi SK, Dubey AN and Maurya SK. Effect of integrated nutrient management of growth and yield attributes of green gram (*Vigna radiata* L.). *J. Pharmacogn. Phytochem*. 2019; 8(3): 2347-2352.

Potter NN and Hotchkiss JH. Food Science. 1997. CBS Publishers, New Delhi, India. pp: 403.

Rajkhowa DJ, Saikia M and Rajkhowa KM. Effect of vermicompost with and without fertilizer on greengram. *Legume Res*. 2002; 25(4): 295-296.

Rupa WS, Miah MS, Shiam IH, Mehraj H and Jamal Uddin AFM. Organic and inorganic fertilizers on growth, yield and nutrient content of mungbean (BARI Mung 5). *Int. J. Bus. Soc. Sci. Res.* 2014; 1(2): 107-11.

Sachan HK, Krishna D and Prasad A. Combined effect of organic and inorganic fertilization on the growth and yield of mung bean (*Vigna radiata*). *Res. Crop,* 2020; 21(4): 676-680.

Salahin N, Islam MS, Begum RA, Alam MK and Hossain KM. Effect of tillage and integrated nutrient management on soil physical properties and yield under tomato- mungbean-t. aman cropping pattern. *Int. J. Sustain. Crop Prod.* 2011; 6(1): 58-62.

Singh G, Aggarwal N and Khanna V. Integrated nutrient management in lentil with organic manures, chemical fertilizers and biofertilizers. *J. Food Legumes*, 2010; 23(2): 149-151.

Tejada M, Hernandez MT and Garcia C. Soil restoration using composted plant residues: Effects on soil properties. *Soil Tillage Res*. 2009; 102(1): 109-117.

J. Bangladesh Acad. Sci. 47(1); 69-90: June 2023 DOI: https://doi.org/10.3329/jbas.v47i1.65144

Journal of Bangladesh Academy of Sciences

Journal homepage: http://www.bas.org.bd/publications/jbas.html

Research Article

Ethnic disparities in the distribution of gene expression modulating polymorphisms in key pro-inflammatory cytokines associated with COVID-19 severities

Tamim Ahsan, Kaniz Fatema[1], Sabrina Samad Shoily[2], Zinia Haidar[2] and Abu Ashfaqur Sajib[2*]

Molecular Biotechnology Division, National Institute of Biotechnology, Ganakbari, Ashulia, Savar, Dhaka, Bangladesh

ARTICLE INFO

Article History

Received: 27 March 2023
Revised: 24 May 2023
Accepted: 11 June 2023

Keywords: Pro-inflammatory cytokines; IL-6; IL-8; TNF-α; Ethnicity; COVID-19; SNP

ABSTRACT

The severity of the coronavirus disease 2019 (COVID-19) is linked to pro-inflammatory cytokine levels. There are still many unanswered questions regarding COVID-19 pathogenesis and prognosis. Significantly increased levels of pro-inflammatory cytokines characterize severe COVID-19 compared to those with a mild-to-moderate form of the disease. In this study, we used *in silico* tools to explore the variant allele frequency distributions of three important pro-inflammatory cytokine genes: interleukin-6 (*IL-6*), interleukin-8 (*IL-8*), and tumor necrosis factor-alpha (*TNFA*), as well as their linkage disequilibrium (LD) patterns in worldwide populations. These cytokines were chosen for their pro-inflammatory properties, importance in determining COVID-19 outcomes, and potential as disease treatment targets. Twenty-two of the variants correlate with altered cytokine expression levels, which may also influence the expression of several other mediators of immune responses. These variants also appear to be associated with several COVID-19 comorbidities, such as diabetes, asthma, obesity, and heart conditions. At least one variant (rs1800795 in *IL6*) is likely associated with an altered response to TNFA inhibitors, which are considered COVID-19 treatment options. The European super-population has high variant allele frequencies (VAF ≥ 0.2) at thirteen of these variant loci. High genetic heterogeneity at these loci is present in the admixed American populations, whereas the East Asian populations appear genetically more homogeneous. Interethnic differences are more pronounced at the *IL6* SNP loci, which may cause variances in the expression level of a long non-coding RNA gene, *IL6-AS1*. Stronger and more extensive LD ($R^2 \geq 0.8$) exists among the *IL6* and *IL8* variants in the European super-population and among the *TNFA* variants in the East and South Asian populations. In general, the European super-population has higher frequencies of haplotypes with multiple variant alleles. Such interethnic differences may shed more light on the disparities in COVID-19 severities and the responses to treatments across ethnic groups.

Introduction

COVID-19 is caused by a coronavirus, aptly named severe acute respiratory syndrome coronavirus 2 (SARS-CoV-2) (Wu et al., 2020). As of the writing of this article, SARS-CoV-2 has infected more than 761 million people and claimed over 6.8 million lives in 225 countries, areas, or territories around the globe (https://covid19.who.int/,Accessed: March 23, 2023). Europe is thus far the most heavily affected area, followed by the Americas, Southeast Asia, and Africa. Interethnic differences in COVID-19 outcomes cannot be fully explained by differences in socio-economic status or pre-existing health conditions (Mulholland and Sinha, 2020). Ethnicity is, however, a complex construct comprising genetic

---

[*] Corresponding author: <abu.sajib@du.ac.bd (AAS)>

[1] *Department of Mathematics and Natural Sciences, Brac University, Dhaka, Bangladesh*
[2] *Department of Genetic Engineering & Biotechnology, University of Dhaka, Dhaka, Bangladesh*

makeup, sociocultural identity, behavioral patterns, environment, historical processes, and socio-political experiences (Lee, 2009; Pan et al., 2020). Thus, differences in COVID-19 severity across ethnic groups can be attributed to multiple factors, such as socio-economic and health inequalities and genetic predisposition (El-Khatib et al., 2020).

Many unanswered questions remain regarding COVID-19 pathogenesis and prognosis (Cevik et al., 2020). Clinical manifestations of SARS-CoV-2 infection in humans range from mild symptoms to severe respiratory failures (Hu et al., 2021). While a proper antiviral immune response can prevent COVID-19 from becoming severe, the absence of such protective immunity can lead to massive destruction of tissues in multiple organs, especially those with high expression of angiotensin-converting enzyme 2 (ACE2) (Shi et al., 2020), and even death (Li et al., 2020). Severe COVID-19 is characterized by significantly increased levels of pro-inflammatory cytokines and reduced T lymphocytes compared to those with a mild-to-moderate form of the disease (Mulchandani et al., 2021). Especially following SARS-CoV-2 infection, host cells undergo pyroptosis and release damage-associated molecular patterns, which cause neighboring cells to produce pro-inflammatory cytokines (Tay et al., 2020). These cytokines recruit monocytes, macrophages, and T cells to the site of infection, promote further inflammation, and thus create a pro-inflammatory feedback loop (Tay et al., 2020). This overproduction of circulating inflammatory mediators, including cytokines and chemokines such as interleukin (IL)-1, IL-2, IL-6, IL-7, IL-8, IL-10, tumor necrosis factor-alpha (TNF-α), granulocyte colony-stimulating factor (G-CSF), monocyte chemoattractant protein-1 (MCP1), macrophage inflammatory protein 1 alpha (MIP1α), CXC-chemokine ligand 10 (CXCL10), C-reactive protein (CRP), ferritin, D-dimers and so forth, generates the "cytokine storm" in patients with severe COVID-19 (Gasparello et al., 2021; Hojyo et al., 2020; Ragab et al., 2020). Although no unifying definition of “cytokine storm” currently exists, it is one of the main focuses of studies exploring COVID-19 pathogenesis as it is the primary suspect for causing multi-organ failures in patients with severe COVID-19 (Fajgenbaum and June, 2020).

Elevated levels of several cytokines have been associated with COVID-19 severity, but specific cytokines among these play more critical roles in the pathogenesis of this disease compared with others. For example, significantly higher levels of circulating IL-6, IL-8, IL-10, IL-2R, and TNF-α, have been consistently found in patients with severe COVID-19 compared to those suffering from a mild-to-moderate form of the disease (Mulchandani et al., 2021). Among these five molecules, serum levels of IL-6, IL-8, and TNF-α in COVID-19 patients during hospitalization are strong and independent predictors of survival (Del Valle et al., 2020). It has been proposed that serum levels of IL-6 and TNF-α can be used to suggest therapeutic options (Del Valle et al., 2020). Moreover, both IL-6 and IL-8 can be used as biomarkers for COVID-19 severity and prognosis(Li et al., 2021). Elevated levels of plasma IL-6 significantly correlate with higher mortality (Smieszek et al., 2021). Additionally, the duration of illness in patients with severe COVID-19 is positively associated with serum levels of IL-8 (Ma et al., 2021). IL-8 is a potent regulator of neutrophil and monocyte chemotaxis that plays a significant role in acute lung damage. In such patients, elevated levels of IL-8 are associated with an increased risk of mortality and reduced ventilator-free and organ failure-free days (Mulchandani et al., 2021). The formation of Neutrophil Extracellular Traps (NETs) followed by neutrophil activation by IL-8 is one of the underlying mechanisms of COVID-19 pathogenesis. NETs promote immunothrombosis and lead to lung cell death, organ failure, massive neutrophil infiltration, and the development of Acute Respiratory Distress Syndrome (ARDS) (Cesta et al., 2022). Elevated levels of TNF-α are strong predictors of poor outcomes and contribute to organ damage in COVID-19 patients (Del Valle et al., 2020). COVID-19 confirmed that patients requiring ICU have a higher plasma TNF-α level than non-ICU patients (Huang et al., 2020). Recent studies have shown that increased levels of pro-inflammatory cytokines are associated with diabetes and its complications (Shoily et al., 2021), cardiovascular diseases (Stentz et al., 2004), hypertension (Liu et al., 2017), acute and chronic kidney diseases (Mihai et al., 2018; Ortega and Fornoni, 2010), and asthma, among others (Lambrecht et al., 2019). These conditions are also associated with COVID-19 severity and/or mortality (Bajgain et al., 2021; Ng et al., 2021).

Indeed, the correlation of elevated pro-inflammatory cytokine levels with COVID-19 severity makes these molecules feasible therapeutic targets. Several therapeutic monoclonal antibodies targeting inflammatory mediators, including IL-1β, IL-1ra, IL-2, IL-6, IL-8, IL-17, IL-33, G-CSF, GM-CSF, IP10, MCP1α, MIP1β, TNF-α, and complement component-5 are currently under clinical trial for managing COVID-19 associated cytokine storm (Hussein et al., 2020; Patel et al., 2021; Robinson et al., 2020). Promising results in this regard have so far been obtained using anti-IL-6 drugs such as tocilizumab, sarilumab, and siltuximab that both inhibit *trans*- and classical signaling (Castelnovo et al., 2021; Du et al., 2021). Whereas anti-IL-6 drugs are associated with some sorts of adverse reactions, the use of specific inhibitors of metalloproteinase 17 (ADAM17) and soluble glycoprotein 130 fused chimera (sgp130Fc) are more effective and safer strategies to specifically inhibit pathological IL-6 *trans*-signaling in patients with severe COVID-19 since IL-6 also offers some anti-inflammatory effects (Du et al., 2021). Two IL-8 inhibitors – HuMax-IL-8 and Reparixin, are also being investigated as potential COVID-19 therapeutic agents. The human monoclonal antibody HuMax-IL-8 targets IL-8 overexpression in multiple cancer types, whereas Reparixin is an allosteric inhibitor of IL-8 that significantly reduces neutrophil recruitment and NET formation (Cesta et al., 2022).

Elevated levels of pro-inflammatory cytokines are associated with increased susceptibility to several COVID-19 comorbidities. Besides, variants in the genes encoding inflammatory mediators can be associated with altered responses to therapies targeting pro-inflammatory cytokines(Enevold et al., 2014; Padyukov et al., 2003). Understanding inter-ethnic differences in pro-inflammatory cytokine levels helps identify the relatively more vulnerable groups, make appropriate public health policies, and make informed therapeutic decisions concerning COVID-19.

There have been a few studies reporting differences in inflammatory cytokine levels among individuals of different ethnicities (Coe et al., 2011; Ho et al., 2005; Mayr et al., 2007; Ness et al., 2004; Stowe et al., 2010; Yao et al., 2018). However, these studies have mostly focused on US residents. Levels of pro-inflammatory cytokines can depend on both non-genetic factors such as age, gender, smoking habits, etc. (Rothaug et al., 2016) as well as genetic factors such as certain genotypes at expression quantitative trait loci (eQTLs) (Guan et al., 2020). Differences in allelic and haplotype frequencies of such variants across ethnic groups may have clinical implications (Hassan et al., 2003).

In the present study, we explored the allele frequency distributions and linkage disequilibrium patterns of gene expression-modulating SNPs in three pro-inflammatory cytokine genes (*IL6*, *TNFA*, and *IL8*) across twenty-six populations belonging to five super-populations, namely African, admixed American, East Asian, European, and South Asian. These cytokines were selected because of their pro-inflammatory nature, significance in determining COVID-19 outcomes, and prospects as therapeutic targets for the disease. We aimed to determine (i) if there are any differences in the genetic architecture of those gene expression-associated SNPs across ethnic groups, (ii) how these differences may contribute to the ethnic disparities in COVID-19 outcomes, and (iii) how these differences may manifest as inter-ethnic variability in response to COVID-19 therapy.

Materials and Methods

Listing gene expression-modulating SNPs

Gene expression-modulating SNPs in *IL6*, *TNFA*, and *IL8* (p <5E-8, the default p-value for gene expression in PhenoScanner V2) were retrieved from the Gene Expression catalog of PhenoScanner V2 (Kamat et al., 2019). Duplicates were removed to retain only the unique reference SNP IDs (rs IDs). Chromosomal location (GRCh38/hg38), consequence, and associated trait for each of these SNPs were obtained through PhenoScanner V2.

Retrieving allele frequencies

Allele frequencies at the gene expression-modulating SNP loci in five super-populations and twenty-six constituent sub-populations were retrieved from the 1000 Genomes Project (1000 Genomes Project Consortium et al., 2015) via the Ensembl Genome Browser (Hunt et al., 2018). The 1000 Genomes Project reconstructed the genomes of individuals from 26 different populations of various ethnic backgrounds and geographic locations. Seven of these populations are from Africa, four from the admixed Americans, and five populations each from East Asia, Europe, and South Asia. Therefore, based on their geographical origins, the 26 populations are divided into 5 super-populations (as described by the 1000 Genomes Project), namely African (AFR), admixed American (AMR), East Asian (EAS), European (EUR), and South Asian (SAS). SNPs not present in the 1000 Genomes Project reference panel were excluded from further analysis. The correlation of these SNPs with gene expression was collected from the eQTLGen Consortium (Võsa et al., 2018).

Listing COVID-19 comorbidities associated with gene expression-modulating SNPs

Diseases associated with the gene expression-modulating SNPs were obtained from PhenoScanner V2 (Kamat et al., 2019) and DisGeNET v7.0 (Piñero et al., 2020). This list of diseases was matched with the list of known COVID-19 comorbidities enlisted by the Center for Disease Control and Prevention (CDC), USA (https://www.cdc.gov, Accessed: April 12, 2022). Only associations between gene expression-modulating SNPs and COVID-19 comorbidities were considered.

Assessing association with drug response

Any association of the gene expression-modulating SNPs with responses to therapies targeting IL-6, TNF-α, or IL-8, each rs ID was collected from the Pharmacogenomics Knowledgebase (PharmGKB) (Whirl-Carrillo et al., 2012).

Calculating haplotype frequencies and analyzing linkage disequilibrium pattern

Frequencies of haplotypes inferred by gene expression-associated SNPs in *IL6*, *TNFA*, and *IL8* genes in the five super-populations were calculated using the LDhap module of LDlink (Machiela and Chanock, 2015). Linkage disequilibrium patterns among those SNPs in five super-populations were obtained from the LDmatrix module of LDlink.

Statistical analysis

The difference in the variant allele frequencies (ΔVAF), which can be defined as the range of variant allele frequencies VAF (maximum VAF-minimum VAF) among the sub-populations belonging to a particular super-population, was calculated at each SNP locus as a measure of genetic diversity within each super-population. ΔVAF values of five super-populations were compared using the Kruskal-Wallis test followed by pairwise Wilcoxon rank sum test. p-values were adjusted using Holm's method. Allele frequency differences (AFDs) were calculated at each SNP locus to show pairwise comparisons among the super-populations (Berner, 2019). Calculations were conducted with LibreOffice Calc. All statistical analyses were performed in R. Boxplot, and bar plots were generated with the ggplot2 and ggsignif packages in R.

Results

Gene expression-modulating SNPs and their variant allele frequencies

Twenty-four gene expression-modulating variants exist in the *IL6*, *TNFA*, and *IL8* genes. Thirteen, six, and five variants are located in the *IL6*, *TNFA*, and*IL8* genes, respectively. Among these, rs2069835 in *IL6* is absent in the 1000 Genomes Project reference panel. rs1799769 in *TNFA* is an INDEL variant. So, these two variants were excluded, and the remaining twenty-two SNPs were used in further analysis (Table 1 and supplementary Table 1). Five of these SNP loci have three alleles each. Only the variant with the highest frequency at the individual locus was considered in such cases. Correlations between these variant alleles and affected genes are listed in supplementary table 2. The relative distribution of VAFs at these loci in different super-populations is shown in Fig. 1. Nine of these SNPs have VAFs ≥ 0.4 in the European super-population. Variant alleles at these SNP loci also have high frequencies in the admixed American super-population. On the contrary, Africans and East Asians mostly carry the reference alleles at these loci. VAFs at rs1800796 and rs2066992 loci are > 0.7 in the East Asians, although the global VAFs at these loci are close to 0.3 (Table 1 and Supplementary Table 1). The variant allele atrs1800795 is highly prevalent in the European super- population (VAF = 0.416), although it is absent or rare in the East Asian populations (VAF = 0.001) (Table 1 and supplementary table 1). VAF at rs1800797 is also higher in the European super-population (VAF > 0.4) compared to the other super-populations (VAF < 0.2) (Table 1).

TNFA variants exhibit comparatively fewer interpopulation differences (Figure 2). Besides, these SNPs generally are not correlated with a higher risk of many COVID-19 comorbidities (Table 2). Compared to the variant alleles in *IL6* and *TNFA*, the variants in *IL8* have higher VAFs in all except the African super-population). At three SNP loci (rs2227306, rs2227543, and rs1126647), the VAFs in the African super-population are < 0.1, while those in the other super-populations are > 0.25 (Table 1 and supplementary Table 1). On the other hand, the global variant allele (G) at rs2227307 is the major allele (VAF = 0.791) in the African super-population.

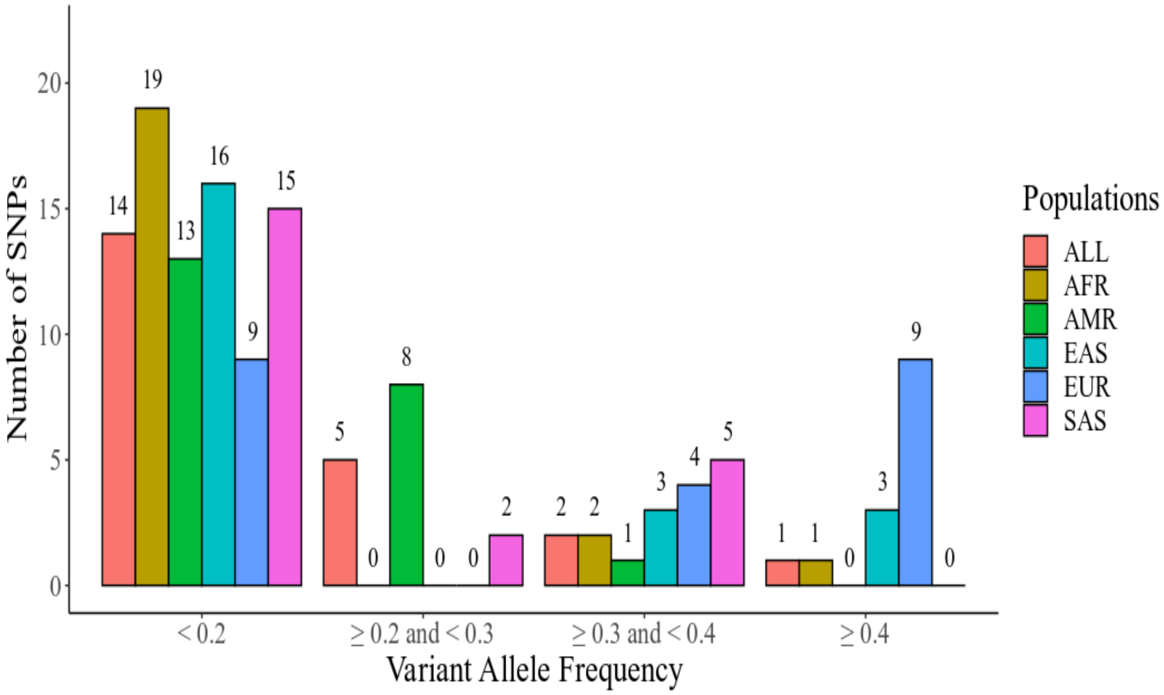

Fig. 1. Distribution of expression-modulating variant allele frequencies of *IL6, TNFA*, and *IL8* genes in different super-populations. ALL = global, AFR = African, AMR = Admixed American, EAS = East Asian, EUR = European, and SAS = South Asian.

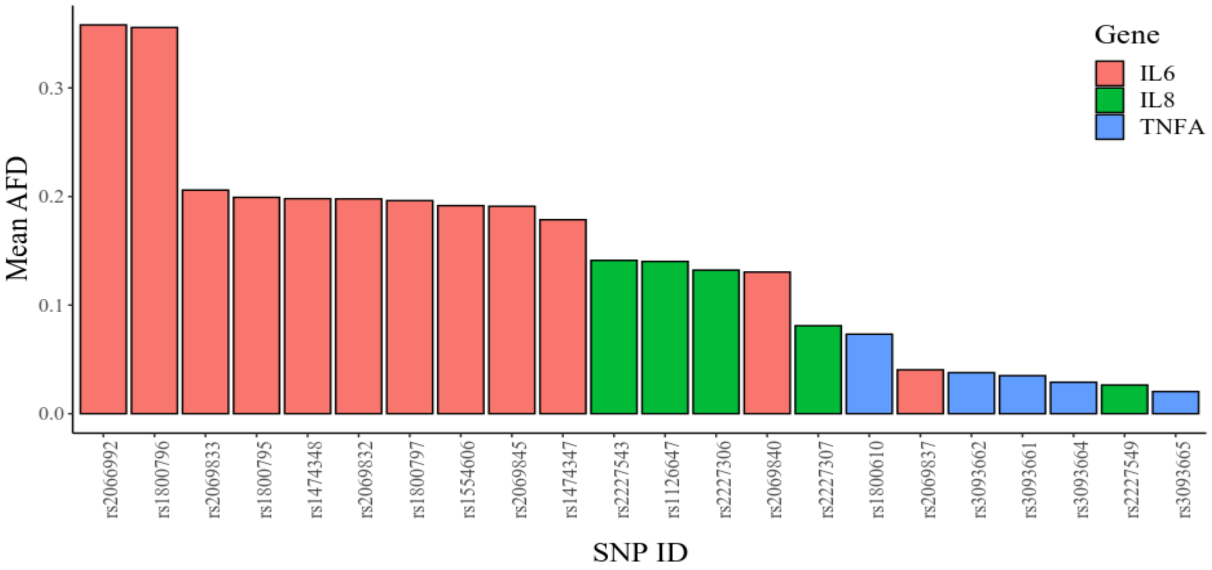

Fig. 2. Mean allele frequency differences (AFD) at each gene expression-associated SNPs in *IL6, TNFA,* and *IL8* across five super-populations.

Table 1. List of gene expression-modulating SNPs in *IL6, TNFA,* and *IL8* alongside their VAFs in five super-populations

Gene	SNP ID	Chromosomal location	Consequence	Reference allele	Variant allele	ALL*	AFR	AMR	EAS	EUR	SAS
IL6	rs1800797	chr7:22726602	Intron	G	A	0.138	0.017	0.184	0.001	0.408	0.134
	rs1800796	chr7:22726627	Intron	G	C	0.314	0.103	0.295	0.791	0.048	0.395
	rs1800795	chr7:22727026	Intron	G	C	0.141	0.018	0.184	0.001	0.416	0.139
	rs2069832	chr7:22727814	Intron	G	A	0.14	0.018	0.187	0.001	0.411	0.134
	rs2069833	chr7:22728045	Intron	T	C	0.14	0.017	0.187	0.001	0.411	0.138
	rs1474348	chr7:22728289	Intron	G	C	0.141	0.017	0.187	0.001	0.411	0.14
	rs2069837	chr7:22728408	Intron	A	G	0.12	0.12	0.081	0.141	0.089	0.156
	rs1474347	chr7:22728505	Intron	C	C	0.168	0.113	0.196	0.007	0.412	0.14
	rs2066992	chr7:22728630	Intron	G	T	0.308	0.085	0.293	0.788	0.048	0.395
	rs2069840	chr7:22728953	Intron	C	G	0.186	0.15	0.262	0.062	0.332	0.155
	rs1554606	chr7:22729088	Intron	T	T	0.249	0.311	0.287	0.009	0.432	0.199
	rs2069845	chr7:22730530	Intron	G	G	0.253	0.317	0.285	0.011	0.433	0.206
TNFA	rs3093661	chr6:31575981	Intron	G	A	0.052	0.03	0.056	0.031	0.048	0.105
	rs1800610	chr6:31576050	Intron	G	A	0.1	0.024	0.183	0.137	0.089	0.119
	rs3093662	chr6:31576412	Intron	A	G	0.08	0.077	0.11	0.031	0.084	0.108
	rs3093664	chr6:31576865	Intron	A	G	0.079	0.084	0.084	0.036	0.083	0.108
	rs3093665	chr6:31577614	3' UTR	A	C	0.019	0.039	0.027	0	0.021	0.003
IL8	rs2227307	chr4:73740952	Intron	T	G	0.424	0.518	0.337	0.414	0.417	0.374
	rs2227549	chr4:73741020	Intron	A	G	0.016	0.005	0.026	0	0.051	0.005
	rs2227306	chr4:73741338	Intron	C	T	0.259	0.097	0.269	0.338	0.388	0.259
	rs2227543	chr4:73742193	3' UTR	C	T	0.289	0.097	0.269	0.383	0.393	0.357
	rs1126647	chr4:73743328	3' UTR	A	T	0.285	0.096	0.265	0.384	0.387	0.349

***All populations (ALL), Africans (AFR), Admixed Americans (AMR), East Asian (EAS), European (EUR), and South Asian (SAS).**

Based on the data from the eQTLGen Consortium, it appears that the variant alleles at rs2066992 and rs1800796 are negatively correlated with the expression of a long non-coding RNA gene- *IL6-AS1* (GRCh38) or *AC073072.5* (GRCh37) (Gene ID: ENSG00000179428) (Supplementary table 2), which encodes an IL-6 antisense RNA, whereas rs2069833, rs1800795, rs1474348, rs2069832, rs1800797, rs1554606, rs2069845, and rs1474347 loci in *IL6* are positively correlated with IL6-AS1 expression.

Genetic diversity and population differentiation

We calculated the AFDs for each possible population pair at each SNP locus to assess genetic diversity and population differentiation. (Supplementary Table 3). We also calculated the mean of these pairwise AFDs at each SNP locus (Figure 3). The mean AFDs at half of the SNPs, *i.e.*, at eleven SNPs, are between 0.1 and 0.2. the values of the mean AFD at rs2066992 and rs1800796 are > 0.3, and at rs2069833 the value is 0.2059. On the opposite end, based on the distribution of ΔVAF values, more within-group variations are present among the admixed American populations than the constituent populations of the other super-populations (Figure 3). The East Asian populations appear to be genetically more uniform, with lower ΔVAF values.

Table 2. Association between gene expression-associated SNPs in three pro-inflammatory cytokine genes (*IL6*, *TNFA* and *IL8*) and COVID-19 comorbidities

Gene	SNP ID	COVID-19 comorbidities											
		Asthma	Cancer	Cystic fibrosis	Diabetes/ Hyperglycemia	Heart conditions	Hypertension	Kidney diseases	Liver disease	Neurological conditions	Obesity/BMI	Pulmonary/ Lung diseases	White blood cell count
IL6	rs1800797	√	√	-	√	√	-	√	√	√	√	-	√
	rs1800796	√	√	-	√	√	-	√	√	√	√	√	√
	rs1800795	√	√	-	√	√	√	√	√	√	√	√	√
	rs2069832	√	√	-	-	-	-	-	-	-	-	-	√
	rs2069833	-	-	-	-	-	-	-	-	-	-	-	-
	rs1474348	√	√	-	-	-	-	-	-	-	-	-	√
	rs2069837	-	√	-	-	-	√	√	-	√	-	√	-
	rs1474347	√	-	-	-	-	-	-	-	-	-	-	√
	rs2066992	-	√	-	-	√	-	-	-	√	-	-	√
	rs2069840	-	√	-	-	√	-	√	-	-	-	-	√
	rs1554606	√	-	-	-	-	-	-	-	-	√	-	√
	rs2069845	√	√	-	-	-	-	-	-	√	-	-	√
TNFA	rs3093661	-	-	-	-	-	-	-	-	-	√	-	√
	rs1800610	-	√	-	√	-	-	-	√	-	-	-	-
	rs3093662	-	-	-	-	-	-	-	-	√	√	√	√
	rs3093664	√	-	-	-	-	-	-	-	-	-	√	-
	rs3093665	-	√	-	-	-	-	-	-	-	-	-	√
IL8	rs2227307	-	√	√	-	-	-	-	-	-	-	√	√
	rs2227549	√	√	-	-	-	-	√	√	-	-	√	-
	rs2227306	-	-	-	-	-	-	-	-	-	-	-	√
	rs2227543	-	-	-	-	-	-	√	-	-	-	-	√
	rs1126647	-	√	-	-	-	√	-	-	√	-	-	√

√ indicates an association between the SNP and the corresponding COVID-19 comorbidity.

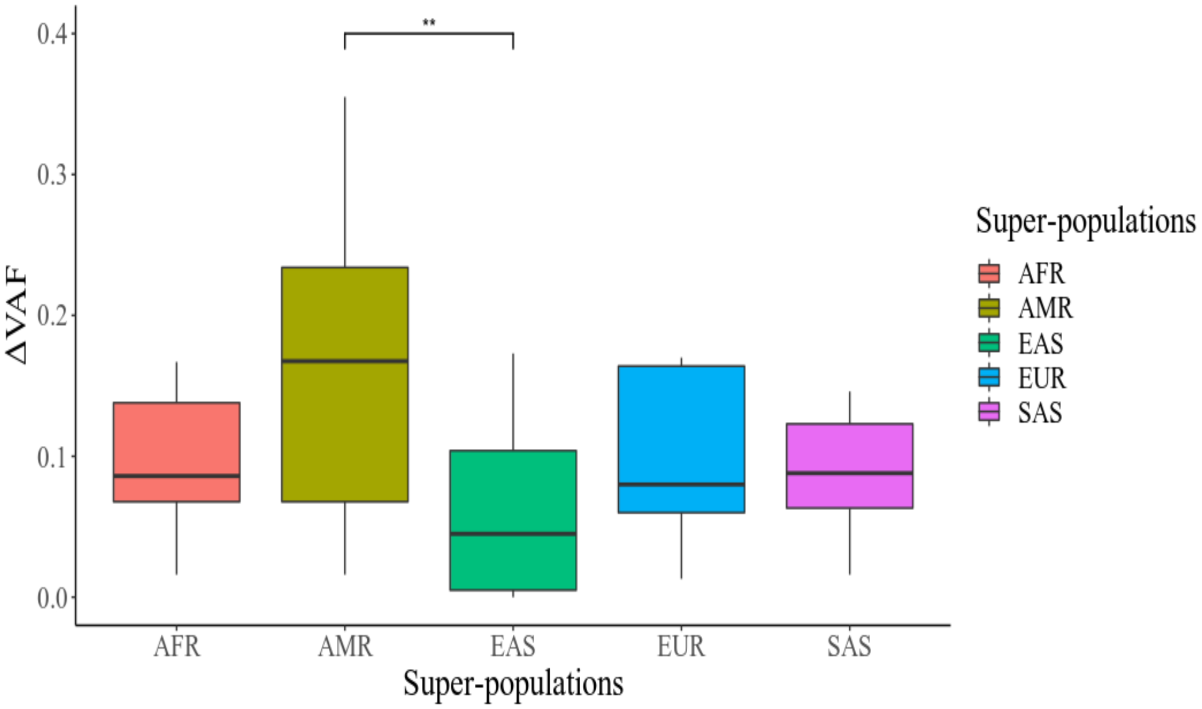

Fig. 3. Variant allele frequencies (ΔVAF) range in different super-populations. ΔVAF values indicate within-population variations. ΔVAFs were compared using the Kruskal-Wallis test and pairwise Wilcoxon rank sum test. p-values were adjusted using Holm's method. AFR = African, AMR = Admixed American, EAS = East Asian, EUR = European, and SAS = South Asian. **p < 0.01.

Disease and drug response associated SNPs

Twenty-one gene expression-associated SNPs correlate with at least two diseases or traits that can increase COVID-19 severity (Table 2). Altogether, these SNPs can modulate susceptibility to twelve COVID-19 comorbidities. Seventeen SNPs are associated with white blood cell count, *i.e.*, possible compromised immunity. SNPs in *IL6*, especially rs1800797, rs1800796, and rs1800795, are associated with more diseases than other SNPs.

Only one of those SNPs (rs1800795 in *IL6*) is associated with drug response. It can influence the efficacy (Level 3 clinical annotation) of TNF-α inhibitors, including adalimumab, etanercept, and infliximab (Dávila-Fajardo et al., 2014; Di Renzo et al., 2012).

Haplotype frequencies and linkage disequilibrium patterns

LD patterns could be illustrated among eleven of the twelve *IL6* SNP loci since one (rs2069833) has more than two alleles (Figure 4). Strong pairwise LD is maintained among rs1800797, rs1800795, rs2069832, and rs1474348; between rs2066992 and rs1800796; and between rs2069845 and rs1554606 in all super-populations. Strong pairwise LD exists among seven SNPs (rs1800797, rs1800795, rs2069832, rs1474348, rs1474347, rs1554606, and rs2069845) only in the European super-population. The highest number of strong pairwise LDs ($R^2 \geq 0.8$) is present in the European super-population. The African super-population has the lowest pairwise LDs with $R^2 \geq 0.8$, followed by the East Asian super-population. Similar LD patterns with $R^2 \geq 0.8$ exist in the admixed American and South Asian super-populations. The haplotype comprising the variant alleles at rs1800797 and rs1800795, and the reference allele at rs1800796, is widespread (0.4086) in the European super-population. Twelve gene expression-modulating SNPs are located in *IL6* (Table 1). Since rs1800797, rs1800796, and rs1800795 in *IL6* are associated with multiple disease conditions, the frequencies of haplotypes comprising these SNPs are shown in Table 3. Haplotype ***A***_G_***C*** contains the variant alleles at rs1800797 and rs1800795. Among all the super-populations, this haplotype is present at the highest frequency (0.408) in the European one (Table 3). Haplotypes comprising variant alleles at rs1800797, rs1800795, rs2069832, rs1474348, rs1474347, rs1554606, and rs2069845 (which has the strongest LD in the European super-population) (***A_C_A_C_C_T_G***) has a frequency of 0.403 in the European super-population. In contrast, its frequency is only 0.134 in the global population (including the European super-population) and much lower, excluding the European super-population (0.067). On the contrary, the frequency of haplotype G_G_G_G_A_G_A, which contains the reference alleles at all of these seven SNP loci, is 0.989 in the East Asian super-population.

Table 3. Haplotypes comprising gene expression-associated SNPs in different super-populations

#	Gene	SNP ID	Haplotype[a]	Populations[b]					
				ALL	**AFR**	**AMR**	**EAS**	**EUR**	**SAS**
1	*IL6*	rs1800797_rs1800796_rs1800795	G_G_G	0.544	0.879	0.517	0.208	0.537	0.461
2			G_***C***_G	0.314	0.103	0.295	0.791	0.048	0.394
3			***A***_G_***C***	0.137	0.017	0.182	0.001	0.408	0.128
4			G_G_***C***	0.004	0.002	0.003	-	0.008	0.010
5			***A***_G_G	0.002	-	0.003	-	-	0.006
6			G_***C_C***	0.000	-	-	-	-	0.001
7	*TNFA*	rs3093661_rs1800610_rs3093662_ rs3093664_rs3093665	G_G_A_A_A	0.811	0.884	0.708	0.827	0.809	0.773
8			G_***A***_A_A_A	0.100	0.024	0.183	0.137	0.090	0.119
9			A_G_***G_G***_A	0.052	0.030	0.056	0.031	0.047	0.105
10			G_G_***G_G_C***	0.019	0.039	0.027	-	0.021	0.003
11			G_G_***G***_A_A	0.009	0.008	0.026	-	0.017	-
12			G_G_A_***G***_A	0.008	0.015	-	0.005	0.016	-
13	*IL8*	rs2227307_rs2227306_rs2227543_rs1126647	T_C_C_A	0.576	0.482	0.663	0.585	0.583	0.626
14			***G_T_T_T***	0.256	0.096	0.265	0.338	0.381	0.252
15			***G***_C_C_A	0.135	0.421	0.068	0.031	0.024	0.017
16			***G***_C_***T_T***	0.029	-	-	0.045	0.005	0.097

variant alleles are written in bold and italic letters

[b]ALL = Global, AFR = African, AMR = Admixed American, EAS = East Asian, EUR = European, SAS = South Asian.

Five gene expression-associated SNPs are located in *TNFA* (Table 1). Haplotype G_G_***G_G_C*** (at rs3093661, rs1800610, rs3093662, rs3093664, and rs3093665 loci, respectively) contains three variant alleles. This haplotype has the highest prevalence (0.0386) in the African super-population. It is, however, not present in the East Asian super-population because the global variant allele (C) at rs3093665 is absent in this super-population (Tables 1 and 3). The haplotype is present at a very low frequency (0.0031) in the South Asian super-population, too, and its frequencies in the admixed American and European super-populations are >0.02. The low VAFs at these loci in the East Asian and South Asian super populations are evident from their similar LD patterns (Figure 5). Strong pairwise LD ($R^2 \geq 0.8$) exists only among rs3093661, rs3093662, and rs3093664 in those two super-populations.

IL8 harbors five gene expression-associated SNPs (Table 1). Frequencies of haplotypes and LD patterns among four of these could be analyzed since one of the SNPs (rs2227549) is not biallelic. The haplotype ***G_T_T_T*** comprising the variant alleles at rs2227307, rs2227306, rs2227543, and rs1126647 loci are present at a high frequency (> 0.25) in all super-populations except the African (0.096). Haplotype ***G***_C_***T_T*** containing the variant alleles at three of the four SNPs is absent in the African and the admixed American super- populations and present at a very low frequency (0.005) in the European super-population. This haplotype is present at a relatively high frequency of (~0.1) in the South Asian super-population. The African super-population has the smallest extent of LD in this connection (Figure 6). In this super-population, rs2227307 does not maintain strong LD with any of the other three SNPs, even though strong LD exists among rs2227306, rs2227543, and rs1126647 (Figure 6). Compared with the African super-population, a larger extent of LD is observed among these four SNPs in the other super-populations. These SNPs have strong LD ($R^2 \geq 0.875$) with each other in the European super-population. A haplotype harboring the variant alleles at these four SNP loci is much less frequent (frequency < 0.1) in the African super-population compared to the other super-populations (frequency > 0.25) (Table 3).

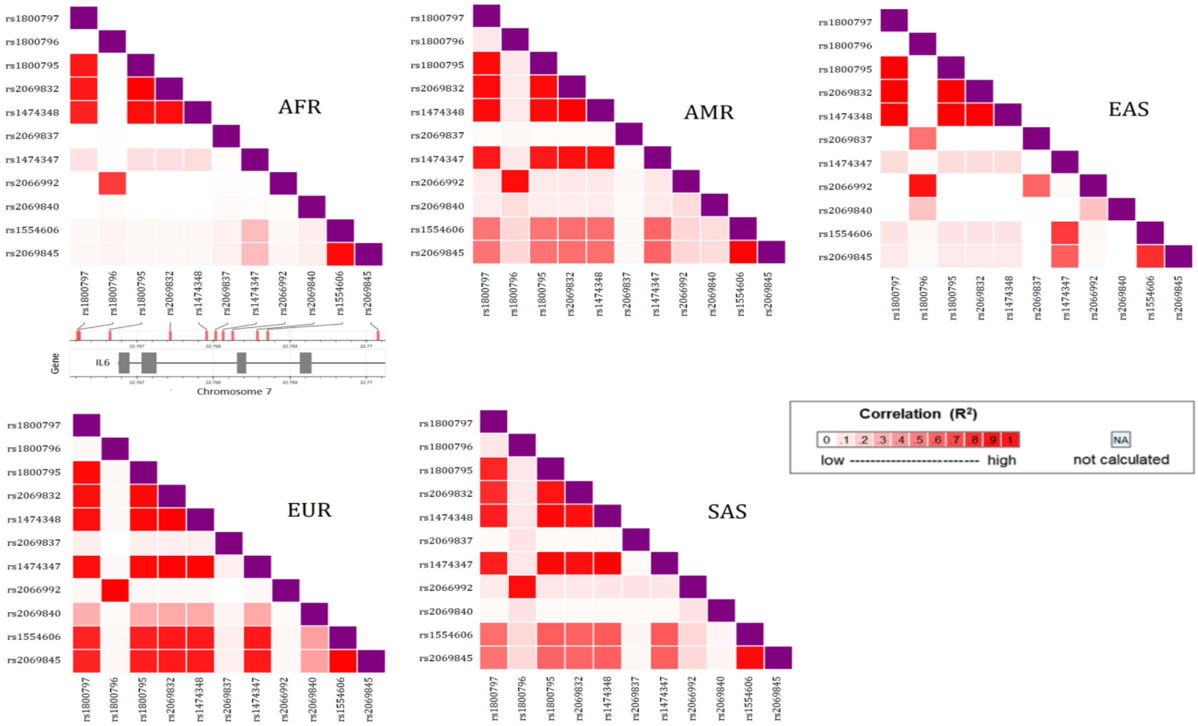

Fig. 4. Linkage disequilibrium (LD) patterns among *IL6* gene expression-associated SNPs in five super-populations. AFR = African, AMR = Admixed American, EAS = East Asian, EUR = European, and SAS = South Asian.

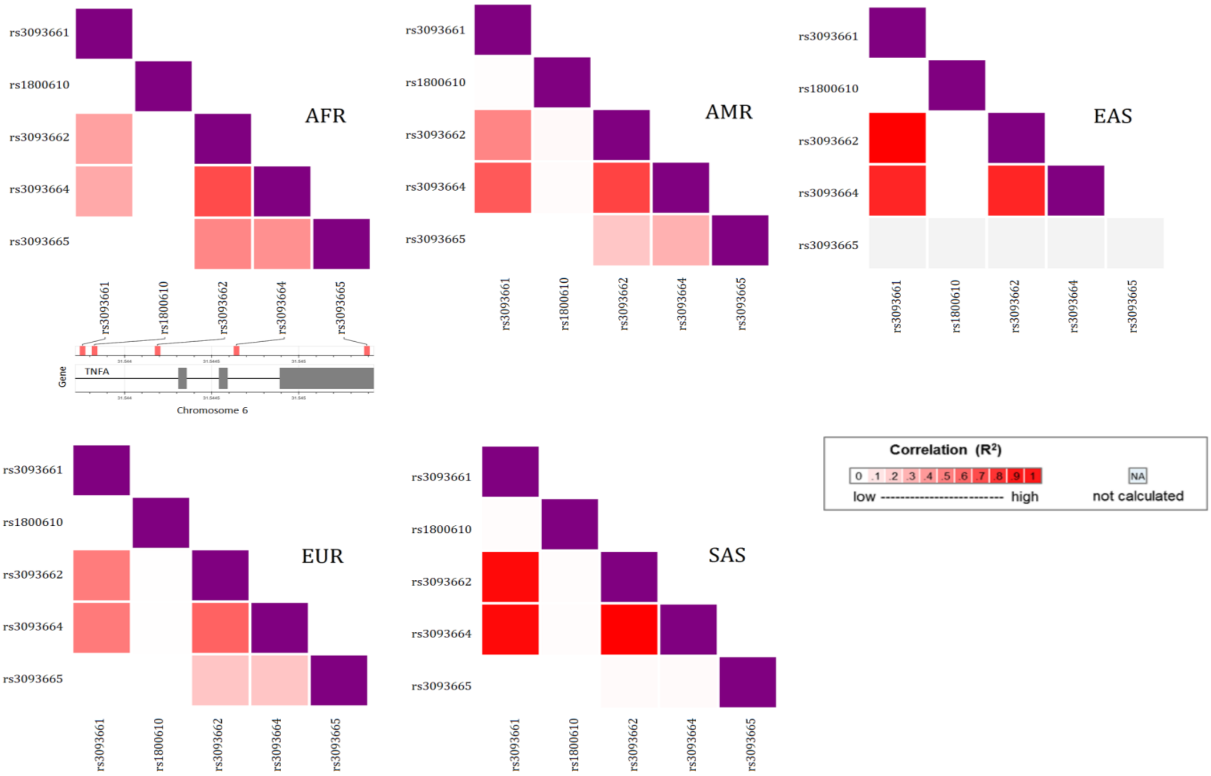

Fig. 5. Linkage disequilibrium (LD) patterns among *TNFA* gene expression-associated SNPs in five super-populations. AFR = African, AMR = Admixed American, EAS = East Asian, EUR = European, and SAS = South Asian.

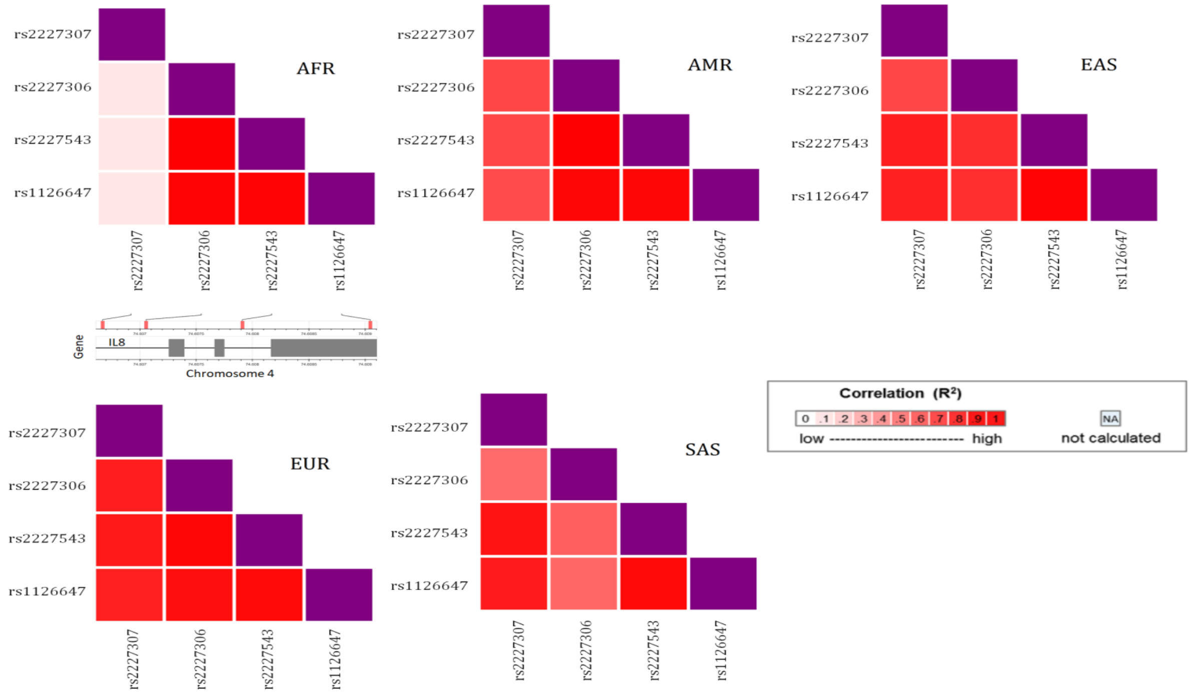

Fig. 6. Linkage disequilibrium (LD) patterns among *IL8* gene expression-associated SNPs in five super-populations. AFR = African, AMR = Admixed American, EAS = East Asian, EUR = European and SAS = South Asian

Discussion

There are substantial interethnic differences in gene expression-associated variant allele frequencies and linkage disequilibrium patterns in *IL6*, *TNFA*, and *IL8*. Since these variants are associated with susceptibilities to COVID-19 comorbidities, differences in allelic distribution might contribute to the interethnic variability in COVID-19 severity and mortality. In addition, these SNPs may be linked to dissimilarities in responses to therapies that target these cytokines.

Interethnic differences in pro-inflammatory cytokine expression

The picture the available literature provides concerning interethnic differences in IL-6 levels is not indubitable. A previous study reported that the differential distribution of alleles of cytokine genes in African American women, in contrast to American women with European ancestry, consistently up-regulates inflammation (Ness et al., 2004), which is consistent with almost 2.5 times higher number of age-adjusted COVID-19-related deaths in African-Americans (Wrigley-Field, 2020). Another study found significantly higher plasma levels of IL-6 in non-Hispanic blacks than Mexican Americans and non-Hispanic whites (Stowe et al., 2010). However, a more recent study could not find any significant difference in the plasma levels of IL-6 between African American and European American women (Yao et al., 2018). A comparison among Japanese, African American, and Caucasians showed that Japanese individuals had the lowest level of IL-6, and African Americans had the highest level of this pro-inflammatory cytokine (Coe et al., 2011). We could not find comparative studies on cytokine profiles incorporating South Asian populations.

Some SNPs at the *IL6* gene also correlate with the expression of the lncRNA *IL6-AS1* gene (supplementary table 2). The variant allele at rs2069833, rs1800795, rs1474348, rs2069832, rs1800797, rs1554606, rs2069845, and rs1474347 loci in *IL6* positively correlates with the expression of the lncRNA IL-6 antisense RNA. On the other hand, variant alleles at rs1800796 and rs2066992 loci are negatively correlated with IL6-AS1 as well as IL-6 expression. IL6-AS1 lncRNA has been found to be up-regulated in airway inflammation, which further promotes the expression of IL-6 by recruiting EBF1 and modulating histone methylation in the IL-6 promoter region. This lncRNA also acts as a competitive inhibitor of miR-149-5p and up-regulates IL-6 expression in the cytoplasm. The expression of IL-8 is also regulated by the IL6-AS1 lncRNA (Yi et al., 2021). An important question may be whether the interethnic variability in *IL6-AS1* expression correlates with differences in IL-6 levels and COVID-19 severities across the globe. Very little information is available regarding this regulatory RNA. A study on Chinese COVID-19 patients included the common Asian IL-6 haplotype defined by the rs1800796, rs1524107, and rs2066992 loci. They found that homozygous carriers of the C-T-T variant haplotype were less likely to develop severe COVID-19. The protective effect resulted from the disturbance of stimulus-dependent bidirectional transcription of the *IL-6/IL-6-AS1* locus through disruption of a conserved CTCF-binding locus at the enhancer elements of *IL-6-AS1*(Chen et al., 2021). In another study conducted on COVID-19 patients in the USA, the variant allele at rs1800795 was found to affect plasma IL-6 levels and confer higher expression levels of IL6-AS1. This allele may be a risk locus for higher mortality and earlier intervention in severe COVID-19 patients if confirmed with further replicative studies (Smieszek et al., 2021). Data from an NCBI BioProject (PRJEB4337) suggests that this gene is expressed in a variety of organs, including, but not limited to, the esophagus, lung, heart, liver, kidney, and small intestine (Fagerberg et al., 2014). These organs are susceptible to damage upon SARS-CoV-2 infection (Jain, 2020; Ma et al., 2020). Alterations in IL6-AS1 expression may thus have important clinical implications with respect to COVID-19.

Conflicting reports regarding differences in IL-6 levels exist for individual SNPs. For example, there are contradictory reports regarding the association between elevated levels of IL-6 and genotypes at rs1800795, rs1800796, and rs1800797 (Ambreen et al., 2015; Fang et al., 2017; Guan et al., 2020; Koh et al., 2009; Li et al., 2016; Siniauskaya et al., 2020; Zakharyan et al., 2012; Zhang et al., 2016). These reports are indicative of a complicated regulation of *IL6* expression. A better understanding of the role of this lncRNA can shed more light on the pathogenesis of COVID-19. Further studies are needed to elucidate how this particular lncRNA plays a role in the outcome of COVID-19.

Almost all East Asians carry an *IL6* haplotype comprising rs1800797, rs1800795, rs2069832, rs1474348, rs1474347, rs1554606, and rs2069845 reference alleles, whereas Europeans carry haplotypes containing variant alleles at a disproportionately high frequency. Haplotype #1 in Table 3 consists of the reference alleles at the three SNP loci of the *IL6* gene. Despite the conflicting evidence of the relationship between genotype and IL6 level, the SNPs (rs1800797_rs1800796_ rs1800795) have evidence of higher serum IL6 levels in the presence of their G alleles. This G_G_G haplotype has a low frequency in the East Asian super-population compared to the others. Haplotype #3, which has two variant alleles at rs1800797 and rs1800795, is highly frequent (frequency 0.408) in the European super-population, whereas in other super-populations its frequency (0.13) is much lower. Many studies have reported the association of various *IL6* haplotypes, including variant alleles of rs1800797, rs1800796, and rs1800795, with diseases such as type 2 diabetes mellitus (Saxena et al., 2014), renal dysfunction (Ng et al., 2008), obesity (Boeta-Lopez et al., 2017), asthma (Lajunen et al., 2018), etc., all of which are COVID-19 comorbidities. Additionally, these promoter polymorphisms are associated with various cancer risks and prognoses, such as cervical cancer, colorectal cancer, breast cancer, prostate cancer, lung cancer, glioma, non-Hodgkin's lymphoma, Hodgkin's lymphoma, B-cell lymphoma, and diffuse large B-cell lymphoma (Peng et al., 2018).

Regarding *TNFA* expression, the variant alleles at rs3093661, rs1800610, rs3093662, and rs3093664 may be associated with elevated plasma levels of TNF-α (Zhang et al., 2020). Although VAFs at these SNP loci are < 0.2 in all super-populations, VAF at rs1800610 is > 0.2 in two admixed American populations (MXL and PEL) (Table 1). A previous study found a higher circulating TNF-α level in non-obese, non-diabetic Mexican Americans than non-Hispanic white adults (Ho et al., 2005). In addition, the strong LD maintained among rs3093661, rs3093662, and rs3093664 in the East Asian and South Asian super-populations could be interesting (Figure 5). These three SNPs are associated with the expression of multiple immune response genes such as *HLA-B*, *HLA-C*, *HLA-DRB5*, *HLA-DRB6*, *MICA*, *MICB*, *LST1*, *LTB*, and *LTA*, among others (Supplementary Table 2). Inflammatory conditions can induce the expression of *HLA* and *MICA*. Because of the interdependent nature of these genes, polymorphisms at the promoter of one gene can affect the expression of others (Jarduli et al., 2013). *HLA* variants may be associated with COVID-19 severity and likely explain some of the differences in the outcome of SARS-CoV-2 infections (Lorente et al., 2021; Tavasolian et al., 2021; Troshina et al., 2020). Hence, inter-ethnic differences in the expression level of *HLA* genes may contribute to variations in COVID-19 severity across ethnic groups. Variant alleles at rs3093661, rs3093662, and rs3093664 are negatively correlated with *MICA* expression level and positively correlated with *HLA-B* expression level (Supplementary Table 2). The variant allele at rs3093664 and the variant alleles at rs3093661 and rs3093662 are negatively correlated with *HLA-DRB5* and *HLA-DRB6* expressions, respectively.

Cells carrying the T_C haplotype at rs2227307 and rs2227306 significantly up-regulate the IL-8 expression at both transcriptional and translational levels (Benakanakere et al., 2016). Carriers of the T_C haplotype (#13 in Table 3) may have an increased influx of neutrophils in inflammatory lesions and can influence disease susceptibility

(Benakanakere et al., 2016). Variant alleles at these SNPs are positively correlated with *IL8* expression (Võsa et al., 2018). Although a previous study found African Americans to have a higher plasma level of IL-8 compared to Caucasians, the IL-8 mRNA level was not significantly different between those two groups (Mayr et al., 2007). This study, however, did not consider other variables such as body mass index, alcohol intake, smoking status, etc., which can influence IL-8 levels as well (Huang et al., 1999; Straczkowski et al., 2002; Wu et al., 2014).

Variant alleles at rs2227307, rs2227306, rs2227543, and rs1126647 are also positively correlated with the expression of three other chemokine genes, namely *CXCL1*, *CXCL2*, and *CXCL6* (Supplementary Table 2). CXCL1 and CXCL5 have neutrophil chemotactic activity (Wuyts et al., 1999). CXCL6 has neutrophil granulocyte chemotactic and antibacterial properties (Linge et al., 2008; Proost et al., 1993). These three chemokines are up-regulated in COVID-19 patients (Chu et al., 2020; Xiong et al., 2020). Therefore, rs2227307, rs2227306, rs2227543, and rs1126647 may contribute to the differences in COVID-19 severity across ethnic groups.

Regarding ΔVAF values, the East Asian populations show more genetic homogeneity, whereas the admixed American populations exhibit more genetic heterogeneity than the other population groups (Figure 2). This observation agrees with previous findings (Auton et al., 2009; Oota et al., 2002). Gene flow among the East Asian populations has decreased population differentiation and made these groups more homogeneous (Pan et al., 2020). Conversely, the high heterogeneity among the admixed American populations could be due to the admixture of genetic components from multiple ethnic origins (Montinaro et al., 2015). An intriguing observation of this study is the apparent low heterogeneity of the African populations at these SNP loci, even though Africa is a source of high genetic diversity (Campbell and Tishkoff, 2008; Rotimi et al., 2017).

Interethnic differences in susceptibility to COVID-19 comorbidities

Twenty-one of the studied SNPs are associated with at least two COVID-19 comorbidities (Table 2). Among the *IL6* variants, rs1800797, rs1800796, and rs1800795 are associated with most comorbidities, *e.g.*, asthma, cancer, diabetes, heart conditions, kidney disease, liver disease, neurological conditions, and obesity. Although the association of severe asthma and inflammation with elevated levels of IL-6 is already proven (Broide et al., 1992; Wong et al., 2001), one study also established that systemic IL-6-mediated inflammation, commonly occurring in obese patients, can worsen the severity of asthma (Peters et al., 2016). A high serum level of IL-6 is also associated with various cancers, including breast cancer (Knüpfer and Preiss, 2007; Kozłowski et al., 2003), colon and gastric cancer (Jones and Jenkins, 2018), ovarian cancer (Lane et al., 2011), etc. A higher IL-6 level may be associated with diabetes and its associated complications, like kidney disease and cardiovascular disease (Liu et al., 2006; Mihara et al., 1998; Shoily et al., 2021). Similarly, as IL-6 has a role in the physiological homeostasis of neural tissue, its overexpression and, consequently, the inflammatory condition lead to neurological damage, leading to many neuropathological changes and neurodegenerative diseases (Aarli, 2003; Rothaug et al., 2016).

It should be noted that variant-disease associations in this context are quite complex. First, there are some contradictory findings regarding such an association. For example, one meta-analysis did not find rs1800797 to be a risk factor for cancer (Qian et al., 2017). In contrast, another meta-analysis reported that rs1800797 is associated with a higher risk of cancer in Caucasians (Peng et al., 2018). Second, the association between SNP and a particular disease may depend on ethnicity. For example, rs1800795 and rs1800796 are associated with an elevated risk of cancer in Caucasians and Asians, but rs1800797 increases the risk of cancer only in Caucasians (Peng et al., 2018). Third, different alleles at the same SNP locus can increase the risk of diseases. For example, the rs1800797 G allele (reference allele) may be associated with adult-onset asthma (Hamid et al., 2005). Conversely, rs1800797 A allele (variant allele) may be associated with major depressive disorder (Zhang et al., 2016). Nonetheless, based on the available resources and information, our study indicates that gene expression-modulating SNPs in *IL6* may contribute to interethnic differences in disease susceptibility.

Seventeen SNPs in this study are associated with white blood cell count (Table 2). Altered leukocyte counts, such as neutrophilia and lymphocytopenia, are important risk factors for COVID-19 mortality (Zhao et al., 2020). An abnormal elevation of IL-8 is possibly associated with COVID-19-induced neutrophilia (Coperchini et al., 2021). The crucial roles of TNF-α and IL-6 in neutrophil trafficking are known (Hashizume et al., 2011; Vieira et al., 2009). Severe COVID-19 patients (including those admitted to the ICU) have a rising neutrophil count and a falling lymphocyte count, accounting for a higher neutrophil-to-lymphocyte ratio (NLR) – a biomarker suggesting poor prognosis in COVID-19 (Borges et al., 2020). However, during the assessment of interethnic differences in leukocyte counts, it should be considered that individuals of African, Middle Eastern, and West Indian descent can have chronic neutropenia (Atallah-Yunes et al., 2019). This condition, known as benign ethnic neutropenia (BEN), does not increase the risk of infection (Atallah-Yunes et al., 2019).

Variability in drug response

We also investigated whether the genotype at any of the twenty-two SNP loci is correlated with altered response to therapies targeting IL-6, TNF-α, or IL-8. Rheumatoid arthritis patients with the *IL6* rs1800795 G allele may show an increased response to anti-TNF therapeutic antibodies, namely adalimumab, etanercept, and infliximab (Dávila-Fajardo et al., 2014). In contrast, psoriasis patients carrying rs1800795 G alleles may respond poorly to TNF-α blockers (Di Renzo et al., 2012). Anti-IL-6 inhibitors may not be a treatment option for all severe COVID-19 patients, even though IL-6 plays an essential role in the pathophysiology of disease progression. The differences in response may account for genetic variants and plasma IL-6 levels. As observed in trials conducted on Chinese (rs1800796 negatively associated with IL6-AS1 expression) and USA (rs1800795 positively associated with IL6-AS1 expression) COVID-19 patients, anti-IL-6 monoclonal antibodies such as tocilizumab and sarilumab may show improvement in response in some while failing in others (Chen et al., 2021; Smieszek et al., 2021). Several recent studies reported that immunosuppressant medications used to treat some autoimmune diseases may have a positive therapeutic effect in severe COVID-19 patients (Esmaeilzadeh and Elahi, 2021). Due to similarities in the cytokine response and damage of autoimmune diseases and COVID-19, the polymorphisms that affect autoimmune conditions might affect COVID-19 severity, too (Liu et al., 2021). High serum IL-6, IL-8, and TNF-α levels at the time of admission to the hospital are predictors of poor outcomes in COVID-19 patients (Del Valle et al., 2020). Again, patients who died of COVID-19 had significantly higher levels of the IL-2 receptor, IL-6, IL-8, IL-10, and TNF-α than those who recovered (Chen et al., 2020).

Similarly, between intensive care unit (ICU) and non-ICU patients, levels of pro-inflammatory cytokines were higher in those admitted to ICUs (Huang et al., 2020), suggesting increased cytokine mediated complications. Therefore, there is much evidence as to why anti-IL6, anti-IL8, and anti-TNF-α therapy could treat COVID-19 (Robinson et al., 2020). Hence, the polymorphisms that could interfere with the therapy should be given proper attention.

Context of our findings

Most of the data concerning differences in COVID-19 outcomes among individuals of different ethnic origins comes from studies on the US and UK populations, and there is a paucity of data regarding this issue from other regions of the world (Pan et al., 2020;Vahidy et al., 2020). Although ethnic minorities in these countries (such as blacks, Asians, and Hispanics, among others) are more susceptible to

COVID-19, it is still unclear if a certain ethnicity can be an independent poor prognostic factor for this disease (Burki, 2021; Pennington et al., 2020; Raharja et al., 2021). The higher burden of COVID-19 comorbidities and lower socio-economic status of these ethnic groups compared with individuals of European origin may explain these observed disparities in COVID-19 outcomes (Kopel et al., 2020). However, these disparities may still exist after adjusting for sociodemographic and comorbidity factors (Vahidy et al., 2020). Therefore, it is possible that genetic differences among ethnic groups can contribute to the differences in COVID-19 severity.

We acknowledge that associations between the SNPs included in our study and the expression levels of *IL6, TNFA,* and *IL8* upon SARS-CoV-2 infection must be elucidated before the role of these polymorphisms in COVID-19 severity can be confirmed. We also acknowledge that socio-economic factors may, directly and indirectly, play a bigger role in ethnic disparities in COVID-19 outcomes than genetic polymorphisms. However, our findings hint at the crucial roles played by differences in allele frequencies and LD patterns of gene expression-associated polymorphisms in pro-inflammatory cytokine genes in creating distinct COVID-19 outcomes across ethnic groups.

Conclusions

Gene expression-associated SNPs in *IL6*, *TNFA*, and *IL8* genes can influence the expression levels of multiple immune response mediators, modulate susceptibility to several COVID-19 comorbidities, and alter responses to COVID-19 therapy. Inter-ethnic differences in the genetic architecture of these SNPs can thus contribute to ethnic disparities in COVID-19 outcomes. However, due to the complex nature of cytokine expression and signaling regulation, conflicting reports regarding the effects of genotypes at these SNPs exist. Nevertheless, understanding the variations in the genetic architecture of gene expression-associated polymorphisms of cytokine genes across ethnic groups can, at least to some extent, explain differences in COVID-19 susceptibility and therapeutic outcomes.

Abbreviations

ACE2: Angiotensin-converting enzyme 2; AFDs: Allele frequency differences; COVID-19: Coronavirus disease 2019; eQTLs: Expression quantitative trait loci; INDEL: Insertion or deletion; IL-6: Interleukin-6, IL-8: Iinterleukin-8; LD: Linkage disequilibrium; SNP: Single nucleotide polymorphism; TNFA: Tumor necrosis factor alpha; VAF: variant allele frequencies.

Ethics approval and consent to participate

This study did not involve human or animal participants, so neither ethical approval nor consent is required.

Consent for publication

This study did not involve human participants, and no consent is required. All authors have read and approved the manuscript.

Availability of data and material

All data are provided in the manuscript.

Conflict of interest

There is no known conflict of interest.

Authors' contributions

TA,AAS- study design, TA, SSS, KF, ZH- data analysis, SSS, TA, KF, ZH- manuscript preparation, AAS- reviewed the manuscript. All authors have read and approved the manuscript.

References

1000 Genomes Project Consortium, Auton A, Brooks LD, Durbin RM, Garrison EP, Kang HM, Korbel JO, Marchini JL, McCarthy S, McVean GA and Abecasis GR. A global reference for human genetic variation. *Nature* 2015; 526(7571): 68-74.

Aarli JA. Role of cytokines in neurological disorders. *Curr. Med. Chem*. 2003; 10(19): 1931-1937.

Ambreen F, Ismail M and Qureshi IZ. Association of gene polymorphism with serum levels of inflammatory and angiogenic factors in Pakistani patients with age-related macular degeneration. *Mol. Vis*. 2015; 21: 985-999.

Atallah-Yunes SA, Ready A and Newburger PE. Benign ethnic neutropenia. *Blood Rev*. 2019; 37: 100586.

Auton A, Bryc K, Boyko AR, Lohmueller KE, Novembre J, Reynolds A, Indap A, Wright MH, Degenhardt JD, Gutenkunst RN, King KS, Nelson MR and Bustamante CD. Global distribution of genomic diversity underscores rich complex history of continental human populations. *Genome Res*. 2009; 19(5): 795-803.

Bajgain KT, Badal S, Bajgain BB and Santana MJ. Prevalence of comorbidities among individuals with COVID-19: A rapid review of current literature. *Am. J. Infect. Control.* 2021;49(2): 238-246.

Benakanakere MR, Finoti LS, Tanaka U, Grant GR, Scarel-Caminaga RM and Kinane DF. Investigation of the functional role of human Interleukin-8 gene haplotypes by CRISPR/Cas9 mediated genome editing. *Sci. Rep*. 2016;6: 31180.

Berner D. Allele Frequency Difference AFD–An intuitive alternative to F_{ST} for quantifying genetic population differentiation. *Genes (Basel)* 2019;10(4): 308.

Boeta-Lopez K, Duran J, Elizondo D, Gonzales E, Rentfro A, Schwarzbach AE and Nair S. Association of interleukin-6 polymorphisms with obesity or metabolic traits in young Mexican-Americans. *Obes Sci Pract*. 2017; 4(1): 85-96.

Borges L, Pithon-Curi TC, Curi R and Hatanaka E. COVID-19 and neutrophils: the relationship between hyperinflammation and neutrophil extracellular traps. *Mediat. Inflamm*. 2020; 2020: 8829674.

Broide DH, Lotz M, Cuomo AJ, Coburn DA, Federman EC and Wasserman SI. Cytokines in symptomatic asthma airways. *J Allergy Clin Immunol.* 1992; 89(5): 958-967.

Burki T. COVID-19 among American Indians and Alaska Natives. *Lancet Infect. Dis*. 2021; 21(3): 325-326.

Campbell MC and Tishkoff SA. African genetic diversity: implications for human demographic history, modern human origins, and complex disease mapping. *Annu. Rev. Genomics Hum. Genet.* 2008; 9: 403-433.

Castelnovo L, Tamburello A, Lurati A, Zaccara E, Marrazza MG, Olivetti M, Mumoli N, Mastroiacovo D, Colombo D, Ricchiuti E, Vigano' P, Paola F and Mazzone A. Anti-IL6 treatment of serious COVID-19 disease: A monocentric retrospective experience. *Medicine (Baltimore)* 2021; 100(1): e23582.

Cesta MC, Zippoli M, Marsiglia C, Gavioli EM, Mantelli F, Allegretti M and Balk RA. The Role of Interleukin-8 in Lung Inflammation and Injury: Implications for the Management of COVID-19 and Hyperinflammatory Acute Respiratory Distress Syndrome. *Front. Pharmacol.* 2022; 12: 808797.

Cevik M, Kuppalli K, Kindrachuk J and Peiris M. Virology, transmission, and pathogenesis of SARS-CoV-2. *BMJ* 2020; 371: m3862.

Chen T, Lin YX, Zha Y, Sun Y, Tian J, Yang Z, Lin SW, Yu F, Chen ZS, Kuang BH, Lei JJ, Nie YJ, Xu Y, Tian DB, Li YZ, Yang B, Xu Q, Yang L, Zhong N and Zheng M. A low-producing haplotype of interleukin-6 disrupting CTCF binding is protective against severe COVID-19. *mBio* 2021; 12(5): e0137221.

Chen T, Wu D, Chen H, Yan W, Yang D, Chen G, Ma K, Xu D, Yu H, Wang H, Wang T, Guo W, Chen J, Ding C, Zhang X, Huang J, Han M, Li S, Luo X and Zhao J. Clinical characteristics of 113 deceased patients with coronavirus disease 2019: retrospective study. *BMJ* 2020; 368: m1091.

Chu H, Chan JF, Wang Y, Yuen TT, Chai Y, Hou Y, Shuai H, Yang D, Hu B, Huang X, Zhang X, Cai JP, Zhou J, Yuan S, Kok KH, To KK, Chan IH, Zhang AJ, Sit KY and Au WK. Comparative replication and immune activation profiles of SARS-CoV-2 and SARS-CoV in human lungs: An ex vivo study with implications for the pathogenesis of COVID-19. *Clin. Infect. Dis*. 2020; 71(6): 1400-1409.

Coe CL, Love GD, Karasawa M, Kawakami N, Kitayama S, Markus HR, Tracy RP and Ryff CD. Population differences in pro-inflammatory biology: Japanese have healthier profiles than Americans. *Brain Behav. Immun*. 2011; 25(3): 494-502.

Coperchini F, Chiovato L, Ricci G, Croce L, Magri F and Rotondi M. The cytokine storm in COVID-19: Further advances in our understanding the role of specific chemokines involved. *Cytokine Growth Factor Rev.* 2021; 58: 82-91.

Dávila-Fajardo CL, Márquez A, Pascual-Salcedo D, Moreno Ramos MJ, García-Portales R, Magro C, Alegre-Sancho JJ, Balsa A, Cabeza-Barrera J, Raya E and Martín J. Confirmation of -174G/C interleukin-6 gene promoter polymorphism as a genetic marker predicting antitumor necrosis factor treatment outcome. *Pharmacogenet Genom.*2014; 24(1): 1-5.

Del Valle DM, Kim-Schulze S, Huang HH, Beckmann ND, Nirenberg S, Wang B, Lavin Y, Swartz TH, Madduri D, Stock A, Marron TU, Xie H, Patel M, Tuballes K, Van Oekelen O, Rahman A, Kovatch P, Aberg JA, Schadt E and Jagannath S. An inflammatory cytokine signature predicts COVID-19 severity and survival. *Nat. Med.* 2020; 26(10): 1636-1643.

Di Renzo L, Bianchi A, Saraceno R, Calabrese V, Cornelius C, Iacopino L, Chimenti S and De Lorenzo A. -174G/C IL-6 gene promoter polymorphism predicts therapeutic response to TNF-α blockers. *Pharmacogenet. Genom.* 2012; 22(2):134-142.

Du P, Geng J, Wang F, Chen X, Huang Z and Wang Y. Role of IL-6 inhibitor in treatment of COVID-19-related cytokine release syndrome. *Int. J. Med. Sci.* 2021; 18(6):1356-1362.

El-Khatib Z, Jacobs GB, Ikomey GM and Neogi U. The disproportionate effect of COVID-19 mortality on ethnic minorities: Genetics or health inequalities?*EClinicalMedicine*2020;23: 100430.

Enevold C, Baslund B, Linde L, Josephsen NL, Tarp U, Lindegaard H, Jacobsen S and Nielsen CH. Interleukin-6-receptorpolymorphisms rs12083537, rs2228145, and rs4329505 as predictors of response to tocilizumab in rheumatoid arthritis. *Pharmacogenet. Genom.* 2014; 24(8): 401-405.

Esmaeilzadeh A and Elahi R. Immunobiology and immunotherapy of COVID-19: A clinically updated overview. *J. Cell Physiol.* 2021; 236(4): 2519-2543.

Fagerberg L, Hallström BM, Oksvold P, Kampf C, Djureinovic D, Odeberg J, Habuka M, Tahmasebpoor S, Danielsson A, Edlund K, Asplund A, Sjöstedt E, Lundberg E, Szigyarto CA, Skogs M, Takanen JO, Berling H, Tegel H, Mulder J and Nilsson P. Analysis of the human tissue-specific expression by genome-wide integration of transcriptomics and antibody-based proteomics. *Mol. Cell Proteomics.* 2014; 13(2):397-406.

Fajgenbaum DC and June CH. Cytokine storm. *N. Engl. J. Med*. 2020; 383(23):2255-2273.

Fang M, Huang Y, Zhang Y, Ning Z, Zhu L and Li X. Interleukin-6 -572C/G polymorphism is associated with serum interleukin-6 levels and risk of idiopathic pulmonary arterial hypertension. *J. Am. Soc. Hypertens.* 2017; 11(3): 171-177.

Gasparello J, Finotti A and Gambari R. Tackling the COVID-19 "cytokine storm" with microRNA mimics directly targeting the 3'UTR of pro-inflammatory mRNAs. *Med. Hypotheses*, 2021; 146: 110415.

Guan Y, Wang S, Wang J, Meng D, Wu H, Wei Q and Jiang H. Gene polymorphisms and expression levels of interleukin-6 and interleukin-10 in lumbar disc disease: a meta-analysis and immunohistochemical study. *J. Orthop. Surg. Res.* 2020;15(1):54.

Hamid YH, Rose CS, Urhammer SA, Glümer C, Nolsøe R, Kristiansen OP, Mandrup-Poulsen T, Borch-Johnsen K, Jorgensen T, Hansen T and Pedersen O. Variations of the interleukin-6 promoter are associated with features of the metabolic syndrome in Caucasian Danes. *Diabetologia* 2005; 48(2): 251-260.

Hashizume M, Higuchi Y, Uchiyama Y and Mihara M. IL-6 plays an essential role in neutrophilia under inflammation. *Cytokine* 2011; 54(1): 92-99.

Hassan MI, Aschner Y, Manning CH, Xu J and Aschner JL. Racial differences in selected cytokine allelic and genotypic frequencies among healthy, pregnant women in North Carolina. *Cytokine* 2003; 21(1):10-16.

Ho RC, Davy KP, Hickey MS and Melby CL. Circulating tumor necrosis factor alpha is higher in non-obese, non-diabetic Mexican Americans compared to non-Hispanic white adults. *Cytokine* 2005; 30(1):14-21.

Hojyo S, Uchida M, Tanaka K, Hasebe R, Tanaka Y, Murakami M and Hirano T. How COVID-19 induces cytokine storm with high mortality. *Inflamm Regen*. 2020; 40: 37.

Hu B, Guo H, Zhou P and Shi ZL. Characteristics of SARS-CoV-2 and COVID-19. *Nat. Rev. Microbiol.* 2021; 19(3): 141-154.

Huang C, Wang Y, Li X, Ren L, Zhao J, Hu Y, Zhang L, Fan G, Xu J, Gu X, Cheng Z, Yu T, Xia J, Wei Y, Wu W, Xie X, Yin W, Li H, Liu M and Xiao Y. Clinical features of patients infected with 2019 novel coronavirus in Wuhan, China. *Lancet* 2020; 395(10223):497-506.

Huang YS, Wu JC, Chang FY and Lee SD. Interleukin-8 and alcoholic liver disease. *Zhonghua Yi Xue Za Zhi (Taipei)* 1999; 62(7): 395-401.

Hunt SE, McLaren W, Gil L, Thormann A, Schuilenburg H, Sheppard D, Parton A, Armean IM, Trevanion SJ, Flicek P and Cunningham F.

Ensembl variation resources. *Database (Oxford)* 2018;2018:bay119.

Hussen J, Kandeel M, Hemida MG andAl-Mubarak AIA. Antibody-based immunotherapeutic strategies for COVID-19. *Pathogens* 2020; 9(11): 917.

Jain U. Effect of COVID-19 on the organs. *Cureus* 2020; 12(8): e9540.

Jarduli LR, Sell AM, Reis PG, Sippert EÂ, Ayo CM, Mazini PS, Alves HV, Teixeira JJ and Visentainer JE. Role of HLA, KIR, MICA, and cytokines genes in leprosy. *Biomed. Res. Int.* 2013; 2013: 989837.

Jones SA and Jenkins BJ. Recent insights into targeting the IL-6 cytokine family in inflammatory diseases and cancer. *Nat. Rev. Immunol.* 2018; 18(12): 773-789.

Kamat MA, Blackshaw JA, Young R, Surendran P, Burgess S, Danesh J, Butterworth AS and Staley JR. PhenoScanner V2: an expanded tool for searching human genotype-phenotype associations. *Bioinformatics* 2019; 35(22): 4851-4853.

Knüpfer H and Preiss R. Significance of interleukin-6 (IL-6) in breast cancer (review). *Breast Cancer Res. Treat.* 2007; 102(2): 129-135.

Koh SJ, Jang Y, Hyun YJ, Park JY, Song YD, Shin KK, Chae JS, Kim BK, Ordovas JM and Lee JH. Interleukin-6 (IL-6) -572C->G promoter polymorphism is associated with type 2 diabetes risk in Koreans. *Clin. Endocrinol. (Oxf)* 2009; 70(2): 238-244.

Kopel J, Perisetti A, Roghani A, Aziz M, Gajendran M and Goyal H. Racial and gender-based differences in COVID-19. *Front. Public Health* 2020; 8: 418.

Kozłowski L, Zakrzewska I, Tokajuk P and Wojtukiewicz MZ. Concentration of interleukin-6 (IL-6), interleukin-8 (IL-8) and interleukin-10 (IL-10) in blood serum of breast cancer patients. *Rocz Akad Med Bialymst*. 2003; 48: 82-84.

Lajunen TK, Jaakkola JJK and Jaakkola MS. IL6 polymorphisms modify the effects of smoking on the risk of adult asthma. *J. Allergy Clin. Immunol.* 2018; 141(2): 799-802.e799.

Lambrecht BN, Hammad H and Fahy JV. The cytokines of Asthma. *Immunity* 2019; 50(4): 975-991.

Lane D, Matte I, Rancourt C and Piché A. Prognostic significance of IL-6 and IL-8 ascites levels in ovarian cancer patients. *BMC Cancer* 2011; 11: 21.

Lee C. "Race" and "ethnicity" in biomedical research: how do scientists construct and explain differences in health? *Soc. Sci. Med.* 2009; 68(6): 1183-1190.

Li B, Xiao Y, Xing D, Ma XL and Liu J. Circulating interleukin-6 and rheumatoid arthritis: A Mendelian randomization meta-analysis. *Medicine (Baltimore)* 2016; 23: e3855.

Li G, Fan Y, Lai Y, Han T, Li Z, Zhou P, Pan P, Wang W, Hu D, Liu X, Zhang Q and Wu J. Coronavirus infections and immune responses. *J. Med. Virol.* 2020; 92(4): 424-432.

Li L, Li J, Gao M, Fan H, Wang Y, Xu X, Chen C, Liu J, Kim J, Aliyari R, Zhang J, Jin Y, Li X, Ma F, Shi M, Cheng G and Yang H. Interleukin-8 as a biomarker for disease prognosis of Coronavirus Disease-2019 patients. *Front. Immunol.* 2021;11: 602395.

Linge HM, Collin M, Nordenfelt P, Mörgelin M, Malmsten M and Egesten A. The human CXC chemokine granulocyte chemotactic protein 2 (GCP-2)/CXCL6 possesses membrane-disrupting properties and is antibacterial. *Antimicrob. Agents Chemother*. 2008; 52(7): 2599-2607.

Liu C, Kellems RE and Xia Y. Inflammation, Autoimmunity, and Hypertension: The Essential Role of Tissue Transglutaminase. *Am. J. Hypertens.* 2017; 30(8): 756-764.

Liu Y, Berthier-Schaad Y, Fallin MD, Fink NE, Tracy RP, Klag MJ, Smith MW and Coresh J. IL-6 haplotypes, inflammation, and risk for cardiovascular disease in a multiethnic dialysis cohort. *J. Am. Soc. Nephrol*. 2006; 17(3): 863-870.

Liu Y, Sawalha AH and Lu Q. COVID-19 and autoimmune diseases. *Curr. Opin. Rheumatol.* 2021; 33(2): 155-162.

Lorente L, Martín MM, Franco A, Barrios Y, Cáceres JJ, Solé-Violán J, Perez A, Marcos Y Ramos JA, Ramos-Gómez L, Ojeda N and Jiménez A. Working Group on COVID-19 Canary ICU; Annex. Members of the BIOMEPOC group. HLA genetic polymorphisms and prognosis of patients with COVID-19. *Med. Intensiva*. 2021; 45(2): 96-103.

Ma A, Zhang L, Ye X, Chen J, Yu J, Zhuang L, Weng C, Petersen F, Wang Z and Yu X. High Levels of circulating IL-8 and soluble IL-2R are associated with prolonged illness in patients with severe COVID-19. *Front. Immunol.* 2121; 12: 626235.

Ma C, Cong Y and Zhang H. Covid-19 and the digestive system. *Am. J. Gastroenterol.*2020; 115(7): 1003-1006.

Machiela MJ and Chanock SJ. LDlink: a web-based application for exploring population-specific haplotype structure and linking correlated alleles of possible functional variants. *Bioinformatics* 2015; 31(21): 3555-3557.

Mayr FB, Spiel AO, Leitner JM, Firbas C, Kliegel T and Jilma B. Ethnic differences in plasma levels of interleukin-8 (IL-8) and granulocyte colony stimulating factor (G-CSF). *Transl. Res.* 2007; 149(1): 10-14.

Mihai S, Codrici E, Popescu ID, Enciu AM, Albulescu L, Necula LG, Mambet C, Anton G and Tanase C. Inflammation-related mechanisms in chronic kidney disease prediction, progression, and outcome. *J. Immunol. Res.* 2018; 2018: 2180373.

Mihara M, Takagi N, Takeda Y and Ohsugi Y. IL-6 receptor blockage inhibits the onset of autoimmune kidney disease in NZB/W F1 mice. *Clin. Exp. Immunol.* 1998; 112(3): 397-402.

Montinaro F, Busby GB, Pascali VL, Myers S, Hellenthal G and Capelli C. Unravelling the hidden ancestry of American admixed populations. *Nat. Commun.* 2015; 6: 6596.

Mulchandani R, Lyngdoh T and Kakkar AK. Deciphering the COVID-19 cytokine storm: Systematic review and meta-analysis. *Eur. J. Clin. Invest.* 2021; 51(1): e13429.

Mulholland RH and Sinha IP. Ethnicity and COVID-19 infection: are the pieces of the puzzle falling into place? *BMC Med.* 2020; 18(1):206.

Ness RB, Haggerty CL, Harger G and Ferrell R. Differential distribution of allelic variants in cytokine genes among African Americans and White Americans. *Am. J. Epidemiol.* 2004; 160 (11):1033-1038.

Ng DP, Nurbaya S, Ye SH and Krolewski AS. An IL-6 haplotype on human chromosome 7p21 confers risk for impaired renal function in type 2 diabetic patients. *Kidney Int*. 2008; 74(4): 521-527.

Ng WH, Tipih T, Makoah NA, Vermeulen JG, Goedhals D, Sempa JB, Burt FJ, Taylor A and Mahalingam S. Comorbidities in SARS-CoV-2 patients: a systematic review and meta-analysis. *mBio* 2021; 12(1): e03647-03620.

Oota H, Kitano T, Jin F, Yuasa I, Wang L, Ueda S, Saitou N and Stoneking M. Extreme mtDNA homogeneity in continental Asian populations. *Am. J. Phys. Anthropol*. 2002; 118(2):146-153.

Ortega LM and Fornoni A. Role of cytokines in the pathogenesis of acute and chronic kidney disease, glomerulonephritis, and end-stage kidney disease. *Int. J. Interferon, Cytokine Mediat. Res.* 2010; 2(1): 49-62.

Padyukov L, Lampa J, Heimbürger M, Ernestam S, Cederholm T, Lundkvist I, Andersson P, Hermansson Y, Harju A, Klareskog L and Bratt J. Genetic markers for the efficacy of tumour necrosis factor blocking therapy in rheumatoid arthritis. *Ann. Rheum. Dis*. 2003; 62(6): 526-529.

Pan D, Sze S, Minhas JS, Bangash MN, Pareek N, Divall P, Williams CM, Oggioni MR, Squire IB, Nellums LB, Hanif W, Khunti K and Pareek M. The impact of ethnicity on clinical outcomes in COVID-19: A systematic review. *EClinicalMedicine* 2020; 23: 100404.

Patel S, Saxena B and Mehta P. Recent updates in the clinical trials of therapeutic monoclonal antibodies targeting cytokine storm for the management of COVID-19. *Heliyon* 2021; 7(2): e06158.

Peng X, Shi J, Sun W, Ruan X, Guo Y, Zhao L, Wang J and Li B. Genetic polymorphisms of IL-6 promoter in cancer susceptibility and prognosis: a meta-analysis. *Oncotarget.* 2018; 9(15): 12351-12364.

Pennington AF, Kompaniyets L, Summers AD, Danielson ML, Goodman AB, Chevinsky JR, Preston LE, Schieber LZ, Namulanda G, Courtney J, Strosnider HM, Boehmer TK, Mac Kenzie WR, Baggs J and Gundlapalli AV. Risk of clinical severity by age and race/ethnicity among adults hospitalized for COVID-19-United States, March-September 2020. *Open Forum Infect Dis.* 2020; 8(2): ofaa638.

Peters MC, McGrath KW, Hawkins GA, Hastie AT, Levy BD, Israel E, Phillips BR, Mauger DT, Comhair SA, Erzurum SC, Johansson MW, Jarjour NN, Coverstone AM, Castro M, Holguin F, Wenzel SE, Woodruff PG, Bleecker ER and Fahy JV. Plasma interleukin-6 concentrations, metabolic dysfunction, and asthma severity: a cross-sectional analysis of two cohorts. *Lancet Respir. Med.* 2016; 4(7): 574-584.

Piñero J, Ramírez-Anguita JM, Saüch-Pitarch J, Ronzano F, Centeno E, Sanz F and Furlong LI.

The DisGeNET knowledge platform for disease genomics: 2019 update. *Nucleic Acids Res.* 2020; 48(D1): D845-D855.

Proost P, De Wolf-Peeters C, Conings R, Opdenakker G, Billiau A and Van Damme J. Identification of a novel granulocyte chemotactic protein (GCP-2) from human tumor cells. In vitro and in vivo comparison with natural forms of GRO, IP-10, and IL-8. *J. Immunol.* 1993; 150(3): 1000-1010.

Qian D, Yan S and Pan X. Association of IL-6 -597 G/A polymorphism with cancer risk: evidence from a meta-analysis. *Crit. Rev. Eukaryot. Gene Expr*. 2017; 27(3):.211-217.

Ragab D, Salah Eldin H, Taeimah M, Khattab R and Salem R. The COVID-19 cytokine storm; what we know so far. *Front Immunol.* 2020; 11: 1446.

Raharja A, Tamara A and Kok LT. Association between ethnicity and severe COVID-19 disease: a systematic review and meta-analysis. *J Racial Ethn. Health Disparities* 2021: 8(6): 1563-1572.

Robinson PC, Liew DFL, Liew JW, Monaco C, Richards D, Shivakumar S, Tanner H and Feldmann M. The potential for repurposing anti-TNF as a therapy for the treatment of COVID-19. *Med.* 2020; 1(1): 90-102.

Rothaug M, Becker-Pauly C and Rose-John S. The role of interleukin-6 signaling in nervous tissue. *Biochim. Biophys. Acta* 2016; 1863(6 Pt A): 1218-1227.

Rotimi CN, Bentley AR, Doumatey AP, Chen G, Shriner D and Adeyemo A. The genomic landscape of African populations in health and disease. *Hum. Mol. Genet*. 2017; 26(R2): R225-R236.

Saxena M, Agrawal CG, Srivastava N and Banerjee M. Interleukin-6 (IL-6)-597 A/G (rs1800797) & -174 G/C (rs1800795) gene polymorphisms in type 2 diabetes. *Indian J. Med. Res*. 2014; 140(1): 60-68.

Shi Y, Wang Y, Shao C, Huang J, Gan J, Huang X, Bucci E, Piacentini M, Ippolito G and Melino G. COVID-19 infection: the perspectives on immune responses. *Cell Death Differ*. 2020; 27(5):1451-1454.

Shoily SS, Ahsan T, Fatema K and Sajib AA. Common genetic variants and pathways in diabetes and associated complications and vulnerability of populations with different ethnic origins. *Sci. Rep.* 2021; 11(1):7504.

Siniauskaya E, Kuzhir T, Yagur V and Goncharova R. IL6 −174G/C (rs1800795) polymorphism rather than IL6R (rs2228145 and rs4845618) polymorphisms is associated with susceptibility to rheumatoid arthritis in the Belarusian population. *J. Genet. Genomic. Sci.* 2020; 5: 015.

Smieszek SP, Przychodzen BP, Polymeropoulos VM, Polymeropoulos CM and Polymeropoulos MH. Assessing the potential correlation of polymorphisms in the IL6R with relative IL6 elevation in severely ill COVID-19 patients'. *Cytokine* 2021; 148: 155662.

Stentz FB, Umpierrez GE, Cuervo R and Kitabchi AE. Pro-inflammatory cytokines, markers of cardiovascular risks, oxidative stress, and lipid peroxidation in patients with hyperglycemic crises. *Diabetes* 2004; 53(8): 2079-2086.

Stowe RP, Peek MK, Cutchin MP and Goodwin JS. Plasma cytokine levels in a population-based study: relation to age and ethnicity. *J. Gerontol. A. Biol. Sci. Med. Sci.* 2010; 65(4): 429-433.

Straczkowski M, Dzienis-Straczkowska S, Stêpieñ A, Kowalska I, Szelachowska M and Kinalska I. Plasma interleukin-8 concentrations are increased in obese subjects and related to fat mass and tumor necrosis factor-alpha system. *J. Clin. Endocrinol. Metab*. 2002; 87(10): 4602-4606.

Tavasolian F, Rashidi M, Hatam GR, Jeddi M, Hosseini AZ, Mosawi SH, Abdollahi E and Inman RD. HLA, immune response, and susceptibility to COVID-19. *Front. Immunol*. 2021; 11: 601886.

Tay MZ, Poh CM, Rénia L, MacAry PA and Ng LFP. The trinity of COVID-19: immunity, inflammation and intervention. *Nat. Rev. Immunol.* 2020; 20(6): 363-374.

Troshina EA, Yukina MY, Nuralieva NF and Mokrysheva NG. The role of HLA genes: from autoimmune diseases to COVID-19. *Probl. Endokrinol. (Mosk)* 2020; 66(4): 9-15.

Vahidy FS, Nicolas JC, Meeks JR, Khan O, Pan A, Jones SL, Masud F, Sostman HD, Phillips R, Andrieni JD, Kash BA and Nasir K. Racial and ethnic disparities in SARS-CoV-2 pandemic: analysis of a COVID-19 observational registry for a diverse US metropolitan population. *BMJ Open* 2020; 10(8): e039849.

Vieira SM, Lemos HP, Grespan R, Napimoga MH, Dal-Secco D, Freitas A, Cunha TM, Verri WA Jr, Souza-Junior DA, Jamur MC, Fernandes KS, Oliver C, Silva JS, Teixeira MM and Cunha FQ. A crucial role for TNFAlpha in mediating neutrophil influx induced by endogenously generated or exogenous chemokines, KC/CXCL1 and LIX/CXCL5. *Br. J. Pharmacol.* 2009; 158(3): 779-789.

Võsa U, Claringbould A, Westra H, Bonder MJ, Deelen P, Zeng B, Kirsten H, Saha A, Kreuzhuber R, Kasela S, Pervjakova N, Alvaes I, Fave M, Agbessi M, Christiansen M, Jansen R, Seppälä I, Tong L, Teumer A and Schramm K. Unraveling the polygenic architecture of complex traits using blood eQTL metaanalysis. bioRxiv 2018. doi.org/10.1101/447367.;

Whirl-Carrillo M, McDonagh EM, Hebert JM, Gong L, Sangkuhl K, Thorn CF, Altman RB and Klein TE. Pharmacogenomics knowledge for personalized medicine. *Clin. Pharmacol. Ther.* 2012; 92(4): 414-417.

Wong CK, Ho CY, Ko FW, Chan CH, Ho AS, Hui DS and Lam CW. Proinflammatory cytokines (IL-17, IL-6, IL-18 and IL-12) and Th cytokines (IFN-gamma, IL-4, IL-10 and IL-13) in patients with allergic asthma. *Clin. Exp. Immunol.* 2001; 125(2): 177-183.

Wrigley-Field E. US racial inequality may be as deadly as COVID-19. *Proc. Natl. Acad. Sci. USA* 2020; 117(36): 21854-21856.

Wu L, Zhou Y, Zhou Z, Liu Y, Bai Y, Xing X and Wang X. Nicotine induces the production of IL-1β and IL-8 via the α7 nAChR/NF-κB pathway in human periodontal ligament cells: an in vitro study. *Cell. Physiol. Biochem.* 2014; 34(2): 423-431.

Wu Y, Ho W, Huang Y, Jin DY, Li S, Liu SL, Liu X, Qiu J, Sang Y, Wang Q, Yuen KY and Zheng ZM. SARS-CoV-2 is an appropriate name for the new coronavirus. *Lancet* 2020; 395 (10228): 949-950.

Wuyts A, Govaerts C, Struyf S, Lenaerts JP, Put W, Conings R, Proost P and Van Damme J. Isolation of the CXC chemokines ENA-78, GRO alpha and GRO gamma from tumor cells and leukocytes reveals NH2-terminal heterogeneity. Functional comparison of different natural isoforms. *Eur. J. Biochem*. 1999; 260(2): 421-429.

Xiong Y, Liu Y, Cao L, Wang D, Guo M, Jiang A, Guo D, Hu W, Yang J, Tang Z, Wu H, Lin Y, Zhang M, Zhang Q, Shi M, Liu Y, Zhou Y, Lan K and Chen Y. Transcriptomic characteristics of bronchoalveolar lavage fluid and peripheral blood mononuclear cells in COVID-19 patients. *Emerg. Microbes Infect*. 2020; 9(1):761-770.

Yao S, Hong CC, Ruiz-Narváez EA, Evans SS, Zhu Q, Schaefer BA, Yan L, Coignet MV, Lunetta KL, Sucheston-Campbell LE, Lee K, Bandera EV, Troester MA, Rosenberg L, Palmer JR, Olshan AF and Ambrosone CB. Genetic ancestry and population differences in levels of inflammatory cytokines in women: Role for evolutionary selection and environmental factors. *PLoS Genet.* 2018; 14(6): e1007368.

Yi E, Zhang J, Zheng M, Zhang Y, Liang C, Hao B, Hong W, Lin B, Pu J, Lin Z, Huang P, Li B, Zhou Y and Ran P. Long noncoding RNA IL6-AS1 is highly expressed in chronic obstructive pulmonary disease and is associated with interleukin 6 by targeting miR-149-5p and early B-cell factor 1. *Clin. Transl. Med*. 2021; 11(7): e479.

Zakharyan R, Petrek M, Arakelyan A, Mrazek F, Atshemyan S and Boyajyan A. Interleukin-6 promoter polymorphism and plasma levels in patients with schizophrenia. *Tissue Antigens* 2012; 80 (2):136-142.

Zhang C, Wu Z, Zhao G, Wang F and Fang Y. Identification of IL6 as a susceptibility gene for major depressive disorder. *Sci. Rep.* 2016; 6: 31264.

Zhang S, Zhan L, Zhu Y, Sun H and Xu X. Tumor Necrosis Factor Alpha gene polymorphisms increase susceptibility to Adenovirus infection in children and are correlated with severity of Adenovirus-associated pneumonia. *Genet. Test. Mol. Biomark.* 2020; 24(12): 761-770.

Zhao Y, Nie HX, Hu K, Wu XJ, Zhang YT, Wang MM, Wang T, Zheng ZS, Li XC and Zeng SL. Abnormal immunity of non-survivors with COVID-19: predictors for mortality. *Infect. Dis. Poverty* 2020; 9(1): 108.

Supplementary table 1: List of gene expression-modulating SNPs in IL6, TNFA and IL8 alongs

Genes	SNP ID	Chromos	Consequence	Alleles	Variant A	ALL	AFR
IL6	rs1800797	chr7:2272	Intron	A/G	A	0.138	0.017
	rs1800796	chr7:2272	Intron	G/C	C	0.314	0.103
	rs1800795	chr7:2272	Intron	C/G	C	0.141	0.018
	rs2069832	chr7:2272	Intron	A/G/T	A	0.14	0.018
	rs2069833	chr7:2272	Intron	C/G/T	C	0.14	0.017
	rs1474348	chr7:2272	Intron	C/G	C	0.141	0.017
	rs2069837	chr7:2272	Intron	A/C/G	G	0.12	0.12
	rs1474347	chr7:2272	Intron	C/A	C	0.168	0.113
	rs2066992	chr7:2272	Intron	G/T	T	0.308	0.085
	rs2069840	chr7:2272	Intron	C/G	G	0.186	0.15
	rs1554606	chr7:2272	Intron	T/A/G	T	0.249	0.311
	rs2069845	chr7:2273	Intron	G/A	G	0.253	0.317
TNFA	rs3093661	chr6:3157	intron	G/A	A	0.052	0.03
	rs1800610	chr6:3157	intron	G/A	A	0.1	0.024
	rs3093662	chr6:3157	intron	A/G	G	0.08	0.077
	rs3093664	chr6:3157	intron	A/G	G	0.079	0.084
	rs3093665	chr6:3157	3_prime_UTR	A/C	C	0.019	0.039
IL8	rs2227307	chr4:7374	intron	T/G	G	0.424	0.518
	rs2227549	chr4:7374	intron	A/C/G	G	0.016	0.005
	rs2227306	chr4:7374	intron	C/T	T	0.259	0.097
	rs2227543	chr4:7374	3_prime_UTR	C/T	T	0.289	0.097
	rs1126647	chr4:7374	3_prime_UTR	A/T	T	0.285	0.096

SNPs with MAFs > 0.2 are highlighted in red

All populations (ALL); African super-population (AFR)- ((Yoruba in Ibadan, Nigeria (YRI); Luhya in Web ide their VAFs in twenty six populations.

ACB	ASW	ESN	GWD	LWK	MSL	YRI	AMR	CLM
0.062	0.074	0	0.004	0	0	0	0.184	0.277
0.089	0.066	0.071	0.115	0.212	0.071	0.079	0.295	0.207
0.062	0.09	0	0.004	0	0	0	0.184	0.287
0.062	0.09	0	0.004	0	0	0	0.187	0.287
0.062	0.082	0	0.004	0.01	0	0	0.187	0.287
0.062	0.082	0	0.004	0	0	0	0.187	0.287
0.12	0.131	0.136	0.128	0.076	0.124	0.13	0.081	0.069
0.172	0.172	0.091	0.071	0.081	0.124	0.111	0.196	0.298
0.062	0.066	0.03	0.115	0.197	0.071	0.042	0.293	0.197
0.151	0.148	0.096	0.204	0.116	0.129	0.19	0.262	0.266
0.349	0.336	0.298	0.279	0.242	0.382	0.315	0.287	0.399
0.354	0.336	0.308	0.283	0.242	0.388	0.329	0.285	0.399
0.01	0.033	0.01	0.066	0.056	0.035	0	0.056	0.037
0.031	0.049	0.025	0.022	0.01	0.024	0.019	0.183	0.17
0.042	0.107	0.076	0.115	0.096	0.071	0.042	0.11	0.085
0.052	0.107	0.101	0.097	0.096	0.059	0.079	0.084	0.064
0.026	0.066	0.066	0.031	0.03	0.024	0.037	0.027	0.027
0.536	0.549	0.515	0.54	0.535	0.471	0.486	0.337	0.34
0	0.016	0	0.013	0.005	0	0	0.026	0
0.167	0.123	0.071	0.111	0.111	0.029	0.069	0.269	0.266
0.167	0.123	0.071	0.111	0.111	0.029	0.069	0.269	0.266
0.167	0.115	0.071	0.111	0.111	0.029	0.069	0.265	0.255

uye, Kenya (LWK); Gambian in Western Divisions in the Gambia (GWD); Mende inSierra Leone (MSL); Es

MXL	PEL	PUR	EAS	CDX	CHB	CHS	JPT	KHV
0.133	0.053	0.24	0.001	0	0	0	0	0.005
0.344	0.518	0.163	0.791	0.823	0.718	0.786	0.822	0.808
0.133	0.053	0.231	0.001	0	0	0	0	0.005
0.141	0.053	0.236	0.001	0	0	0	0	0.005
0.141	0.053	0.236	0.001	0	0	0	0	0.005
0.141	0.053	0.236	0.001	0	0	0	0	0.005
0.078	0.047	0.12	0.141	0.156	0.16	0.143	0.111	0.136
0.148	0.053	0.25	0.007	0.005	0.005	0.01	0.005	0.01
0.336	0.518	0.168	0.788	0.817	0.714	0.786	0.822	0.803
0.273	0.247	0.264	0.062	0.016	0.117	0.062	0.062	0.051
0.234	0.147	0.332	0.009	0.016	0.005	0.01	0.005	0.01
0.227	0.147	0.332	0.011	0.016	0.01	0.01	0.01	0.01
0.062	0.1	0.034	0.031	0.011	0.034	0.038	0.014	0.056
0.203	0.282	0.101	0.137	0.134	0.17	0.071	0.197	0.111
0.133	0.135	0.096	0.031	0.011	0.034	0.038	0.014	0.056
0.094	0.118	0.067	0.036	0.011	0.034	0.038	0.014	0.081
0.031	0.018	0.034	0	0	0	0	0	0
0.383	0.235	0.389	0.414	0.5	0.417	0.424	0.327	0.409
0.023	0	0.053	0	0	0	0	0	0
0.32	0.188	0.308	0.338	0.344	0.374	0.367	0.279	0.328
0.32	0.188	0.308	0.383	0.452	0.393	0.4	0.298	0.379
0.32	0.188	0.303	0.384	0.452	0.393	0.4	0.303	0.379

an in Nigeria (ESN); Americans of African Ancestry in SW USA (ASW); African Caribbeans in Barbados (A

EUR	CEU	FIN	GBR	IBS	TSI	SAS	BEB	GIH
0.408	0.505	0.434	0.401	0.35	0.355	0.134	0.116	0.141
0.048	0.045	0.051	0.038	0.051	0.051	0.395	0.384	0.33
0.416	0.515	0.455	0.412	0.35	0.355	0.139	0.116	0.155
0.411	0.515	0.449	0.401	0.346	0.35	0.134	0.116	0.141
0.411	0.515	0.449	0.401	0.346	0.35	0.138	0.116	0.155
0.411	0.515	0.449	0.401	0.346	0.35	0.14	0.116	0.155
0.089	0.076	0.101	0.088	0.079	0.103	0.156	0.221	0.107
0.412	0.515	0.449	0.401	0.346	0.355	0.14	0.116	0.155
0.048	0.045	0.051	0.038	0.051	0.051	0.395	0.372	0.335
0.332	0.298	0.237	0.385	0.407	0.332	0.155	0.134	0.184
0.432	0.53	0.465	0.423	0.383	0.369	0.199	0.151	0.228
0.433	0.53	0.465	0.423	0.388	0.369	0.206	0.163	0.233
0.048	0.061	0.04	0.082	0.019	0.042	0.105	0.105	0.17
0.089	0.051	0.061	0.06	0.131	0.136	0.119	0.076	0.107
0.084	0.081	0.04	0.093	0.084	0.121	0.108	0.122	0.17
0.083	0.086	0.081	0.126	0.051	0.079	0.108	0.122	0.17
0.021	0.015	0	0.016	0.033	0.037	0.003	0.017	0
0.417	0.414	0.424	0.379	0.458	0.402	0.374	0.32	0.466
0.051	0.04	0.051	0.049	0.051	0.061	0.005	0	0
0.388	0.389	0.399	0.346	0.416	0.383	0.259	0.244	0.311
0.393	0.389	0.404	0.357	0.421	0.388	0.357	0.308	0.447
0.387	0.394	0.399	0.352	0.411	0.374	0.349	0.297	0.442

CB)); Admixed Americans (AMR)- ((Mexican Ancestry fromLos Angeles USA (MXL); Puerto Ricans from Pu

ITU	PJL	STU
0.167	0.141	0.103
0.456	0.328	0.471
0.176	0.13	0.113
0.172	0.13	0.108
0.172	0.13	0.113
0.176	0.135	0.113
0.137	0.167	0.162
0.176	0.135	0.113
0.456	0.339	0.466
0.103	0.193	0.162
0.245	0.193	0.172
0.245	0.193	0.186
0.132	0.047	0.069
0.118	0.151	0.137
0.132	0.047	0.069
0.132	0.047	0.069
0	0	0
0.377	0.349	0.348
0.005	0.016	0.005
0.25	0.26	0.225
0.363	0.318	0.338
0.348	0.318	0.328

ıerto Rico (PUR); Colombians from Medellin, Colombia (CLM); Peruvians from Lima, Peru (PEL)); East Asi an (EAS)- ((Han Chinese in Beijing,China (CHB); Japanese in Tokyo, Japan (JPT); Southern Han Chinese (C

HS); Chinese Dai in Xishuangbanna, China (CDX); Kinh in Ho Chi Minh City, Vietnam (KHV)); European (EU

JR)-((Utah Residents (CEPH) with Northern and Western European Ancestry (CEU); Toscani in Italia (TSI);

Finnish in Finland (FIN); British in England and Scotland (GBR); Iberian Population inSpain (IBS)); South sian (SAS)- ((Gujarati Indian from Houston, Texas (GIH); Punjabi from Lahore, Pakistan (PJL); Bengali fro m Ba

Supplementary table 2: Influence of gene expression-modulating SNPs of *IL6, TNFA* and *IL8* on the expression of other genes.

SNP ID	Variant allele	P-value	ID of affected gene	Symbol of affected gene	Z-score	Assessed allele	Other allele	Number of Cohorts	Number of Samples	FDR
rs1800797	A	1.67E-16	ENSG00000105889	STEAP1B	8.2434	A	G	13	7931	0.000
		1.35E-15	ENSG00000179428	AC073072.5	7.9904	A	G	22	18941	0.000
		3.32E-13	ENSG00000232759	AC002480.3	7.2809	A	G	12	4994	0.000
		8.53E-07	ENSG00000230658	KLHL7-AS1	-4.9227	A	G	12	5164	0.003
rs1800796	C	1.30E-08	ENSG00000179428	AC073072.5	-5.6859	C	G	21	18612	0.000
		8.29E-08	ENSG00000196683	TOMM7	5.3609	C	G	35	31140	0.000
		1.04E-05	ENSG00000226816	AC005082.12	-4.4088	C	G	13	5501	0.027
rs1800795	C	1.13E-17	ENSG00000179428	AC073072.5	8.5604	C	G	22	18941	0.000
		2.72E-17	ENSG00000105889	STEAP1B	8.4584	C	G	13	7931	0.000
		2.26E-13	ENSG00000232759	AC002480.3	7.3324	C	G	12	4991	0.000
rs2069832	A	4.84E-18	ENSG00000179428	AC073072.5	8.6571	A	G	22	18941	0.000
		1.16E-17	ENSG00000105889	STEAP1B	8.5566	A	G	13	7931	0.000
		1.26E-13	ENSG00000232759	AC002480.3	7.41	A	G	12	4994	0.000
		5.81E-07	ENSG00000230658	KLHL7-AS1	-4.9974	A	G	12	5164	0.002
rs2069833	C	6.38E-18	ENSG00000179428	AC073072.5	8.6257	C	T	22	18941	0.000
		1.04E-17	ENSG00000105889	STEAP1B	8.5693	C	T	13	7931	0.000
		1.12E-13	ENSG00000232759	AC002480.3	7.4259	C	T	12	4994	0.000
		5.81E-07	ENSG00000230658	KLHL7-AS1	-4.9974	C	T	12	5164	0.002
rs1474348	C	7.09E-18	ENSG00000179428	AC073072.5	8.6135	C	G	22	18941	0.000
		9.26E-18	ENSG00000105889	STEAP1B	8.583	C	G	13	7931	0.000
		1.03E-13	ENSG00000232759	AC002480.3	7.4369	C	G	12	4994	0.000
		5.67E-07	ENSG00000230658	KLHL7-AS1	-5.002	C	G	12	5164	0.002
		1.68E-05	ENSG00000196683	TOMM7	-4.3032	C	G	35	31355	0.042
rs2069837	G	2.20E-10	ENSG00000232759	AC002480.3	-6.3466	G	A	10	4169	0.000
		5.55E-06	ENSG00000196683	TOMM7	-4.5428	G	A	34	30644	0.015
rs1474347	C	6.29E-18	ENSG00000179428	AC073072.5	8.6272	C	A	22	18941	0.000
		1.98E-17	ENSG00000105889	STEAP1B	8.495	C	A	13	7931	0.000
		9.93E-14	ENSG00000232759	AC002480.3	7.4419	C	A	12	4994	0.000
		3.84E-07	ENSG00000230658	KLHL7-AS1	-5.0767	C	A	12	5164	0.001
		1.40E-05	ENSG00000196683	TOMM7	-4.3434	C	A	35	31355	0.036
rs2066992	T	1.85E-08	ENSG00000179428	AC073072.5	-5.6253	T	G	21	18612	0.000
		7.73E-08	ENSG00000196683	TOMM7	5.3736	T	G	35	31141	0.000
		1.80E-06	ENSG00000226816	AC005082.12	-4.7748	T	G	13	5502	0.005
rs2069840	G	7.69E-08	ENSG00000105889	STEAP1B	-5.3741	G	C	13	7931	0.000
		8.02E-07	ENSG00000230658	KLHL7-AS1	4.935	G	C	12	5164	0.002
		4.64E-06	ENSG00000232759	AC002480.3	-4.5805	G	C	12	4989	0.012
rs1554606	T	8.54E-16	ENSG00000179428	AC073072.5	8.0462	T	G	22	18941	0.000
		5.27E-15	ENSG00000105889	STEAP1B	7.8203	T	G	13	7931	0.000
		2.93E-13	ENSG00000232759	AC002480.3	7.2979	T	G	12	4994	0.000
		8.21E-07	ENSG00000230658	KLHL7-AS1	-4.9304	T	G	12	5164	0.002
		6.81E-06	ENSG00000122591	FAM126A	4.4997	T	G	35	31529	0.018

rs2069845	G	8.19E-16	ENSG00000179428	AC073072.5	8.0516	G	A	22	18941	0.000
		7.74E-15	ENSG00000105889	STEAP1B	7.772	G	A	13	7931	0.000
		1.88E-13	ENSG00000232759	AC002480.3	7.3569	G	A	12	4993	0.000
		1.23E-06	ENSG00000230658	KLHL7-AS1	-4.8502	G	A	12	5164	0.003
		9.00E-06	ENSG00000122591	FAM126A	4.4398	G	A	35	31528	0.023
rs3093661	A	3.2717e-310	ENSG00000204516	MICB	-38.036	A	G	13	10799	0.000
		1.66E-55	ENSG00000204520	MICA	-15.694	A	G	12	5724	0.000
		3.82E-34	ENSG00000204482	LST1	-12.183	A	G	13	10799	0.000
		1.59E-29	ENSG00000234745	HLA-B	11.2834	A	G	11	4805	0.000
		3.21E-21	ENSG00000229391	HLA-DRB6	-9.4556	A	G	27	21469	0.000
		2.00E-15	ENSG00000204580	DDR1	7.9418	A	G	13	10799	0.000
		2.09E-13	ENSG00000240053	LY6G5B	7.3429	A	G	13	10799	0.000
		2.05E-11	ENSG00000204472	AIF1	6.7025	A	G	13	10799	0.000
		4.73E-11	ENSG00000204428	LY6G5C	6.5793	A	G	13	10799	0.000
		3.32E-10	ENSG00000137331	IER3	-6.2828	A	G	13	10799	0.000
		3.88E-06	ENSG00000227507	LTB	4.6177	A	G	13	10799	0.010
		4.44E-06	ENSG00000204528	PSORS1C3	-4.5898	A	G	12	5724	0.012
		5.89E-06	ENSG00000137312	FLOT1	-4.5301	A	G	12	5724	0.016
		1.27E-05	ENSG00000248290	TNXA	4.365	A	G	7	3134	0.033
rs1800610	A	4.11E-194	ENSG00000204475	NCR3	-29.721	A	G	14	13564	0.000
		4.31E-68	ENSG00000204520	MICA	-17.437	A	G	13	8489	0.000
		6.40E-33	ENSG00000204525	HLA-C	-11.951	A	G	32	24777	0.000
		9.59E-29	ENSG00000213760	ATP6V1G2	11.1242	A	G	14	13564	0.000
		3.11E-28	ENSG00000229391	HLA-DRB6	11.0188	A	G	29	24563	0.000
		2.07E-24	ENSG00000232810	TNF	10.1962	A	G	14	13564	0.000
		1.23E-17	ENSG00000204528	PSORS1C3	8.5499	A	G	13	8489	0.000
		5.79E-17	ENSG00000206344	HCG27	8.3695	A	G	13	10797	0.000
		1.12E-15	ENSG00000204472	AIF1	8.0127	A	G	14	13564	0.000
		6.30E-14	ENSG00000204463	BAG6	7.5016	A	G	13	8489	0.000
		2.05E-13	ENSG00000204531	POU5F1	7.3459	A	G	12	5722	0.000
		9.94E-11	ENSG00000204428	LY6G5C	6.4678	A	G	14	13564	0.000
		7.47E-10	ENSG00000204536	CCHCR1	-6.1557	A	G	14	13564	0.000
		1.16E-09	ENSG00000204516	MICB	6.0864	A	G	14	13564	0.000
		9.02E-09	ENSG00000204396	VWA7	5.7484	A	G	12	7570	0.000
		1.29E-07	ENSG00000225851	HLA-S	5.2808	A	G	9	3833	0.000
		3.94E-07	ENSG00000226979	LTA	5.0717	A	G	14	13564	0.001
		8.23E-07	ENSG00000199332	Y_RNA	-4.9297	A	G	8	3325	0.002
		1.41E-06	ENSG00000204435	CSNK2B	-4.8236	A	G	14	13564	0.004
		2.31E-06	ENSG00000137411	VARS2	4.7245	A	G	14	13564	0.006
rs3093662	G	6.52E-131	ENSG00000204516	MICB	-24.345	G	A	14	13566	0.000
		5.99E-46	ENSG00000204482	LST1	-14.23	G	A	14	13566	0.000
		3.12E-43	ENSG00000204520	MICA	-13.785	G	A	13	8491	0.000
		1.21E-23	ENSG00000234745	HLA-B	10.0227	G	A	12	7572	0.000
		5.52E-12	ENSG00000204580	DDR1	6.8917	G	A	14	13566	0.000
		1.90E-11	ENSG00000204525	HLA-C	-6.7131	G	A	31	24395	0.000
		7.08E-11	ENSG00000229391	HLA-DRB6	-6.5189	G	A	28	24181	0.000
		1.41E-09	ENSG00000204528	PSORS1C3	-6.0545	G	A	13	8491	0.000

		1.63E-09	ENSG00000226979	LTA	-6.0309	G	A	14	13566	0.000
		8.05E-09	ENSG00000227507	LTB	5.7675	G	A	14	13566	0.000
		1.85E-08	ENSG00000204438	GPANK1	5.626	G	A	13	8491	0.000
		3.17E-08	ENSG00000198502	HLA-DRB5	-5.5317	G	A	32	24609	0.000
		3.77E-08	ENSG00000137331	IER3	-5.5011	G	A	14	13566	0.000
		1.03E-05	ENSG00000214894	LINC00243	-4.4098	G	A	11	4805	0.027
		1.21E-05	ENSG00000137312	FLOT1	-4.3753	G	A	13	8491	0.031
rs3093664	G	3.98E-149	ENSG00000204516	MICB	-26.008	G	A	13	10799	0.000
		1.23E-28	ENSG00000234745	HLA-B	11.1016	G	A	11	4805	0.000
		1.88E-22	ENSG00000204520	MICA	-9.7478	G	A	12	5724	0.000
		1.75E-17	ENSG00000204525	HLA-C	-8.5096	G	A	31	22012	0.000
		4.22E-14	ENSG00000198502	HLA-DRB5	-7.5539	G	A	32	22226	0.000
		1.24E-12	ENSG00000227507	LTB	7.1012	G	A	13	10799	0.000
		3.96E-12	ENSG00000204438	GPANK1	6.9387	G	A	12	5724	0.000
		7.26E-12	ENSG00000204580	DDR1	6.8524	G	A	13	10799	0.000
		6.85E-10	ENSG00000204482	LST1	-6.1695	G	A	13	10799	0.000
		9.08E-09	ENSG00000206344	HCG27	5.747	G	A	13	10799	0.000
		1.30E-08	ENSG00000204338	CYP21A1P	5.6866	G	A	10	4171	0.000
		1.98E-06	ENSG00000248290	TNXA	4.7559	G	A	7	3134	0.005
		2.74E-06	ENSG00000213760	ATP6V1G2	4.6898	G	A	13	10799	0.007
		7.10E-06	ENSG00000226979	LTA	-4.4906	G	A	13	10799	0.019
		7.44E-06	ENSG00000204528	PSORS1C3	4.4808	G	A	12	5724	0.020
		1.05E-05	ENSG00000213676	ATF6B	-4.4074	G	A	12	5724	0.027
rs3093665	C	6.99E-29	ENSG00000204482	LST1	-11.152	C	A	11	10206	0.000
		2.11E-18	ENSG00000204438	GPANK1	8.7515	C	A	10	5131	0.000
		1.78E-10	ENSG00000227507	LTB	6.3791	C	A	11	10206	0.000
		1.61E-06	ENSG00000204428	LY6G5C	-4.7972	C	A	11	10206	0.004
		4.05E-06	ENSG00000240053	LY6G5B	-4.6088	C	A	11	10206	0.011
		1.62E-05	ENSG00000204301	NOTCH4	-4.3119	C	A	11	10206	0.041
rs2227307	G	3.36E-184	ENSG00000109272	PF4V1	28.9439	G	T	37	31682	0.000
		2.67E-66	ENSG00000169429	IL8	17.1996	G	T	34	25644	0.000
		3.73E-35	ENSG00000163735	CXCL5	12.3715	G	T	36	31468	0.000
		3.48E-16	ENSG00000124875	CXCL6	8.1556	G	T	36	31642	0.000
		9.12E-08	ENSG00000163739	CXCL1	5.3435	G	T	37	31682	0.000
rs2227549	G	3.50E-14	ENSG00000169429	IL8	7.5783	G	A	29	20523	0.000
		1.84E-12	ENSG00000109272	PF4V1	7.0458	G	A	32	26561	0.000
rs2227306	T	1.97E-176	ENSG00000109272	PF4V1	28.32	T	C	37	31683	0.000
		7.75E-79	ENSG00000169429	IL8	18.7986	T	C	34	25645	0.000
		1.50E-18	ENSG00000124875	CXCL6	8.7896	T	C	36	31643	0.000
		8.04E-18	ENSG00000163735	CXCL5	8.5991	T	C	36	31469	0.000
		1.36E-10	ENSG00000163739	CXCL1	6.4209	T	C	37	31683	0.000
rs2227543	T	5.62E-190	ENSG00000109272	PF4V1	29.3993	T	C	37	31684	0.000
		1.72E-76	ENSG00000169429	IL8	18.5102	T	C	34	25646	0.000
		1.29E-18	ENSG00000124875	CXCL6	8.8062	T	C	36	31644	0.000
		3.21E-17	ENSG00000163735	CXCL5	8.4388	T	C	36	31470	0.000
		3.19E-09	ENSG00000163739	CXCL1	5.9216	T	C	37	31684	0.000
rs1126647	T	2.66E-178	ENSG00000109272	PF4V1	28.4714	T	A	37	31683	0.000

		7.46E-77	ENSG00000169429	IL8	18.5549	T	A	34	25645	0.000
		8.12E-19	ENSG00000163735	CXCL5	8.8585	T	A	36	31469	0.000
		2.65E-15	ENSG00000124875	CXCL6	7.9066	T	A	36	31643	0.000
		3.27E-09	ENSG00000163739	CXCL1	5.9175	T	A	37	31683	0.000

Supplementary table 3: Allele frequency differences (AFDs) at each gene expression-modulating SNP locus between all possible super-population pairs.

Genes	SNP ID	Population Pairs									
		AFR-AMR	**AFR-EAS**	**AFR-EUR**	**AFR-SAS**	**AMR-EAS**	**AMR-EUR**	**AMR-SAS**	**EAS-EUR**	**EAS-SAS**	**EUR-SAS**
IL6	rs1800797	0.167	0.016	0.391	0.117	0.183	0.224	0.05	0.407	0.133	0.274
	rs1800796	0.192	0.688	0.055	0.292	0.496	0.247	0.1	0.743	0.396	0.347
	rs1800795	0.166	0.017	0.398	0.121	0.183	0.232	0.045	0.415	0.138	0.277
	rs2069832	0.169	0.017	0.393	0.116	0.186	0.224	0.053	0.41	0.133	0.277
	rs2069833	0.17	0.095	0.394	0.121	0.186	0.224	0.049	0.41	0.137	0.273
	rs1474348	0.17	0.016	0.394	0.123	0.186	0.224	0.047	0.41	0.139	0.271
	rs2069837	0.039	0.021	0.031	0.036	0.06	0.008	0.075	0.052	0.015	0.067
	rs1474347	0.083	0.106	0.299	0.027	0.189	0.216	0.056	0.405	0.133	0.272
	rs2066992	0.208	0.703	0.037	0.31	0.495	0.245	0.102	0.74	0.393	0.347
	rs2069840	0.112	0.088	0.182	0.005	0.2	0.07	0.107	0.27	0.093	0.177
	rs1554606	0.024	0.302	0.121	0.112	0.278	0.145	0.088	0.423	0.19	0.233
	rs2069845	0.032	0.306	0.116	0.111	0.274	0.148	0.079	0.422	0.195	0.227
TNFA	rs3093661	0.026	0.001	0.018	0.075	0.025	0.008	0.049	0.017	0.074	0.057
	rs1800610	0.159	0.113	0.065	0.095	0.046	0.094	0.064	0.048	0.018	0.03
	rs3093662	0.033	0.046	0.007	0.031	0.079	0.026	0.002	0.053	0.077	0.024
	rs3093664	0	0.048	0.001	0.024	0.048	0.001	0.024	0.047	0.072	0.025
	rs3093665	0.012	0.039	0.018	0.036	0.027	0.006	0.024	0.021	0.003	0.018
IL6	rs2227307	0.181	0.104	0.101	0.144	0.077	0.08	0.037	0.003	0.04	0.043
	rs2227549	0.021	0.01	0.046	0.005	0.029	0.025	0.024	0.052	0.005	0.047
	rs2227306	0.172	0.241	0.291	0.162	0.069	0.119	0.01	0.05	0.079	0.129
	rs2227543	0.172	0.286	0.296	0.26	0.114	0.124	0.088	0.01	0.026	0.036
	rs1126647	0.169	0.288	0.291	0.253	0.119	0.122	0.084	0.003	0.035	0.038

J. Bangladesh Acad. Sci. 47(1); 91-99: June 2023 DOI: https://doi.org/10.3329/jbas.v47i1.65129

Journal of Bangladesh Academy of Sciences

Journal homepage: http://www.bas.org.bd/publications/jbas.html

Research Article

Jute endophyte *Grammothele lineata* SDL-CO-2015-1 produces an anticancer compound epothilone B

Mirza Ashikul Beg[1], Sumaiya Binte Hannan, Rabeya, Shafi Ahmad Talukder, Aftab Uddin[1], Shammi Akter, Rifath Nehleen Reza, Haseena Khan and Mohammad Riazul Islam*

Molecular Biology Laboratory, Department of Biochemistry and Molecular Biology, University of Dhaka, Dhaka, Bangladesh

ARTICLE INFO

Article History

Received: 27 March 2023
Revised: 28 May 2023
Accepted: 11 June 2023

Keywords: *Grammothele lineata*, Endophyte, Epothilone B, Anti-Cancer drug, NaPDoS

ABSTRACT

Jute (*Corchorus olitorius*) endophytic fungi *Grammothele lineata* SDL-CO-2015-1 was found to produce epothilone B, a well-reported anticancer compound. The genome and RNA sequence data of *G. lineata* revealed the presence of epothilone gene clusters. *In silico* mining using Natural Product Domain Seeker (NaPDoS) identified four genes matching the epothilone gene cluster (Epo D). Epothilone was extracted from the extracellular extract of this fungus using XAD-16 resin. Different analytical techniques, including Thin Layer Chromatography (TLC), Reverse Phase High-Performance Liquid Chromatography (RP-HPLC), and Mass Spectrometry (MS), were used to identify and characterize epothilone following its extraction. TLC bands were visible at 365 nm for both standard epothilone B and samples with identical R_f values. Extracted epothilone bands from the TLC plate were further purified using RP-HPLC. Using a linear gradient system with methanol and formic acid, LC-MS spectroscopy was done with RP-HPLC purified fraction. The monoisotopic mass of epothilone $(M+H^+)$ = 508.10 Da was present in the mass chromatogram. The product ions of 508.10 Da were found with the m/z values at 320.20 Da and 420.20 Da, the typical MS_2 fragments for standard epothilone B. This finding suggests that the fungal endophyte, *G. lineata* can be a potential source of epothilone B.

Introduction

Endophytes are microorganisms that can reside within the plant tissues without causing any harm to the host. In the past few decades, plant scientists have discovered that plants may serve as a reservoir for endless endophytes (Stone et al., 2000). It is generally hypothesized that endophytic bacteria and fungi may produce bioactive compounds and secondary metabolites similar to those made by the host plants (Strobel, 2003). Isolation of endophytes and studying their natural products is now a ubiquitous scientific approach (Schulz et al., 2002). Because it is generally assumed that the endophytes produce antimicrobial compounds which protect the host plants, some of these compounds are of high medicinal interest because of their antifungal, antibacterial, antimalarial, and other biological activities.

Endophytes gained enormous attention when the detection of taxol in the endophytic fungus (*Taxomyces andreanae*) isolated from the yew plant (*Taxus brevifolia*) was reported at first (Gangadevi & Muthumary, 2008). Taxol was also

---

*Corresponding author:<mriazulislam@du.ac.bd>

[1] *Department of Genetic Engineering and Biotechnology, University of Dhaka, Dhaka, Bangladesh*

isolated from Southern Chinese yew (*Taxus mairei*) in the Fujian province of Southeastern China (Wang et al., 2000). In addition, at least three endophytes of *Taxus wallichiana* produce taxol, including *Sporormia minima* and *Trichothecium* spp (Shrestha et al., 2001).

Although an annual dicotyledonous crop, jute (*Corchorus* spp.) is known mostly for its high-quality tensile natural fiber, *C. olitorius* has long been recognized as a medicinal herb, and its extract is known to have apoptotic activity on tumor cell lines (Li et al., 2012). In addition, *C. olitorius* has also been described to possess promising antibacterial and antifungal activity. In the Molecular Biology Laboratory, Department of Biochemistry and Molecular Biology, University of Dhaka, many endophytic fungi were isolated from different parts like roots, stems, leaves, flowers, and fruits of a jute plant (*Corchorus olitorius* var. O-9897) (Zaman, 2019), later they were sequenced and analyzed to see whether they contained any beneficial gene clusters or not. *G. lineata*, a basidiomycete fungus, was an endophyte isolated from jute seedlings, later sequenced, and reported producing Taxol (Das et al., 2017). Some findings suggested another taxol-like substance named epothilone in *G. lineata* extract. Following the discovery of epothilone gene clusters in the genome sequence and RNA-Seq data of *G. lineata*, four genes matching the epothilone gene cluster (Epo D) were identified using NaPDoS (Natural Product Domain Seeker) mining tool.

Epothilones are 16-membered macrocyclic lactones first identified in 1996 (Höfle et al., 1996). The critical structure of epothilones is the macrolide ring with a thiazole-containing side chain and a ketone (Lee et al., 2008). As of September 2008, epothilones A to F have been identified and characterized. Based on the presence or lack of an epoxide group at the C-12 to C-13 position of the macrolide ring, naturally occurring epothilones are categorized as either epoxides (epothilones A, B, E, and F) or olefins (epothilones C and D) (Fig. 1) (Lee et al., 2008).

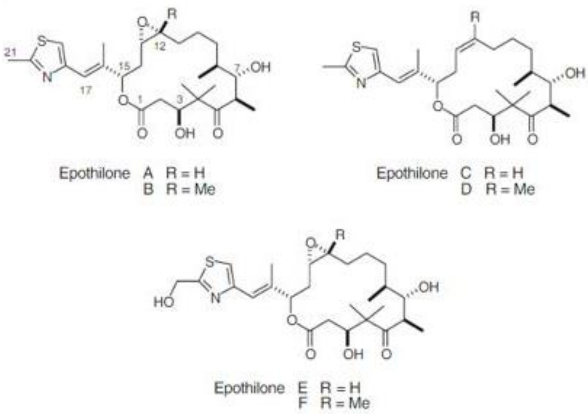

Fig. 1. Chemical structure of Epothilone A-F (Lee et al., 2008)

Epothilone has great commercial value. Such as ixabepilone, which is a second-generation epothilone B derivative and where an azide group had replaced oxygen on position 16 of the macrolide ring, has been approved for injection in combination with capecitabine against metastatic or locally advanced breast cancer resistant-to-taxane by FDA, in 2007 (Conlin et al. 2007; Nicolaou et al. 1997).

In this study, purification and characterization of epothilone in the crude extract of *G. lineata* were performed. *G. lineata* was grown in liquid media to extract epothilone, and after 21 days of growth, epothilone was extracted using well-established procedures. Chemical characterization included spectroscopic analyses such as TLC, HPLC, and LC-MS. This endophyte SDL-CO-2015-1, identified as *G. lineata* is the first-ever Basidiomycete found to possess a capacity for epothilone production.

Materials and Methods

Sequencing of *G. lineata*

G. lineata SDL-CO-2015-1 isolated from jute seedlings in the Molecular Biology laboratory, Dept. of Biochemistry and Molecular Biology, University of Dhaka, was sequenced and submitted to NCBI (accession number NDFF02000000) (Das et al., 2017).

In silico identification of epothilone in *G. lineata*

Natural product database-based screening was done for the sequence of *G. lineata* SDL-CO-2015-1 to find the potential of this fungus to produce important metabolites. Initially, screening was done with NaPDoS. NaPDoS is a bioinformatic tool that detects and analyzes secondary metabolite genes (Ziemert et al., 2012). This tool detects and extracts condensation (C-) and ketosynthase (KS-) domains from DNA or amino acid sequence data, including PCR amplicon products, individual genes, whole genomes, and metagenomic data sets. Choosing KS as domain type and predicted protein sequences (amino acid) as query type, protein sequence data of *G. lineata* SDL-CO-2015-1 was entered to identify candidate KS domains for significant secondary metabolite production. BLASTx was done to check whether these four genes found by NaPDoS can also be found in the RNA-Seq data. NaPDoS prediction of *G. lineata* producing epothilone was based on the presence of four genes mentioned above that matched with EposD of *S. cellulosum*. We further analyzed the similarity of these proteins with EpoD.

In vitro identification of Epothilone

Culture of the *G. lineata*

G. lineata SDL-CO-2015-1 was grown in potato dextrose agar (PDA) media to maintain regular subculture and later in potato dextrose broth (PDB) media to obtain the fungal extract and to examine if *G. lineata* produced epothilone. For the submerged culture, the fungus was allowed to grow in an Erlenmeyer flask (500 mL) containing PDB medium (potato 200 g/L and glucose 20 g/L) (Fig. 2).

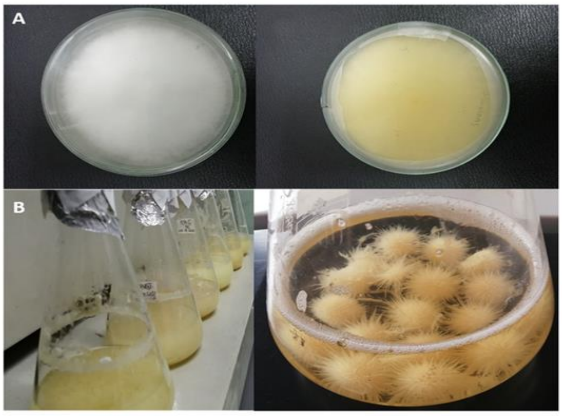

Fig. 2. Cell culture images of *G. lineata*. (A) Solid culture of *G. lineata* (left, front, and right, back view). (B) Submerged culture of *G. lineata* in PDB media to obtain fungal extracts. Twenty-one days old submerged culture (left) and 10 days old submerged culture (right).

The overall pH was adjusted to 5.5-5.6, which was optimal for the growth of basidiomycete. Following the inoculation, the flask was incubated at ~28^{0}C and 180 rpm for 21 days in an incubating shaker (LabTech, Model LSI-1005R).

Extraction of epothilone from culture supernatant using XAD-16

After 21 days of culture, the fungus was filtered to obtain the extracellular components. Firstly, the mycelia were separated from the broth using a gauze bandage in the funnel. Then the supernatant was filtered using filter paper (Whatman ® Schleicher and Schuell Ashless filter paper, 110cm). XAD-16 resin extracted epothilone from the supernatant (Cao et al., 2018). 1.5% (w/v) XAD-16 resin was weighed, activated, and shacked with 200 mL filtered culture broth in an Erlenmeyer flask (500 mL). Shaking allowed proper agitation, so XAD-16 could absorb epothilone and its related compounds.

The resins were rescued and dried after 2-3 days of continuous shaking. Dried resins were eventually soaked into carbon tetrachloride where the resin-tetrachloromethane ratio was maintained at 1:4 (w/v). After soaking for 2-3 hours, filtration was carried out using a small-sized column with glass wool placed at the bottom to restrict the flow of resins. Residues were extracted in the same way after filtering 2-3 times. Finally, after combining all extracts, they were evaporated under a vacuum at 45^{0}C in a 25 mL round bottom flask using a rotary evaporator. After complete evaporation, the residues attached to the bottom of the flask were dissolved in 2 mL of HPLC-grade methanol and collected. The samples were then preserved at -80°C until their subsequent use.

Chromatographic separation of epothilone crude extract

To detect the presence of epothilone, thin layer chromatographic (TLC) analysis was carried out on

Macherey Nagel & Co. KG 0.2 mm (20×20 cm) silica gel pre-coated plate where petroleum ether: acetone (5:1, v/v) was used as the mobile phase. Samples were loaded at one end, 1 cm from the edge, along with the standard (commercial Epothilone B, Sigma-Aldrich). The TLC bands were then visualized under UV light at a wavelength of 365 nm. A reverse phase C18 column (AcclaimTM 120, C18, 250×4.6 mm, particle size 5µm, pore size 120 A^0) was used to analyze the crude extract by RP-HPLC. Standard epothilone and lyophilized epothilone extract were dissolved in HPLC-grade methanol, filtered, and injected into the column at 20 µL. A multistep gradient system of fifty minutes was performed with methanol and nano-pure water with 0.05%TFA (Tri-Fluoro Acetic Acid) with an optimized protocol (retention time 0-10 min, H_2O+0.05%TFA combination 90%, methanol 10%, retention time 10-30 min, H_2O+0.05%TFA combination 40%, methanol 60%, retention time 30-40 min, H_2O+0.05%TFA combination 40%, methanol 60% and retention time 40-50 min, H_2O+0.05%TFA 90%, methanol 10%). The fraction with the same retention time as the standard was collected. 249 nm wavelength was used to detect compounds eluted from the column. The LC-MS measurement was performed on an Agilent 6400 series Triple Quadrupole B.09.00 utilizing a Waters Acquity BEH C-18 column (100 × 2.1 mm, 2.2-µm particle size). Separation of the sample was obtained with a multistep gradient of A (methanol + 0.1% formic acid) and B (water) at a flow rate of 0.2 mL/min at 25°C. UV spectra were recorded by a DAD (Diode Array Detector) at 254 nm and 249 nm. MS measurement was carried out using the standard ESI (Electrospray Ionization) source that was equipped with a turbo ion spray source operating at 350°C with the fragmentation voltage set to 135V and collision energy at 35V. Mass spectra were acquired in centroid mode ranging from 100-600 m/z in positive ionization mode with auto MS2 fragmentation.

Results

Morphological Characterization of PCR Positive Fungal Isolate, SDL-CO-2015-1

The SDL-CO-2015-1 colonies are white and cottony type, and on the reverse side, they are yellowish-white (Fig. 2), widely effused, growing over the edge of the petri dish and becoming dark with age. No color change is observed when it ~~became~~ becomes dry. The texture of the intermediate layer is highly gelatinized.

In silico identification of epothilone

Screening of *G. lineata* sequence based on natural product database

NaPDoS identified four protein sequences from the *G. lineata* sequence data that matched with EpoD of the epothilone gene cluster (Table 1). Notably, the EpoD (EpoD_Q9L8C7_4mod) gene of the epothilone gene cluster is crucial in the epothilone production pathway (Fig. 3) (Hardt et al., 2001).

Identification of NaPDoS predicted epoD gene product in RNA-seq data

In BLASTx, three out of four genes identified by NaPDoS matched 100% with different genes from RNA-seq data (Table 2).

They are epo2 (>maker-jcf7180000002626-augustus-gene-0.115-mRNA-1 protein AED:0.06 eAED:0.06 QI:0|1|1|1|1|1|17|0|1935), epo3 (>maker-jcf7180000002765-augustus-gene-0.65-mRNA-1 protein AED:0.06 eAED:0.06 QI:0|1|1|1|1|1|17|0|1955) and epo4 (>maker-jcf7180000002765-snap-gene-0.98-mRNA-1 protein AED:0.07 eAED:0.07 QI:0|1|1|1|0.94|0.88|18|0|1914) which showed 100% similarity with the genes from RNA-Seq data.

Table 1. *In silico* identification of epothilone gene cluster in *G. lineata* by NaPDoS

Query ID	Database Match ID*	E-value	Pathway Product
maker-jcf7180000002760-snap-gene-0.98-mRNA-1	EpoD_Q9L8C7_4mod	$6e^{-64}$	epothilone
maker-jcf7180000002626-augustus-gene-0.115-mRNA-1	EpoD_Q9L8C7_4mod	$7e^{-57}$	epothilone
maker-jcf7180000002765-augustus-gene-0.65-mRNA-1	EpoD_Q9L8C7_4mod	$3e^{-67}$	epothilone
maker-jcf7180000002765-snap-gene-0.98-mRNA-1	EpoD_Q9L8C7_4mod	$3e^{-54}$	epothilone

*From the *G. lineata* sequencing data, NaPDoS discovered four protein sequences that matched EpoD (EpoD_Q9L8C7 _4mod) of the epothilone gene cluster.

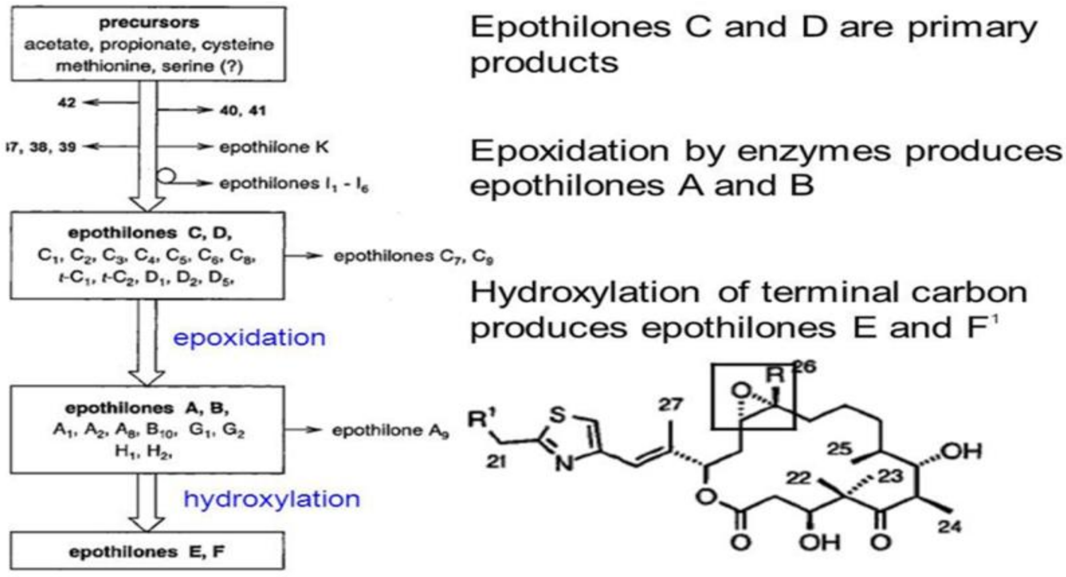

Epothilones C and D are primary products

Epoxidation by enzymes produces epothilones A and B

Hydroxylation of terminal carbon produces epothilones E and F[1]

Fig. 3. Biosynthesis of Epothilones (Hardt et al., 2001)

Table 2. Identification of epothilone-producing gene cluster in *G. lineata* RNA analysis

Query	Subject	Identity	Alignment	q_start	q_end	s_start	s_end
[a]maker-jcf7180000002626-augustus-gene-0.115-mRNA-1	epo2	100	1935	1	5805	1	1935
[b]maker-jcf7180000002765-augustus-gene-0.65-mRNA-1	epo3	100	1955	1	5865	1	1955
[c]maker-jcf7180000002765-snap-gene-0.98-mRNA-1	epo4	100	1914	1	5742	1	1914

***In the BLASTx analysis, three out of the four genes identified by NaPDoS showed a 100% match with different genes from RNA-seq data. These genes are [a]epo2, [b]epo3, and [c]epo4.

Molecular and phylogenetic analysis of epothilone genes

Based on the existence of the four genes listed above that corresponded with EposD of *S.cellulosum*, NaPDoS predicted that *G. lineata* would produce epothilone. Therefore, we further approached to examine how closely these proteins resemble EpoD. BLAST result showed around 35% similarities for all four proteins with EpoD. This result is reasonable as *S. cellulosum* is a bacterium, whereas *G. lineata* is a fungus. So, epothilone must be produced in different pathways in these two microorganisms. However, recently *Aspergillus fumigatus* has been reported to produce epothilone B.

Since it is a fungus, we tried to see if our four protein sequences identified by NaPDoS had better similarity with the EpoA of *A. fumigatus* than with *S. cellulosum*. A phylogenetic tree was constructed using four matched proteins: *A. fumigatus* EpoA, *A. alternata* EpoA, *S. cellulosum* EpoA, and EpoD. *A. fumigatus* EpoA showed the best similarities with the four matched proteins. Four matched proteins had 77 percent similarity with the *A. fumigatus* EpoA (Fig. 4). Moreover, a BLAST search of the four matched proteins in the NCBI database found different polyketide synthase (PKS) gene clusters from different basidiomycete fungi. As the epothilone gene cluster is present in PKS or NRPS, it suggested the involvement of four matched proteins in epothilone production. With all these bioinformatics data, we stepped forward to extract epothilone from *G. lineata*.

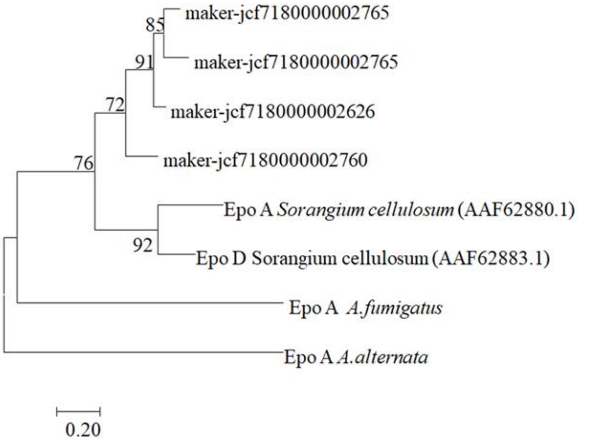

Fig. 4. Phylogenetic analysis of Epothilone genes cluster. The phylogenetic tree was designed based on genome sequences of *A. fumigatus*, *G. lineata*, *A. alternata*, and *S. cellulosum*.

In vitro identification of Epothilone

Chromatographic Separation of *G. lineata* Extract

TLC plate showed matching bands of bluish-green color for standard epothilone B and the fungal extract obtained from XAD-16 resin at the UV wavelength of 365 nm (Fig. 5). R_f values for both these bands were 0.78, which was similar to the previously reported value for epothilone B under the same solvent system of petroleum ether: acetone (5:1, v/v). Standard epothilone B was eluted at a retention time of 40.9 minutes. This peak generated at the 41st minute produced a typical spectrum for epothilone B (Yang et al., 2015). A characteristic peak with an almost similar retention time as standard epothilone B was obtained for the extracellular crude extract of the fungus in RP-HPLC, in a multistep gradient solvent system (Fig. 6). The reference epothilone B and the HPLC sample of the SDL-CO-2015-1 extract both produced a distinctive molecular ion peak $(M+H^+)$ at 508.1 Da during the LC-MS/MS scan. They also had the typical MS2 fragments at m/z 420.0 Da and 320.2 Da in the production mode (Fig. 7).

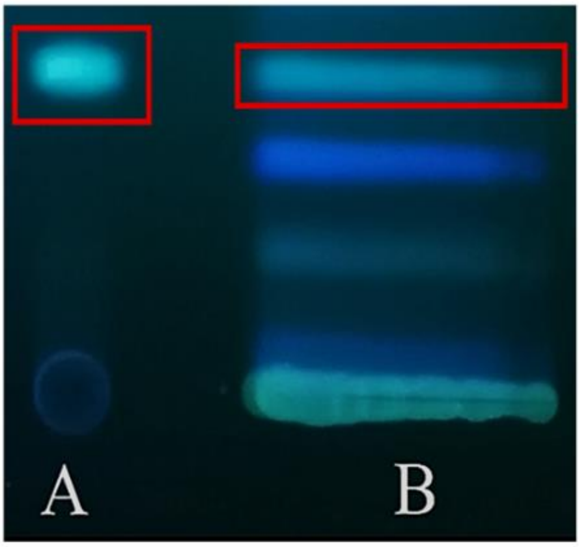

Fig. 5. Putative epothilone B was visualized under UV at 365 nm in TLC plate. (A) The Standard Epothilone B as a control and (B) Bands for the Fungal Extract was seen in the experimental samples performed in this study.

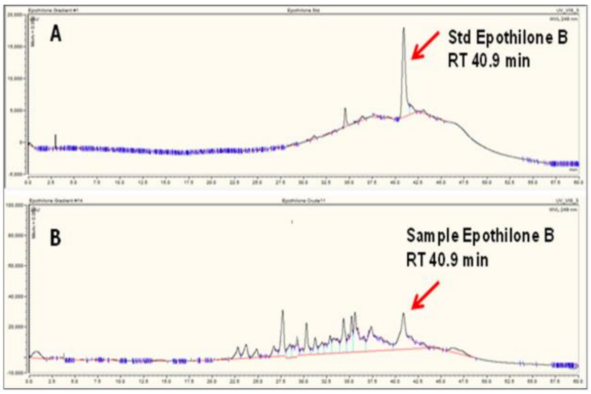

Fig. 6. Active fractions images of RP-HPLC column chromatography. (A) Standard epothilone B was eluted at 40.9 minutes. (B) Crude extract from *G. lineata* runs under the same condition generating a peak at 40.9 minutes.

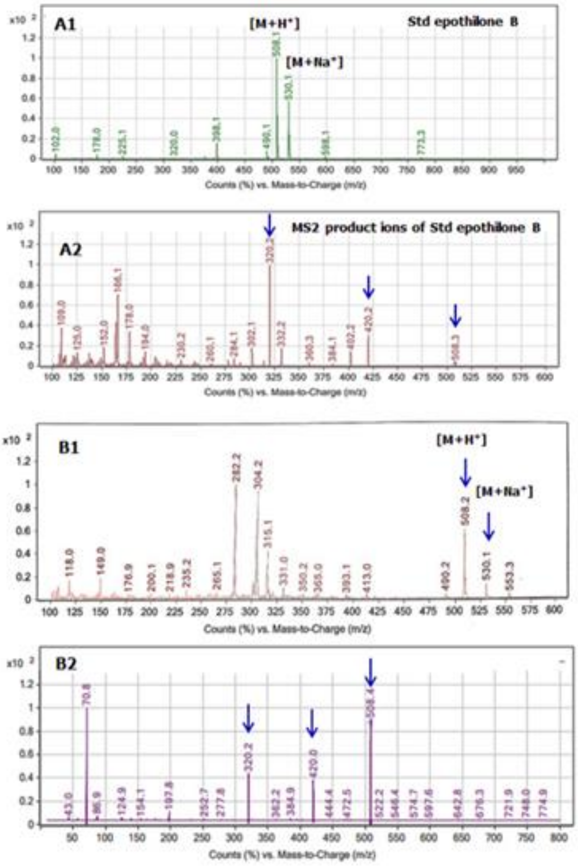

Fig. 7. HPLC fractions of *G. lineata* crude extract. Several strong peaks were found in each mass/charge (m/z) state. (A1) Molecular mass [M+H$^+$] 508.10, [(M+Na$^+$) 530.10] of standard epothilone B and (A2) its MS2 fragments (m/z 420.20 and 320.20) (top right). (B1) Molecular mass [M+H$^+$] 508.20, [M+Na$^+$] 530.10, and (B2) MS2 fragments (m/z 420.00 and 320.20) of the 40.9 minute.

Discussion

G. lineata SDL-CO-2015-1 is an endophytic fungus that had been isolated from jute. It is a basidiomycete fungus and has been reported to produce paclitaxel. The draft genome of this potential fungus sequence was declared in 2017 (Das et al., 2017). During different screening techniques both *in silico* and *in vitro*, there were indications of *G. lineata* SDL-CO-2015-1 producing another important compound named epothilone. These indications led us to work further to extract and identify epothilone from this fungus.

NaPDoS predicted that *G. lineata* SDL-CO-2015-1 might produce epothilone. It was predicted that four endophytic fungus genes showed similarities with the EposD gene of *S. cellulosum*. EposD comprises two of the eight PKS modules (module 6 and module 7) of the epothilone gene cluster in this bacterium. One vital factor to be noted is that the synthesis of the gem-dimethyl unit in epothilone is done by module seven from EPOS D. This gem-dimethyl formation is a striking feature in epothilone production (Molnár et al., 2000). So, the similarity of *G. lineata* with EposD increases the chances of epothilone being produced by this fungus.

The jute endophyte *G. lineata* SDL-CO-2015-1 was found to be able to produce epothilone B in our investigation. This assertion was verified by various *in silico* and *in vitro* analytical techniques, although the whole process took a very long time. Firstly, from the *G. lineata* sequencing data, NaPDoS discovered four protein sequences that matched EpoD of the epothilone gene cluster. To determine whether these four genes discovered by NaPDoS can also be found in the RNA-Seq data, another *in silico* approach BLASTx, was used. In BLASTx results, three of the four genes, epo2, epo3, and epo4, were also found to have 100% similarity to other genes in the RNA-seq data. Molecular and phylogenetic analysis of epothilone genes also supported it. In the case of *in vitro* analysis, TLC, RP-HPLC, and LC-MS/MS were performed to confirm the presence of epothilone in the sample. TLC plate presented bands of the same color and R_f value for the standard and the purified epothilones from the endophyte culture. R_f values for each of these bands were 0.78, comparable to the value for epothilone B in the same petroleum ether: acetone solvent system that was previously reported. The standard epothilone B and the purified epothilones from the endophyte culture gave a characteristic peak at the same retention time, 40.9 minute. Finally, LC-MS data identified epothilone B's molecular mass and MS2 fragments.

G. lineata has not been reported to produce epothilone in any literature. It is not only the first fungus but also the first eukaryote to produce epothilone. Epothilone is produced by only a few strains of the soil myxobacterium, *Sorangium* (S. guang Li et al., 2014). No other myxobacterium, and indeed no other organism, has been found to produce epothilone so far. So, *G. lineata* is the second organism after *Sorangium* to produce this valuable compound. The discovery of the first-ever epothilone-producing Basidiomycota fungus is another significant finding. Fungi under the phylum of Basidiomycota are known to produce a variety of cytotoxic compounds (Sandargo et al., 2019). Endophytic fungi that produce anticancer components have been described up to this point in time in roughly 46 genera and 111 species. Taxonomically, 96% of them are Ascomycota, with just 3% of them being from the Basidiomycota phylum (Chen et al., 2016) Thus, *G. lineata* with the ability to produce epothilone may not be surprising under these circumstances. The largely untapped fungal kingdom may reveal more members capable of producing diverse bioactive compounds.

Epothilone has been reported to have narrow antifungal activity (Hofle et al., 1996). Since the epothilone-producing fungus, *G. lineata* is an endophyte; it may be assumed that epothilone production may have a role in providing an extracellular barrier against pathogens (fungicidal) to its host plant, or it may be produced to defeat other fungi as a survival instinct.

Conclusion

Only a few strains of myxobacterium produce epothilone, *Sorangium* has reported so far. Due to the limited production of this expensive compound from microbial origin, there are no options other than chemical synthesis for large-scale production. In this study, we report that a novel fungi *G. lineata* SDL-CO-2015-1, isolated in our lab, can produce epothilone B in culture conditions. The culture condition and production is yet to be optimized for scale-up. Moreover, strain improvement can be done using mutational analysis. Cytotoxicity tests in the cancer cell line must be performed using purified epothilone.

Conflict of Interest

The authors declare no competing financial interest.

Acknowledgments

The project is funded by ICGEB, Trieste, Italy (CRP/BGD17-01). The authors thank the Bangladesh Council for Scientific and Industrial Research (BCSIR) for their LC/MS support.

References

Cao YN, Zheng LL, Wang D, Liang XX, Gao F and Zhou XL. Advances in microtubule-stabilizing agents.*Eur. J. Med. Chem.*2018; 143: 806-828.

Chen L, Zhang QY, Jia M, Ming QL, Yue W, Rahman K, Qin LP and Han T. Endophytic fungi with antitumor activities: Their occurrence and anticancer compounds. *Crit. Rev. Microbiol.*2016; 42(3): 454-473.

Conlin A, Fornier M, Hudis C, Kar S and Kirkpatrick P. Ixabepilone. *Nat. Rev. Drug Discov.*2007; 6(12): 953-954.

Das A, Rahman MI, Ferdous AS, Amin A, Rahman MM, Nahar N, Uddin MA, Islam MRand Khan H. An endophytic basidiomycete, grammothele lineata, isolated from corchorus olitorius, produces paclitaxel that shows cytotoxicity. *PLOS ONE*, 2017;12(6): e0178612.

Gangadevi V and Muthumary J. Taxol, an anticancer drug produced by an endophytic fungus Bartalinia robillardoides Tassi, isolated from a medicinal plant, Aegle marmelos Correa ex Roxb. *World J. Microbiol. Biotechnol.* 2008;24(5):717-724.

Gong GL, Sun X, Liu XL, Hu W, Cao WR, Liu H, Liu WFand Li YZ. Mutation and a high-throughput screening method for improving the production of Epothilones of Sorangium. *J. Ind. Microbiol. Biotechnol.* 2007; 34(9): 615-623.

Hardt IH, Steinmetz H, Gerth K, Sasse F, Reichenbach H and Höfle G. New natural epothilones from Sorangium cellulosum, strains So ce90/B2 and So ce90/D13: Isolation, structure elucidation, and SAR studies. *J. Nat. Prod.*2001; 64(7): 847-856.

Höfle G, Bedorf N, Steinmetz H, Schomburg D, Gerth K and Reichenbach H. Epothilone A and B-Novel 16-Membered macrolides with cytotoxic activity: Isolation, crystal structure, and conformation in solution. *Angew. Chem. Int. Ed. Engl.* 1996; 35(13-14): 1567-1569.

Lee FYF, Borzilleri R, Fairchild CR, Kamath A, Smykla R, Kramer R and Vite G. Preclinical discovery of ixabepilone, a highly active antineoplastic agent. *Cancer Chemother. Pharmacol.*2008; 63(1):157-166.

Li CJ, Huang SY, Wu MY, Chen YC, Tsang SF, Chyuan JH and Hsu HY. Induction of apoptosis by ethanolic extract of corchorus olitorius leaf in human hepatocellular carcinoma (HepG2) cells via a mitochondria-dependent pathway. *Molecules (Basel, Switzerland)*, 2012;17(8): 9348-9360.

Li S guang, Zhao L, Han K, Li P fei, Li Z, feng Hu W, Liu H, Wu Z hong and Li Y zhong. Diversity of epothilone producers among Sorangium strains in producer-positive soil habitats. *Microb. Biotechnol.*2014; 7(2):130-141.

Molnár I, Schupp T, Ono M, Zirkle RE, Milnamow M, Nowak-Thompson B, Engel N, Toupet C, Stratmann A, Cyr DD, Gorlach J, Mayo JM, Hu A, Goff S, Schmid Jand Ligon JM. The biosynthetic gene cluster for the microtubule-stabilizing agents epothilones A and B from Sorangium cellulosum So ce90. *Chem. Biol.* 2000;7(2):97-109.

Nicolaou KC, Winssinger N, Pastor J, Ninkovic S, Sarabia F, He Y, Vourloumis D, Yang Z, Li T, Giannakakou P and Hamel E. Synthesis of epothilones A and B in solid and solution phase. *Nature*, 1997;387(6630): 268-272.

Sandargo B, Chepkirui C, Cheng T, Chaverra-Munoz L, Thongbai B, Stadler M and Huttel S. Biological and chemical diversity go hand in hand: Basidiomycota as source of new pharmaceuticals and agrochemicals. *Biotechnol. Adv*. 2019; 37(6): 107344.

Schulz B, Boyle C, Draeger S, Römmert AKand Krohn K. Endophytic fungi: a source of novel biologically active secondary metabolites. *Mycol. Res.*2002; 106(9): 996-1004.

Shrestha K, Strobel GA, Shrivastava SP and Gewali MB. Evidence for paclitaxel from three new endophytic fungi of Himalayan Yew of Nepal. *Planta Med.*2001; 67(4): 374-376.

Stone JK, Bacon CW and White JF. An overview of endophytic microbes: endophytism defined. In: *Microbial Endophytes*, 1st Edition, Chapter 3, Bacon CW and White JF (eds.), Marcel Dekker, New York, 2000, pp. 3-29.

Strobel GA. Endophytes as sources of bioactive products. *Microbes Infect.*2003;5(6):535-544.

Wang J, Li G, Lu H, Zheng Z, Huang Yand Su W. Taxol from Tubercularia sp. strain TF5, an endophytic fungus of Taxus mairei. *FEMS Microbiol. Lett.*2000;193(2): 249-253.

Yang H, Zhang Z, Tang W, Ren L, Wang D, Sun Fand Zheng W. Preparative isolation and purification of epothilones from *Sorangium cellulosum* fermentation broth by high-speed counter-current chromatography. *J. Liq. Chromatogr. Relat. Technol.*2015; 38(1):123-127.

Zaman NR. Characterization of jute endophytes with inhibiting activity against Macrophomina phaseolina. Ph.D. Thesis, Department of Biochemistry and Molecular Biology, University of Dhaka, 2019.

Ziemert N, Podell S, Penn K, Badger JH, Allen E, and Jensen PR. The natural product domain seeker NaPDoS: A phylogeny based bioinformatic tool to classify secondary metabolite gene diversity. *PLOS ONE*,2012;7(3): e34064.

J. Bangladesh Acad. Sci. 47(1); 101-108: June 2023 DOI: https://doi.org/10.3329/jbas.v47i1.64895

Journal of Bangladesh Academy of Sciences

Journal homepage: http://www.bas.org.bd/publications/jbas.html

Research Article

Physiological causes of yield variation in similar durated mungbean genotypes

M. Monjurul Alam Mondal*, Md. Azadul Haque and Md. Mohimenul Islam[1]

Crop Physiology Division, Bangladesh Institute of Nuclear Agriculture
BAU Campus, Mymensingh, Bangladesh

ARTICLE INFO

Article History

Received: 01 January 2022
Revised: 31 May 2023
Accepted: 11 June 2023

Keywords: Growth, Reproductive characters, Yield, Mungbean, Variation, Physiology

ABSTRACT

The experiment was conducted during February to May, 2019 at the research farm of Bangladesh Institute of Nuclear Agriculture, Mymensingh-2202. The objective of the study was to evaluate the growth, reproductive characteristics, yield and yield components of four similar durated mungbean genotypes, namely BARI Mung-2, Binamoog-2, MB-29, and MB-43. At most of the growth stages, the mutant MB-29 showed superiority in terms of growth parameters such as total dry matter, leaf area index, absolute growth rate, relative growth rate, and net assimilation rate whilst MB-43 showed the inferiority. Furthermore, MB-29 outperformed the other three genotypes in yield attributing features, resulting in a higher seed yield than the other three genotypes. In comparison, the MB-43 mutant showed the lowest value for the yield parameters. The seed yield correlated positively and significantly with leaf area, total dry matter, absolute growth rate, and number of pods plant^{-1}.

Introduction

Mungbean [*Vigna radiata* (L.) Wilzsek] is a superior supplementary source of protein for a rice-based diet. Mungbean contains more protein than cereals do. 51% of mungbean is made up of carbohydrates, 26% of it is protein, 4% is mineral, and 3% is vitamin (Mwangi et al., 2021). In addition to adding important protein to the diet, mungbean has the impressive property of assisting the symbiotic root rhizobia in fixing atmospheric nitrogen, thus improving the soil (Bam et al., 2022). It is typically grown in the dry season after winter crops, though it can also be grown in the Kharif-II season. The largest barrier to the production of mungbean is its low yield potential (average 960 kg ha^{-1}; BBS, 2020). There are numerous causes for the low yield (Mondal et al., 2011a). The cultivars used have a low genetic yield potential and are vulnerable to disease and pests. According to Mondal et al. (2011b), between 70 and 85 percent of mungbean flowers do not mature into mature pods, indicating that the number of potential fruits or seeds is typically much higher than the number that the plant vegetation actually generates. After growth stage R1 (fruit setting stage), the number of fruits with working to develop seeds rises, and it reaches its maximum after growth period R5 (maximum seed growth stages) (Mondal et al., 2012). However, during this time, the plant is still growing vegetatively. As a result, generating reproductive sinks is in competition with vegetative sinks for nutrients. It is evident that the number of seeds per unit area influences canopy photosynthesis during flowering and pod development. Additionally, canopy photosynthesis rate determines through leaf area index and crop growth rate.

---

*Corresponding author: <mmamondal@gmail.com>

[1] *Adaptive Research and Extension Division, Bangladesh Institute of Nuclear Agriculture, BAU Campus, Mymensingh, Bangladesh.*

Significant physiological characteristics such as leaf area index (LAI), relative growth rate (RGR), crop growth rate (CGR), specific leaf weight (SLW), and net assimilation rate (NAR) could indeed discuss a variety's productivity limitations. A plant with best LAI and NAR may have a greater biological yield. The ability to efficiently partition between vegetative and reproductive parts may result in high yield potential (Mondal et al., 2011c). For optimum yield in mungbean, the LAI should be ranged from 3.5 to 4.5 (Ali et al., 2021). Any reduction in leaf area or light amount or intensity may have a negative impact on yield (Mondal et al., 2011d). If the LAI reaches its maximum value in the shortest time, the dry matter accumulation may be the greatest (Mondal et al., 2012).

Several research institutes in Bangladesh, including BARI, BINA, and BSMRAU, have developed a couple of summer mungbean varieties that are higher yielding than local landraces, with yield variation ranging from 1100 to 1600 kg ha^{-1} (Mondal et al., 2015). The yield variation of similar durated mungbean genotypes need to be assessed for its physiological growth and morphological maneuvering that takes place yield variation

The current study has been designed to study various growth and reproductive characteristics that contribute to higher biological and grain yields. Thus, the research work was carried out to evaluate the growth and development of similar durated (duration 69–72 days) two elite summer mungbean mutants (MB-29 and MB-43) compared to the existing two varieties (BARI Mung-2 and Binamoog-2), and to find out the physiological reason for yield variation in similar durated mungbean genotypes.

Materials and Methods

The experiment was conducted during February to May, 2019 at the research farm of Bangladesh Institute of Nuclear Agriculture, Mymensingh-2202. Similar duration (69-72 days) of two high yielding promising mutants namely MB-29 and MB-43 and two released varieties viz., BARI Mung-2 and Binamoog-2 were used as planting material. At first, the seeds of the mungbean genotypes were sown 05 March 2019. The experiment was conducted with randomized complete design with three replications. Each unit plot size and plant spacing were 3 m × 3 m and 30 cm × 10 cm, respectively. The dose of fertilizers (N-P-K-S) were 20, 60, 40 and 15 kg ha^{-1} respectively (BARC, 2018). The total fertilizer except nitrogen was applied at the time of land preparation as basal dose. Twenty days after sowing the first weeding was performed. The irrigation was supplied at 21 days after sowing. For controlling shoot and fruit borer, Ripcord 50 EC insecticide was sprayed at 0.025% at the stage of flowering and grain filling.

To study ontogenetic growth characteristics, a total of five harvests were made. The second and third rows of each plot were used for sampling (Hunt, 1978). A first plant sample was taken at 20 DAS, and it was taken every ten days interval until the crop reached fruit physiological maturity maturity at 70 DAS. From each sampling, five plants were randomly selected from second and third rows of each plot and uprooted to collect necessary parameters. The plant's parts (roots, stems, leaves and pods) were separated. Then the separated plant parts were oven-dried at 80°C for 72 hours, and their oven-dry weight was taken. A leaf area meter (Model: LICOR 3000, automatic, USA) was used to measure the leaf area. The Hunt formulae (1978) was applied to analyze the growth characters such as absolute growth rate and relative growth rate. The opened flowers per plant were counted from fifteen plants, five plants from each plot. The opened flowers per plant were counted daily. The opening flower counting was done following the method of Fakir et al. (2011). The flowering duration was 12 to 18 days depending on genotypes. Reproductive efficiency was calculated using following formulae: % pod set = (Number of pods plant^{-1} ÷ Number of opened flowers plant^{-1}) ×100. The yield contributing characters were recorded at the time of harvest from ten plants. Five rows from each plot (1.50 m × 3.0 m) were used to measure the seed yield, which was then converted into seed yield per hectare. The seed weight per plant was calculated by seed weight of 10 plants divided by 10. Harvest index was calculated from the collected data using formula: (economic yield/plot ÷biological yield/plot)×100. The computer package program MSTAT-C was used to analyze the collected data. The LSD test was also performed to investigate the pairwise difference between the treatments means.

Results and Discussion

Growth parameters

Fig. 1 depicts the evolution of leaf area (LA) and leaf area index (LAI) in mungbean genotypes over time. The results showed that LA and LAI increased until 60 days after sowing (DAS), then decreased due to leaf shedding. At all growth stages except 20 DAS, the increasing levels of LA and LAI differed widely due to genotype. At all growth stages, the mutant MB-29 had the highest LA and LAI, followed by BARI Mung-2. MB-43, on the other hand, had the lowest LA and LAI during its growth period. The variation in LA and LAI might occur due to the variation in leaf number and the expansion of leaves. The result obtained from the present study was consistent with the result obtained by Lema et al. (2018) in mungbean, who stated that variation in LA and LAI could be attributed to changes in the number of leaves and rate of leaf expansion and abscission.

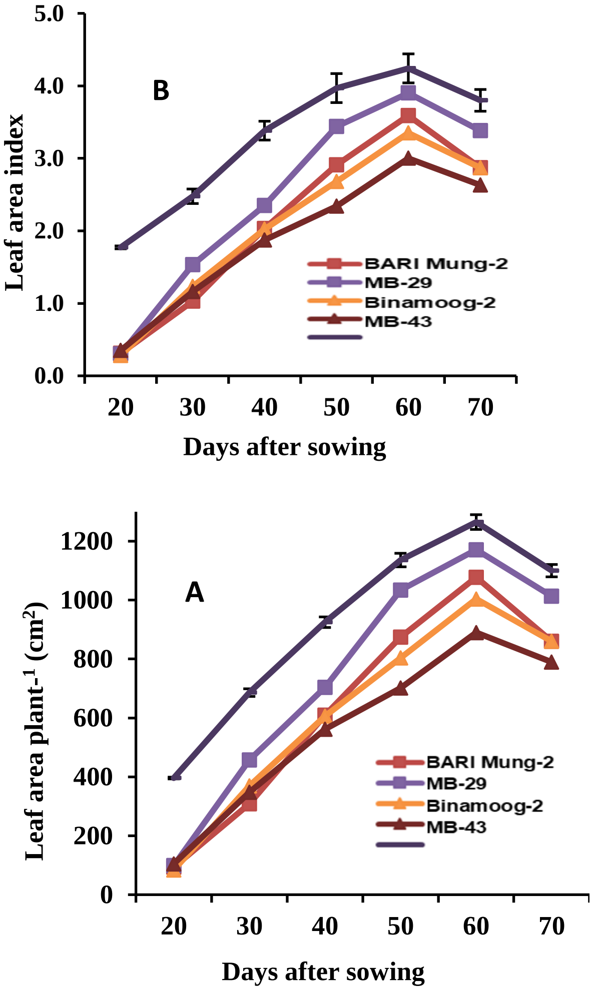

Fig. 1. Showing (A) leaf area and (B) leaf area index of similar durated four mungbean genotypes at different growth stages.

At all growth stages, mungbean genotypes showed considerable ontogenetic differences in total dry matter (TDM) production and absolute growth rate (AGR) (Fig. 2). TDM was gradually increased in all genotypes up to 40 DAS before increasing quickly until maturity. Comparing the mutant MB-29 to other genotypes, it produced more TDM at all growth stages, whereas MB-43 produced less TDM at all growth stages. TDM may have been increased in the MB-29 due to higher AGR and LAI (Fig. 1B) (Fig. 2B). The finding was corroborated by research from Mondal et al. (2012), who found that TDM increased as plant age increased up to physiological maturity.

The AGR increased gradually until 40 DAS, then increased quickly until 60 DAS, and then decreased as maturity progressed. Over the course of the growth period, MB-29, the high yielding mutant, consistently maintained the highest AGR value. The low yielding genotype MB-43, on the other hand, had the lowest AGR throughout the majority of the growth stages. Additionally, for all genotypes, the highest AGR was seen during the development of the pod and the grain filling stage (50–60 DAS). AGR and LAI have a positive correlation (Hamid et al., 1991). Along with the LAI growth, the AGR also

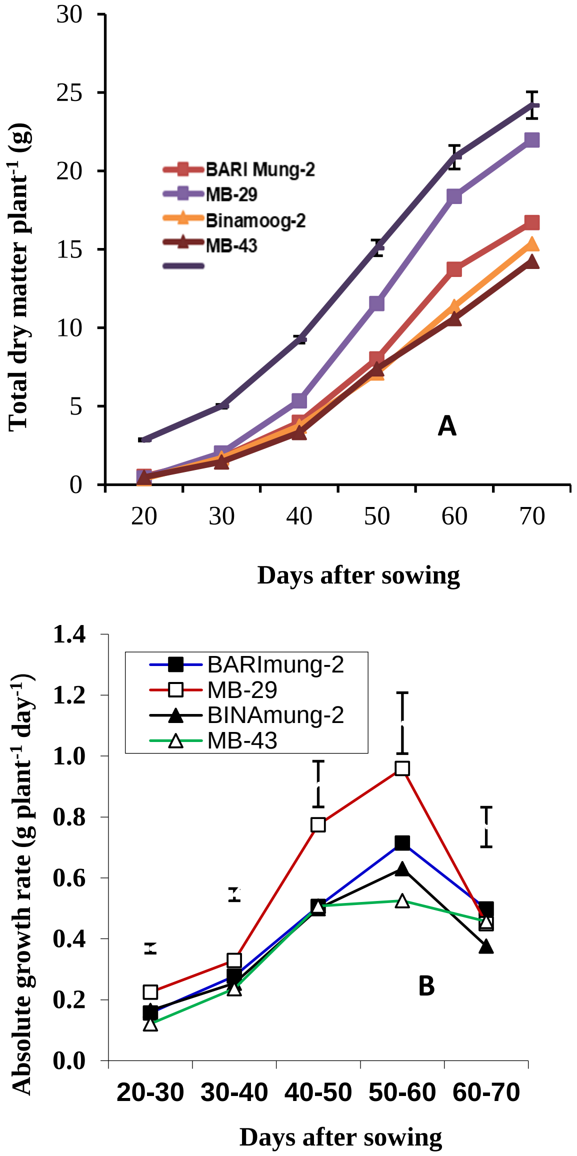

Fig. 2. Pattern of (A) total dry mass production and (B) absolute growth rate of similar durated four mungbean genotypes during their growth period.

increased. Lower LAI caused the lower AGR value during the early growth stages (Fig. 1B). The AGR value was found to be at its maximum at 50–60 DAS, indicating that the plant had increased its ability to assimilate for the growth of leaf area and feeding of pods. The abscission of leaves may have caused the AGR to decline after reaching its peak in all genotypes. These outcomes were in line with those of Mondal (2012) and Dutta and Mondal (1998) for mungbean and lentil, respectively.

At all growth stages, mungbean genotypes showed significant variation in their relative growth rates (RGR) and net assimilation rates (NAR) (Fig. 3). Initially, the RGR and NAR values were high and decreasing with age until maturity. RGR decreased substantially in the majority of field crops as plant age increased (Mondal et al., 2011c; Malek et al., 2012; Mondal et al., 2015). The genotypes' RGR and NAR values peaked between 20 and 30 DAS and then began to decline, reaching their lowest points at maturity (60–70 DAS). The mutant MB-29 showed superiority in AGR, RGR and NAR at most of the growth stages compared to other

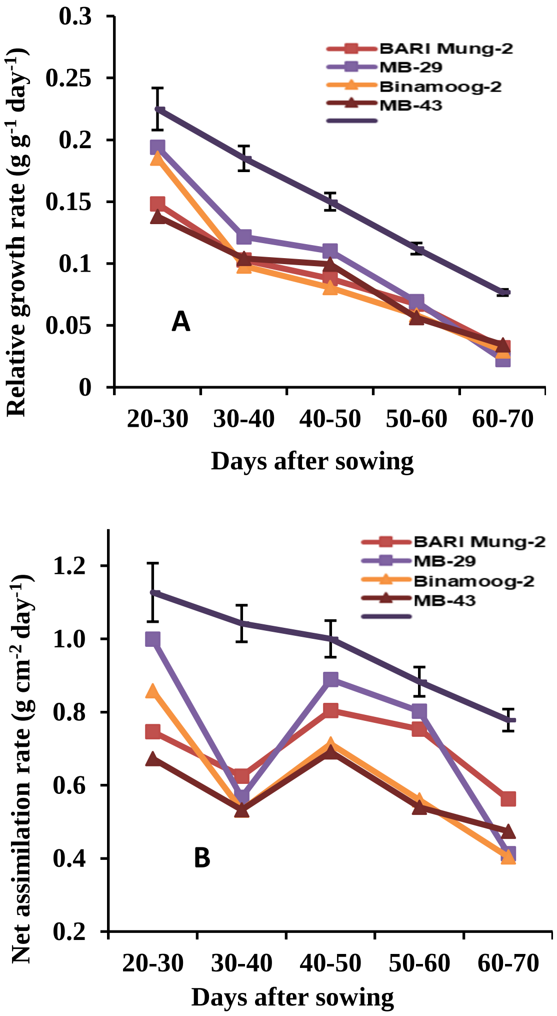

Fig. 3. Changes in (A) relative growth rate and (B) Net assimilation rate of similar durated four mungbean genotypes during their growth period.

three genotypes whilst MB-43 showed inferiority. A higher growth rate was positively correlated with seed yield (Mondal et al., 2013; Lema et al., 2018). In the current experiment, the mutant MB-29 demonstrated superiority in growth characters at all stages of growth resulting the maximum seed yield, and vice versa for the mutant, MB-43.

Morphological and reproductive characters

Considerable genotypic variation was also found in the mungbean genotypes in terms of plant height, number of branches, flowers, and racemes, as well as reproductive effectiveness, days to flowering, and maturity (Table 1). Out of all the genotypes, the MB-29 genotype had the tallest plant height (57.67 cm), most branches (3.17), racemes (17.67), and flowers (43.2). The mutant, MB-29 required the longest days to maturity (72 DAS) than the other genotypes. The MB-43 genotype, on the other hand, had the fewest branches (1.83 plant^{-1}), racemes (10.97 plant^{-1}), and flowers (26.2 plant^{-1}). MB-43 also had the shortest flowering and maturation times (37.3 and 68.5 DAS, respectively). The results also showed that, compared to low yielding genotypes, high yielding genotypes (Binamoog-2 and MB-29) produced more branches, racemes, and flowers (plant^{-1}) (Table 1). This finding suggests that the number of racemes and flowers is one of the key factors influencing seed yield. The association between high yielding and an increase in racemes and flowers could be explained by the possibility that high yielding genotypes have more raceme-bearing nodes that are borne on more branches, which would result in the production of more flowers (sink size). In other words, genotypes with higher flower production had lower RE, and vice versa, and the number of flowers showed a negative association with RE (Table 1). This result might be explained in a way that less competition for assimilates amongst the flowers/pods in the low yielding genotypes by being their fewer flowers. These results are corroborated with the results of Mondal (2012) who also reported that reproductive abscission (abortion) had inverse relationships with flower number and seed yield. MB-43 had the highest RE (52.4%), despite producing fewer flowers plant^{-1} (26.2). The genotypes with the lowest RE were in Binamoog-2 (47.1%) and MB-29 (49.5%), both of which had the same statistical rank and produced more flowers plant^{-1}.

Table 1. Some morphological and reproductive parameters and days required to maturity of similar durated four mungbean genotypes conducted during Kharif-I season, 2019

Mutants/ cultivars	Morphological parameters		Reproductive parameters			Phenological parameters	
	Plant height (cm)	Branches plant^{-1} (no.)	Racemes plant^{-1} (no.)	Opened flowers plant^{-1}	Repro-ductive efficiency (%)	Days to flowering	Days to maturity
BARI Mung-2	37.77 c	2.67 ab	13.47 b	35.5 b	50.7 ab	38.3 ab	69.8 b
Binamoog-2	49.43 b	3.00 a	16.07 a	41.4 a	47.1 b	39.0 a	70.0 b
MB-29	57.67 a	3.17 a	17.67 a	43.2 ab	49.5 b	40.0 a	71.9 a
MB-43	53.57ab	2.23 b	10.97 c	26.2 c	54.2 a	37.3 b	68.5 b
F-test	**	*	**	**	**	**	*
CV (%)	6.92	10.98	8.24	9.44	14.12	2.83	2.20

In a column, the figure having similar letter (s) do not differ significantly at $p \leq 0.05$; *, ** indicates significant at 5% and 1% levels of probability, respectively.

Yield attributes and seed yield

Genotypes had a significant impact on yield-contributing traits and seed yield (Table 2). MB-29 produced the highest pods plant^{-1} (21.6) and seeds pod^{-1} (11.7), whereas MB-43 showed the least amount of each (14.2 and 10.7 for pod plant^{-1} and seeds pod^{-1}, respectively). According to the findings, high yielding genotypes (MB-29 and Binamoog-2) had smaller pod and seed sizes (pod length, single pod, and 100-seed weight). In contrast, low-yielding genotypes (MB-43 and BARI Mung-2) had larger pod and seed sizes. The longest pod (8.66 cm), larger single pod (756 mg), and heaviest 100-seed weight (4.99 g) were found in MB-43. This outcome was consistent with that of Mondal et al. (2011a), who investigated the effects of pod number plant^{-1} and seed size on seed yield in 45 mungbean genotypes. The main objective of any agronomic or varietal development scheme is yield. The mutant MB-29 produced the highest total dry mass and seed weight (21.99 and 8.85 g, respectively) as well as seed yield (1328 kg ha^{-1}),while MB-43 produced the least(14.26 and 7.01 g plant^{-1} for TDM and seed weight plant^{-1}, respectively, and 1050 kg ha^{-1}). The genotypes, MB-29 and BINAmung-2 produced higher seed yield due to higher number of pods plant^{-1}. This finding supported by numero us researchers who found that in legumes, seed yield was positively associated with TDM and pods plant^{-1} (Singh et al., 2008; Mondal et al., 2015; Mwangi et al., 2021). Harvest index was greater in varieties than in mutants indicating assimilates partitioning to economic yield is better in released varieties than the mutants. The highest yielder genotypes MB-29 showed the lowest HI (28.70%). This result indicates that selection of higher yielding genotype on the basis of HI may be deceiving. It agreed with Poehlman's (1991) who found that a high harvest index alone did not result in a high yield. Rather he had the opinion that many physiological process particularly efficient photoassimilation and it's partitioning into plant and seed determines high yield. The current study has also taken this viewpoint into consideration.

Conclusion

It is concluded that high-yielding mungbean cultivars have a greater number of branches and leaves, in addition to LAI, TDM, and AGR, resulting in higher pods number per plant than low yielding mungbeans genotypes. Among the similar durated mungbean genotypes, MB-29 performed the best with respect to growth, yield attributes and seed yield. The knowledge about the study of growth and yield of mungbeans could be useful in future breeding programs.

Table 2. Some yield contributing characters and yield in four mungbean genotypes conducted during Kharif-I season, 2019

Mutants/ cultivars	Pods plant^{-1} (no.)	Pod length (cm)	Single pod weight (mg)	Seeds pod^{-1} (no.)	100-seed weight (g)	Seed weight plant^{-1} (g)	Seed yield (kg ha^{-1})	Total dry mass plant^{-1} (g)	Harvest index (%)
BARI Mung-2	18.0 b	7.90 b	704 b	10.9 ab	4.65 b	7.67 c	1180 bc	16.72 b	33.45 a
Binamoog-2	19.5 b	7.22 c	640 d	11.2 ab	4.30 b	8.33 b	1250 ab	17.38 b	36.68 a
MB-29	21.6 a	7.78 b	680 c	11.7 a	4.56 b	8.85 a	1328 a	21.99 a	28.70 b
MB-43	14.2 c	8.66 a	756 a	10.7 b	4.99 a	7.01 d	1050 c	14.26 c	28.92 b
F-test	**	**	**	*	*	**	**	**	*
CV (%)	4.73	2.60	1.45	3.08	7.45	4.30	5.05	6.31	7.45

In a column, the figure having similar letter (s) do not differ significantly at $P \leq 0.05$ as per LSD; *, ** indicates significant at 5% and 1% levels of probability, respectively.

Acknowledgments

The author acknowledged the Bangladesh Institute of Nuclear Agriculture (BINA) for financial support

Conflicts of Interest

The authors declare that they have no conflicts of interest regarding the publication of this article.

Author's Contribution

M. Monjurul Alam Mondal: Concepts, literature review, conduct experiment, data collection, simulation, analysis, manuscript writing and revision.

Md. Azadul Haque: literature review, formatting, ,manuscript writing and revision.

Md. Mohimenul Islam: Literature review, formatting, manuscript writing and revision.

References

Ali A, Arooj K, Khan BA, Nadeem MA, Imran M, Safdar ME, Amin MM, Aziz A and Ali MF. Optimizing the growth and yield of mungbean cultivars by altering sowing dates. *Pak. J. Agri. Res.* 2021; 34 (3): 559-568.

Bam R, Mishra SR, Khanal S, Ghimire P and Bhattarai S. Effect of biofertilizers and nutrient sources on the performance of mungbean at Rupandehi, Nepal. *J. Agric. Food Res*. 2022; 10:

BARC (Bangladesh Agricultural Research Council). Fertilizer Recommendation Guide. 2018. p. 54.

BBS (Bangladesh Bureau of Statistics). Hand book of Agricultural Statistics, December, 2015. Ministry of Planning, Govt. People's Repub. Bangladesh; 2020. p. 107.

Dutta RK and Mondal MMA. Evaluation of lentil genotypes in relation to growth characteristics, assimilate distribution and yield potential. *LENS Newsl*. 1998; 25: 51-55.

Fakir MSA, Mondal MMA, Ismail MR and Ashrafuzzaman M. Flowering pattern and reproductive efficiency in mungbean. *Inter. J. Agric. Biol.* 2011; 13(6): 966-970.

Hamid A, Agata W, Maniruzzaman AFM and Ahad AM. Physiological aspects of yield improvement in mungbean. *In*: Advances in pulses research in Bangladesh. Proceedings of the second national workshop on pulses. June 6-8, 1989, BARI, Gazipur-1701, Bangladesh; 1991. pp. 95-102.

Hunt R. Plant growth analysis studies in biology. Edward Arnold Ltd. London; 1978. p. 67.

Lema M, Konnen B and Gudero G. Performance and growth growth analysis of three mungbean genotypes at Hawassa, Ethiopia. *Current Trends Biom. Engin. Biosci*. 2018; 16(3): 85-88.

Malek MA, Mondal MMA, Ismail MR, Rafii MY and Berahim Z. Physiology of yield in soybean: Growth and dry matter production. *African J. Biotech.* 2012; 11: 7643-7649.

Mondal MMA, Fakir MSA, Islam MN and Samad MA. Physiology of seed yield in mungbean: growth and dry matter production. *Bangladesh J. Bot.* 2011c; 40(2): 133-138

Mondal MMA, Fakir MSA, Ismail MR and Ashrafuzzaman M. Effect of defoliation on growth, reproductive characters and yield in mungbean. *Australian J. Crop Sci.* 2011d; 5: 961-966.

Mondal MMA, Fakir MSA, Juraimi AS, Hakim MA, Islam MM and Shamsuddoha ATM. Effects of flowering behavior and pod maturity synchrony on yield of mungbean. *Australian J. Crop Sci*. 2011b; 5: 945-953.

Mondal MMA, Hakim MA, Juraimi AS and Azad MAK. Contribution of morpho-physiological attributes in determining yield of mungbean. *African J. Biotech.* 2011a; 10: 12897-12904

Mondal MMA, Malek MA and Puteh AB. Variation in morpho- physiological characters and yield components of summer mungbean varieties. *Bangladesh J. Bot.* 2015; 44(3): 469-473.

Mondal MMA, Puteh AB, Malek MA, Ismail MR, Rafii MY and Latif MA. Seed yield in relation to growth and developmental aspects of mungbean. *The Scientific World J.* 2012.

Mondal MMA, Puteh AB, Malek MA, Roy S and Rafii MY. Contribution of morpho-physiological attributes on yield in lentil. *Australian J. Crop Sci.* 2013; **7**: 1167-1172.

Mondal MMA. Source-sink relationship in mungbean. LAMBERT Acadamic Publishing, Humburk, Germany. ISBN 978-3-8484-4690-2; 2012. p. 88-93.

Mwangi JW, Okoth OR, Kariuki MP and Piero NM. Genetic and phynotypic diversity of selected Kenyan mungbean genotypes. *J. Geneti Engin. Biotech.* 2021; 19: 141-154.

Poehlman JM. The mungbean. Oxford and IBH Publishing Co. Pvt. Ltd. 66 Janapath, New Delhi 110001, India; 1991. pp. 262-269.

Singh SK, Singh IP, Singh BB and Singh O. Correlation and path coefficient studies for yield and its components in mungbean. *Legume Res.* 2008; 32(3): 316-318.

J. Bangladesh Acad. Sci. 47(1); 109-117: June 2023 DOI: https://doi.org/10.3329/jbas.v47i1.63349

Journal of Bangladesh Academy of Sciences

Journal homepage: http://www.bas.org.bd/publications/jbas.html

Research Article

Implementation of intuitionistic fuzzy soft set theoretic scheme in decision making

Mousumi Akter, Kaniz Fatema and [1]Md. Sahadat Hossain

Department of Mathematics, Pabna University of Science and Technology, Pabna, Bangladesh

ARTICLE INFO

Article History

Received: 18 December 2022
Revised: 02 April 2023
Accepted: 11 June 2023

Keywords: Fuzzy soft set (FSS), Intuitionistic Fuzzy soft set (IFSS), Resultant IFSS, Comparison table.

ABSTRACT

Fuzzy soft set theory is becoming more and more important for coming up with coherent and logical answers to numerous real-world issues that are riddled with uncertainty, imprecision, and vagueness. The intuitionistic fuzzy soft set was investigated theoretically later on. Wherever uncertainty resulting from ambiguity manifests in more sophisticated ways, the combination of intuitionistic fuzzy set and intuitionistic fuzzy soft set is more efficient from an implementational standpoint. In this paper, the motivation of our work is to establish a new methodology to select an object from an inexact multi-observer data with the idea of intuitionistic fuzzy soft set theory. Our methodology includes an algorithm based on "and", "or" operation, max, min comparison data and comparison table.

Introduction

Most of our modern life problems, such as socio-economic, medical science and engineering, involve inexact data and some of these problems are basically humanistic. In current days so many theories have been developed to dealing with inexact situation in a feasible way. Fuzzy set theory (Roy and Maji 2007; Zadeh 1965; Zimmerman 1996; Prade and Dubois, 1980), Intuitionistic fuzzy set theory (Atanassov 1986, 1994; Islam et al., 2018; Mahbub et al., 2019), vague sets (Gau and Buehrer 1993), etc. are some of them, and can be employed as an adequate tool for dealing with any inexact circumstances and uncertainty situated in a discipline. However, all of these theories are consisting of some constraints, which is the lack of the parameterization tool accompanied with the mentioned theories. To avoid the limitations the idea of soft set theory is inaugurated by Molodtsov (1999), Pawlak (1982, 1994), etc. which has been employed in varied vexation. The problem of object determination has placed prime implication in this day. Majji et al., 2001; 2003 and Roy (2007) analyzes the concept of comparison table on SS theory and established a method for decision making problems. In this article we describe an application of IFSS theory in decision making problem and improve Majji and Roy (2001, 2003, 2007) given method to investigate a suitable object from a multi-observer data for a decision making problem. Section two consists of a summary note on the preliminaries concerned to FS theory and IFS theory. Later then section three explains a brief summary on soft set theory, fuzzy soft set theory and intuitionistic fuzzy soft set theory. The mathematical algorithm, used in our paper is illustrated in section four. A concise discussion of a decision making problem and its solution is illustrated in section five. Finally, the conclusion is narrated in section six.

Preliminary

In latter section we will briefly reflex the primary concept of FS and IFS which would be obligate for posterior platform.

---

*Corresponding author: <mousumiakter@pust.ac.bd, mousumiakter.ru@gmail.com>

[1]*Department of Mathematics University of Rajshahi, Rajshahi, Bangladesh*

Fuzzy Set

Consider *U* be the universe of discourse. A fuzzy set *V* in *U* is characterized by a mapping μ_V from *U* to $[0,1]$(Zadeh 1965), that is, $\mu_V : U \to [0,1]$. Where, μ_V describes the grade of membership. Thus *V* can be defined by the set of order pair $V = \{(v, \mu_V(v)) \mid v \in U\}$.

Union of Two FS

The union of two fuzzy subsets A_1 and A_2 over the same universe of discourse *U* is symbolized by $A_1 \cup A_2$ and is defined by (Zadeh 1965; Zimmerman 1996)

$$(A_1 \cup A_2)(a) = \{(a, \max(\mu_{A_1}(a), \mu_{A_2}(a))), \forall a \in U\}.$$

Intersection of Two FS

The intersection of two fuzzy subsets A_1 and A_2 over the same universe of discourse *U* is symbolized by $A_1 \cap A_2$ and is defined by (Zadeh 1965)

$$(A_1 \cap A_2)(a) = \{(a, \min(\mu_{A_1}(a), \mu_{A_2}(a))), \forall a \in U\}.$$

Intuitionistic Fuzzy Set

Consider *U* be the universe of discourse. A IFS *V* in *U* is characterize by two mappings μ_V and γ_V from *U* to $[0,1]$(Atanassov et al., 1986), that is, $\mu_V : U \to [0,1]$ and $\gamma_V : U \to [0,1]$ such that value of μ_V and γ_V describe the grad of membership and non-grad of membership gradually. Thus *V* can be defined as the order triplet

$$V = \{(a, \mu_V(a), \gamma_V(a)) \mid a \in U\}.$$

Here

$$(\mu_V(a) + \gamma_V(a)) \le 1.$$

Union of Two IFS

Union of two IFS's A_1 and A_2 over the same universe of discourse *U* is symbolized by $A_1 \cup A_2$ and is defined for all $\forall a \in U$ as (Atanassov 1986)

$$(A_1 \cup A_2)(a) = \{(a, \max(\mu_{A_1}(a), \mu_{A_2}(a)), \min(\gamma_{A_1}(a), \gamma_{A_2}(a))\}.$$

Here

$$\mu_{A_1}(a) + \gamma_{A_1}(a) \le 1 \text{ and } \mu_{A_2}(a) + \gamma_{A_2}(a) \le, \forall a \in U.$$

Intersection of Two IFS

The intersection of two intuitionistic fuzzy subsets symbolized by $A_1 \cap A_2$ and is defined $\forall a \in U$ as (Atanassov 1986)

$$(A_1 \cap A_2)(a) = \{(a, \min(\mu_{A_1}(a), \mu_{A_2}(a)), \max(\gamma_{A_1}(a), \gamma_{A_2}(a))\}.$$

Here

$$\mu_{A_1}(a) + \gamma_{A_1}(a) \le 1 \text{ and } \mu_{A_2}(a) + \gamma_{A_2}(a) \le 1, \forall a \in U.$$

Fuzzy Soft Sets in Decision Making

This section consists of some basic definition of fuzzy soft set theory, great portion of them explained by Maji (2001). Let, the set of m objects $U = \{u_1, u_2, u_3, \cdots, u_m\}$ is characterized by a set of parameters $\{E_1, E_2, E_3, \cdots, E_i\}$ The parameter extension Q may be formed as

$$Q \supseteq \{E_1, E_2, E_3, \cdots, E_i\},$$

where each parameter set E_i stand for ith class of parameters and the components of E_i recite an especial characteristic set.

Soft Set

Presume *U* and *Q* is the universe of discourse and set of parameters gradually. For the power set *P(U)* of *U* and a subset *B* of *Q* define a mapping *g* from *B* to *P(U)* as $g : B \to P(U)$. The couple $(g, P(U))$ is known as a soft set on *U* (Molodtsov 1999; Roy and Maji 2007).

Soft Subset

Consider two soft sets (F_1, C_1) and (F_2, C_2) over the same universe of discourse *U*. Then (F_1, C_1) is said to be a subset of (F_2, C_2) if (Molodtsov 1999)

(i) $C_1 \subset C_2$ and

(ii) $\forall\, b \in B,\ f_1(b)$ and $f_2(b)$ are uniform approximations.

"and" Operation of Two Soft Sets

For two soft sets (F_1, C_1) and (F_2, C_2) over the same universe of discourse *U*, "(F_1, C_1) and (F_2, C_2)" is symbolized by $(F_1,C_1)\wedge(F_2,C_2)$ and is defined as (Molodtsov 1999)

$$(F_1,C_1)\wedge(F_2,C_2)=(F_3,C_1\times C_2),$$

where

$$F_3(a,b)=F_1(a)\bigcap F_2(b),\forall(a,b)\in C_1\times C_2.$$

"or" Operation of Two Soft Sets

For two soft sets (F_1,C_1) and (F_2,C_2) over the same universe of discourse *U*, "(F_1,C_1) or (F_2,C_2)" is symbolized as $(F_1,C_1)\vee(F_2,C_2)$ and is defined by (Molodtsov 1999)

$$(F_1,C_1)\vee(F_2,C_2)=(F_4,C_1\times C_2),$$

where,

$$F_4(a,b)=F_1(a)\bigcup F_2(b),\forall(a,b)\in C_1\times C_2.$$

Fuzzy Soft Set

Presume *P(U)* to be the class of all fuzzy subsets of *U* and $E_i\subseteq Q$. Then the pair (f_i,E_i) is known as a FSS over *U*, where f_i describe a mapping from E_i to $P(U)$ that is,

$$f_i:E_i\to P(U).$$

Fuzzy Soft Subset

Presume two FSS (F_1,C_1) and (F_2,C_2) over the same universe of discourse *U*. Then (F_1,C_1) is said to be a subset of (F_2,C_2) if (Roy and Maji 2007)

(i) $C_1\subset C_2$, and

(ii) $\forall\, a\in C, F_1(a)$ is a fuzzy subset of $F_2(a)$.

"and" Operation of Two FSS

For two soft sets (F_1,C_1) and (F_2,C_2) over the same universe of discourse *U*, "(F_1,C_1) and (F_2,C_2)" is symbolized by $(F_1,C_1)\wedge(F_2,C_2)$ and is defined as (Molodtsov 1999)

$$(F_1,C_1)\wedge(F_2,C_2)=(F_3,C_1\times C_2),$$

where

$$F_3(a,b)=F_1(a)\bigcap F_2(b),\forall(a,b)\in C_1\times C_2.$$

"or" Operation of Two Fuzzy Soft Sets

Presume two FSS (F_1,C_1) and (F_2,C_2) over the same universe of discourse *U*. Then "(F_1,C_1) or (F_2,C_2)" is denoted by $(F_1,C_1)\vee(F_2,C_2)$ and is defined by (Roy and Maji 2007)

$$(F_1,C_1)\vee(F_2,C_2)=(F_4,C_1\times C_2),$$

where,

$$F_4(a,b)=F_1(a)\bigcup F_2(b),\forall(a,b)\in C_1\times C_2.$$

Intuitionistic Fuzzy Soft Set

Suppose *Q(U)* explain the class of all IFS's of *U* and $E_i\subseteq Q$. IFSS over *U* is denoted by (g_i,E_i) where g_i defined as

$$g_i:E_i\to Q(U).$$

Intuitionistic Fuzzy Soft Subset

Consider two IFSS's (G_1,C_1) and (G_2,C_2) over the same universe of discourse *U*. Then (G_1,C_1) is said to be a subset of (G_2,C_2) if

(i) $C_1\subset C_2$, and

(ii) $\forall\, a\in C_1, G_1(a)$ is a intuitionistic fuzzy subset of $G_2(a)$.

"and" operation of Two IFSS

Consider two IFSS's (G_1,C_1) and (G_2,C_2) over the same universe of discourse *U*. Then "(G_1,C_1) and (G_2,C_2)" is denoted by $(G_1,C_1)\wedge(G_2,C_2)$ and is defined by

$$(G_1,C_1)\wedge(G_2,C_2)=(G_3,C_1\times C_2),$$

where

$$G_3(a,b)=G_1(a)\bigcap G_2(b),\forall\, a\in C_1 \text{ and } b\in C_2,$$

and "$\bigcap$" represent the intersection of two IFS.

"or" operation of Two IFSS

Consider two IFSS's (G_1,C_1) and (G_2,C_2) over the same universe of discourse *U*. Then "(G_1,C_1) or (G_2,C_2)" is denoted by $(G_1,C_1)\vee(G_2,C_2)$ and is defined by

$$(G_1,C_1)\vee(G_2,C_2)=(G_4,C_1\times C_2),$$

where

$$G_4(a,b)=G_1(a)\bigcup G_2(b),\forall\, a\in C_1 \text{ and } b\in C_2,$$

"$\bigcup$" represent the union of two intuitionistic fuzzy sets.

Comparison Table and Algorithm

In a comparison table count of rows and columns are identical and they are specified by the objects ϑ_i of the universe *U*. In our paper the entries C_{ij} of the comparison table is illustrated by the count of parameters for those the grade of membership ϑ_i differ or same to the grade of membership ϑ_i. If k describe count of parameters in a IFSS, then disputably $0 \leq C_{ij} \leq k.$ If r_i and c_j represent the row sum and the column sum respectively of an object ϑ_i then it can be defined as

$$r_i = \sum_{j=1}^{n} C_{ij} \text{ and } c_j = \sum_{i=1}^{n} C_{ij},$$

where n represent the number of objects. In this paper our aim is to select an adequate object from a class of objects regarding to a class of choice parameters Q. We thus developed an algorithm to determinate an object from some multiobservers data specified by color, shape and price.

Algorithm

1. Input the parameter set Q.
2. Input the IFSS's $(F_1, C),\ (F_2, S),$ and $(F_3, P).$
3. Perform "(F_1, C) and (F_2, S)".
4. Illustrate a comparison data for row max and row min in case of membership and non- membership value.
5. Select a new resultant IFSS $(R_1, Q),$ with respect to the comparison data.
6. Finally calculate the corresponding resultant IFSS $(R_2, Q),$ for the IFSS's $(F_1, C),$ $(F_2, S),$ and $(F_3, P),$ and place it in tabular form.
7. Build up a comparison-table for the IFSS $(R_2, Q),$ and calculate r_i and c_i for all i.
8. Calculate $V_i = r_i - c_i$, for all i, define as score.
9. If $V_k = \max\{V_i\}$, then the decision is V_k.

Application

Presume $O = \{\vartheta_1, \vartheta_2, \vartheta_3, \vartheta_4, \vartheta_5, \vartheta_6\},$ to be the class of components having varied colors, shape and price. Q={darkish, stone, grey, rosy, big, small, very small, medium, very big, very cheap, cheap, high, average}, represent the set of parameters consisting of three subsets C, S and P. Here C stands for color space, S for size space and P for price space gradually. Take IFSS $(F_1, C),$ relate the components having color space, IFSS $(F_2, S),$ relate the 'components having size' and IFSS $(F_3, P),$ relate the 'the components having price'. Our motivation is to ascertain the desired component from the multi observer's fuzzy data, mark by varied observers, in terms of IFSS $(F_1, C),\ (F_2, S),$ and $(F_3, P),$ as described before. All of the three IFSS are represented in tabular form in Tables. $1(a) - 1(c).$

	Darkish	**Stone**	**Grey**	**Rosy**
ϑ_1	(0.3, 0.4)	(0.4, 0.5)	(0.6, 0.2)	(0.9, 0.1)
ϑ_2	(0.3, 0.5)	(0.9, 0.1)	(0.3, 0.6)	(0.5, 0.2)
ϑ_3	(0.4, 0.4)	(0.5, 0.4)	(0.8, 0.1)	(0.7, 0.1)
ϑ_4	(0.8,0.1)	(0.2, 0.7)	(0.4, 0.4)	(0.8, 0.2)
ϑ_5	(0.7, 0.3)	(0. , 0.6)	(0.6, 0.3)	(0.5, 0.2
ϑ_6	(0.9, 0.1)	(0.2, 0.6)	(0.4, 0.3)	(0.3, 0.5)

Table 1(a): IFSS (F_1, C).

	Big	**Very big**	**Small**	**Very small**	**Medium**
ϑ_1	(0.4, 0.3)	(0.2, 0.7)	(0.8, 0.2)	(0.6, 0.2)	(0.5, 0.3)
ϑ_2	(0.8, 0.1)	(0.6, 0.1)	(0.3, 0.5)	(0.1, 0.6)	(0.7, 0.2)
ϑ_3	(0.6, 0.2)	(0.4, 0 3)	(0.4, 0.4)	(0.1, 0.5)	(0.7, 0.1)
ϑ_4	(0.9, 0.1)	(0.8, 0.2)	(0.2, 0.6)	(0.1, 0.7)	(0.4, 0.5)
ϑ_5	(0.2, 0.5)	(0.1,0.6)	(0.9, 0.1)	(0.8, 0.1)	(0.7, 0.3)
ϑ_6	(0.3, 0.6)	(0.2, 0.5)	(0.8, 0.1)	(0.6, 0.2)	(0.5, 0.4)

Table 1(b): IFSS (F_2, S).

	Very cheap	**Cheap**	**High**	**Average**
ϑ_1	(0.3, 0.5)	(0.4, 0.4)	(0.1, 0.7)	(0.9, 0.1)
ϑ_2	(0.6, 0.2)	(0.5, 0.3)	(0.4, 0.4)	(0.5, 0.2)
ϑ_3	(0.5, 0.4)	(0.6, 0.1)	(0.3, 0.4)	(0.6, 0.1)
ϑ_4	(0.7,0.2)	(0.6, 0.3)	(0.6, 0.2)	(0.3, 0.6)
ϑ_5	(0. , 0.3)	(0.6, 0.2)	(0.5, 0 3)	(0.4, 0.5)
ϑ_6	(0.8, 0.1)	(0.7, 0.1)	(0.7, 0.3)	(0.9, 0.1)

Table 1(c): IFSS (F_3, P).

Performing "(F_1, C) and (F_2, S)" for the first two IFSS (F_1, C) and (F_2, S), we get 20 strategies of the type f_{ij}, where

$$f_{ij} = ((\mu_{F_1(a_i)} \wedge \mu_{F_2(b_j)}), (\lambda_{F_1(a_i)} \vee \lambda_{F_2(b_j)}))$$

for $1 \le i \le 4$ and $1 \le j \le 5$, which are represented in Tables. $2(a) - 2(d)$. Here meet operation table represent the membership and join operation table explained the non-membership values for each.

$$f_{ij} = ((\mu_{F_1(a_i)} \wedge \mu_{F_2(b_j)}), (\lambda_{F_1(a_i)} \vee \lambda_{F_2(b_j)}))$$

meet	f_{11}	f_{12}	f_{13}	f_{14}	f_{15}	raw max
ϑ_1	0.3	0.2	0.3	0.3	0.3	0.3
ϑ_2	0.3	0.3	0.3	0.1	0.3	0.3
ϑ_3	0.4	0.4	0.4	.1	0.4	0.4
ϑ_4	0.8	0.8	0.2	0.1	0.8	0.8
ϑ_5	0.2	0.1	0.7	0.7	0.7	0.7
ϑ_6	0.3	0.2	0.8	0.6	0.8	0.8
CD	2	3	1	4	2	

join	f_{11}	f_{12}	f_{13}	f_{14}	f_{15}	raw min
ϑ_1	0.4	0.7	0.4	0.4	0.4	0.4
ϑ_2	0.5	0.5	0.5	0.6	0.5	0.5
ϑ_3	0.4	0.4	0.4	0.5	0.4	0.4
ϑ_4	0.1	0.2	0.6	0.7	0.5	0.1
ϑ_5	0.5	0.6	0.3	0.3	0.3	0.3
ϑ_6	0.6	0.6	0.1	0.2	0.4	0.1
CD	2	4	1	4	2	

Table 2(a): f_{1j} $(\mathit{for}\ \mathrm{j} = 1,2,3,4,5)$

meet	f_{21}	f_{22}	f_{23}	f_{24}	f_{25}	raw max
ϑ_1	0.4	0.2	0.4	0.4	0.4	0.4
ϑ_2	0.8	0.6	0.3	0.1	0.7	0.8
ϑ_3	0.5	0.4	0.4	0.1	0.5	0.5
ϑ_4	0.2	0.2	0.2	0.1	0.2	0.2
ϑ_5	0.2	0.1	0.3	0.3	0.3	0.3
ϑ_6	.2	0.2	0.2	0.2	0.2	0.2
CD	1	4	2	3	1	

join	f_{21}	f_{22}	f_{23}	f_{24}	f_{25}	raw min
ϑ_1	0.5	0.7	0.5	0.5	0.5	0.5
ϑ_2	0.1	0.1	0.5	0.6	0.2	0.1
ϑ_3	0.4	0.4	0.4	0.5	0.4	0.4
ϑ_4	0.7	0.7	0.7	0.7	0.7	0.7
ϑ_5	0.6	0.6	0.6	0.6	0.6	0.6
ϑ_6	0.6	0.6	0.6	0.6	0.6	0.6
CD	0	1	0	2	1	

Table 2(b): f_{2j} $(\mathit{for}\ \mathrm{j} = 1,2,3,4,5)$

meet	f_{31}	f_{32}	f_{33}	f_{34}	f_{35}	raw max
ϑ_1	0.4	0.2	0.6	0.6	0.5	0.6
ϑ_2	0.3	0.3	0.3	0.1	0.3	0.3
ϑ_3	0.6	0.4	0.4	0.1	0.7	0.7
ϑ_4	0.4	0.4	0.2	0.1	0.4	0.4
ϑ_5	0.2	0.1	0.6	0.6	0.6	0.6
ϑ_6	0.3	0.2	0.4	0.6	0.4	0.6
CD	4	4	3	3	2	

join	f_{31}	f_{32}	f_{33}	f_{34}	f_{35}	raw min
ϑ_1	0.3	0.7	0.2	0.2	0.3	0.2
ϑ_2	0.6	0.6	0.6	0.6	0.6	0.6
ϑ_3	0.2	0.3	0.4	0.5	0.1	0.1
ϑ_4	0.4	0.4	0.6	0.7	0.5	0.4
ϑ_5	0.5	0.6	0.3	0.3	0.3	0.3
ϑ_6	0.6	0.5	0.3	0.3	0.4	0.3
CD	4	4	2	2	3	

Table 2(c): f_{3j} $(\mathit{for}\ \mathrm{j} = 1,2,3,4,5)$

meet	f_{41}	f_{42}	f_{43}	f_{44}	f_{45}	raw max
ϑ_1	0.4	0.2	0.8	0.6	0.5	0.8
ϑ_2	0.5	0.5	0.3	0.1	.5	0.5
ϑ_3	0.6	0.	0.4	0.1	0.7	0.7
ϑ_4	0.8	0.8	0.2	0.1	0.4	0.8
ϑ_5	0.2	0.1	0.5	0.5	0.5	0.5
ϑ_6	0.3	0.2	0.3	0.3	0.3	0.3
CD	3	4	3	4	2	

join	f_{41}	f_{42}	f_{43}	f_{44}	f_{45}	raw min
ϑ_1	0.3	0.7	0.2	0.2	0.3	0.2
ϑ_2	0.2	0.2	0.5	0.6	0.2	0.2
ϑ_3	0.2	0.3	0.4	0.5	0.1	0.1
ϑ_4	0.2	0.2	0.6	0.7	0.5	0.2
ϑ_5	0.5	0.6	0.2	0.2	0.3	0.2
ϑ_6	0.6	0.5	0.5	0.5	0.5	0.5
CD	3	3	3	3	3	

Table 2(d): $f_{4j}\ (for\ j=1,2,3,4,5)$

In each table CD stand for comparison data, which we determine by comparing the raw min and raw max column with the other column entries for membership and non-membership values respectively.

The parameters $Q=\{f_{11}, f_{13}, f_{15}, f_{21}, f_{23}, f_{25}\}$ are then computed by using the comparison data for row maxima and column minima. Here we choose those of the strategies which have comparison value zero, one and two. Let us introduce the new resultant IFSS by (R_1, Q), that's represented in Table 3.

f_{11}	f_{13}	f_{15}	f_{21}	f_{23}	f_{25}
(0.3, 0.4)	(0.3, 0.4)	(0.3, 0.4)	(0.4, 0.5)	(0.4, 0.5)	(0.4, 0.5)
(0.3, 0.5)	(0.3, 0.5)	(0.3, 0.5)	(0.8, 0.1)	(0.3, 0.5)	(0.7, 0.2)
(0.4, 0.4)	(0.4, 0.4)	(0.4, 0.4)	(0.5, 0.4)	(0.4, 0.4)	(0.5, 0.4)
(0.8, 0.1)	(0.2, 0.6)	(0.4, 0.5)	(0.2, 0.7)	(0.2, 0.7)	(0.2, 0.7)
(0.2, 0.5)	(0.7, 0.3)	(0.7, 0.3)	(0.2, 0.6)	(0.3, 0.6)	(0.3, 0.6)
(0.3, 0.6)	(0.8, 0.1)	(0.5, 0.4)	(0.2, 0.6)	(0.2, 0.6)	(0.2, 0.6)

Table 3: Resultant IFSS (R_1, Q).

Finally Performing the same logical formula for "(R_1, Q)" and "(F_3, P)" we achive 24 new strategies of the type d_{ij}, where

$$d_{ij} = ((\mu_{R_1(a_i)} \wedge \mu_{F_3(b_j)}), (\lambda_{R_1(a_i)} \vee \lambda_{F_3(b_j)}))$$

for $1 \le i \le 6$ and $1 \le j \le 4$, which are represented in Tables. $4(a)-4(f)$.

meet	d_{11}	d_{12}	d_{13}	d_{14}	raw max
ϑ_1	0.3	0.3	0.1	0.3	0.3
ϑ_2	0.3	0.3	0.3	0.3	0.3
ϑ_3	0.4	0.4	0.3	0.4	0.4
ϑ_4	0.7	0.6	0.6	0.3	0.7
ϑ_5	0.2	0.2	0.2	0.2	0.2
ϑ_6	0.3	0.3	0.3	0.3	0.3
CD	0	1	3	1	

join	d_{11}	d_{12}	d_{13}	d_{14}	raw min
ϑ_1	0.5	0.4	0.7	0.4	0.4
ϑ_2	0.5	0.5	0.5	0.5	0.5
ϑ_3	0.4	0.4	0.4	0.4	0.4
ϑ_4	0.2	0.3	0.2	0.6	0.2
ϑ_5	0.5	0.5	0.5	0.5	0.5
ϑ_6	0.6	0.6	0.6	0.6	0.6
CD	1	1	1	1	

Table 4(a): $d_{1j}\ (for\ j=1,2,3,4)$.

meet	d_{21}	d_{22}	d_{23}	d_{24}	raw max
ϑ_1	0.3	0.3	0.1	0.3	0.3
ϑ_2	0.3	0.3	0.3	0.3	0.3
ϑ_3	0.4	0.4	0.3	0.4	0.4
ϑ_4	0.2	0.2	0.2	0.2	0.2
ϑ_5	0.6	0.6	0.5	0.4	0.
ϑ_6	0.8	0.7	0.7	0.8	0.8
CD	0	1	4	1	

join	d_{21}	d_{22}	d_{23}	d_{24}	raw min
ϑ_1	0.5	0.4	0.7	0.4	0.4
ϑ_2	0.5	0.5	0.5	0.5	0.5
ϑ_3	0.4	0.4	0.4	0.4	0.4
ϑ_4	0.6	0.6	0.6	0.	0.6
ϑ_5	0.3	0.3	0.3	0.5	0.3
ϑ_6	0.1	0.1	0.3	0.1	0.1
CD	1	0	2	1	

Table 4(b): $d_{2j}\ (for\ \mathrm{j}=1,2,3,4)$.

meet	d_{31}	d_{32}	d_{33}	d_{34}	raw max
ϑ_1	0.3	0.3	0.1	0.3	0.3
ϑ_2	0.3	0.3	0.3	0.3	0.3
ϑ_3	0.4	0.4	0.3	0.4	0.4
ϑ_4	0.4	0.4	0.4	0.3	0.4
ϑ_5	0.6	0.6	0.5	0.4	0.6
ϑ_6	0.5	0.5	0.5	0.5	0.5
CD	0	0	3	2	

join	d_{31}	d_{32}	d_{33}	d_{34}	**raw min**
ϑ_1	0.5	0.4	0.7	0.4	0.4
ϑ_2	0.5	0.5	0.5	0.5	0.5
ϑ_3	0.4	0.4	0.4	0.4	0.4
ϑ_4	0.5	0.5	0.5	0.6	0.5
ϑ_5	0.3	0.3	0.3	0.5	0.3
ϑ_6	0.4	0.4	0.4	0.4	0.4
CD	1	0	0	2	

Table 4(c): $d_{3j}\ (for\ \mathrm{j}=1,2,3,4)$.

meet	d_{41}	d_{42}	d_{43}	d_{44}	raw max
ϑ_1	0.3	0.4	0.1	0.4	0.4
ϑ_2	0.6	0.5	0.4	0.5	0.6
ϑ_3	0.5	0.5	0.3	0.5	0.5
ϑ_4	0.2	0.2	0.2	0.2	0.2
ϑ_5	0.2	0.2	0.2	0.2	0.2
ϑ_6	0.2	0.2	0.2	0.2	0.2
CD	1	1	3	1	

join	d_{41}	d_{42}	d_{43}	d_{44}	raw min
ϑ_1	0.5	0.5	0.7	0.5	0.5
ϑ_2	0.2	0.3	0.4	0.2	0.2
ϑ_3	0.4	0.4	0.4	0.4	0.4
ϑ_4	0.7	0.7	0.7	0.7	0.7
ϑ_5	0.6	0.6	0.6	0.6	0.6
ϑ_6	0.6	0.6	0.6	0.6	0.6
CD	0	1	2	0	

Table 4(d): $d_{4j}\ (for\ \mathrm{j}=1,2,3,4)$.

meet	d_{51}	d_{52}	d_{53}	d_{54}	raw max
ϑ_1	0.3	0.4	0.1	0.4	0.4
ϑ_2	0.3	0.3	0.3	0.3	0.3
ϑ_3	0.4	0.4	0.3	0.4	0.4
ϑ_4	0.2	0.2	0.2	0.2	0.2
ϑ_5	0.3	0.3	0.3	0.3	0.3
ϑ_6	0.2	0.2	0.2	0.2	0.2
CD	1	0	2	0	

join	d_{51}	d_{52}	d_{53}	d_{54}	raw min
ϑ_1	0.5	0.5	0.7	0.5	0.5
ϑ_2	0.5	0.5	0.5	0.5	0.5
ϑ_3	0.4	0.4	0.4	0.4	0.4
ϑ_4	0.7	0.7	0.7	0.7	0.7
ϑ_5	0.6	0.6	0.6	0.6	0.6
ϑ_6	0.6	0.6	0.6	0.6	0.6
CD	0	0	1	0	

Table 4(e): $d_{5j}\ (for\ \mathrm{j}=1,2,3,4)$.

meet	d_{61}	d_{62}	d_{63}	d_{64}	raw max
ϑ_1	0.3	0.4	0.1	0.4	0.4
ϑ_2	0.6	0.5	0.4	0.5	0.6
ϑ_3	0.5	0.5	0.3	0.5	0.5
ϑ_4	0.2	0.2	0.2	0.2	0.2
ϑ_5	0.3	0.3	0.3	0.3	0.3
ϑ_6	0.2	0.2	0.2	0.2	0.2
CD	1	1	3	1	

join	d_{61}	d_{62}	d_{63}	d_{64}	raw min
ϑ_1	0.5	0.5	0.7	0.5	.5
ϑ_2	0.2	0.3	0.4	0.2	0.2
ϑ_3	0.4	0.4	0.4	0.4	0.4
ϑ_4	0.7	0.7	0.7	0.7	0.7
ϑ_5	0.6	0.6	0.6	0.6	0.6
ϑ_6	0.6	0.6	0.6	0.6	0.6
CD	0	1	2	0	

Table 4(f): d_{6j} $(for\ j = 1,2,3,4)$.

On basis of the previous algorithm the final resultant IFSS is view in Table 5. Here strategies comparison values are zero and one.

MB	d_{11}	d_{21}	d_{31}	d_{32}	d_{52}	d_{54}
ϑ_1	0.3	0.3	0.3	0.3	0.4	0.4
ϑ_2	0.3	0.3	0.3	0.3	0.3	0.3
ϑ_3	0.4	0.4	0.4	0.4	0.4	0.4
ϑ_4	0.7	0.2	0.4	0.4	0.2	0.2
ϑ_5	0.2	0.6	0.6	0.6	0.3	0.3
ϑ_6	0.3	0.8	0.5	0.5	0.2	0.2

NMB	d_{11}	d_{21}	d_{31}	d_{32}	d_{52}	d_{54}
ϑ_1	0.5	0.5	0.5	0.4	0.5	0.5
ϑ_2	0.5	0.5	0.5	0.5	0.5	0.5
ϑ_3	0.4	0.4	0.4	0.4	0.4	0.4
ϑ_4	0.2	0.6	0.5	0.5	0.7	0.7
ϑ_5	0.5	0.3	0.3	0.3	0.6	0.6
ϑ_6	0.6	0.1	0.4	0.4	0.6	0.6

Table 5: Resultant IFSS.

Tables. 6(a)-6(b) illustrates the comparison-table of the above resultant IFSS.

MV	ϑ_1	ϑ_2	ϑ_3	ϑ_4	ϑ_5	ϑ_6
ϑ_1	6	6	2	3	3	3
ϑ_2	4	6	0	4	4	4
ϑ_3	6	6	6	5	3	3
ϑ_4	3	3	3	6	1	3
ϑ_5	3	5	3	5	6	4
ϑ_6	4	4	3	5	2	6

Table 6(a): Comparison table for membership values (MV).

NMV	ϑ_1	ϑ_2	ϑ_3	ϑ_4	ϑ_5	ϑ_6
ϑ_1	6	6	2	3	3	3
ϑ_2	4	6	0	4	4	4
ϑ_3	6	6	6	5	3	3
ϑ_4	3	3	3	6	1	3
ϑ_5	3	5	3	5	6	4
ϑ_6	4	4	3	5	2	6

Table 6(b): Comparison table for membership values (NMV).

And, finally we calculate the row-sum (RS), column-sum (CS). The computation table is demonstrated in Table 6(c).

MV	RS	CS	Diff	NMV	RS	CS	Diff
ϑ_1	23	26	-3	ϑ_1	25	26	-1
ϑ_2	22	30	-8	ϑ_2	22	28	-6
ϑ_3	29	17	12	ϑ_3	31	14	17
ϑ_4	19	28	-9	ϑ_4	14	31	-17
ϑ_5	26	19	7	ϑ_5	27	19	8
ϑ_6	24	23	1	ϑ_6	23	24	-1

Table 6(c): Difference of RS and CS for MV and NMV.

From the above computation, we observe that for $k = 3$ the difference is maximum, thus the decision is in favors of selecting ϑ_3.

Conclusion

In our present work we deliver an appliance of IFSS theory in object determination problem. For the convenience of our work, we first select some parameters like color, size and price for the selected objects and define them with the concept of IIFS in Tables. 1(a) – 1(c). Sequentially using "and" operation and comparison data for the three IIFSs, we get a resultant IIFS. Finally, by formatting and analyzing a comparison table for the resultant IFSS we ascertain that the desired object is ϑ_3.

References

Atanassov K. Intuitionistic fuzzy sets. *Fuzzy Sets and Systems*. 1986; 20(1): 87-96.

Atanassov K. Operators over interval valued intuitionistic fuzzy sets. *Fuzzy Sets and Systems.* 1994; 64(2): 159-174.

Gau WL and Buehrer DJ. Vague sets, IEEE Trans. *System Man Cybernet*. 1993; 23 (2): 610-614.

Islam MS, Hossain MS and Asaduzzaman M. Level separation on Intuitionistic fuzzy T1 spaces. *J. Bangladesh Acad. Sci* 2018; 42(1): 73-85.

Mahbub MA, Hossain MS and Hossain MA. On Q-compactness in Intuitionistic Fuzzy topological spaces. *J. Bangladesh Acad. Sci.* 2019; 43(2): 197-230.

Maji PK, Biswas R and Roy AR. Fuzzy soft sets. *J. Fuzzy Math*. 2001; 9(3): 589-602.

Maji PK, Biswas R and Roy AR. Soft set theory. *Comput. Math. Appl*. 2003; 45(4-5): 555-562.

Molodtsov D. Soft set theory-first results. *Comput. Math. Appl*. 1999; 37: 19-31.

Pawlak Z. Rough sets, Internat. *J. Inform. Comput. Sci*. 1982; 11: 341-356.

Pawlak Z. Hard set and soft sets, ICS Research Report. *Ins. Comput. Sci. Poland.* 1994

Prade H and Dubois D. Fuzzy Sets and Systems Theory and Applications. *Academic Press, London*. 1980.

Roy AR and Maji PK. A fuzzy soft set theoretic approach to decision making problems. *J. Comput. Appl. Math*. 2007; 203(2): 412-418.

Zadeh LA. Fuzzy sets. *Infor Control.* 1965; 8: 338-353.

Zimmerman HJ. Fuzzy Set Theory and Its applications. *Kluwer Academic Publishers, Boston*. 1996.

J. Bangladesh Acad. Sci. 47(1); 119-125: June 2023 DOI: https://doi.org/10.3329/jbas.v47i1.61838

Journal of Bangladesh Academy of Sciences

Journal homepage: http://www.bas.org.bd/publications/jbas.html

Research Article

Comparative assessment of *moringa oleifera* seed extract and aluminum sulfate solution efficiency as coagulants for storm water treatment

Garba Barde Bate, Adeniyi Olarewaju Adeleye*, Afeez Oladeji Amoo, Emmanuel Madu Ijanu, Catherine Iyabo Asaju and Haruna Sale Mohammed

Department of Environmental Sciences, Federal University Dutse, Nigeria

ARTICLE INFO

Article History

Received: 12 October 2022
Revised: 05 March 2023
Accepted: 02 April 2023

Keywords: Storm water, *Moringa oleifera*, Alum, Coagulants, Water treatment

ABSTRACT

Chemical coagulants used in water treatment are detrimental to human health. This research assessed the viability of *Moringa oleifera* (MO) seed extract compared with Aluminium Sulphate (Alum) as coagulants for treating stormwater. Five hundred mL of each of the eight storm water samples were analyzed through the Jar test method and zone settling rate experiment. Temperature, pH, conductivity, turbidity, and total suspended solids were assessed before and after adding the coagulants. Results obtained on the percentage reduction in interface height show lesser percentages (0.47, 0.76, 1.14, and 0.19%) when varying concentrations (50, 60, 70, and 80 mg/L) of MO seed extract were employed compared to the superior reduction percentages (87.07, 90.09, 95.27 and 94.57%.) when the same varying concentrations of Alum solution were added. Nonetheless, the percentage reduction in interface heights of the coagulants are significantly ($p<0.05$) different from each other.

Introduction

The literature has overwhelmingly established that to avert public health crisis, water from surface sources must be purified before it can be considered potable for human consumption (Guchi, 2015). According to USEPA (2014), storm water emanates from the sky in the form of rain, hail, or snow and flows over streets, parking space, and roofs of buildings into a water body or storm drain. If properly harnessed and treated, the all-year availability of storm water in Dutse can serve as a panacea to water scarcity, especially in the dry season.

Various methods are used to make water safe and attractive to consumers. However, the method that can be employed depends largely on the character of the raw water involved (Dinka, 2018). One of the difficulties with the treatment of surface water is the large seasonal variations in turbidity (McConnachie et al.,1999). According to Pillai (2004), the use of natural coagulants had been documented for over 100 years and had been used in the past before chemical coagulants were discovered (Bratby, 2016).

It has been reported that *Moringa oleifera* (MO) can eliminate river water's turbidity and dissolved organic matter (Damayanti et al., 2011). Aluminium sulphate [$Al_2(SO_4)_3$], generally known as Alum, has been in existence for over 100 years and has been comprehensively adopted as a flocculating agent in the treatment of wastewater (Harper et al., 1998). Further, adding Alum to water produces chemical precipitates that aid the removal of pollutants in suspended solids,

---

*Corresponding author:<adeniyadeleye@fud.edu.ng>

algae, phosphorus, heavy metals, and bacteria. The use of Alum, however, leaves behind both dissolved and residual aluminum compounds in the drinking water, which is associated with several human health problems, including Alzheimer's disease, osteomalacia, osteodystrophy, Parkinson's disease, etc. (Krupinska, 2020). Based on this scientific background, this study assessed the suitability of MO seed extract compared to Alum solution in treating water samples collected from a storm water reservoir in Dutse North West, Nigeria.

Materials and Methods

Sampling Technique and Preparation of Coagulants

A grab sampling technique was employed to collect the storm water samples along the mechanic village in Dutse urban, Jigawa State. MO seeds were collected, sun-dried, de-shelled, and subsequently crushed to a fine powder using a mortar to make it an effective coagulant, as Ndabigengesere et al. (1995) recommended.

Experimental Design

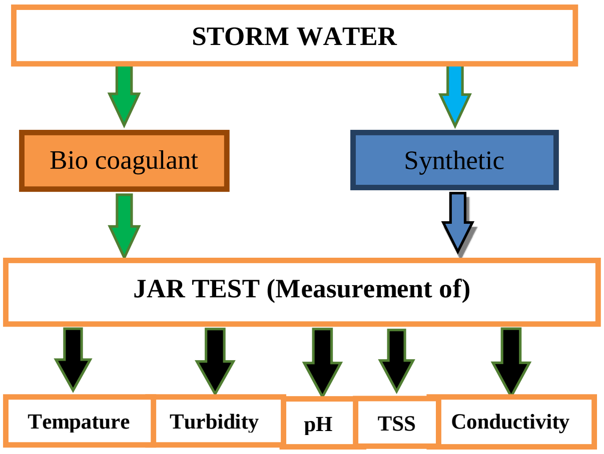

Fig. 1. A flow chart of the experimental design

The powder was then sieved, weighed, and dissolved in distilled water to make a 50 g/L solution, stirred for 30 minutes using a centrifuge, and filtrated through a Whatman filter paper (No. 40).

Aluminum sulfate was bought from a vendor in Dutse ultra-modern market. It was completely crushed to a finely sieved powder using a mortar to attain the desired effect. The powder was weighed and dissolved in distilled water to make a 50 g/L solution. The solution was stirred for 30 minutes and filtrated through a Whatman filter paper (No. 40). As Ukanwa and Verstraete (2010) prescribed, the fresh solution was prepared daily to avoid the aging effects of the MO and aluminum sulfate powder solution.

Jar Test

To assess the coagulation and flocculation effect of the coagulants (MO seeds extract and aluminium sulphate solution) on their coagulating capacity due to the continuous stirring mechanism, the standard Jar test method was performed as recommended by Ndabigengesere and Narasiah (1998) and Khader et al. (2018). The Jar test in this study involved a combination of rapid and slow mixing processes before sedimentation was achieved. The rotational speed of the mixers was changed accordingly to simulate different mixing intensities such that flocculation would occur, as Katayon et al. (2007) and Vieira et al. (2010) reported.

The procedure involved using 500 mL glass beakers filled with storm water which was agitated using the Jar test apparatus. The measured amounts (5, 60, 70, and 80 mg/L) of MO and Alum coagulants were added to each storm water sample (500 mL) while agitating the suspension. The suspension was initially mixed at a higher speed (120 rpm), followed by a slow mixing at 80 rpm, and finally set at 20 rpm for 30 minutes to enable sedimentation. The solid/liquid interface in the beakers was recorded during the settling period.

Zone Settling Rate

The effectiveness of the coagulants assessed in this study was determined by measuring the amount of settleable sludge attained and the rate at which it settled.

The methodology adopted in this current study can be connected with previous and similar studies conducted on conditioning sludge with different chemicals. The effectiveness of the coagulants found in terms of the reduction of suspension of solids particles in the supernatant fluid can then be calculated based on the percentage reduction of the solid/liquid interface height (Amirtharajah and O'Melia, 1990).

The standard methods recommended a column of one meter in height and ten cm in diameter (Amirtharajah and O'Melia, 1990), corresponding to a large volume of sludge. In contrast, this experiment used one L measuring cylinders approximately forty-one cm in height and six cm in diameter with a one L volume of sludge, similar to the method used by Muyibi et al. (2001).

Assessment of Coagulation Efficiency of Coagulants

A storm water sample weighing 0.5 L was measured and put in each beaker in which varying concentrations of coagulants were added. The extract of MO seeds and solution of Alum, which were introduced into each beaker containing the storm water in different concentrations, were mixed for 5 minutes. The samples were then allowed to settle for 30 minutes until all the settleable flocs had fully settled. Before and after treatment, samples were measured for turbidity, temperature, pH, conductivity, and total suspended solids (TSS). This was done to identify the dose of the MO seed extract and Alum solution required to achieve turbidity below International standards. The tests were performed at doses of 0 (control, before), 5, 6, 7, 8, and 50, 60, 70, and 80 mg/L of Alum solution and MO seed extract, respectively.

Data Analysis

Data were analyzed using SPSS version 20.0. Results were summarized using descriptive statistics. Student's T-test was used to determine the significant difference in the effectiveness of MO seed extracts and Alum solution in effecting coagulation of the sampled stormwater.

Results and Discussion

The initial temperature of the stormwater was 33 ˚C before the addition of MO (Table 1). After adding varying concentrations (50, 60, 70, and 80 mg/L) of MO, the temperature dropped to 29 ˚C across all the varying concentrations added (Table 2). This indicates that MO facilitated a reduction in the temperature of the storm water, thereby enhancing the slight conformity with the temperature range (27-28.8 ˚C) recommended by Mata-Alvarez et al. (2000).

Table 1. Physicochemical parameters of storm water (before treatment)

	Temperature (˚C)	**Conductivity (µs/cm)**	**pH**	**Turbidity (NTU)**	**TSS (mg/L)**
Values	33	634	8.09	1050	9672
APHA recommended Limits	27-28.1	8.50-14.14	6.50-8.50	5-25	-----

NTU= NephelometricTurbidity Units, TSS= Total Suspended Solids

Table 2. Efficiency of *Moringaoleifera* seed extracts and Aluminium Sulphate solution for the purification of stormwater

VSW (L)	Dose (g)	Concentration (mg/L)	Temperature (°C)	Turbidity (NTU)	pH	Conductivity (µs/cm)	TSS (mg/L)
***Moringa oleifera* seed extracts**							
0.5	5	50	29.0	1045	8.9	627	962.6
0.5	6	60	29.0	1042	8.9	621	959.8
0.5	7	70	29.0	1038	8.9	602	956.1
0.5	8	80	29.0	1048	8.9	620	966.2
Alumnium Sulphate solution							
0.5	5	50	27.7	216	8.9	627	99.448
0.5	6	60	26.4	206	8.9	628	59.88
0.5	7	70	25.6	99.2	8.9	618	45.68
0.5	8	80	25.5	114	8.9	620	52.62

VSW═ Volume of Storm Water, MO═ *Moringa oleifera*, NTU= NephelometricTurbidity Units, TSS═ Total Suspended Solids

However, the addition of Alum concentrations (50, 60, 70, and 80 mg/L) brought the temperature about 27.7, 26.4, 25.6, and 25.5 °C, respectively (Table 2). These results show a better effect of Alum on the temperature of sampled storm water. In this case, the results are all within the normal range (27 °C) recommended by Mata-Alvarez et al. (2000).

Percentage (%) reduction in *Moringa oleifera* seeds extracts was calculated using the formula:

$$\% \text{ Reduction} = \frac{\mathrm{Ti} - \mathrm{Tf}}{Ti} \times 100$$

where T_i= Initial Turbidity and T_f =Final Turbidity

The conductivity of storm water was initially measured before (634 µs/cm) (Table 1) and after the addition of MO seed extracts at varying concentrations (50, 60, 70, and 80 mg/L). The conductivity of the storm water dropped to 627, 621, 602, and 620 µs/cm, respectively (Table 2). Unfortunately, the addition of MO did not facilitate the conformity of the storm water samples with the recommended standard range (8.50-14.14 µs/cm) of GE (2012). Likewise, the same effect was recorded after the addition of Alum concentrations (50, 60, 70, and 80 mg/L) as the conductivity (627, 628, 618, and 620 µs/cm) were recorded, respectively (Table 2). This indicates that both coagulants did not aid the conformity of the storm water with the conductivity standard recommended by GE (2012). The results recorded in this study regarding the effect of Alum on the conductivity of the stormwater are contrary to the report of Harper and Herr (2000) on storm water as the conductivity before (587 µs/cm) the addition of Alum solution increased to 600, 609, 619 and 627 µs/cm after the addition of 5, 10, 15 and 20 mg/L of Alum solution, respectively.

When measured before treatment, the storm water's pH was recorded at 8.09 but increased to 8.9 with the addition of MO seed extracts (50, 60, 70, and 80 mg/L) and Alum solution (Table 2). These results show that both coagulants did not change the pH of the storm water appreciably during this study. Apart from the fact that the pH results obtained in this study are slightly above the normal range recommended by Appels et al. (2008), it also contradicts the pH results reported by Harper and Herr (2000) and Adeniran et al. (2017).

The initial turbidity of the storm water was 1050 (NTU) before adding varying concentrations (50, 60, 70, and 80 mg/L) of MO seed extracts. However, after the addition and subsequent retention time, it recorded 1045, 1042, 1038, and 1048 NTU, respectively (Figure 2). These results are, however, high above the standard range (5-25 NTU) recommended and reported by Raghuwanshi et al. (2002). Again, applying the same Alum solution concentrations facilitated massive and better reduction (216, 208, 99.2, and 114 NTU) in turbidity compared to the results obtained when varying concentrations of MO were employed (Fig. 2).

The percentage reduction in interface height had lesser percentages (0.47, 0.76, 1.14, and 0.19%) when varying concentrations of MO seed extract were employed compared to the superior reduction percentages (87.07, 90.09, 95.27, and 94.57%.) when Alum solution was used (Tables 3).

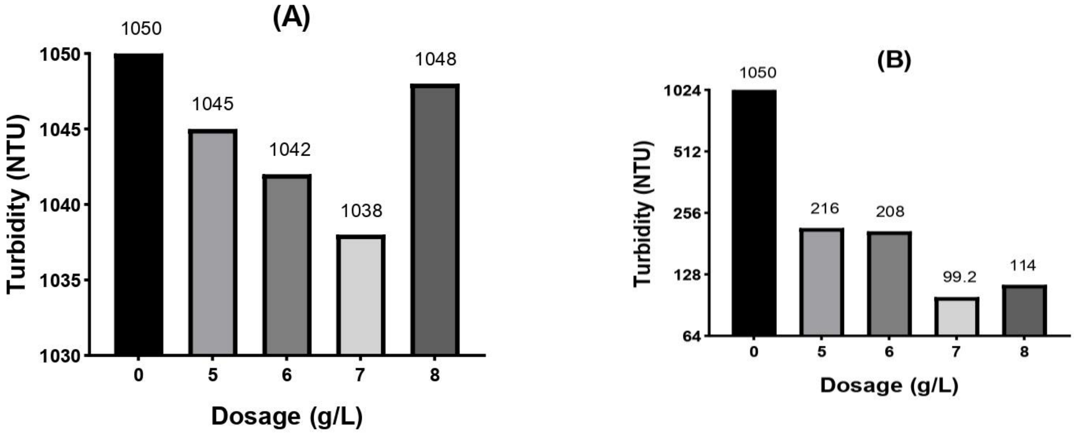

Fig. 2. Turbidity of storm water after adding (A) *Moringa oleifera* seed extract and (B) Alum solution.

Table 3. Interface height reduction (%) of the coagulants (*Moringa oleifera* seed extract and Alum solution).

Concentration of Coagulant (mg/L)	Total height reduction of the interface (%)	
	***MO* seed extract**	**Alum solution**
50	0.47^{a}	87.07^{b}
60	0.76^{a}	90.09^{b}
70	1.14^{a}	95.27^{b}
80	0.19^{a}	94.57^{b}

Means in the same row having different superscripts are significantly different from each other ($p<0.05$).

The superiority of chemical coagulants against natural polymers have been documented by International Water Association (2022). Nonetheless, in Table 3, it can be seen that the percentage reduction in interface heights of the coagulants are significantly ($p<0.05$) different from each other. The results obtained in this study agree with the reports of Muyibi and Alfugara (2010), and Adeniran et al. (2017), who reported that the higher the quantity of MO extract added for water purification, the better result was obtained.

Despite the efficiency of chemical coagulants in water purification, they certainly have disadvantages, as Vieira et al. (2010) reported in their study that there is an association between residual Aluminium in treated water and Alzheimer's disease. Additionally, Kaggwa et al. (2001) reported that sludge that has been thickened with chemical coagulants and polymers poses a threat to the environment by contributing to ground water pollution. MO seed extract, on the contrary, is non-toxic and was reported to be efficient in removing and preventing bacterial growth and heavy metals from the water, along side many advantages (Shan et al., 2017).

Conclusion

Varying concentrations of Alum solution had the best reduction percentages across all the measured parameters in this current study. However, MO-treated samples had lower reduction percentages than treated sludge samples suggesting that MO coagulant is not as effective in settling the suspended particles in the storm water samples. Due to the human health effects associated with using Alum, it is strongly suggested that further research be carried out on using MO seed extract as a coagulant in water treatment because of its natural availability, non-toxicity, and other immense benefits.

Author Contributions

G.B. Bate and A.O. Adeleye designed the experiment and wrote the manuscript, H.S. Mohammed carried out the laboratory work, and A.O. Amoo and E.M. Ijanu did the statistical analyses. C.I. Asaju helped with the manuscript arrangement. The final manuscript was reviewed and approved by all authors.

Conflict of interest

The authors declare that there is no conflict of interest as regards this study.

References

Adeniran KA, Akpenpuun TD., Akinyemi BA and Wasiu RA. Effectiveness of *Moringa oleifera* seed as a coagulant in domestic waste water treatment. *Afr. J. Sci., Technol. Innov. Dev.* 2017; 9(3): 323-328.

Amirtharajah A and O'Melia CR. Coagulation processes: destabilization, mixing, and flocculation. In: *Water Quality and Treatment*. Pontius FW (ed.), 4th Edition, Mcgraw-Hill, New York, 1990, pp.269-365.

Appels L, Baeyens J, Degrève J and Dewil R. Principles and potential of the anaerobic digestion of waste-activated sludge. *Prog. Energy Combust. Sci.* 2008; 34(6): 755-781.

Bratby J. Coagulation and flocculation in water and wastewater treatment. 3rd Edition, International Water Association. 2016.

Damayanti A, Ujang Z and Salim MR.The Influence of PAC, Zeolite, and *Moringa oleifera* as biofouling reducer (BFR) on hybrid membrane bioreactor of palm oil mill effluent (POME). *Bioresour. Technol.* 2011; 102(6): 4341-4346.

Dinka MO. Safe drinking water: concepts, benefits, principles and standards. In: *Water Challenges of an Urbanizing World*. Matjaž G. (Eds.), Chapter 10. Intechopen, London, 2018. pp.163-181.

GE. WATER AND PROCESS TECHNOLOGIES 2012. Handbook of Industrial Water Treatment. Clarification. United States: G.E. Water and Process Technologies.

Guchi E. Review on slow sand filtration in removing microbial contamination and particles from drinking water. *Am. J. Food Nutr.* 2015; 3(2): 47-55.

Harper HH, Herr JL and Livingston EH. Alum treatment of stormwater: The first ten years**.** New Applications in Modeling Urban Water Systems – Monograph 7. Proceedings of the Conference on *Stormwater and Urban Water Systems Modeling Conference*, Toronto, Canada, February 19-20, 1998.

Harper HH and Herr JL. Chemical coagulation of storm water runoff: An economical alternative for reducing nonpoint source impacts.Proceedings of the Delaware Urban Erosion, Sediment & Stormwater Conference. Newark, Delaware, October 24-26, 2000**.**

Kaggwa RC, Mulalelo CI, Denny P and Okurut TO. The impact of Alum discharges on a natural tropical wetland in Uganda. *Water Resour.* 2001; 35(3)**:** 795-807.

Katayon S, Noor MJMM, Wai KT, Ghazali AH, Thamer AM and Badronisa Y. Effect of natural coagulant application on microfiltration performance in treatment of secondary oxidation pond effluent. *Desalination*,2007; 204(1-3)**:** 204-212.

Khader EH, Mohammed THJ and Mirghaffari N. Use of natural coagulants for removal of COD, Oil and turbidity from produced waters in the petroleum industry. *J. Pet. Environ. Biotechnol.* 2018; 9(3): 1-7.

Krupinska I. Aluminium drinking water treatment residuals and their toxic impact on human health. *Molecules* 2020; *25*(3): 641.

Mata-Alvarez J, Mace S and Llabres P. Anaerobic digestion of organic solid wastes: An overview of research achievements and perspectives. *Bioresour.Technol.*.2000; 74(1): 3-16.

McConnachie GL, Folkard GK, Mtawali MA and Sutherland JP. Field trials of appropriate hydraulic flocculation processes. *Water Resour.* 1999; 33(6): 1425-1434.

Muyibi S and Alfugara A. Treatment of surface water with *Moringa oleifera* seed extract and Alum: A comparative study using a pilot scale water treatment plant. *Int. J. Environ. Sci.* 2010; 60(6): 617-626.

Muyibi SA, Noor MJMM, Ong DT and Kai KW. *Moringa oleifera* seeds as a flocculants in waste sludge treatment. *Int. J. Environ. Sci.* 2001; 58(2)**:** 185-195.

Ndabigengesere A, NarasiahK. S and Talbot BG. Active agents and mechanism of coagulation of turbid waters using *Moringa oleifera*. *Water Res*our. 1995; 29**:** 703-710.

Ndabigengesere A and Narasiah KS. Quality of water treated by coagulation using *Moringa oleifera s*eeds. *Water Res*our. 1998; 32**:** 781-791.

Pillai J. Flocculants and coagulants: The keys to water and waste management in aggregate production. *Illinois: Nalco Company, USA* 2004; pp. 308.

Raghuwanshi PK, Mandloi M, Sharma AJ, Malviya HS and Chaudhari S. Improving filtrate quality using agro-based materials as coagulant aid. *Water Qual. Res. J. Canada* 2002; 37(4): 745-756.

Shan TC, Matar MA, Makky EA and Eman NA. The use of *Moringa oleifera* seed as a natural coagulant for wastewater treatment and heavy metals removal. *Appl. Water Sci.* 2017; 7: 1369-1376.

Ukanwa W and Verstraete W. Anaerobic digestion of primary sludge from chemical pre-precipitation. *Water Sci. Technol.* 2010; 36**:** 357-365.

United States Environmental Protection Agency (USEPA) Coastal Stormwater Management through Green Infrastructure: A Handbook for Municipalities 2014; USEPA Publication.

Vieira AMS, Vieira MF, Silva GF, Araújo AA, Fagundes-Klen MR., Veit MT and Bergamasco R. Use of *Moringa oleifera* seed as a natural adsorbent for wastewater treatment. *Water Air Soil Pollut.* 2010; 206**:** 273-281.

J. Bangladesh Acad. Sci. 47(1); 127-137: June 2023 DOI: https://doi.org/10.3329/jbas.v47i1.63983

Journal of Bangladesh Academy of Sciences

Journal homepage: http://www.bas.org.bd/publications/jbas.html

Research Article

MHD convection in a square cavity with a heated cone: Effects of magnetic field and cone orientation

Saika Mahjabin and Md. Abdul Alim[1]

Department of Mathematics, National University, Gazipur, Bangladesh

ARTICLE INFO

Article History

Received: 21 December 2022
Revised: 05 June 2023
Accepted: 11 June 2023

Keywords: MHD free convection, Hartmann number, Square cavity, Heated cone, Finite element method

ABSTRACT

This paper presents a study on the influence of Magnetic Force impressed upon MHD fluid contained in a square cavity with a heated cone. The novelty of this work includes a heated cone whose orientation is varied at different angles. Calculations are performed for Prandtl number Pr = 0.71; Rayleigh number Ra = 10, 1000, and 100000; and Hartmann number Ha = 0, 50, and 100. The results are illustrated with streamlines, isotherms, and other relevant plots. It is observed that the influence of *Ha* becomes more noticeable with increasing *Ra*. *Ha* affects the flow by retarding the fluid movement and thus affects convective heat transfer. It is also observed that the cone orientation influences both fluid circulation and heat transfer. At high *Ra*, the vertical orientation of the cone resulted in lower heat flux than the left/right orientations. Also, under the same condition, the system remains cooler with the vertical cone at lower *Ha*, but becomes hotter after a certain value of *Ha*. These findings have practical design implications.

Introduction

The thermal behavior of Magneto-hydro-dynamic (MHD) fluids is an interesting subject. It has both theoretical and practical interests. Some practical applications include liquid metals, plasma, and high-velocity objects. The cone is an important shape, frequently seen in connection with fluid motion. The air molecules break apart at hypersonic speeds, producing electrically charged plasma around the aircraft (NASA 2022). Conical objects are also frequently used in pressure and flow control devices. The square is a basic shape, which provides scope for a baseline study, which can be extended to other shapes by changing the aspect ratio. For these reasons, square cavities and conical objects are chosen.

Much researched has been published on MHD fluid. Yang (1987), Kulacki et al. (1987), Moreau (1990), Vives and Perry (1987) published reviews on this subject. Many of the works mentioned in these reviews involve MHD fluid in enclosures, while the walls are maintained at different temperatures. The enclosures sometimes also contained objects of various shapes. A few recent works are mentioned next.

Sathiyamoorthy and Chamkha (2012) reported MHD fluid in a square cavity with an impressed magnetic field. The magnetic field strongly influenced the heat transfer regardless of wall heating conditions.

Bakhshan and Ashoori (2012) reported similar findings with a rectangular enclosure Nusselt number increased with Grashof (*Gr*) and Prandtl (*Pr*) numbers, indicating better heat transfer, and Hartmann number (*Ha*) had the opposite effect. Öztop and Al-Salem (2012) included joule heating in their study, along with a magnetic field. In their case, a strong magnetic field slowed the fluid motion and made the thermal

---

*Corresponding author: <mahjabinsaika.bd@gmail.com>

[1] *Department of Mathematics, Bangladesh University of Engineering & Technology, Dhaka, Bangladesh*

boundary layer thicker. Taghikhani and Chavoshi (2013) considered internal heating also, observing the reduction of convective heat transfer with *Ha*. Bhuiyan et al. (2014) placed a heated square block in the cavity and found that both the position of the block and *Ha* had influenced heat transfer. Hossain et al. (2015) investigated an open square cavity with a heated cylinder. It was found that the heat flux decreased with increasing *Ha*. Thus, the magnetic field had a retarding effect on flow and heat transfer. Ashouri et al. (2014) considered the cavity partially filled with conducting solid square obstacles. They also investigated the effect of the thermal conductivity ratio between the solid and fluid materials for different numbers of solid blocks. It was observed that the Nusselt number varied with solid-to-fluid thermal conductivity ratio, *Ha*, and the number of solid blocks. Hossain et al. (2015) also reported that the temperature and flow fields significantly varied between *Ra* and *Ha*. Mokaddes et al. (2021) investigated Casson fluid in double-lid driven square cavities. They found that the flow strength increases with the Reynolds number (Re) and Casson parameter and decreases with *Ha*. Ciofalo (2023) reported on MHD convection in one-dimensional configuration, i.e., indefinitely long vertical duct. It was shown that the system could be operated in different ways, such as an Electromagnetic pump, MHD generator, or a heat engine, depending on the boundary conditions. Mythreye (2023) studied MHD convection through a porous medium bounded by two vertical walls, together with chemical reactions and radiation. It is reported that velocity decreases with the increase in *Ha*, Chemical reaction parameter, *Kr*, and *Pr*. Bakar et al. (2020) reported the effects of *Ha* on MHD mixed convection in a li-driven rectangular cavity. As *Ha* increases, the flow convection is attenuated, and the heat transfer rate decreases. Goud et al. (2023) investigated the MHD flow of nanofluid on an inclined spinning disk with heat absorption and chemical reaction. The velocity of the fluid decreased with increasing *Ha*. A rise in thermal radiation (*Rd*) causes the temperature graphs to grow substantially, although the concentration profiles exhibit the opposite tendency. The short review presented indicates the number and variations of research works. The studies covered different fluids with different geometries of the cavity, the object inside the cavity, and heating conditions. The most common finding from all these works is that, for MHD fluid, the magnetic force retards fluid flow and hampers heat transfer. However, to the best of the authors' knowledge, the issue of the present work, i.e., the effect of cone orientations, has not been reported.

Model and Mathematical Formulation

The physical model is shown in Fig.1.

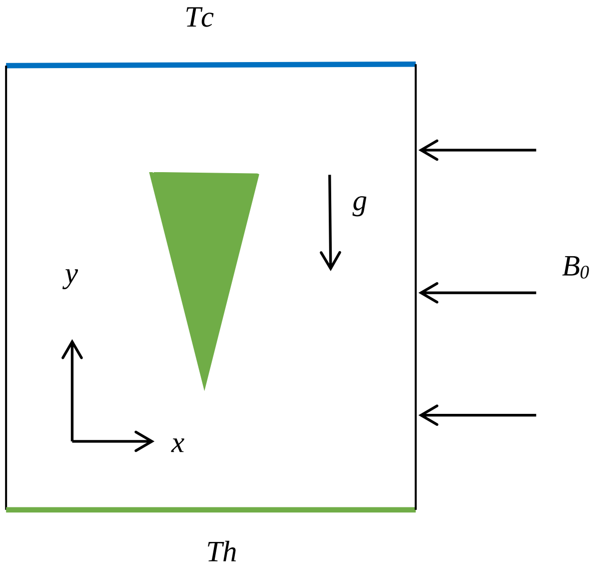

Fig. 1. Schematic diagram of the model

The top wall is held at a lower constant temperature (T_c), and the lower wall is at a higher temperature (T_h). Both the left and right walls are adiabatic. The cone temperature is constant at (T_h). The cone is placed at three angles: i) vertical, ii) left inclined, and iii) right inclined. The magnetic field B_0 acts perpendicularly to the flow.

The density of the fluid varies with the temperature, and other properties remain constant. Radiation and Joule heating are not considered. With these assumptions, we get the following:

i) Conservation of mass $\frac{\partial u}{\partial x} + \frac{\partial v}{\partial y} = 0$ (1)

ii) Conservation of momentum:

ii.a) x-momentum equation $\rho\left(u\frac{\partial u}{\partial x} + v\frac{\partial u}{\partial y}\right) = -\frac{\partial p}{\partial x} + \mu\left(\frac{\partial^2 u}{\partial x^2} + \frac{\partial^2 u}{\partial y^2}\right)$

ii. b) y-momentum equation

$$\rho\left(u\frac{\partial v}{\partial x} + v\frac{\partial v}{\partial y}\right) = -\frac{\partial p}{\partial y} + \mu\left(\frac{\partial^2 v}{\partial x^2} + \frac{\partial^2 v}{\partial y^2}\right) + \rho g\beta\,(T - T_c) - \sigma B_0^2 v$$

iii) Conservation of Energy: $u\frac{\partial T}{\partial x} + v\frac{\partial T}{\partial y} = \alpha\left(\frac{\partial^2 T}{\partial x^2} + \frac{\partial^2 T}{\partial y^2}\right)$

The governing equations are made dimensionless using the following dimensionless variables:

$$X = \frac{x}{L} \quad Y = \frac{y}{L} \quad U = \frac{uL}{\alpha} \quad V = \frac{vL}{\alpha}$$

$$P = \frac{pL^2}{\rho\alpha^2} \quad \theta = \frac{T - T_c}{T_h - T_c} \quad \sigma = \frac{\rho^2\alpha}{L^2} \quad \alpha = \frac{k}{\rho C_p}$$

$$\nu = \frac{\mu}{\rho}$$

Applying these definitions, the following dimensionless equations are obtained.

$$\frac{\partial U}{\partial X} + \frac{\partial V}{\partial Y} = 0$$

$$U\frac{\partial U}{\partial X} + V\frac{\partial U}{\partial Y} = -\frac{\partial P}{\partial X} + Pr\left(\frac{\partial^2 U}{\partial X^2} + \frac{\partial^2 U}{\partial Y^2}\right)$$

$$U\frac{\partial V}{\partial X} + V\frac{\partial V}{\partial Y} = -\frac{\partial P}{\partial Y} + Pr\left(\frac{\partial^2 V}{\partial X^2} + \frac{\partial^2 V}{\partial Y^2}\right)$$

$$+ \frac{Ra}{Pr}\theta - Ha^2\,\mathrm{Pr}\,V\,U\frac{\partial \theta}{\partial X} + V\frac{\partial \theta}{\partial Y} = \frac{\partial^2 \theta}{\partial X^2} + \frac{\partial^2 \theta}{\partial Y^2}$$

Where,

Prandtl number, $Pr = \frac{\nu}{\alpha}$;

Hartmann number, $Ha^2 = \frac{\sigma B_0^2 L^2}{\mu}$;

Grashof number, $Gr = \frac{g\,\beta\,L^3(T_h - T_c)}{\nu^2}$;

Rayleigh number, $Ra = \frac{g\,\beta\,L^3(T_h - T_c)\,Pr}{\nu^2}$;

Boundary Conditions

After applying the above dimensionless quantities, the dimensionless boundary conditions become:

$U = V = 0,\ \theta = 1$ at the bottom wall and heated conical body

$U = V = 0,\ \theta = 0$ at the top wall

$U = V = 0,\ \frac{\partial \theta}{\partial N} = 0$ at side walls

$P = 0$ Fluid pressure at the inside and on the walls of the cavity

Moreover, μ is the fluid's viscosity, β is the coefficient of thermal expansion, and B_0 is the magnetic force.

Numerical Procedure

The finite element method is used to solve the equations shown above. The detailed procedures of finite elements can be found in the works of Taylor and Hood (1973), Reddy (1993), and Dechaumphai (1999), etc.

Grid Generation

The model is discretized into elements. The governing and boundary equations are applied to each element to get a solution for the entire system. Therefore, the finer the mesh, the more accurate the result. However, finer meshing involves a much greater number of operations and time. Therefore, a reasonable number of elements are taken to obtain results with acceptable accuracy and not over-taxing computer resources or time. This is presented next.

Grid Refinement Check

The accuracy of the finite element method is sensitive to the number of cells or the mesh size. In general, a finer mesh is expected to yield greater accuracy. However, taking finer mesh for a short time is only practical for two reasons. Firstly, more cells result in longer runtime and may overtax the computer's resources. Secondly, adding more cells does not significantly improve the accuracy after a certain number of cells. Therefore, an optimum number of cells should be selected. In this study, the average Nusselt number was calculated for benchmarking accuracy.

The average Nusselt number (Nu) was calculated with different numbers of elements. The results are shown in Fig. 2. It is seen that beyond 8,000 elements, the change in Nu diminishes. Thus, the mesh with 8,039 elements was chosen. The resulting mesh structure is displayed in Fig.3.

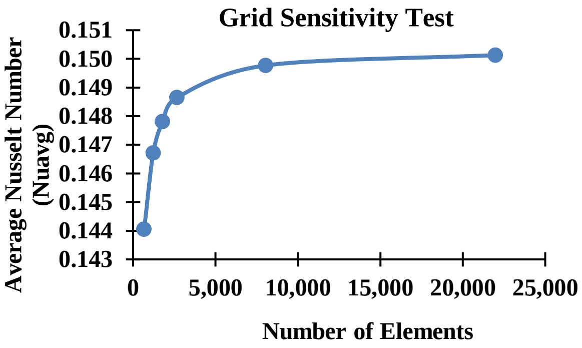

Fig. 2. Grid sensitivity (*Ha* = 0, *Ra* =1E5).

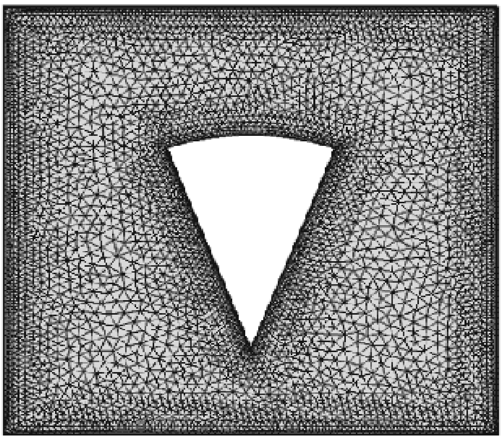

Fig. 3. Mesh with 8,039 elements.

Code Validation

There is no experimental data available to validate our code. Therefore, the only option was to check it against some published numerical results. The code underlying the present model was checked against that of the work of Bhuiyan et al. (2014). Current work involves a conical object in a square cavity, while their work involves a square object placed at different corners. Therefore, we replaced the cone with a heated square object and generated streamlines and isotherms. Fig. 4 shows the comparisons graphically. It is seen that the results are very similar. Thus, our code was validated.

Results and Discussions

The following parameter values were used in the calculations:

Prandtl number *Pr* = 0.71

Rayleigh number *Ra* = 10, 1000, and 100,000;

Hartmann number *Ha* = 0, 50, and 100. The results and discussions are presented in two main segments- ***i) fluid motion and ii) heat transfer***. Only the results involving *Ha* = 0 and 100 are presented for brevity.

i) Fluid Motion Study

The fluid inside the cavity is set in motion by convection. Since it is a closed system, the fluid remains in the cavity and circulates. In a steady-state laminar flow system, fluid particles follow fixed paths, but velocity along a certain arbitrary path may vary. This is best illustrated with streamlines.

Streamlines

Fig. 5 presents streamlines for the three-cone orientations. The parameters are Raleigh number (*Ra*), which represents the degree of fluid movement or circulation, and Hartmann number (*Ha*), which represents the intensity of the magnetic field. It was observed before (Mahjabin and Alim, 2018) that the effect of *Ha* became more noticeable with high *Ra*. Therefore only the results with *Ra* = 100,000 are presented.

The flow patterns for the left and right inclinations of the cone are like a mirror image. At *Ha* = 0, one vortex is created on either side of the cone. Two main and two sub-vortices are seen for the vertical cone.

A color scale indicates fluid velocities. Local fluid velocities are greater while passing through narrow channels, as expected.

At *Ha* = 100, the streamlines for left and right cone positions remained somewhat the same, although the position of the vortex changed. For the vertical position, the sub-vortices disappeared, and the main vortices moved towards the colder surface, i.e., to the top wall. The most important phenomenon, however, is the dramatic reduction of velocity, as shown in the color legend scale next to each figure. For example, for the vertical cone position, the velocity range reduced from 60-10 to 6-1, i.e., a ten-fold reduction was achieved by impressing the magnetic field. Therefore, the effect of *Ha* is to retard fluid movement. The reason can be explained as follows.

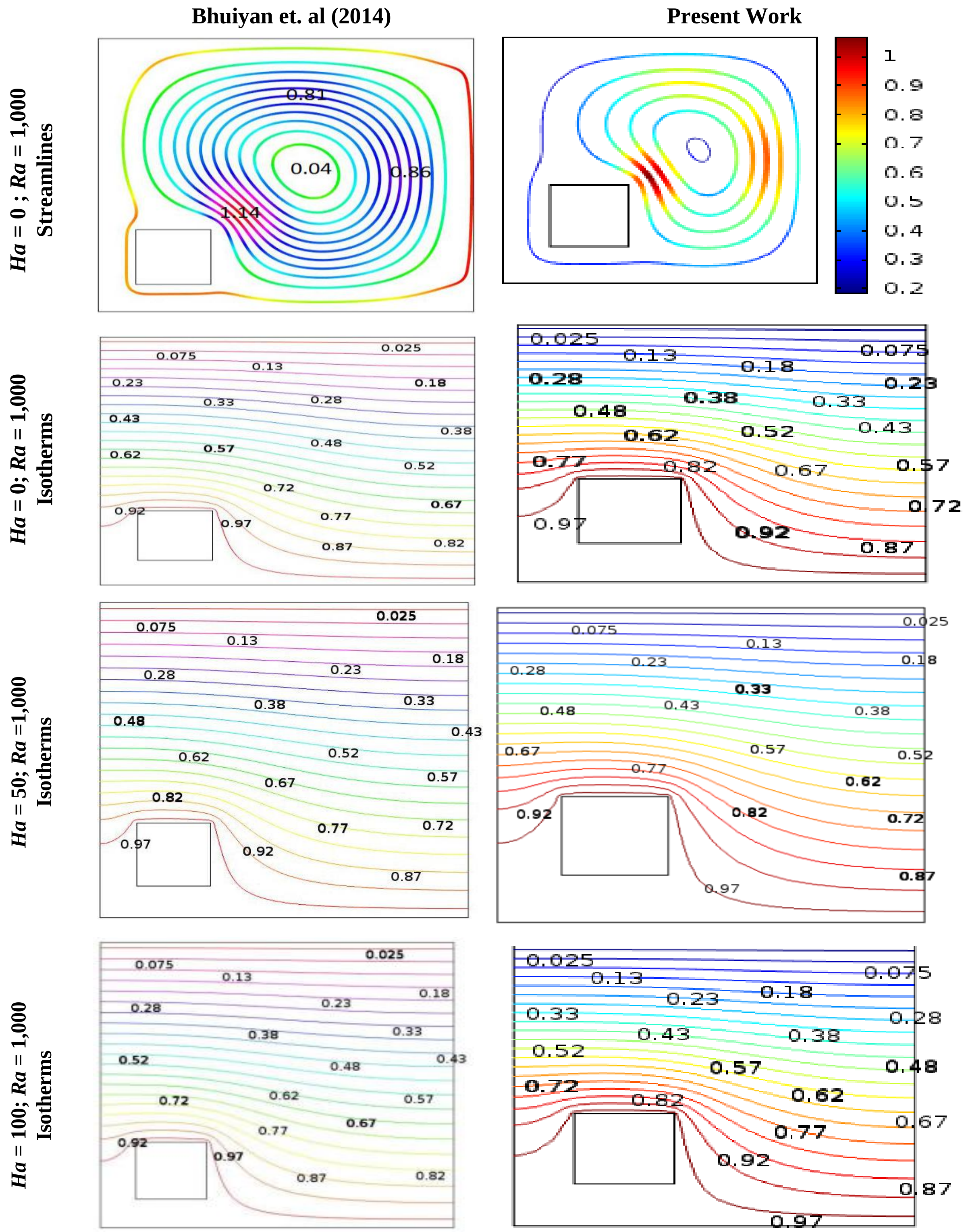

Fig. 4. Code validation: Comparison of results between present work and Bhuiyan et al. (2014)

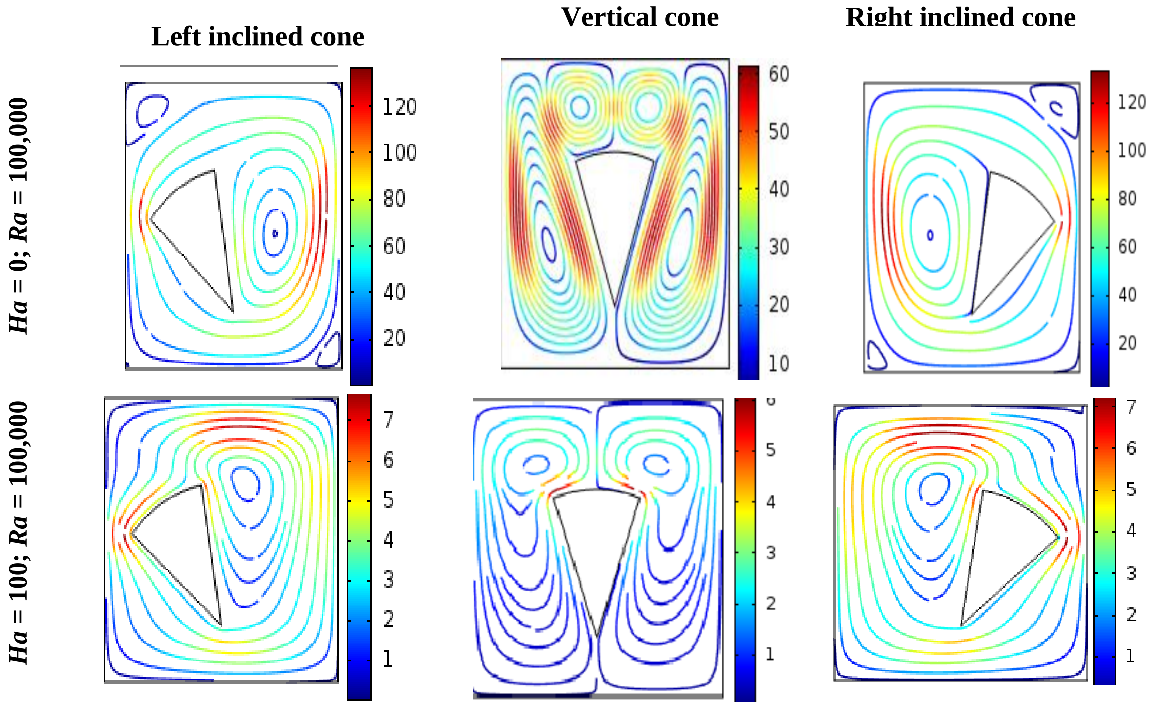

Fig. 5. Streamlines illustrating the effect of *Ha* on fluid movement.

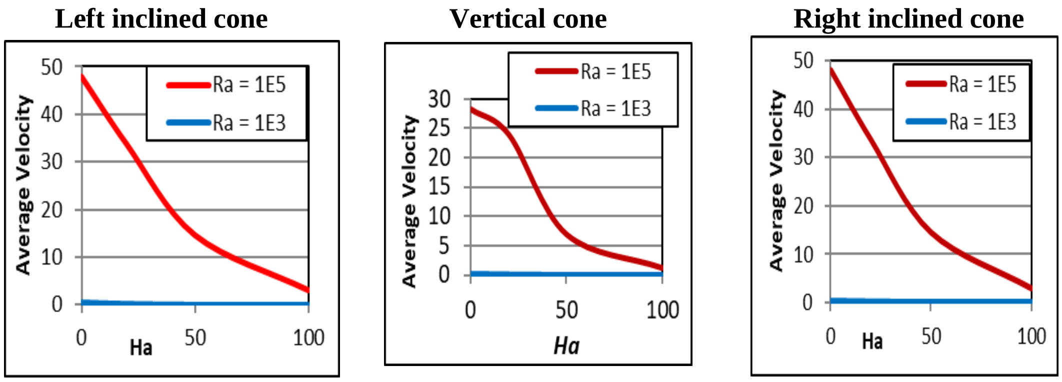

Fig. 6. Volumetric Average velocity for different *Ha* and *Ra*.

Three forces are acting on the system- the body force, which is the weight of the fluid, and it always works downwards. There is buoyancy force, which arises from the density difference of the fluid. The density difference is caused by the heat applied through the bottom wall and from the cone. Hotter fluid is less dense and tends to rise toward the colder region. Denser fluid from the colder region moves downward. Thus, initially, the fluid starts to move at rest, and circulation is established. However, the fluid circulation cannot increase indefinitely. The fluid circulation eventually reaches equilibrium for a given condition, such as at a fixed Ra. The fluid velocity, or the circulation rate, is directly related to the Raleigh number. The greater value of *Ra* implies more circulation and greater fluid velocity. The third force in the system is the magnetic field. When applied to an MHD fluid, it produces a drag-like force called the Lorentz force. It causes a reduction in the fluid velocity.

It should be noted that the fluid must be in motion to manifest any effect of a magnetic force. Thus, greater intensity of the magnetic force (Ha) is expected to slow down the fluid circulation. This physical explanation applies to all the results presented in the subsequent sections.

Average Velocity

Streamlines indicate the fluid circulation paths and velocity variations, but the average velocity can provide insight into the overall flowing condition in the cavity. Therefore, the average volumetric velocity of the fluid was calculated for each configuration and presented in Fig. 6.

The variation of the volumetric average velocity for the three orientations of the cone is quite similar, although the magnitudes are slightly different. For high *Ra*, the average velocity decreases sharply with increasing *Ha*. For example, for the vertical cone, average velocity is reduced from 28 to 2, i.e., about 14 times reduction was achieved when *Ha* was increased from 0 to 100. This is consistent with previous observations (Fig. 5). The impact of *Ha* at lower *Ra* is not noticeable.

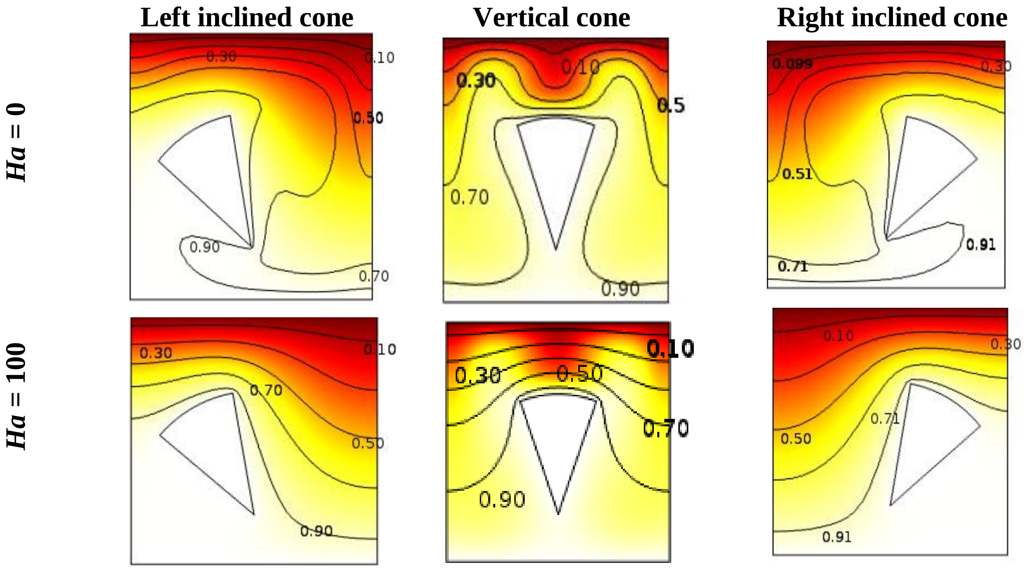

Fig. 7. Isotherms illustrating the effect of *Ha* on temperature distribution (*Ra* = 100,000).

ii) Heat transfer Study

Heat transfer is studied in terms of temperature distribution (isothermal lines), average temperature, local Nusselt number, and Heat flux. These are presented next.

Isotherms

In a steady-state system, the temperature is distributed over the system, which isothermal lines can illustrate. These lines remain fixed for a given configuration and a fixed set of parameters. As mentioned before, the effect of *Ha* is more noticeable with large values of *Ra*. Therefore, only isotherms with *Ra* = 100,000 and *Ha* =0 and 100 are presented in Fig.7. Asymmetric, closely packed isotherms imply uneven and inefficient heat transfer. In contrast, more evenly spaced isotherms indicate smoother temperature distribution and more efficient heat transfer.

Fig. 7 shows isotherms with color shades. Numbers next to the isotherms are dimensionless temperatures. The lighter shades indicate hotter zones.

The isotherms for the left and right inclinations of the cone are like a mirror image and symmetric around the vertical cone. At high *Ra* and zero *Ha*, the lines are distorted and spread across more cavity areas for all three cone positions. The hotter fluid covers lesser parts of the body. With the greater circulation of the fluid, heat is carried more efficiently from the hotter to the colder region.

With *Ha* = 100, the isotherms become smoother and more compacted. The hotter fluid covers more portions of the cavity. It means the heat is less efficiently removed from the hotter to the colder region. Since convective heat transfer mainly depends on fluid movement, any restriction on fluid movement will influence heat transfer. The heat transfer mechanism becomes more like conduction than convection. The temperature distribution thus becomes more even, as seen in the isotherms. It may be inferred that *Ha* retarded both fluid circulation and heat transfer.

Average Temperature

Isotherms indicate the temperature distribution, but the average temperature can provide insight into the heating condition in the cavity. Therefore, the volumetric average temperature of the fluid was calculated for each configuration and presented in Fig. 8.

Nusselt Number

The local and average Nusselt numbers were evaluated *for the vertical cone only*, and the results are shown in Table 1. The average Nusselt Number decreased with increasing *Ha*, indicating a retarding effect on heat transfer.

The local Nusselt number was evaluated along the bottom hot wall and plotted in Fig. 9. It shows *Nu* is lowest at the center. This is consistent because this point is just below the heated cone. Heat transfer should be the minimum between two hot bodies of the same temperature, as indicated by the dip of the curves.

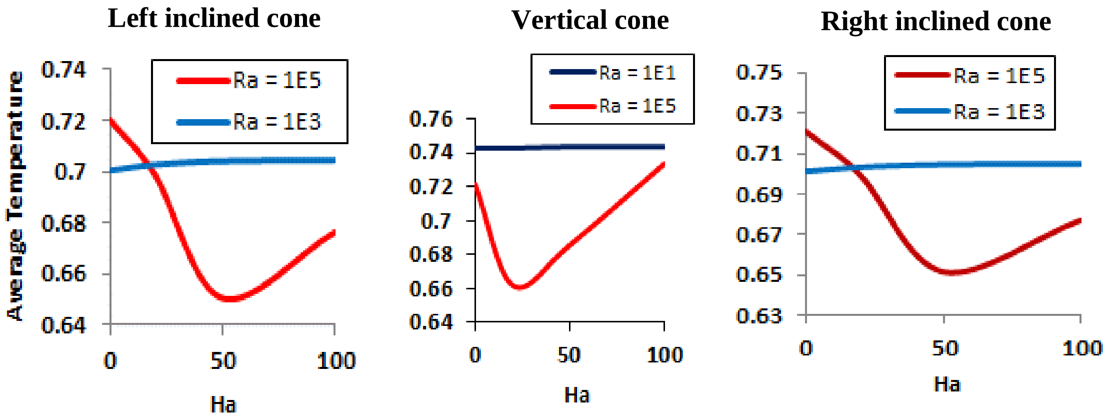

Fig. 8. Volumetric average temperature for different *Ha* and *Ra*.

The average temperature variation for the left and right cone orientations is identical, and for the vertical position, it is somewhat different. For high *Ra*, the average temperature decreases first and then increases with *Ha*. The average temperature remains generally higher for all three orientations for low *Ra* and slightly varies with *Ha*. This observation has practical design implications. For example, if there is a requirement to keep the system cool, the corresponding *Ha* should be applied. *Ha* greater or smaller than this value will make the system hotter.

Table 1. Average Nusselt Number

Ha	*Ra*	Nu_{avg}
0	1.00E+05	1.16098
50	1.00E+05	0.45942
100	1.00E+05	0.1793

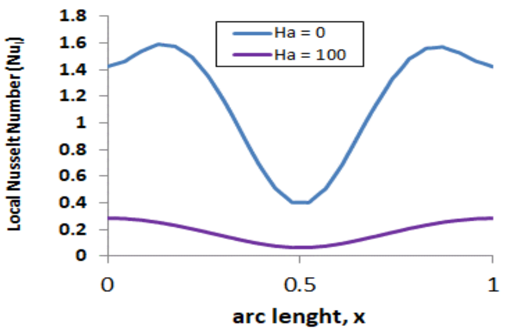

Fig. 9. Local Nusselt number as a function of *Ha* (*Ra* = 1E5)

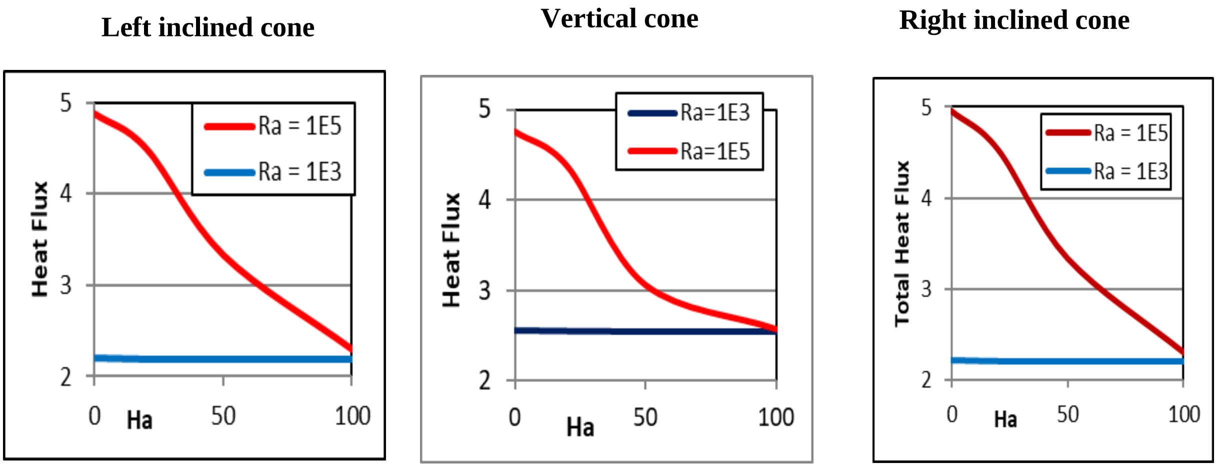

Fig. 10. Heat flux as a function of *Ha* and *Ra*

Heat Flux

The most direct and quantitative study of heat transfer is heat flux, which indicates the amount of heat energy passing through a plane of unit area. It was calculated for a plane adjacent to the top wall of the cavity with different values of *Ha* and *Ra*, and shown in Fig. 10.

The patterns are quite similar for all cone positions for high *Ra*. Heat flux decreases noticeably with *Ha*. For example, for the vertical cone, at *Ra* = 100,000, the heat flux reduced from 4.8 to 2.5 when *Ha* was increased from 0 to 100. The effect of *Ha* at low *Ra* is minimal. However, at low *Ra*, heat flux is greater for the vertical position. This observation is consistent with all previous observations. It is interesting to note that the plots look very similar.

Comparison of Average Velocity

Fig. 11 compares the three curves, representing the volumetric average velocity for the three cone orientations, for a given *Ra* = 100,000 and different *Ha*. At high *Ra* (100,000) and *Ha* = 0, average velocity is about 42% lower for the vertical cone compared to the inclined cones. With increasing *Ra*, this difference diminishes.

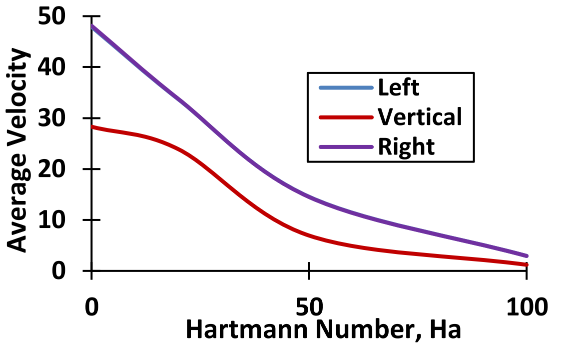

Fig. 11. Effect of cone orientation on average volumetric velocity (*Ra* = 100,000). Note: Left & right orientation produced identical results. Hence the 2 curves merged.

The average velocity variation with *Ha* is identical for the left and right orientation of the cone, while it is somewhat different for the vertical position. In all cases, the average velocities gradually reduce with increasing *Ra*. Most noticeably, the vertical position results in lower average velocity than the inclined positions.

Comparison of Average Temperature

Fig. 12 shows the volumetric average temperature for the three-cone orientations.

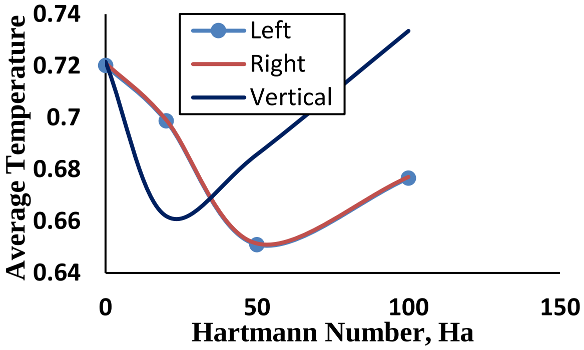

Fig. 12. Effect of cone orientation on volumetric average temperature (*Ra* = 100,000). Note: Left & right orientation produced identical results. Hence the 2 curves merged.

The average temperature variation with *Ha* is identical for the left and right orientation of the cone, while it is noticeably different for the vertical position. In all cases, the temperature decreases first and then increases with *Ha*. For the vertical position, the lowest temperature appears earlier, at a lower *Ha*, and remains lower than the other two curves representing the left and right inclined cone. However, after about *Ha* = 40, the temperature remains higher for the vertical position. The design implication of this phenomenon is that the system will be hotter with the vertical cone for *Ha* > 40.

Comparison of Heat Flux

The effect of orientation on heat flux is shown in Fig. 13.

At lower *Ha*, the left and right orientations of the cone show identical results and indicate a greater heat flux.

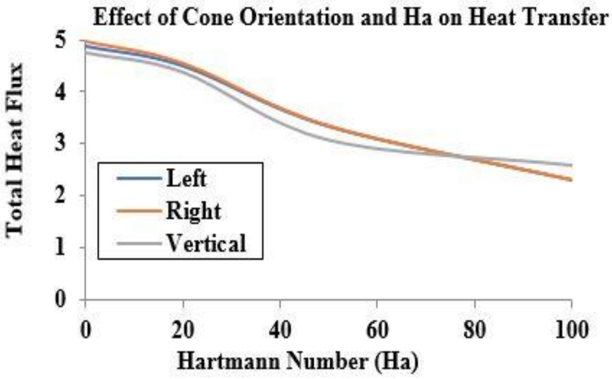

Fig. 13. The effect of orientation on heat flux (*Ra* = 100,000).

The vertical position after about Ha = 80 resulted in greater heat flux. It implies that the system is more efficient for heat transfer with the inclined positions if circulation needs to be high. Otherwise, the vertical position should result in a more efficient system (Fig. 10).

Conclusion

At high *Ra*, fluid particles move at a higher velocity without any magnetic force. Impressing a magnetic field in this situation produced a noticeable effect by slowing the fluid movement. For example, in the case of the vertical cone, with Ra held at 100,000, the fluid velocity reduced almost 10 times when *Ha* was increased from 0 to 100. The average velocity is reduced from 28 to 2, i.e., about 14 times reduction was achieved when *Ha* was increased from 0 to 100 for the vertical cone. The velocity reduction effect caused by *Ha* also affects the temperature distribution and heat flux. For example, at Ra = 100,000 for the vertical cone, the heat flux reduced from 4.8 to 2.5 when *Ha* increased from 0 to 100. The cone's orientation also significantly impacts the average velocity, temperature, and heat flux. At *Ra*=100,000 and *Ha* = 0, the average velocity is about 42% lower for the vertical cone than the inclined cones. With increasing *Ha*, this difference in average velocity diminishes. At a high *Ra*, inclined cones show better heat transfer efficiency, while the opposite happens at low *Ra* for most values of *Ha*.

Acknowledgments

The authors would like to deeply appreciate the Department of Mathematics, Bangladesh University of Engineering and Technology, for supporting this research using supervision and providing computational facilities. They also thank the Mathematics Department, National University, Gazipur, for allowing the time and opportunity to conduct this research.

Author Contribution

Md. Abdul Alim: Concept, supervision, manuscript review. Saika Mahjabin: Literature review, simulation, results analysis, manuscript writing, and revision.

References

Ali MM, Akhter R and Alim MA. Performance of flow and heat transfer analysis of mixed convection in Casson fluid filled lid driven cavity including solid obstacle with magnetic impact. *SN Appl. Sci.* 2021; 3: 250.

Ashouri M, Shafii MB and Kokande HR. MHD natural convection flow in cavities filled with square solid blocks. *Int. J. Num. Methods Heat Fluid Flow.* 2014; 24(8): 1813-1830.

Bakar NA, Roslan R and Karimpour A. Magnetic field effect on mixed convection heat transfer in a Lid-driven rectangular cavity. *CFD Letters*. 2020; 12(1):13-21.

Bakhshan Y and Ashoori H. Analysis of a fluid behavior in a rectangular enclosure under the effect of magnetic field. *J. World Acad. Sci. Engg. Tech.* 2012*;* 6(1): 637-641.

Bhuiyan AH, Alim MA and Uddin MN. Effect of hartmann number on free convective flow in a square cavity with different positions of heated square block. *Int. J. Mat. Phy. Elect. Comp. Eng.* 2014; 8(2): 385-390.

Ciofalo, M. One-dimensional mixed MHD convection. In: *Thermo Fluid Dynamics*. UNIPA Springer Series. Springer, Cham. 2023.

Dechaumphai P. *Finite Element Method in Engineering.* 2nd ed. Chulalongkorn University Press, Bangkok; 1999.

Goud S, Yalana DR and Wakif A. Numerical analysis on the heat and mass transfer MHD flow characteristics of nanofluid on an inclined spinning disk with heat absorption and chemical reaction. *J. Heat Trans*. 2023, 52(2): 3615-3639.

Hossain SA, Alim MA and Saha SK. A Finite element analysis on MHD free convection flow in open square cavity containing heated circular cylinder. *Am. J. Comp. Mat.* 2015; 5(1): 41-54.

Kulacki FA, Davidson PF and Dunn JH. Convective heat transfer with electric and magnetic field. In: *Handbook of Single-Phase Convective Heat Transfer.* Kakac S, Shah RK and Aung W, eds., Wiley, NY; 1987.

Mahjabin S and Alim MA. Effect of hartmann number on free convective flow of MHD fluid in a square cavity with a heated cone of different orientation. *Am. J. Comp. Mat.* 2018; 8(4): 314-325

Moreau, M. *Magnetohydrodynamics*, Kluwer Acadamic, Dordrecht, The Netherlands. 1990.

Mythreye A. Chemical reaction effects on MHD free convection heat and mass transfer flow through a porous medium bounded by two vertical walls in the presence of radiation. *J. New Zealand Herpetology*. 2023, 12(1).

NASA https://www.grc.nasa.gov/www/k-12/airplane/lowhyper.html Retrieved on June 20, 2023.

Öztop FH and Al-Salem K. Effects of joule heating on MHD natural convection in non-isothermally heated enclosure. *J. Thermal Sci. Tech.* 2012; 32(1): 81-90.

Reddy JN. *An Introduction to Finite Element Method.* McGraw-Hill, NY. 1993.

Sathiyamoorthy M and Chamkha AJ. Natural convection flow under magnetic field in a square cavity for uniformly (or) linearly heated adjacent walls. *Int. J. Num. Methods Heat Fluid Flow.* 2012. 22(5): 677-698

Taghikhani MA and Chavoshi HR. Two dimensional MHD free convection with internal heating in a square cavity. *J. Therm. Energy Power Eng*. 2013; 2: 2-28.

Taylor C and Hood P. A Numerical solution of the navier-stokes equations using finite element technique. *J. Comp. Fluids.* 1973; 1(1): 73-89.

Vives C. and Perry C. Effects of magnetically damped convection during the controlled solidification of metals and alloys. *Int. J. Heat Mass Transf.* 1987; 30(3): 479-496.

Yang KT. Natural convection in enclosures. In: *Handbook of Single-Phase Convective Heat Transfer*, Kakac S, Shah RK and Aung W, eds., Wiley, NY. 1987.

INSTRUCTION FOR AUTHORS

The Journal of Bangladesh Academy of Sciences is published four times a year in March, June, September and December. Original research articles, review articles, and short communications of high standards of all branches of Science and Technology are considered for publication in this journal. Review articles are generally by invited authors; however, the Editor welcomes suggestions of potential topics and potential authors.

The following instructions must be followed while preparing the manuscript intended for publication in this journal:

1. **Research Article:** Manuscripts should be concise and consistent with the style of the journal. The manuscript must be typed using Times New Roman font, size 12 on A4 size page, and wide (1 inch) margins on all four sides. The main text must be typed in a two-column format with 1.5 spacing, and for full papers, it should not exceed 10-20 typed pages, including figures, tables, and references. In general, an article may contain the following sub-titles in sequence: **Title, Abstract, Keywords, Introduction, Materials and Methods, Results and Discussion, Acknowledgement (**if any), and **References.**

A. Title: The first page of the paper, the title page, should have the title and the names of the authors. The title should be brief and specific. Abbreviations and formulae should be avoided where possible. The next line in italics should be the authors' affiliation addresses (where the actual work was done) below the names. Indicate all affiliations with a lowercase superscript letter immediately after the author's name and in front of the appropriate address. The corresponding author, along with email address, should be indicated at the footnote with a proper asterisk.

B. The second page should carry the Title of the paper, Abstract, and Keywords. Author(s) name must not be typed on this page.

- **(i) Abstract:** It should not exceed 150 words and should briefly state the purpose of the research, the significant results, and meaningful conclusions. Nonstandard or uncommon abbreviations should be avoided, but if essential, they must be defined at their first mention in the abstract itself.
- **(ii) Keywords:** Immediately after the abstract, provide a maximum of 6 keywords.

C. The next pages (a maximum of 15 printed pages), will contain the main text of the paper.

(i) Introduction: It should be concise and relevant to the objectives of the study. The importance of the research work described should be pointed out. An appropriate review of the current literature should be made to identify the frontier of existing knowledge and point out the need for further work. The knowledge contributed to the study should be mentioned.

(ii) Materials and Methods: Materials used should be mentioned precisely along with their sources and any pre-treatment undertaken.

The description of methods must be brief but clear enough to enable a reader to reproduce the results. References must be considered sufficient for methods described in earlier publications: only relevant modifications should be described.

It is recommended that authors use the nomenclature and symbols adopted by IUPAC document UIFII (S.U.N. 65-3) 1965, symbols, units, and nomenclature in Physics or by IUPAC Manual of Physiochemical symbols, Terminology and similarly for other disciplines.

(iii) Results and Discussion: This section should include descriptions of results obtained with the help of figures, tables, graphs, and photographs as may be necessary. Tables should have a descriptive title. Large and cumbersome tables should be avoided. Figures and graphs should be prepared and should be properly labelled with bold solid lines such that no further size reduction will be necessary. The paper should contain a minimum number of **Tables, Graphs,** and **Figures.** The same data should not be depicted using both tables and figures. The photographs are to be submitted in JPEG format.

The discussion should include thorough analysis and interpretation of results, and comparison with existing relevant published results, if any, and self-evaluation of the new knowledge contributed, avoiding extensive citations and discussion of published literature.

(iv) Conclusions

The study's main conclusions may be presented in a short Conclusions section, which may stand alone or form a part of the Results and Discussion section.

(v) Acknowledgment: The following support for the research work should be acknowledged:

- Funding by any agency;
- The use of instruments in a laboratory other than those of the authors;
- Individual’s help during the research (e.g., providing an interpretation of results, language help, writing assistance, or proofreading, etc.).

(vi) Author contributions

For transparency, we encourage authors to submit an author contribution statement outlining each author's contributions to the paper. The authors should have participated sufficiently in the work to take public responsibility for appropriate portions of the content.

(vii) References and Text Citations:

In the text, references should be cited within brackets quoting the first author's surname followed by et al. if necessary and the year of publication in the appropriate place, e.g. (Bhuiyan, 2020), Khan et al. (2021) or (Khan et al., 2021). In the case of only two authors, surnames of both need to be mentioned, e.g., (Khan and Rahman, 2021). A semi colon should separate two or more references when putting within the same bracket. At the end of the manuscript, references should be listed and arranged alphabetically according to the first author's surname according to the style described below:

(a) Journal article:

In each reference, names of all authors' will have to be given in the same style, e.g., surname followed by initials, lumped together without using a full stop. The names will be followed by the full title of the article and the journal's abbreviated title (in italics). The year of publication will be given next, followed by volume number (issue number) and page ranges. For abbreviations of the names of journals, authors are advised to follow the *World List of Scientific Periodicals.* For online publications, the URL address must be given. Note: Please list ALL authors’ names in the list of references, do not use (et al.). **Examples:**

Islam S. The Induced Morphological and Root Anatomical Changes in Lentil. *J. Bangladesh Acad. Sci.* 2019; 43(2):107-112.

James BD and Bennett DA. Causes and Patterns of Dementia: An Update in the Era of Redefining

Alzheimer's Disease. *Annu. Rev. Public Health;* 2019; 40: 65-84.

Moniruzzaman M, Khatoon R and Qamruzzaman AKM. Influence of Plant growth Regulators on Vegetative Growth, Sex Expression and Yield of Summer Bottle Gourd. *Bangladesh J. Agril. Res*. 2019; 44(4): 577-590.

(b) Book or Chapter in a Book:

The place and name of the publisher, year of publication, will have to be given in addition to the name of the author(s), the title of the book (in italics), edition number (if not first), and the number of pages. In the case of an article or chapter in a book or proceedings of a conference, author(s) name and the title of the article or chapter will be followed by the title of the book (in italics), the names of the editors of the book, edition number (if not first), the place and name of the publisher, year of publication and page or page numbers of chapter. **Examples:**

Book:

Carlson BM. *Human Embryology and Developmental Biology*. 4th ed. St. Louis: Mosby; 2009. p. 541.

Cassese A, Acquaviva G, Fan M and Whiting A. *International Criminal Law: Cases and Commentary*. Oxford University Press; 2011, p. 600.

Chapter in an edited book:

Muhammad HFL and Dickinson KM. Nutrients, energy values and health impact of conventional beverages, Chapter 3. In: *The Science of Beverages, Volume 12: Nutrients in Beverages*. Grumezescu AM, Holban AM, eds., Elsevier Science; 2019; pp. 77-109.

Balsam KF, Martell CR, Jones KP, Safren SA. Affirmative cognitive behavior therapy with sexual and gender minority people. In: *Culturally Responsible Cognitive Behavior Therapy: Practice and Supervision*. Iwamasa GY, Hays PA, eds., 2nd edition, American Psychological Association. 2019; p. 287-314.

(c) Proceedings of a Conference:

Luca J and Tarricone P. Does emotional intelligence affect successful teamwork? In: *Meeting at the Crossroads*. Kennedy G, Keppell M, McNaught C (eds.), Proceedings of the 18th Annual Conference of the Australasian Society for Computers in Learning in Tertiary Education, 2001 Dec 9-12; Melbourne: Biomedical Multimedia Unit, The University of Melbourne; 2001. pp. 367-376.

(d) Reports:

Bangladesh Bureau of Statistics (BBS). Population census - 2011. Preliminary report. Bangladesh Bureau of Statistics, Ministry of Planning, Government of the People's Republic of Bangladesh, Dhaka, 2011.

Rowe IL and Carson NE. *Medical manpower in Victoria. East Bentleigh (AU)*: Monash University, Department of Community Practice; 1981. p. 35. Report No.: 4.

2. **Short communication:** Important research findings that may initiate further research in the relevant field may be published in the form of a short communication. This should not exceed three printed pages (900 words), including Graphs, Tables, and Figures. The presentation should be continuous and paragraphed, i.e., without headings like Introduction, Materials, and Methods, etc. A short communication paper should have an **Abstract** containing the gist of the article and should not exceed 60 words, followed by **Keywords.**

3. **Declarations:** While submitting, the corresponding **a**uthor will have to make a declaration mentioning the laboratory/laboratories in which the work was carried out and certifying that the contents of the paper were not published before or submitted for publication in any other journal and that all the co-authors have given their consent for the article to be considered by the Editorial Board for publication in the Journal of Bangladesh Academy of Sciences.

Declaration of conflicting interests

The corresponding author must provide a formal conflict of interest statement for all authors disclosing any financial and personal relationships with other people or organizations that could inappropriately influence (bias) their work. If no conflict exists, please state that 'The author(s) declare(s) that they have no conflicts of interest regarding the publication of this article.'

4. The manuscript should be submitted in pdf or MS Word or LaTex files through online at www.bas.org.bd/publications/jbas.html. Equations generated by using Math Type or Math ML should be incorporated in the text.

   Soft copies of manuscripts with tables, graphs, illustrations, and photographs placed correctly in a printable format are to be submitted. Authors wishing to publish coloured schemes/diagrams/ sketches/photographs in their papers need to pay for the printing charges of one format. This will be charged only after the acceptance of the manuscripts for publication in the JBAS.

   The manuscript submitted should also contain a separate list of tables, figures, illustrations, photographs, and sketches with appropriate captions.

5. Electronic versions of final galley proofs will be sent to authors. No alteration in the title or additions in the text is desirable at this stage.

6. All correspondence for publication should be made on www.bas.org.bd/publications/jbas.html to the **Editor, Journal of Bangladesh Academy of Sciences, National Science and Technology Complex, Agargaon, Dhaka 1207.**

N.B.: No paper will be accepted for publication if it does not conform to the style specified for the journal and approved by the Editorial Board, which has the authority to accept or reject the manuscript of a paper submitted without showing any reason.